

**INTEGRATED FLOOD MODELING FOR IMPROVED
UNDERSTANDING OF RIVER-FLOODPLAIN HYDRODYNAMICS:
MOVING BEYOND TRADITIONAL FLOOD MAPPING**

by

Siddharth Saksena

A Dissertation

Submitted to the Faculty of Purdue University

In Partial Fulfillment of the Requirements for the degree of

Doctor of Philosophy



Lyles School of Civil Engineering

West Lafayette, Indiana

August 2019

**THE PURDUE UNIVERSITY GRADUATE SCHOOL
STATEMENT OF COMMITTEE APPROVAL**

Dr. Venkatesh Merwade, Chair

Department of Civil Engineering

Dr. Dennis Lyn

Department of Civil Engineering

Dr. Sara McMillan

Department of Agricultural and Biological Engineering

Dr. Marty Frisbee

Department of Earth, Atmospheric and Planetary Sciences

Approved by:

Dr. Dulcy Abraham

Head of the Graduate Program

For my wife, Vaidehi

ACKNOWLEDGMENTS

I thank Dr. Venkatesh Merwade for being a wonderful advisor and mentor over the last several years. His constant support and guidance have had an immeasurable impact on my development as a researcher. I would also like to extend my sincere gratitude to my dissertation committee members, Dr. Dennis Lyn, Dr. Sara McMillan and Dr. Marty Frisbee, who have provided insights and helpful comments for improving the quality of this research. I also thank Ms. Kimberly Peterson for proof-reading the research papers submitted as a part of this dissertation.

I would especially like to thank Sayan Dey for being a great friend and colleague during my PhD and offering his help whenever I needed it. Adnan Rajib, your continued support, friendship and advice has been invaluable during my journey as a graduate student. I am also grateful to Peter Singhofen for his constant guidance, support, mentorship and encouragement. Finally, I would thank all my department colleagues with whom I have had a memorable journey.

TABLE OF CONTENTS

LIST OF TABLES	ix
LIST OF FIGURES	xi
ABSTRACT	xv
1. INTRODUCTION	1
1.1 Background and Motivation	1
1.2 Research Objectives.....	4
1.3 Organization of this Dissertation	6
2. FLOOD INUNDATION MODELING AND MAPPING BY INTEGRATING SURFACE AND SUBSURFACE HYDROLOGY WITH RIVER HYDRODYNAMICS.....	7
2.1 Abstract	7
2.2 Introduction.....	7
2.3 Study Area and Data	10
2.4 Model Description	12
2.4.1 The surface system	13
2.4.2 The vadose zone	14
2.4.3 The saturated groundwater system	16
2.4.4 Integrating surface and subsurface systems.....	16
2.4.5 Time marching scheme.....	17
2.5 Model Description	19
2.5.1 Creation of ICPR model configurations	19
2.5.1.1 Subsurface model discretization (C1)	19
2.5.1.2 Subsurface model discretization (C2 and C3).....	20
2.5.2 Model simulations using three configurations.....	24
2.5.3 Statistical comparison of model.....	25
2.5.4 Spatial aggregation of model	25
2.6 Results and Discussion	26
2.6.1 Comparison of the three model configurations	26
2.6.1.1 Comparison of model outputs with observed data	26
2.6.1.2 Statistical comparison of model performance	32

2.6.2	Quantification of the relative contribution of watershed processes.....	33
2.6.3	Evaluating the effect of antecedent soil conditions on flood output	36
2.6.4	Further validation of C3 model.....	39
2.7	Summary and Conclusion	44
3.	ANALYZING THE INFLUENCE OF SPATIAL SCALE ON PHYSICAL PROCESS REPRESENTATION IN INTEGRATED MODELS FOR IMPROVED FLOOD SIMULATIONS	48
3.1	Abstract	48
3.2	Introduction.....	48
3.3	Study Area and Data	51
3.4	Model Description	54
3.4.1	Characteristics of surface and subsurface zones.....	54
3.4.1.1	Surface water zone or overland flow region.....	54
3.4.1.2	Vadose zone characterization	55
3.4.1.3	Two-dimensional groundwater characterization	58
3.4.2	Mesh development for surface and GW zones	58
3.4.3	Model parameterization	60
3.5	Model Development and Numerical Simulation	62
3.5.1	Development of model configurations	62
3.5.1.1	Effect of spatial scaling of model extents.....	62
3.5.1.2	Two model structures for analyzing the effect of spatial extent scaling	62
3.5.1.3	Effect of stream length scaling	65
3.5.1.4	Effect of changing the intrinsic scale (or resolution) of the GW sub-model.....	68
3.5.2	Numerical simulation and statistical analysis of watershed responses.....	68
3.6	Results and Discussion	69
3.6.1	Validation of uncalibrated model parameters for multiple events using <i>S-2</i>	69
3.6.2	Analyzing the effect of spatial extent scaling.....	71
3.6.2.1	Comparison of streamflow and flood extents.....	71
3.6.2.2	Comparing volumetric contributions for ' <i>S-2</i> ' and ' <i>L-2</i> '	74
3.6.2.3	Temporal scale analysis of GW fluxes for <i>S-2</i>	75
3.6.3	Analyzing the effect of spatial stream length scaling.....	76

3.6.3.1	Effect of modifying channel roughness for a fixed stream length for <i>S-2</i>	76
3.6.3.2	Effect of stream length scaling assuming a constant channel roughness	77
3.6.3.3	Effect of variable roughness distribution on a fixed reach length	80
3.6.4	Evaluating the effect of changing the intrinsic scale of the GW sub-model	81
3.6.5	Scaling of model extents by modifying the intrinsic scales of sub-models.....	83
3.6.6	Validation of improved spatial scale representation at another watershed.....	86
3.7	Summary and Conclusions	89
4.	OBJECTIVE-ORIENTED HYBRID FLOOD MODELING BY COUPLING EMPIRICALLY-BASED AND PHYSICALLY-BASED MODEL FORMULATIONS IN A SINGLE SYSTEM.....	92
4.1	Abstract	92
4.2	Introduction.....	93
4.3	Study Area and Data	97
4.4	Development and illustration of the hybrid flood modeling approach.....	100
4.4.1	Hybrid model structure for the SW system	100
4.4.2	Hybrid model structure for the vadose zone.....	101
4.4.3	Hybrid model structure for the GW region.....	102
4.4.4	Differences in model design across the three basins	103
4.5	Spatial aggregation, computational parameters and numerical simulation	106
4.6	Results and Discussion	108
4.6.1	Computational performance of ' <i>H</i> ' and ' <i>I</i> ' models	108
4.6.2	Comparison of streamflow, hydrologic volumes and extent of inundation.....	109
4.7	Summary and Conclusions	117
5.	A COMPUTATIONALLY-EFFICIENT FLOOD MODELING APPROACH FOR SIMULATING THE HYDRODYNAMICS OF UNPRECEDENTED EVENTS IN COMPLEX URBAN SYSTEMS.....	119
5.1	Abstract	119
5.2	Introduction.....	119
5.3	Study Area and Data	123
5.3.1	Study area description and history.....	123
5.3.2	Description of Hurricane Harvey.....	125

5.3.3	Study area delineation.....	125
5.3.4	Data acquisition	126
5.4	Methodology.....	128
5.4.1	Incorporating a computationally-efficient model structure	129
5.4.2	Model parameterization and numerical simulation	132
5.5	Results and Discussion	134
5.5.1	Evaluation of the computational efficiency of the proposed approach	134
5.5.2	Comparison of modeled stages across scales	136
5.5.3	Statistical evaluation of model performance	140
5.5.4	Comparison of the proposed approach with a fixed-resolution approach	143
5.5.5	Assessment of flood inundation volumes and extents	145
5.5.6	Importance of inclusion of local hydraulics of urban systems	150
5.6	Summary and Conclusions	151
6.	SYNTHESIS.....	154
6.1	Summary.....	154
6.2	Limitations and Future Work.....	156
	APPENDIX.....	158
	REFERENCES	172
	VITA.....	185

LIST OF TABLES

Table 2.1 Watershed Characteristics.....	11
Table 2.2 ICPR uncalibrated subsurface and surface roughness parameters.....	23
Table 2.3 Spatial aggregation of C1, C2 and C3	26
Table 2.4 Comparison of model performance for peak and lowest streamflow	28
Table 2.5 Statistical analysis of model performance	33
Table 2.6 Hydrologic and hydraulic outputs for multiple antecedent soil conditions.....	36
Table 2.7 Statistical analysis of streamflow prediction for model validation.....	42
Table 3.1 Description of datasets and watershed characteristics.....	53
Table 3.2 ICPR initial subsurface and surface roughness parameters	61
Table 3.3 Description of model configurations	64
Table 3.4 Spatial aggregation and geometric characteristics for the integrated model configurations with different SW-GW mesh resolutions.....	65
Table 3.5 Geomorphologic characteristics of study reaches used for analyzing the effect of stream length scaling on hydraulic outputs	67
Table 3.6 Statistical comparison of streamflow hydrographs for small and large spatial extents	71
Table 3.7 Effect of reach length and river channel roughness on hydraulic routing characterized by comparing streamflow hydrographs	78
Table 3.8 Improvement in streamflow estimation using a distributed channel roughness and optimal process interaction scales.....	81
Table 4.1 Description of watershed characteristics	97
Table 4.2 Spatial aggregation and computational parameters for UWR, WCC and WHR basins	107
Table 4.3 Simulation times for hybrid (<i>H</i>) and fully-integrated (<i>I</i>) models	109
Table 4.4 Statistical parameters for streamflow comparison.....	110
Table 5.1 Watershed characteristics for the ‘ <i>large</i> ’ and ‘ <i>small</i> ’ model.....	128
Table 5.2 Initial values of subsurface parameters using in ICPR.....	133
Table 5.3 Computational elements and performance for ‘ <i>small</i> ’, ‘ <i>large</i> ’, and ‘ <i>small-fixed</i> ’ models	135
Table 5.4 Median values of model performance statistics across all gages.....	141

Table 5.5 Quantitative assessment of flood extents with the FEMA Damage Assessment dataset
..... 149

LIST OF FIGURES

Fig. 1.1 FEMA 100-year flood zone and groundwater recharge map for a portion of the Wabash River Basin in Indiana, USA	2
Fig. 2.1 Location and land use map for the unregulated portion of the UWR basin	12
Fig. 2.2 ICPR project process diagram	14
Fig. 2.3 Mesh structure within ICPR for the Upper Wabash Basin.....	17
Fig. 2.4 Conceptual illustration of C1, C2, C3 and vadose zone infiltration.....	21
Fig. 2.5 (a) Streamflow hydrographs at the outlet; (b) stage at outlet gage station; (c) streamflow scatterplots; and (d) stage scatterplots for C1, C2, and C3 for a 25-day simulation (April 16th to May 10th, 2013).....	29
Fig. 2.6 Cross-sectional profiles for C1, C2 and C3 for (a) peak streamflow and (b) lowest streamflow.....	31
Fig. 2.7 (a) Streamflow hydrograph; (b) cumulative surface volumes; (c) volumetric contributions from rainfall; and (d) volumetric contributions from the subsurface for a 25-day simulation (April 16th to May 10th, 2013).....	34
Fig. 2.8 (a) Streamflow at outlet; (b) cumulative outflow volume through the outlet; (c) cumulative change in vadose zone storage; (d) cumulative GW recharge; and flood inundation maps at peak flow for (e) dry (D); (f) moderate (M); and (g) wet (W) subsurface conditions for 12.5 day simulation (April 16 th to April 28 th , 2013).....	38
Fig. 2.9 Model comparison and validation for a three-month continuous simulation (February 17 th to May 15 th , 2018) for the UWR basin	40
Fig. 2.10 Location map for East Branch Croton River Basin in New York.....	41
Fig. 2.11 Streamflow comparison against observed data across two gages for East Branch Croton River, NY for a five-month simulation (May 1st to September 30th, 2011).....	43
Fig. 3.1 Study area description for the UWR and WHR basin.....	54
Fig. 3.2 (a) Conceptual model identifying the physical systems, processes, and model structure used for integrated modeling; (b) illustration of the vertical layer method for infiltration; (c) 2D overland flow routing and finite volume illustration; and (d) elemental description of finite element formulation used for 2D GW flow.....	57
Fig. 3.3 (a) Road network and pond ingestion in ICPR for WHR region and (b) illustration of breaklines and breakpoints used for mesh generation	59
Fig. 3.4 Illustration of (a) two spatial extents used in this study with upstream USGS gages; (b) location of USGS gages used for testing the effect of spatial stream length scaling(c) fine resolution triangular mesh; and (d) fine resolution honeycomb mesh.....	63

Fig. 3.5 Model validation using <i>S-2</i> for (a) streamflow at outlet (April-July 2013); (b) depth at outlet (April-July 2013); (c) streamflow at Tippecanoe River (April-July 2013); (d) maximum flood extent comparison with reference map (HEC-RAS) for April-July 2013; (e) streamflow at outlet (February-May 2018); and (f) streamflow at outlet (May 2009).....	70
Fig. 3.6 (a) – (f) Effect of spatial extent scaling on streamflow hydrographs; and (g) – (h) evolution of subsurface processes at small (<i>S-2</i>) and large (<i>L-2</i>) spatial extents	72
Fig. 3.7 Illustration of difference in extent of inundation when peak streamflow is observed at the outlet for <i>S-1</i> , <i>S-2</i> , <i>L-1</i> , and <i>L-2</i>	73
Fig. 3.8 Evolution of GW seepage fluxes over time for <i>S-2</i>	76
Fig. 3.9 Flow hydrographs using <i>L-2</i> model for (a) Eel River at Logansport; (b) Tippecanoe River at Delphi; and Wabash River at (c) Wabash; (d) Peru; (e) Logansport and (f) Lafayette	79
Fig. 3.10 Flow hydrographs for <i>L-3</i> at (a) Wabash River at Logansport; and (b) Wabash River at Lafayette	80
Fig. 3.11 Flow hydrographs for (a) <i>S-3</i> and (b) <i>S-4</i> at Lafayette; (c) <i>L-4</i> at Wabash; (d) <i>L-4</i> at Peru; (e) <i>L-4</i> at Logansport; and (f) <i>L-4</i> at Lafayette	83
Fig. 3.12 Variation of statistical performance in streamflow prediction across four USGS gages using <i>L-1</i> , <i>L-2</i> and <i>L-4</i> model configurations	85
Fig. 3.13 Analysis of change in median water table depth during the 120-day simulation across the common region of small and large scale models	86
Fig. 3.14 (a) and (b) Streamflow hydrographs for <i>WHR 1</i> and <i>WHR 2</i> ; (c) and (d) scatter plots at the outlet for <i>WHR 1</i> and <i>WHR 2</i> ; (e) and (f) volumetric contributions from hydrologic processes for <i>WHR 2</i>	88
Fig. 4.1 (a) Flood modeling using loosely-coupled hydrologic-hydraulic models and (b) flood modeling using integrated models	96
Fig. 4.2 Location and land use distribution of three study areas in Indiana (a) a portion of the Upper Wabash River (UWR) basin; (b) Wildcat Creek (WCC) basin; and (c) White River (WHR) basin	99
Fig. 4.3 Illustration of the hybrid modeling structure for (a) UWR and (b) WCC basin	104
Fig. 4.4 Hybrid model for WHR basin used for validation	105
Fig. 4.5 Streamflow hydrographs and scatter plots showing the performance of integrated (<i>I</i>) and hybrid (<i>H</i>) models for (a) – (d) 25-day period from April 16 th to May 9 th 2013; and (e) – (h) 90-day period from February 15 th to May 15 th 2018.....	112
Fig. 4.6 Streamflow hydrographs and scatter plots for (a) – (d) 21-day period for the WCC basin from April 5 th to April 25 th 2013; (e) – (f) 45-day period for the WCC basin from April 20 th to June 4 th 2016; (g) – (h) 31-day period for the WHR basin from April 7 th to May 7 th 2013.....	113
Fig. 4.7 Maximum extent of inundation (2013) for (a) fully-integrated model (<i>I</i>) and (b) hybrid model (<i>H</i>) for the UWR basin.....	114

Fig. 4.8 Maximum extent of inundation (April 2013) for (a) hybrid (<i>H</i>) model and (b) fully-integrated model (<i>I</i>) for the WCC basin	115
Fig. 4.9 Volumetric contributions from hydrologic processes for the hybrid (<i>H</i>) and fully-integrated (<i>I</i>) models for the WCC basin.....	116
Fig. 5.1 (a) Study area location, USGS gage locations, drainage network and NLDAS fishnet for a portion of the Harris County, TX (b) land use distribution, reservoir location and extents of ‘ <i>small</i> ’ and ‘ <i>large</i> ’ models	124
Fig. 5.2 Isohyetal map of rainfall distribution during Hurricane Harvey	127
Fig. 5.3 Conceptual illustration of physical processes using ICPR.....	129
Fig. 5.4 Computationally-efficient model structure (1): 1D flow region inside the stream; (2) Interface between 1D and 2D regions usually along the levees; (3) road networks delineated as ‘breaklines’ to establish important topographic variations; (4) 2D overland flow region solved using diffusive wave equation; (5) location denotes example of flexible mesh structure where more vertices are placed near bends and confluences; (6) 1D node-link structure and cross sections along nodes denoting locations where energy equation is applied; (7) locations where USGS stream gage inflow is used as boundary condition; (8) ungaged streams inside subbasins where no gage information is available; (9) location denoting the direction of flow in the stream; (10) location denoting fine resolution mesh around the streams and coarser elsewhere; and (11) fine resolution (15-m) delineation of important features such as George Bush Intercontinental Airport (IAH) in Houston, TX.....	130
Fig. 5.5 Honeycomb mesh resolution across (a) <i>large</i> model and (b) <i>small</i> model	132
Fig. 5.6 Stage comparisons with observed data for <i>small</i> and <i>large</i> model across HCFCD gages	138
Fig. 5.7 (a) Stage comparisons at gages upstream of Lake Houston; (b) stage comparisons for streams draining into the HSC for <i>large</i> model.....	139
Fig. 5.8 Stage comparisons at streams without upstream gage inflow (fully-distributed rainfall-runoff-routing)	140
Fig. 5.9 Scatter plots of observed versus predicted WSE and depth for <i>small</i> and <i>large</i> model; and box plots showing the variability in model performance statistics across all gages.....	142
Fig. 5.10 Scatter plots showing the performance of the ‘ <i>small-fixed</i> ’ model in predicting WSE and depth.....	144
Fig. 5.11 Volumetric contributions from watershed processes scaled with respect to total area for (a) subsurface and (b) surface; and flood extent at peak surface storage volume for (c) <i>small</i> model and (d) <i>large</i> model.....	146
Fig. 5.12 Qualitative assessment of predicted flood inundation extents across four locations: (a) North Braeswood Boulevard, Houston, TX ; (b) South Freeway towards downtown Houston; (c) West District Waste Water Treatment Plant (WWTP); and (d) San Jacinto River – Houston Shipping Channel Confluence at Lynchburg, TX (Image source: Fig. 5.12a and 5.12b:	

https://www.washingtonpost.com/graphics/2017/national/harvey-photos-before-after/ and Fig. 5.12c and 5.12d: https://storms.ngs.noaa.gov/storms/harvey/index.html).....	148
Fig. 5.13 Histogram depicting the percentage of points against the error in predicted depth for <i>small</i> and <i>large</i> model.....	150
Fig. 5.14 Illustration of the effect of local hydraulics along the Brays Bayou (Image source: https://www.google.com/maps).....	151

ABSTRACT

Author: Saksena, Siddharth. PhD

Institution: Purdue University

Degree Received: August 2019

Title: Integrated Flood Modeling for Improved Understanding of River-Floodplain

Hydrodynamics: Moving beyond Traditional Flood Mapping

Committee Chair: Venkatesh Merwade

With increasing focus on large scale planning and allocation of resources for protection against future flood risk, it is necessary to analyze and improve the deficiencies in the conventional flood modeling approach through a better understanding of the interactions between river hydrodynamics and subsurface processes. Recent studies have shown that it is possible to improve the flood inundation modeling and mapping using physically-based integrated models that incorporate observable data through assimilation and simulate hydrologic fluxes using the fundamental laws of conservation of mass at multiple spatiotemporal scales. However, despite the significance of integrated modeling in hydrology, it has received relatively less attention within the context of flood hazard. The overall aim of this dissertation is to study the heterogeneity in complex physical processes that govern the watershed response during flooding and incorporate these effects in integrated models across large scales for improved flood risk estimation. Specifically, this dissertation addresses the following questions: (1) Can physical process incorporation using integrated models improve the characterization of antecedent conditions and increase the accuracy of the watershed response to flood events? (2) What factors need to be considered for characterizing scale-dependent physical processes in integrated models across large watersheds? (3) How can the computational efficiency and process representation be improved for modeling flood events at large scales? (4) Can the applicability of integrated models be improved for capturing the hydrodynamics of unprecedented flood events in complex urban systems?

To understand the combined effect of surface-subsurface hydrology and hydrodynamics on streamflow generation and subsequent inundation during floods, the first objective incorporates an integrated surface water-groundwater (SW-GW) modeling approach for simulating flood conditions. The results suggest that an integrated model provides a more realistic simulation of flood hydrodynamics for different antecedent soil conditions. Overall, the findings suggest that the

current practice of simulating floods which assumes an impervious surface may not be providing realistic estimates of flood inundation, and that an integrated approach incorporating all the hydrologic and hydraulic processes in the river system must be adopted.

The second objective focuses on providing solutions to better characterize scale-dependent processes in integrated models by comparing two model structures across two spatial scales and analyzing the changes in flood responses. The results indicate that since the characteristic length scales of GW processes are larger than SW processes, the intrinsic scale (or resolution) of GW in integrated models should be coarser when compared to SW. The results also highlight the degradation of streamflow prediction using a single channel roughness when the stream length scales are increased. A distributed channel roughness variable along the stream length improves the modeled basin response. Further, the results highlight the ability of a dimensionless parameter η_L , representing the ratio of the reach length in the study region to maximum length of the single stream draining at that point, for identifying which streams may require a distributed channel roughness.

The third objective presents a hybrid flood modeling approach that incorporates the advantages of both loosely-coupled ('downward') and integrated ('upward') modeling approaches by coupling empirically-based and physically-based approaches within a watershed. The computational efficiency and accuracy of the proposed hybrid modeling approach is tested across three watersheds in Indiana using multiple flood events and comparing the results with fully-integrated models. Overall, the hybrid modeling approach results in a performance comparable to a fully-integrated approach but at a much higher computational efficiency, while at the same time, providing objective-oriented flexibility to the modeler.

The fourth objective presents a physically-based but computationally-efficient approach for modeling unprecedented flood events at large scales in complex urban systems. The application of the proposed approach results in accurate simulation of large scale flood hydrodynamics which is shown using Hurricane Harvey as the test case. The results also suggest that the ability to control the mesh development using the proposed flexible model structure for incorporating important physical and hydraulic features is as important as integration of distributed hydrology and hydrodynamics.

1. INTRODUCTION

1.1 Background and Motivation

According to the National Weather Service, the United States recorded four major Hurricanes (Harvey, Irma, Jose and Maria) in the year 2017 alone resulting in severe flooding with multiple fatalities and over \$300 billion in economic damages. Recent studies have highlighted that human-induced climate change may have been an important factor in increasing the total and maximum rainfall during these hurricanes (Risser and Wehner, 2017). Further, the reduction of hurricane translation speed and increase in moisture-content carrying capacity due to increasing surface temperatures are factors that may result in more intense storms and subsequent rainfall in the future (Kossin, 2018; van Oldenborgh et al., 2018). Increasing urbanization can cause significant shifts in land use patterns in coastal cities, resulting in increased impervious surface, which can further intensify flood risk in the future. With the increasing intensity and spatial influence of unprecedented flood events, the question that the research community needs to address is whether the conventional techniques for flood prediction can capture the dynamic and compound nature of these events across large scales and identify regions that are more susceptible to flooding.

One of the major limitations of the conventional flood modeling approach is that it does not account for antecedent subsurface conditions and existing floodplain storage due to the lack of model physicality. In the case of streamflow prediction for large watersheds, the importance of antecedent moisture conditions is well accepted and studied within the hydrologic community (Castillo et al. 2003; Meyles et al. 2003; Rajib et al. 2016). However, when it comes to simulating the hydrodynamics of rivers and their floodplains for flood modeling, the role of subsurface storage and/or floodplain storage has been ignored. Saturated conditions in subsurface and floodplain can lead to more severe inundation from low intensity but continuous flood events (Govindaraju and Kavvas 1991; Ivkovic et al. 2009). An example of such a catastrophe is Hurricane Frances (2004), where the rainfall due to Hurricane Ivan (2004) had already saturated the subsurface in North Carolina, and therefore, the impact of Frances-induced rainfall became more severe and caused significant flooding and landslides. Recently, this phenomenon was repeated in North Carolina during Hurricane Matthew (Weaver et al. 2016).

Thus, evaluating the relative contribution from subsurface flow during and after flood events needs further investigation to identify flood-prone areas more accurately. There is a direct correlation between the regions that have a higher flood risk and the regions that have physical characteristics conducive to high groundwater recharge as shown in Fig. 1.1. Therefore, it is imperative to relate subsurface and river-floodplain hydrodynamics to understand and quantify the physical processes that occur simultaneously during highly intense flood events.

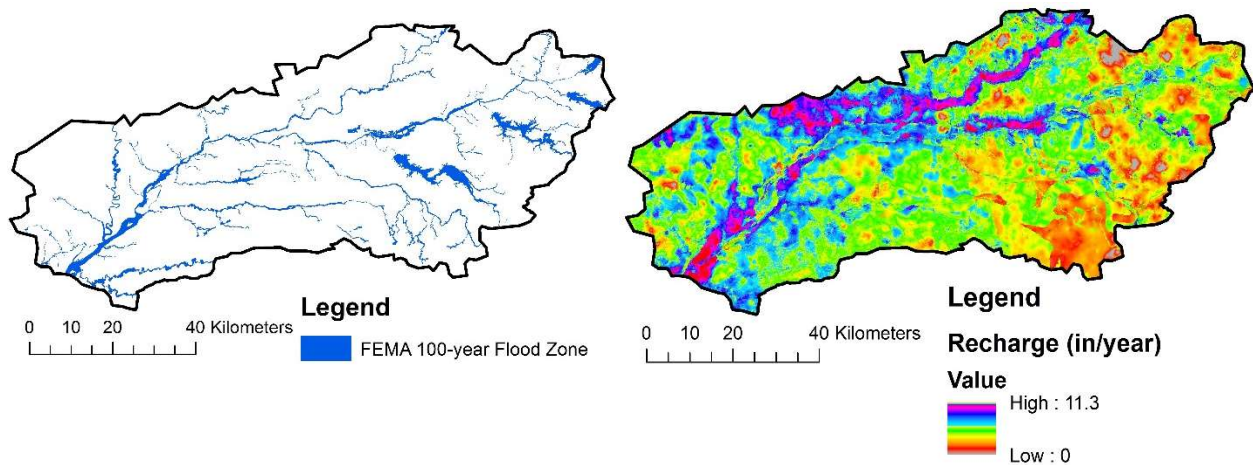


Fig. 1.1 FEMA 100-year flood zone and groundwater recharge map for a portion of the Wabash River Basin in Indiana, USA

Large scale water management decisions often rely on a thorough understanding of how one water resource affects another which can only be accomplished by tracking the flow of water from the atmospheric system to the surface-groundwater system. Several water-resource issues arise at large watershed scales affecting multiple states, and therefore, national agencies such as the United States Geological Survey (USGS) and the Environmental Protection Agency (EPA) are focusing on developing large scale water management policies (Winter et al., 1999). For example, over the last century, several natural wetlands and river floodplains that contributed in attenuating the impact of extreme rainfall were replaced for constructing levees, reservoirs, agricultural growth, and urbanization, leading to increased impervious regions and an alteration of existing flow paths, thereby leading to higher runoff volumes and subsequent flooding (Hutchins et al., 2017). Due to these issues, even the U.S. Army Corps of Engineers (USACE), that led the implementation of most structural measures in the U.S., is focusing on implementation of more and more nonstructural measures in the form of floodplain storage or creating wetlands for

attenuating flood peaks (Brody et al., 2008; Kundzewicz, 2002). Therefore, instead of focusing on construction of reservoirs for surface storage, there is a growing interest in addressing flood related issues through natural alternatives.

This shift in focus from structural to nonstructural measures is driven by the goal to achieve environmental sustainability in flood damage reduction (Bednarek, 2001). For example, nonstructural or “soft” flood mitigation measures involve retaining the natural characteristics of floods, by letting the regions in the floodplain sustain the extra volume of water during a flood (Kundzewicz, 2002). In addition to providing flood protection by increasing surficial storage, restored floodplains around the riverbanks can cause the underlying shallow water table to directly transpire water to the atmosphere which can increase the lateral inflow of surface water for recharging groundwater, thereby reducing the overland storage. However, to predict flood risk accurately through nonstructural measures, it is essential to know the factors that are responsible for causing floods under various settings and revisit the assumptions of the conventional flood modeling approach. In addition to flood protection, improved understanding of river-floodplain hydrodynamics can be used for reducing environmental impacts of fertilizer applications through nutrient and pollutant retention (Noe and Hupp 2005; Tuttle et al. 2014). Identification of locations ideal for floodplain restoration can not only help in reducing the impact of floods, but due to increased river-floodplain interactions, it can also help in improving the water quality of streams (McMillan and Noe 2017; Richardson et al. 2011). This can only be accomplished by integrating the feedbacks from multiple watershed processes during flood events in a single system.

This dissertation addresses the issues and challenges with the conventional flood modeling approach, while advocating for a large scale integrated approach to flood inundation modeling and mapping. The overall aim of this dissertation is to study the heterogeneity in complex physical processes that govern the watershed response during flooding and incorporate these effects in integrated models across large scales for improved flood risk estimation. The broader goal of this dissertation is to enhance the science of flood modeling through a better understanding of watershed processes to enable real-time flood prediction and forecasting across large watershed scales. Specifically, this dissertation addresses the following questions: (1) Can physical process incorporation using integrated models improve the characterization of antecedent conditions and increase the accuracy of the watershed response to flood events? (2) What factors need to be

considered for characterizing scale-dependent physical processes in integrated models across large watersheds? (3) How can the computational efficiency and process representation be improved for modeling flood events at large scales? (4) Can the applicability of integrated models be improved for capturing the hydrodynamics of unprecedented flood events in complex urban systems?

1.2 Research Objectives

Considering that the application of integrated models for flood simulation is in a nascent stage, this dissertation aims to improve the physical process characterization and computational efficiency of integrated models across large spatial scales. The following are the specific research objectives of this dissertation:

1. **Evaluate the impact of physical process integration on flood modeling:** This objective hypothesizes that the overall flood response is not only influenced by the surface water flow, but also by SW-GW interactions. Specific tasks in this objective include: (i) Comparing the change in flood prediction by changing the level of process-based detail in flood models; (ii) Quantifying the relative contribution of watershed processes during flooding; (iii) Evaluating the effect of antecedent soil conditions on flood outputs; and (iv) application of integrated models under different flow and watershed conditions.
2. **Identify optimal spatial scaling schemes for large scale integrated flood modeling:** This objective aims to improve the spatial extent scaling of integrated models through a better representation of the intrinsic scales of the physical processes for providing a more realistic simulation of the basin response not only at the outlet, but also within the watershed. This objective is accomplished through the following steps: (i) Analyzing the effect of spatial scaling of model extents on the SW-GW physical processes by quantifying the changes in basin response across a small and large sub-watershed for the same region; (ii) Relating the change in the basin response using a single channel roughness to the stream length scales within a watershed; and (iii) Evaluating the effect of changing the intrinsic scale (or resolution) of GW with respect to SW by quantifying the change in streamflow prediction.
3. **Incorporate computationally-efficient hybrid techniques for improved physical process representation:** This objective aims to test a hybrid flood modeling approach that

incorporate the advantages of both loosely-coupled ('downward') and integrated ('upward') modeling approaches by coupling empirically-based and physically-based models within a watershed. Specific steps include: (i) Reducing the model complexity using fully-integrated modeling only across specific user-defined regions inside the watersheds; (ii) Coupling an empirically-based hydrologic modeling approach with the one-dimensional energy equation in the lower order streams to improve the streamflow prediction; and (iii) Incorporating a physically-based infiltration method, coupled with a simplistic NRCS Unit Hydrograph method to improve computational efficiency.

4. **Improve the applicability of integrated models for flood simulation across complex urban systems:** This objective aims to simulate the hydrology and hydrodynamics of unprecedented events in complex urban systems at large scales by: (i) Integration of physical processes including river-floodplain and surface-subsurface interactions; (ii) Application of a flexible spatiotemporal mesh structure for maximizing efficiency while maintaining accuracy; and (iii) Incorporation of engineered systems such as weirs, bridges, man-made channels, road networks and levees. The efficacy of this approach in capturing the flood hydrodynamics of unprecedented flood events at large scales is evaluated by using Hurricane Harvey as the test case.

Since the objectives highlighted above require an extensive analysis of physical processes using high resolution datasets at variable spatiotemporal scales, the Interconnected Channel and Pond Routing (ICPR) software, developed by Streamline Technologies (2018), is chosen for this research. ICPR's capabilities to simulate the complex surface-subsurface dynamics are unmatched by other models in both industry and academia. Being a physically-based, distributed, two-dimensional, integrated model, it is ideally suited to address the research questions posed in this dissertation. The objectives of this dissertation are accomplished using three watersheds in Indiana, namely, Upper Wabash River Basin, White River Basin and Wildcat Creek Basin. Additionally, the Croton River Basin in New York and a system of multiple urban watersheds located in Harris County, Texas are also used. More details on these watersheds are provided in subsequent chapters.

1.3 Organization of this Dissertation

This dissertation consists of six chapters. Chapters 2-5 are based on the four research objectives highlighted in Section 1.2. While these chapters are connected under the overarching goal to understand the role of the fundamental physical processes influencing watershed response and improve the science of flood prediction, each chapter individually identifies its specific objectives. Therefore, each chapter has its own abstract, introduction, description of study area, methodology, results and conclusions. Chapter 6 summarizes the dissertation and provides directions for future applications.

2. FLOOD INUNDATION MODELING AND MAPPING BY INTEGRATING SURFACE AND SUBSURFACE HYDROLOGY WITH RIVER HYDRODYNAMICS

2.1 Abstract

Modeling and mapping of floods using one (1D) and two-dimensional (2D) models has resulted in significant progress in our understanding of river hydraulics and hydrology. The conventional modeling approach can be improved further through a better understanding of the interactions between river hydrodynamics and subsurface processes. Saturated conditions in subsurface and floodplains can lead to longer and deeper inundation from low intensity but continuous flood events. To understand the combined effect of surface-subsurface hydrology and hydrodynamics on streamflow generation and subsequent inundation during floods, this study uses an integrated surface water-groundwater (SW-GW) modeling approach for simulating flood conditions. Simulation of a high flooding event for the Upper Wabash River basin in Indiana, USA, shows that the river-floodplain hydrodynamics is simulated more accurately without the need for extensive calibration by using a two-dimensional integrated SW-GW model. Additionally, an integrated model provides a more realistic simulation of flood hydrodynamics for different antecedent soil conditions. Specifically, results show that the streamflow, flood stages and inundation area obtained for the dry scenario are significantly lower when compared to the saturated scenario. These findings are further validated by applying the integrated modeling approach for an entirely different watershed (Croton River) in the state of New York. Overall, the findings from this study suggest that the current practice of simulating floods which assumes an impervious surface may not be providing realistic estimates of flood inundation, and that an integrated approach incorporating all the hydrologic and hydraulic processes in the river system must be adopted.

2.2 Introduction

Most flood models are primarily driven by an upstream flow boundary condition to simulate the river hydrodynamics in one- or two dimensions to get the water surface elevation (WSE), velocity and extent of inundation for a study reach. The key inputs for this approach include

topography to define the river geometry, streamflow, and the roughness coefficient (Manning's n). It is well documented in the literature that the current flood modeling approach is affected by several uncertainties arising from discharge estimates, topographic data, model selection, and parameterization, among others (Cook and Merwade, 2009; Hall et al., 2005; Legleiter et al., 2011; Merz and Thielen, 2005; Pappenberger et al., 2006; Saksena and Merwade, 2015; Straatsma and Huthoff, 2011). Some of these uncertainties can be addressed by using accurate topographic data at fine resolution (Bhuyian et al., 2015; Saksena and Merwade, 2015), accurate discharge data, and better model parameterization and calibration through satellite-based products (Cohen et al., 2018; Dey et al., 2019; Di Baldassarre et al., 2009; Schumann et al., 2007).

One of the limitations of simulating floods in rivers using a hydrodynamic model is that it cannot incorporate the interaction between the river reach and the subsurface, which can play a critical role in dictating the duration and extent of inundation. This interaction becomes even more critical when floods are simulated over a larger stream network as opposed to individual reaches. For example, models such as RAPID (Routing Application for Parallel Computation of Discharge), LISFLOOD-FP, and AutoRoute (Bates and De Roo, 2000; David et al., 2011b; Follum et al., 2016) have been applied at the river network scale, but these models simulate only the surface water hydrodynamics. One way these models compensate for excluding some of the related physical processes in the flood hydrodynamics is through the calibration of surface roughness in the form of the Manning's n parameter (Mukolwe et al., 2014; Pappenberger et al., 2005). This calibration is generally performed by estimating stage or streamflow at the downstream model boundary. In some studies, the extent of inundation located inside the model domain (obtained from remote sensing) is used to calibrate roughness parameters (Di Baldassarre et al., 2009).

Thus, the current hydrodynamic modeling approach assumes that the observed streamflow, stage and extent of inundation are solely functions of the roughness parameter distribution, upstream streamflow forcing and topography (Bales and Wagner, 2009; Dimitriadis et al., 2016; Teng et al., 2017). However, studies have shown that several combinations of roughness parameters, even unrealistic ones, can produce reasonable results for a specific event, but not necessarily for events outside the calibration range, especially for events with different antecedent conditions (Pappenberger et al., 2006, 2005). Nevertheless, this practice of ignoring physical processes variability has continued despite several studies concluding that the lack of linkage

between surface water (SW) and groundwater (GW) contributions leads to uncertainties in the conventional flood risk models (Kidmose et al., 2015; Pahar and Dhar, 2014; Panday and Huyakorn, 2004).

Numerous models exist to individually simulate overland flow, river hydraulics, and GW flow, but these models do not account for relative interactions between these processes (Fleckenstein et al., 2010; Faulkner et al., 2012; Osei-Twumasi et al., 2016). Additionally, several past studies have highlighted the importance of subsurface contributions and antecedent conditions on the streamflow hydrograph (Berthet et al., 2009; Cooper and Rorabaugh, 1963; Hughes et al., 2011; Moench et al., 1974), but how the SW-GW interaction affects the flow hydrodynamics between the river and its floodplain needs more investigation. This study is advocating that floods should be simulated using an integrated SW-GW modeling approach that is based on the solution of the mass balance equation at every time-step and can provide a more physical representation of the river-floodplain hydrodynamics by simultaneously incorporating physical processes such as precipitation, vadose zone storage, hydraulic routing, and GW flow. In the past, integrated SW-GW modeling procedures were deemed unsuitable primarily due to the absence of accurate data, and insufficient computational power (Grimaldi et al., 2013; Saleh et al., 2011). As a result, studies focused on creating tools for loosely coupling hydraulic and hydrologic models (David et al., 2011a; Jackson and Maidment, 2014), but these techniques fail to incorporate real-time impacts of SW-GW interaction in floodplains during high flows.

With the increasing access to open source datasets and computational capabilities, more studies are focusing on using integrated SW-GW modeling procedures to simulate the hydrology and hydrodynamics of rivers (Gleeson and Manning, 2008; Kaser et al., 2014; Kollet and Maxwell, 2008; Liu et al., 2015; Saksena and Merwade, 2017a). However, many of these studies have focused on simulating hydrologic fluxes, such as streamflow, soil moisture and water table (WT) depth, without looking at how the interactions between some of these fluxes will affect the flood hydrodynamics and the subsequent inundation during a high flow event.

This study aims to address this gap by applying an integrated SW-GW model over a relatively large (area greater than 5000 km²) watershed. This study hypothesizes that an integrated SW-GW model will not only provide a better streamflow prediction, but will also result in more

accurate and robust simulation of the flood hydrodynamics with less dependence on hydraulic model calibration using Manning's n . Specifically, this study aims to prove that both the upstream and downstream boundary conditions in a flood model are dynamic, and they are not only influenced by the surface water flow, but also by SW-GW interactions.

2.3 Study Area and Data

The Upper Wabash River (UWR) basin in Indiana (5840 km²) is chosen as the test site for this study. The UWR basin is characterized by glacial till deposits, gentle slopes, fertile soils and shallow aquifers, with a deep confining layer of shale (Frisbee et al., 2017; Saksena and Merwade, 2017b). According to the National Resources Conservation Services' (NRCS) hydrologic soil group classification (Table 2.1), there is a dominance of soil group 'C' for the UWR basin, with an average vadose zone depth of 150 cm, and a shallow WT around the Wabash River. Although the watershed is primarily agricultural, the Wabash River floodplain consists of three major cities in Indiana, namely, Lafayette, Logansport, and Huntington. Additionally, according to the Flood Insurance Rate Maps (FIRMs) in this region, over 8% of the entire study area (468 km²) falls under the 100-year 'flood zone'. Because of the existence of dams and control structures on the Wabash River, only the unregulated region in the UWR basin (shown in Fig. 2.1) is selected for this analysis. Table 2.1 presents a summary of the watershed characteristics for the study area. Considering the critical role of topography and river bathymetry in hydrodynamic simulation of rivers (Dey, 2016; Saksena, 2015), a 9 m resolution topographic Digital Elevation Model (DEM) based on a LiDAR survey, obtained from the Indiana Spatial Data Portal (ISDP), is used in this study after river bathymetry incorporation.

The SW-GW integration for UWR basin is achieved by linking the unsaturated (vadose) zone with the overland flow region and the saturated zone (surficial aquifer). This type of modeling for a large area is data intensive and requires surface information in the form of topography, land use, and surface roughness (Manning's n); climate information in the form of rainfall and streamflow; and subsurface information in the form of vadose zone and aquifer properties. The land use data for the study are obtained from the National Land Cover Database (NLCD: <http://nationalmap.gov/viewer.html>). The values of Mannings' roughness corresponding to the eleven land use classes in NLCD are adapted from Chow (1959). Impervious cover data in the

form of a raster grid is downloaded from the Indiana Map Data Server (USGS, 2006). For the subsurface part, vadose zone properties such as moisture content, vertical conductivity and soil type are characterized using information from the NRCS's Gridded Soil Survey Geographic (gSSURGO) Database. Hourly rainfall data for the 9 climate stations in the UWR basin are obtained from the National Oceanic and Atmospheric Administration's (NOAA) Climate Data Online (CDO), and instantaneous streamflow and gage height data for 9 stations are obtained from the United States Geological Surveys' (USGS) National Water Information System (<http://waterdata.usgs.gov/nwis/rt>). Information on crop-type and frequency of crop plantation for calculating evapotranspiration rates is obtained from the 2011 National Cropland Data Layer (NCDL), which is developed by the United States Department of Agriculture (USDA: <https://nassgeodata.gmu.edu/CropScape/>).

Table 2.1 Watershed Characteristics

Drainage Area, km ²	5,840
Landuse as per NLCD 2011 (%)	
Agricultural	82
Forest	7
Water	2
Urban/Impervious	9
No. of NCDC rainfall weather stations	9
No. of USGS streamflow gages	9
Soil Type as per NRCS gSSURGO (%)	
A	2
B	36
C	61
D	1

Water surface elevations obtained from USGS gage data are used as an upstream boundary forcing for the Wabash River and its tributaries within the watershed. The outlet of the model is located at the USGS gage 03335500, Wabash River at Lafayette. Water table information in the form of contour maps are obtained from the Indiana Department of Natural Resources' (IDNR) Potentiometric Surface Maps (<http://www.in.gov/dnr/water/7256.htm>), which are converted into gridded raster formats at a spatial resolution of 30 m. using ArcGIS. Similarly, the shallow aquifer thickness information found in the Indiana Geographic Information Council's (IGIC) Indiana Map

server (<http://maps.indiana.edu/index.html>) is used for characterizing the surficial aquifer for the study area.

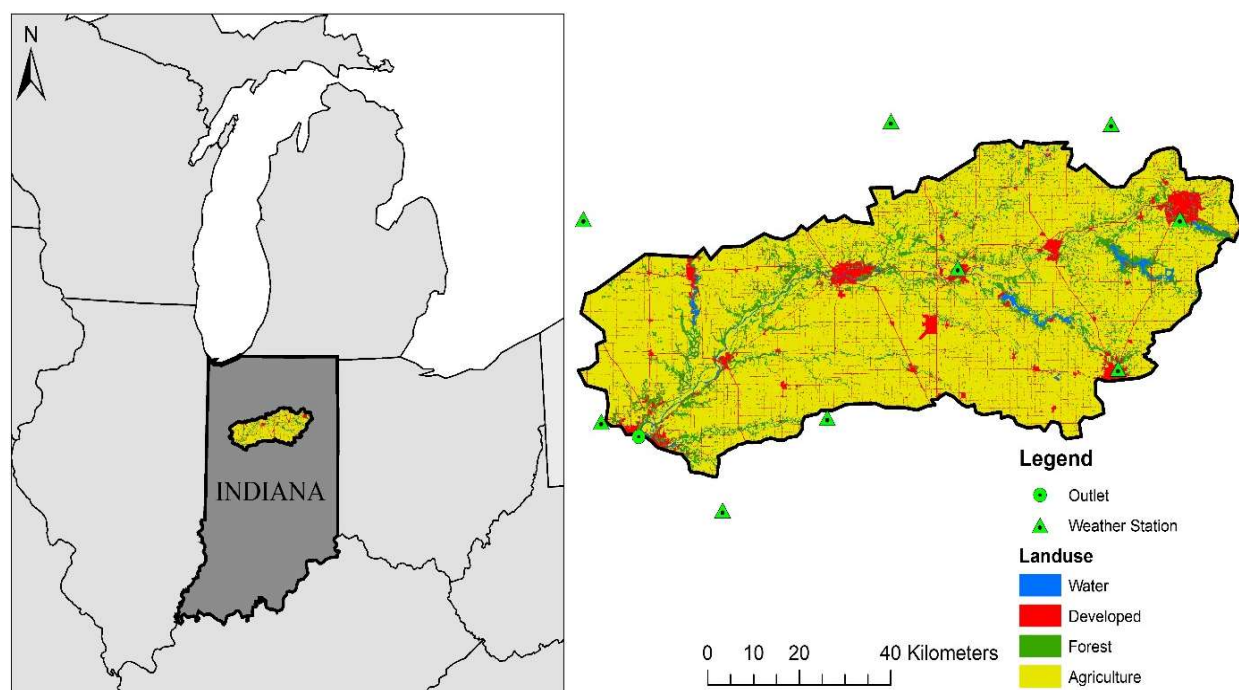


Fig. 2.1 Location and land use map for the unregulated portion of the UWR basin

2.4 Model Description

Several fully integrated models are available for simulating hydrologic responses from reach to continental scale using a distributed modeling approach (Paniconi and Putti, 2015), including but not limited to, the Integrated Hydrology Model (InHM: (VanderKwaak and Loague, 2001), GSSHA (Gridded Surface Subsurface Hydrologic Analysis: Downer et al., 2002; Downer and Ogden, 2006), ICPR (Streamline Technologies, 2018), DrainFlow (Shokri and Bardsley, 2016), ParFlow (Maxwell et al., 2014), CATHY (Bixio et al., 2002), MIKE SHE (Hughes and Liu, 2008), tRIBS (Ivanov et al., 2004), HydroGeoSphere (Brunner and Simmons, 2012), and ADHydro (Ogden et al., 2014). However, considering the focus on flood inundation modeling and application over a large area, Interconnected Channel and Pond Routing (ICPR; Fig. 2.2) is used in this study. ICPR is a FEMA-approved integrated hydraulic and hydrologic model for the State of Florida that has been extensively validated for both SW and GW simulations across several watersheds in the United States (Streamline Technologies, 2016). ICPR is a two-dimensional (2D), integrated SW-

GW modeling software, based on distributed model parameterization procedures (Streamline Technologies, 2018). The ICPR model has capabilities of combining precipitation, 2D surface flow, pond storage and GW simulations, for both event-based and continuous storm events (Ahmad et al., 2014; Booker, 2006; Jackson and Maidment, 2014; Joyce et al., 2017; Singhofen and McClung, 2014). As shown in Fig. 2.2, there are three basic components of an integrated ICPR model: (1) the surface system; (2) the vadose zone; and (3) the saturated groundwater system. Detailed description on these components including the methodology used to couple surface and subsurface systems is provided below.

2.4.1 The surface system

ICPR uses a finite volume approach for surface flow using unstructured mesh networks. Momentum equations (with options for energy and diffusive wave equations) are lumped along triangle edges, and the mass balance equations (Appendix A, Equations A.4 to A.7) are lumped at the triangle vertices where irregular shaped polygons are formed establishing local control volumes. This set of polygons is referred to as the surface honeycomb mesh. As shown in Fig. 2.3, the polygons are formed by connecting adjacent triangle midpoints and centroids. A diamond mesh is also formed along triangle edges for roughness classification (as shown in Fig. 2.3) and extends from vertices to adjacent triangle centroids (Streamline Technologies, 2018). The advantage of using unstructured networks in characterizing the topography and hydrologic processes is well documented in previous studies (Begnudelli and Sanders, 2006; Bunya et al., 2010).

ICPR allows the application of variable surface roughness for shallow and deep overland flow. During large flood events, the roughness changes over time when the depth of the water in the floodplain increases due to persistent flooding (Arcement Jr. and Schneider, 1984). Popular hydraulic models such as the Hydrologic Engineering Center's River Analysis System (HEC-RAS) and LISFLOOD-FP, do not account for this variability (Bates and De Roo, 2000; Brunner, 2010). ICPR uses an exponential decay function (presented in Appendix A, Equations A.11 and A.12) dependent on surface depth to incorporate the variability in surface roughness. The shallow and deep roughness values corresponding to the NLCD land use classes are directly obtained from the maximum and minimum roughness values recommended in Chow, 1959 and are shown in Table 2.2.

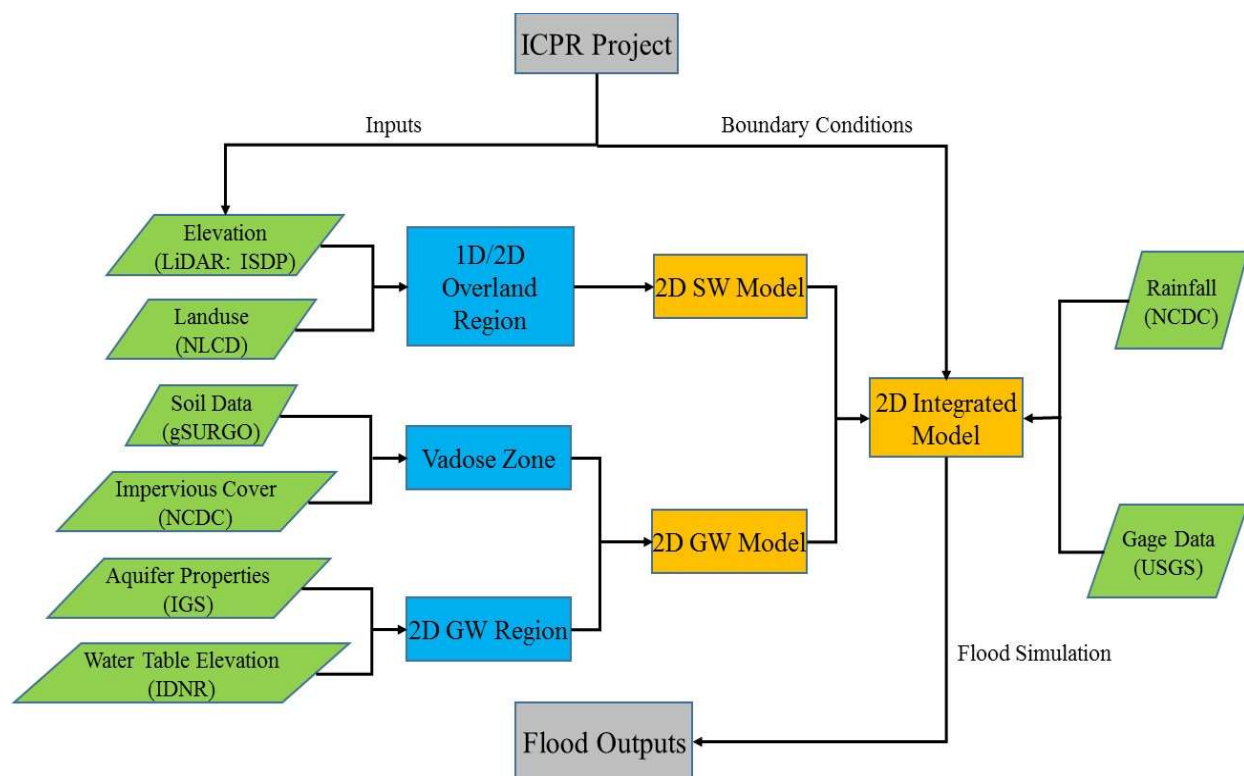


Fig. 2.2 ICPR project process diagram

2.4.2 The vadose zone

The vadose zone forms the primary communication link between the surface and groundwater systems. ICPR has several options for modeling the vadose zone (Streamline Technologies, 2018), including the Green-Ampt method (single homogeneous layer discretized into two cells), a refined Green-Ampt method (single homogeneous layer discretized into user specified number of computational cells), and the Vertical Layer method (soil properties vary by layer and each layer is further discretized into multiple cells). In all three cases, the Brooks-Corey soil water retention–hydraulic conductivity relationship (Rawls et al., 1982; Rawls and Brakensiek, 1982) is used to determine unsaturated conductivities based on current soil moisture contents. The refined Green-Ampt method is used in this study because it provides a more realistic distribution of soil moisture in the soil column compared to the standard Green-Ampt method. In this method, the soil moisture accounting and subsequent GW recharge from the vadose zone is computed using a non-iterative kinematic approach. Unlike the standard Green-Ampt method that permits only one soil moisture value within a single computational element (e.g. honeycomb or grid), the refined Green-Ampt allows the entire unsaturated soil zone to be divided into multiple cells (as illustrated

in Fig. 2.4) which can contain different moisture contents based on the volume of water percolating into the vadose zone. In essence, the refined Green-Ampt method is identical to the Vertical Layer method except that the soil parameters are homogeneous for a given soil zone.

The non-iterative kinematic approach involves two passes through the various cells for every time-step. The first pass is from the ground surface downward to the last cell. Water enters the soil column at the top of the first cell based on an infiltration rate that cannot exceed the saturated vertical conductivity. The fluxes are calculated at the bottom of each cell based on the current moisture content in a cell and the corresponding unsaturated vertical conductivity as estimated by the Brooks-Corey method (Appendix A, Equation A.13). A mass balance is performed for each cell based on the flux into the cell from its upper face minus the flux out of the cell across its bottom face. The moisture contents are updated based on the fluxes. The flux across the bottom face of the last cell is removed from the vadose zone and delivered to appropriate groundwater node. In the second pass, the cells are rebalanced from the bottom to the surface, to ensure that the moisture content in any cell does not exceed saturation. At this step, if any cell contains water in excess of saturation, the difference (excess water content) is moved upward to adjacent cells and eventually delivered to the surface system, if necessary. Since the WT is dynamic, the cells are “swallowed” as the WT moves upward. Therefore, if a cell is inundated by more than 75% due to the rising WT, it is merged with the saturated cell below it, and the soil moisture is redistributed accordingly. Similarly, as the WT drops, the moisture content of the newly exposed portion of a given cell is automatically set to field capacity. If more than 25% of a given cell is exposed, it becomes active again. The 75% threshold for merging cells and 25% threshold for unmerging cells as the WT moves upwards or downwards is provided to ensure continuity and consistency in the wetting and drying of cells in the vadose zone.

The volume of water available for infiltration at every time-step is calculated as the rainfall volume in that time plus the volume of water ponded on the surface minus the amount of evapotranspiration (ET). The potential evapotranspiration (PET) at every time-step is first removed from the rainfall volume and ponded water. In case the amount of PET required is higher than the rainfall and ponded water, the difference is extracted from the soil column available for ET (ground surface to root depth). The current soil moisture content in each cell is adjusted based on actual ET (AET) requirements before proceeding with the unsaturated vertical flow

computations. The reference evapotranspiration (RET) in ICPR is calculated using the Penman-Monteith equation (Appendix A, Equation A.14). The empirical equations provided in Allen et al., 1998 are used in conjunction with meteorological data to calculate the RET. Since the RET is calculated assuming the surface to be ‘turf grass’ in good condition, the RET is converted into PET using crop coefficients which can vary based on the crop-type, soil-type, and time of year. Evapotranspiration is not included in the first part of this study (described in Section 2.4) as it deals with event-based simulations. However, ET calculations are included for the continuous simulations presented in Section 2.5.4.

2.4.3 The saturated groundwater system

A finite element approach with a six-point quadratic triangular element as described by Martínez, 1989 is used in ICPR to solve the continuity equation (Appendix B, Equation B.1) for unsteady phreatic two-dimensional groundwater flow (Streamline Technologies, 2018). Nodes are placed at triangle vertices and midpoints along the triangle edges. Like the surface flow computational mesh, polygons are formed around the triangle vertices. Polygons are also formed around the triangle midpoints. This set of polygons is referred to as the subsurface honeycomb.

2.4.4 Integrating surface and subsurface systems

The surface and subsurface honeycomb meshes are simultaneously intersected with soils, land use and rainfall zone thematic polygon map layers (Fig. 2.3), forming a system of sub-polygons or soil cylinders. Each soil cylinder has a surface node, a groundwater node, as well as soil, land use and rainfall zone attributes. A portion of the rainfall may enter the soil column and flow vertically through the vadose zone. Water that does not enter the soil column is assigned to its respective surface node. Water is aggregated if multiple soil cylinders share the same surface node and then moved horizontally on the surface along triangle edges. Any water for a given soil cylinder crossing the interface between the vadose zone and the saturated zone is aggregated and delivered to its respective groundwater node. If the soil column becomes saturated and the surface is inundated, a known head condition is applied to the corresponding groundwater node based on the surface node stage. Seepage into or out of the groundwater system at that location is calculated by the groundwater model and removed from or delivered to the surface node.

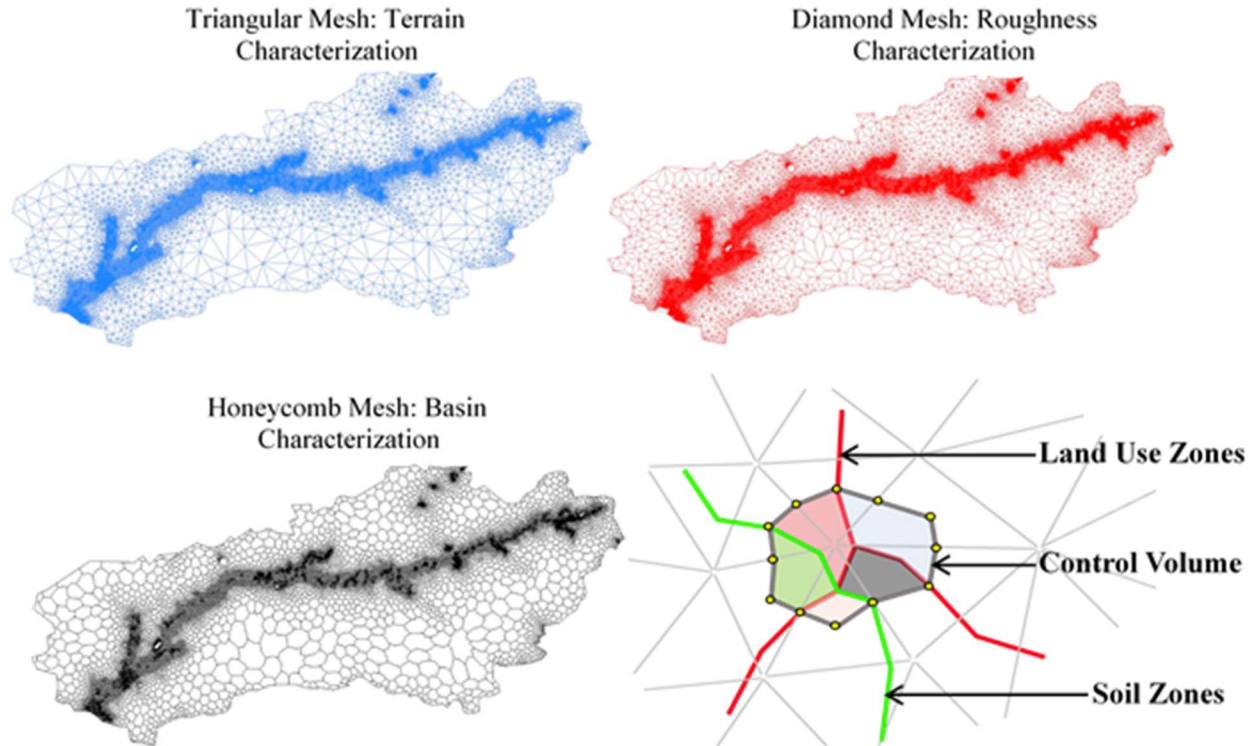


Fig. 2.3 Mesh structure within ICPR for the Upper Wabash Basin

2.4.5 Time marching scheme

The coupling sequence between the vadose zone, the surface hydraulics and the saturated groundwater system is as follows: (1) Start incrementing the hydrology clock (vadose zone); (2) Start incrementing surface hydraulics clock until it catches up to the hydrology clock; (3) If the hydrology clock is less than the groundwater clock plus groundwater time increment, go to step 1; and (4) Start incrementing the groundwater clock.

The hydrology (vadose zone) and groundwater time increments are static. The hydrology time increment is usually several minutes in duration whereas the groundwater time increment is typically an hour or longer. Hydrology runoff rates are saved at the beginning and end of a hydrology time increment and delivered to the appropriate surface node. Pondered water at the beginning of the hydrology time increment is applied across the full hydrology time increment. Groundwater recharge volume based on fluxes across the vadose zone–saturated zone interface is aggregated and delivered to the groundwater model at its time increment. The surface hydraulics time increment is typically in seconds or fractions of seconds in duration and operates between a user-specified minimum and maximum time increment.

There are two (2) time marching options in ICPR. The first option is a Successive Approximation technique with Over-Relaxation (SAOR). This is an iterative solution that solves for heads at nodes and flow rates along triangle edges. It has an adaptive time-step and changes between user-specified minimum and maximum time increments. However, a constant time-step is used throughout the computational mesh at a given point in time. Consequently, the time-step is typically driven by the node with the least amount of storage.

The second option (used in this study) is based on a second order Runge-Kutta technique (modified Euler method) that varies the time-step not only in time, but also spatially (Domingues et al., 2008). It is referred to as the “FIREBALL” method in ICPR and is 2.5 to 30 times faster than the SAOR method for large projects (Streamline Technologies, 2018). The method involves establishing a set of time-step levels at the beginning of a simulation based on the minimum and the maximum calculation times, with each successive level doubling in duration. For example, if the minimum and maximum calculation times are set to 0.01 and 5.12 seconds, respectively, then ten (10) time-step levels are established, and routing calculations are based on these time-step levels. A maximum allowable time-step is then determined for each node based on inflows, outflows, and available storage, such that the change in stage does not exceed the user specified change in stage tolerance, which is typically set such that the mass-balance error is minimal. The time-steps are rounded down to the closest time-step level, following which, a pass is made through the entire network, beginning at nodes with the lowest time-step level, to ensure that the neighboring nodes do not increase more than one time-step level.

For example, if a total of ten (10) time-step levels are chosen, the inner-most level with the smallest time-step will be calculated 512 times compared to the outer-most level with the largest time-step, but the neighboring cells do not increase by more than one level. Once all cells on all time-step levels are calculated, the maximum allowable time-steps for all the nodes are re-evaluated and the process is repeated. A finite element time marching scheme is used for the groundwater model based on a quadratic shape function. The algorithm solves for heads at every node (triangle vertex and midpoint) in the computational mesh. In this study, the hydraulic routing time-interval is set between 0.01 to 5.12 seconds (ten time-steps), the hydrology is updated after every 300 seconds (5 minutes), and the groundwater flows, seepages and recharge rates are calculated at every hour (3600 seconds).

2.5 Model Description

The overall goal of this study is to show that an integrated SW-GW modeling approach provides more robust and accurate results compared to the conventional surface water modeling approach. This goal is accomplished by creating three modeling configurations (Fig. 2.4) by gradually increasing physical complexity to show the relative improvement in the model results. More details on these configurations, including the steps involved in creating them are provided below.

2.5.1 Creation of ICPR model configurations

2.5.1.1 Subsurface model discretization (C1)

The C1 model represents a 2D surface water model, which uses gage data at upstream USGS stations, and routes the water solely based on topographic variation and roughness characteristics. This configuration represents the default conventional approach to flood modeling driven by upstream discharge hydrograph. The elevation data for this model is obtained from the gridded 9 m resolution LiDAR DEM. The river geometry for this configuration is defined using a triangular mesh, which is dense in the channel and its floodplain (as shown in Fig. 2.3), and coarse for the land surface away from the river to reduce computation time. This ensures that the mass balance is simulated accurately where most of the water transport is taking place. The triangular mesh in ICPR is overlain on the LiDAR DEM and the elevation of LiDAR cell directly intersecting with a specific triangular vertex is extracted and assigned to the vertex. The flow hydrodynamics is simulated by using a 2D overland flow routing that is based on the solution of diffusive wave formulations (Appendix A, Equations A.8 to A.10). Additionally, C1 does not require any additional hydrologic inputs (e.g. rainfall), since it has no subsurface connectivity, and is based solely on the traditional hydraulic routing techniques used for estimating flood depths and extent of inundation. Basically, the ground surface is assumed to be impervious for C1 and the streamflow from eight upstream gages are routed without any rainfall, thereby representing a configuration that is synonymous to the traditional 2D surface water routing models such as HEC-RAS 2D and LISFLOOD-FP.

This triangular mesh for the 2D overland flow region is generated using the ‘breakline’ and ‘breakpoint’ feature in ICPR. The ‘breakline’ feature is a polyline shapefile generated by digitizing

the river channels in the study area using aerial imagery and LiDAR data. Each point used to create the polyline 'breakline' feature is assigned a triangular vertex node in ICPR and the triangle edges are formed along the polyline. Therefore, the channel flow rates are computed along the triangle edges within the ICPR computational scheme. Since more points are required to digitize river bends, the resultant mesh is denser along the river bends and at confluences. Since the DEM resolution for the LiDAR data is 9 m, the 'breakline' feature is digitized such that the minimum distance between any two vertices is 9 m and the maximum edge length along straight channels is 27 m. Therefore, the average triangular edge length in the river channels is 15 m. For mesh digitization outside the river channels, the 'breakpoint' feature, which is a point shapefile, is used for mesh generation. Every point in the 'breakpoint' shapefile is assigned a triangular vertex in the mesh and these features can be automatically generated in ICPR at a specified distance (for more information on breakpoints and breaklines, please refer to, Streamline Technologies, 2018). Using this principle, triangular 'breakpoint patterns' with an average edge length of 60 m and 300 m are assigned inside and outside the floodplain respectively.

2.5.1.2 Subsurface model discretization (C2 and C3)

The overland flow in C1 configuration is modified to include two subsurface configurations. In the first modification, referred to as C2, the overland flow can only interact with the unsaturated soil layer (vadose zone) with a static WT. The vadose zone thickness is determined using gSSURGO data for the region, which remains constant throughout the simulation. The C2 configuration is like other commonly used hydrologic models such as Hydrologic Engineering Center's Hydrologic Modeling System (HEC-HMS) and Soil Water Assessment Tool (SWAT) that route the rainfall excess surface flow and the water percolating beyond the vadose zone is lost as aquifer recharge. The initial soil moisture in the vadose zone is assumed to be equivalent to field capacity at the beginning of the simulation.

As mentioned in Section 2.3.2, the water movement in the vadose zone, and subsequent GW recharge is computed using the refined Green-Ampt method (Streamline Technologies, 2018). A total of twenty-five cells are used for the vadose zone in this study. Initially, all the cells start with the same parameters as shown in Table 2.2, but the moisture content across each cell can vary with time as the fluxes through each individual cell are tracked in both upward and downward directions. During the simulation at each time-step, the wetting front moves through individual

unsaturated cells, which are wetted or dried using the available soil storage and unsaturated hydraulic conductivity. Fig. 2.4 provides an illustration of the vadose zone discretized into multiple cells which are used to redistribute the soil moisture.

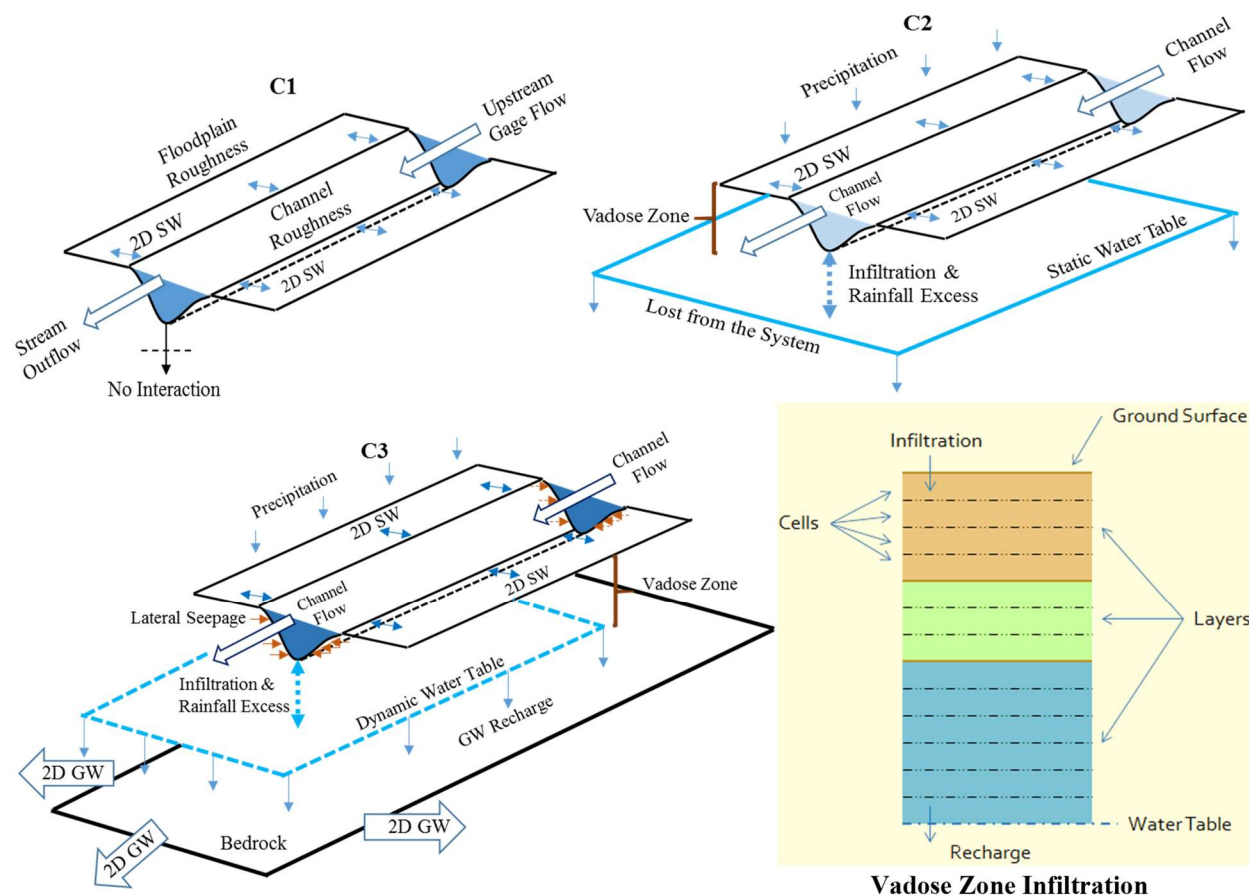


Fig. 2.4 Conceptual illustration of C1, C2, C3 and vadose zone infiltration

In the third configuration, referred to as C3, the WT in C2 is made dynamic so the water that percolates beyond the vadose zone is used to increase the storage in the surficial aquifer, which results in the rise of the WT. Similarly, during dry conditions, the WT recedes and increases the vadose zone depth. Along with vertical movement of the WT, C3 also incorporates GW contributions from horizontal gradients causing seepage fronts that discharge into the Wabash River. Within the subsurface in C3, the GW recharge rates from the vadose zone for a given WT elevation are converted to a volume, which is based on the hydrological computational time increments. This volume in-turn determines the change in the WT elevation for the next time increment.

To simulate the GW dynamics in C3, an initial WT surface is required at the beginning of the simulation. To generate this surface, first, the WT depth contours obtained from IDNR's potentiometric surface maps are interpolated using the inverse distance weighting (IDW) method to form a WT depth raster at a spatial resolution of 30 m. Second, this WT depth raster is subtracted from the ground LiDAR (resampled to 30 m) to obtain a WT elevation surface. Third, this surface is imported into an initial version of the C3 model, which is then simulated at steady-state for one month using the daily average streamflow for the streams in the watershed. Finally, it is assumed that the WT surface reaches equilibrium at the end of this steady-state simulation. The WT surface obtained at the end of the steady-state simulation is used as the initial WT surface for the C3 model used in this study.

Within the surficial aquifer, the GW flow is calculated using the 2D unsteady phreatic solution of the continuity equation using a finite element formulation. More specifically, a six-point triangular element is used with a quadratic interpolation function, and the system of equations is solved using the Cholesky method (Kuiper, 1981; Martínez, 1989). A 2D subsurface discretization also allows C3 to account for the non-uniform distribution of the hydraulic properties in the vadose zone and surficial aquifer. For the GW region, a coarser resolution mesh, with an average edge length of 45 m in the channel, 240 m in the floodplain, and 900 m outside the floodplain, is created. A detailed description of the modification of the continuity equation for finite element formulation is described in Appendix B and can also be accessed from ICPR's Technical Reference Manual (Streamline Technologies, 2018).

Table 2.2 presents the uncalibrated Green-Ampt parameters used for C2 and C3, and surficial aquifer parameters used for C3, that are classified based on soil zones and the type of aquifer system respectively. The gSSURGO database contains spatially distributed hydrologic soil group classification based on runoff potential and the four soil zones used in this study are based on this classification. The saturated vertical conductivity, moisture content at field capacity, and at wilting point (presented in Table 2.2) reflect the median values of the specific soil zones in the gSSURGO database. The other parameters require information on the soil texture percentages, which are also available from the gSSURGO database. Using the soil texture percentages, and the equations provided in Rawls, 2004, the other subsurface parameters such as pore size index, soil matric potential, and residual moisture content are evaluated (Streamline Technologies, 2018).

Table 2.2 ICPR uncalibrated subsurface and surface roughness parameters

No.	Vadose Zone*	Description	A	B	C	D
1	K _v	Saturated vertical conductivity, mm/h	15.2	6.2	2.3	1.4
2	MCS	Moisture content at saturation	0.30	0.540	0.458	0.62
3	MCR	Residual moisture content	0.031	0.068	0.078	0.090
4	MCI	Initial moisture content	0.125	0.270	0.310	0.360
5	MCF	Moisture content at field capacity	0.125	0.270	0.310	0.360
6	MCW	Moisture content at wilting point	0.063	0.135	0.155	0.180
7	PSI	Pore size index	0.398	0.220	0.250	0.168
8	Ψ	Soil matric potential, cm	205.7	111.5	280.9	291.6
No.	GW Zone	Description	Moraine	Complex	Till	Outwash
1	η _e	Aquifer effective porosity	0.175	0.270	0.310	0.360
2	K	Aquifer hydraulic conductivity, mm/h	30.5	12.4	4.67	6.35
Surface roughness parameters (Manning's n)						
No.	Type of land use	Shallow		Deep		
1	Open Water	0.045		0.030		
2	Low Intensity Residential	0.020		0.011		
3	High Intensity Residential	0.015		0.011		
4	Commercial / Industrial	0.014		0.010		
5	Transportation	0.013		0.010		
6	Barren Land	0.100		0.050		
7	Deciduous Forest	0.198		0.184		
8	Evergreen Forest	0.198		0.184		
9	Mixed Forest	0.198		0.184		
10	Shrub/Scrub	0.200		0.100		
11	Grasslands	0.350		0.240		
12	Hay / Pasture	0.200		0.100		
13	Row Crops	0.180		0.100		
14	Woody Wetlands	0.060		0.045		
15	Herbaceous Wetlands	0.060		0.035		

* The soil zone A has the highest infiltration potential representing loamy sand, followed by soil zone B, which has moderately low runoff potential representing loamy silt. Similarly, soil zone C has slightly restricted vertical conductivity representing silty clay loam texture, followed by soil zone D, which represents clayey soil with a higher moisture content but low vertical conductivity. The four GW zones represent the unconsolidated aquifer systems that form the saturated subsurface for the UWR basin. The roughness parameters transition from shallow (maximum) to deep (minimum) based on an exponential decay function dependent on depth of flow.

For the GW zones, the map of the spatial distribution of different unconsolidated aquifer systems for Indiana is available from IGIC's Indiana Map Server (<http://maps.indiana.edu/index.html>). The aquifer properties for Wabash Valley are obtained from a study on the investigation of groundwater resources in Indiana (Pohlmann, 1987).

2.5.2 Model simulations using three configurations

The three configurations are run in an unsteady-state to simulate hourly streamflow, stage and extent of inundation for a month from April 11th, 2013 to May 10th, 2013. During this period, multiple rainfall events of varying magnitude were observed in Indiana that resulted in a peak streamflow corresponding to a 50-year return period in the Wabash River at Lafayette. The first 5 days of simulation are used for model initialization, which is completed when all the models reach equilibrium and all reaches are connected. The equilibrium is reached when the mass balance error in the system stabilizes to a value less than 1%. The outputs from the three model configurations are compared with observed data for the next 25 days at the watershed outlet. A period of 25 days is chosen to simulate both high and low flow conditions that occurred during and after the storm event, respectively. Evapotranspiration is not included in C2 and C3 during the one-month simulation based on the assumption that the effect of ET would be negligible during a short and extremely wet period.

The input parameters are kept unchanged for different model configurations because the goal is to investigate the sensitivity of flood simulation from the three configurations to subsurface flow integration under normal climatic conditions. It should also be noted that the model comparisons are based on uncalibrated parameter inputs because calibration can result in unrealistic representation of relative contributions from the overland and subsurface processes due to the existence of equifinality (Pappenberger et al., 2005; Beven, 1993). After applying the three models to simulate the one-month period, the streamflow, stage, and extent of inundation are evaluated and compared between models. The stage is evaluated by subtracting the channel bed elevation at the gage from the WSE. The stage is used instead of WSE as WSE is a scale-dependent parameter, which can create bias in the results due to the elevation (or altitude) of the location. The relative performance of these models is also evaluated by comparing the simulated results with observed data.

2.5.3 Statistical comparison of model

In order to evaluate the goodness of fit between the three configurations and observed data, the coefficient of determination (R^2) is calculated. While R^2 is used as a measure of linear trend, the Nash-Sutcliffe Efficiency (NSE, Nash and Sutcliffe, 1970) which reflects the overall fit of a hydrograph, is also evaluated. Similarly, the slope parameter, which provides a measure of overprediction or underprediction of model outputs with increasing magnitude, is evaluated. In addition, Percent Bias (PBIAS, Sorooshian et al., 1993), a statistic used to measure if the average tendency of simulated data is larger or smaller than observed data, is also calculated (Gupta et al., 1999). Finally, the RMSE-observations standard deviation ratio (RSR), which is a scaled-normalized parameter, is evaluated to estimate the variation in model residuals.

2.5.4 Spatial aggregation of model

Table 2.3 presents the spatial aggregation parameters of the surface and GW meshes (provided in parenthesis for C3) generated for the UWR basin (Fig. 2.3). Since the same surface mesh is used for the three configurations, the number of triangles and the mean triangular area is the same. To compare the spatial resolution of triangulated irregular networks (TINs) with gridded DEMs, Vivoni et al., 2005 used two spatial aggregation parameters, the horizontal point density (d) and the equivalent cell size (r_e), which can be evaluated using Equations 2.1 and 2.2.

$$d = \frac{n_t}{n_g} \quad \text{Equation 2.1}$$

$$r_e = \sqrt{\frac{A}{n_t}} \quad \text{Equation 2.2}$$

Where, d = horizontal point density; n_t = number of triangular nodes (or vertices); n_g = number of DEM nodes; r_e = equivalent cell size (or length scale); and A = basin area. The number of DEM nodes (n_g) are evaluated using the 9 m LiDAR for the surface region and the 30 m initial WT raster for the GW region. The ' r_e ' values for the surface (156 m) and GW (428 m) meshes represent the equivalent spatial resolution of the TINs used in this study. Similarly, the ' d ' values provide a ratio of the number of computational elements used in the surface (0.003) and GW (0.004) meshes in comparison to the fixed-resolution gridded DEMs.

Table 2.3 Spatial aggregation of C1, C2 and C3

Computational Elements	<i>C1</i>	<i>C2</i>	<i>C3</i>
Number of triangles in the mesh	392,148	392,148	392,148 (43,509)
Mean triangular area (km ²)	0.015	0.015	0.015 (0.134)
Equivalent cell size, r_e (m)	156	156	156 (428)
Horizontal point density, d	0.003	0.003	0.003 (0.004)

2.6 Results and Discussion

The results are presented in four parts: (i) comparison of the three model configurations (C1, C2 and C3); (ii) quantification of the relative contribution of watershed processes during flooding; (iii) evaluating the effect of antecedent soil conditions on flood outputs; and (iv) further validation of results by applying C3 under different flow and watershed conditions.

2.6.1 Comparison of the three model configurations

2.6.1.1 Comparison of model outputs with observed data

In this section, the observed streamflow and stage is compared with the simulated streamflow and stage for C1, C2, and C3, respectively. It should be noted that all the models begin from the same initial surface storage, and C1 does not have any infiltration into the soil column. The results presented in Fig. 2.5a show that C1 overpredicts the streamflow significantly near the peak and underpredicts during low flows. This result suggests that the surface water models produce higher outflow during flood events as the water flowing into the surface system (inflow) is fully recovered as either surface storage or outflow. Since the inflow volume in C1 is not removed from the surface system due to the absence of processes like infiltration, evapotranspiration, GW seepage and recharge, the resulting outflow volumes are higher for C1. On the other hand, C2 severely underpredicts the streamflow during low flow conditions, but predicts the peak streamflow accurately when compared to observed data. While a portion of the infiltrated water is stored in the vadose zone and some is delivered to the surface as excess runoff in C2, most of the water exits the system by percolating out of the vadose zone and is lost as subsurface recharge, resulting in an underprediction in C2.

Due to a better physical process representation, C3 performs well in predicting the streamflow for the entire duration of the simulation. Fig. 2.5b suggests that C1 fails to predict the stage accurately for the duration of the simulation. In comparison to streamflow, the error in estimating stage for all models is less severe near the hydrograph peak, because the stage is more resistant to fluctuations in streamflow when the water inundates outside the main channel and into the floodplain, causing a significant increase in the flow area. Additionally, a change in streamflow can also affect the flow velocities, resulting in a less severe impact on stage. The scatterplots about the line $Y=X$ shown in Fig. 2.5c and 2.5d further highlight the overall accuracy of C3 in estimating streamflow and stage.

The streamflow and stage hydrographs for the three configurations highlight the importance of including a dynamic WT and a variable vadose zone thickness. In the context of streamflow generation, current hydrologic models such as HEC-HMS and SWAT, are severely limited in considering this dynamic nature. To improve the prediction using such models, the parameters need to be calibrated to produce a best-fit combination of parameters (Arnold et al., 2012; Zhang et al., 2013). However, this process of calibration does not guarantee model performance during different hydrologic and climatic conditions (Liew et al., 2005; Schuol and Abbaspour, 2006). Assuming a fixed vadose zone thickness can also restrict the maximum volume of water available to plants in the root zone which, in turn, may influence other processes such as evapotranspiration, which is a dominant variable during normal climatic conditions. Here, C2 represents hydrologic models that do not account for groundwater movement, and therefore, underpredicts the streamflow and stage.

On the other hand, C3 includes a dynamic WT along with the surficial aquifer characterization, which significantly improves the prediction. The C3 outflows suggest that the total amount of water infiltrating into the subsurface reduces on inclusion of a dynamic WT. Additionally, a fraction of the water is also recovered from the subsurface in the form of seepage due to the direct interaction of the WT with the surface, which contributes towards a more accurate low flow estimation.

Table 2.4 Comparison of model performance for peak and lowest streamflow

Condition	Variable	Observed	C1	C2	C3
Peak	Streamflow (m ³ /s)	2317.0	2850.8 (+23.0)	2369.0 (+2.2)	2389.3 (+3.1)
	Stage (m)	7.71	8.39 (+8.9)	7.58 (-1.7)	7.93 (+2.9)
	Inundation Area (km ²)	NA	171.4	155.1	188.2
Lowest	Streamflow (m ³ /s)	411.3	355.4 (-13.6)	278.1 (-32.4)	406.8 (-1.1)
	Stage (m)	2.99	2.87 (-4.1)	2.27 (-24.1)	2.99 (-0.2)
	Inundation Area (km ²)	NA	119.4	106.3	118.9

*The values in parenthesis represent the relative error (%) with respect to observed data

Even though C2 has a better physical process representation than C1, its performance is worse than C1, as shown in Table 2.4 and Fig. 2.5. These results suggest that a fixed vadose zone model that permits water percolation into an infinite GW region, without properly quantifying recharge and WT location, performs worse than simply using a model with an impervious surface (C1). To improve the performance of models like C2, it may be more beneficial to restrict the percolation out of the unsaturated zone by assuming an impervious bottom soil layer, thereby, providing a fixed storage in the soil system. This modification can reduce the underprediction in C2, as it may improve the simulation of Hortonian runoff (infiltration excess), even though Dunne runoff (saturation excess) may not be simulated accurately without proper conceptualization of GW processes (Xie et al., 2003). For events that are primarily affected by Hortonian runoff, the error induced by excluding GW processes may be offset by incorporating an unsaturated zone without GW recharge. However, several factors can result in Hortonian-runoff-dominated events across watersheds, for example, the spatial heterogeneity in soil properties, antecedent soil conditions, watershed topography, and rainfall intensity. Therefore, before choosing a model configuration like C2, these factors should be considered, otherwise, the results may not be accurate without GW incorporation, as shown in this study.

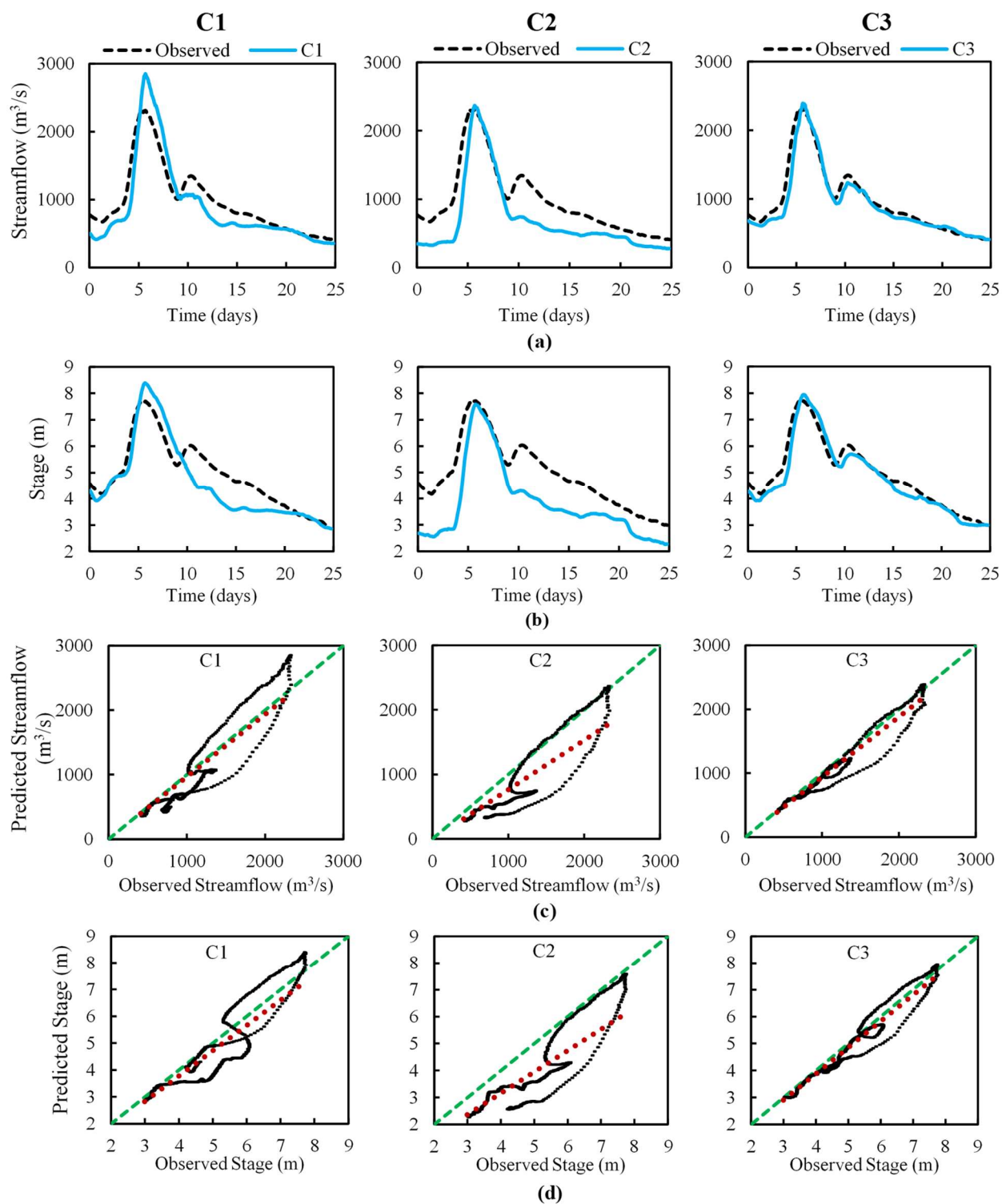


Fig. 2.5 (a) Streamflow hydrographs at the outlet; (b) stage at outlet gage station; (c) streamflow scatterplots; and (d) stage scatterplots for C1, C2, and C3 for a 25-day simulation (April 16th to May 10th, 2013)

Fig. 2.6 presents the flood inundation maps near the Wabash-Tippecanoe confluence for the highest (peak) and lowest streamflow during the simulation. The difference in the location and magnitude of inundation between the three models is evident from the flood maps at peak streamflow (Fig. 2.6a, 2.6b and 2.6c). For C2, the inundation area measured at both peak and lowest streamflow is significantly lower (Fig. 2.6b and 2.6e) than C1 and C3. As shown in Table 2.4, the peak flow flood inundation area is smallest for C2 (155.1 km²), followed by C1 (171.4 km²) and C3 (188.2 km²). Overall, C3 has the highest flood inundation extent since it accounts for surface ponding during extreme rainfall as the subsurface becomes saturated. Additionally, water seeping laterally from the rivers into the subsurface can seep out elsewhere causing ponding. Therefore, C3 can capture river-floodplain interactions across both the surface and subsurface regions. In contrast, C1 only shows inundation due to riverine flow that inundates into the floodplain, and hence, the flooding is localized around the river channel. The flood inundation area corresponding to the lowest flow for C1 (119.4 km²) and C3 (118.9 km²) are approximately equal, which suggests the traditional surface water routing approach and the integrated approach produce similar results during low flows, when the water remains inside the river channels.

The results presented in this section suggest that the overall model performance for C3 is superior when compared to C1 and C2. However, the extent of inundation does not depend only on streamflow and stage, but also on the accuracy of topographic data. In this study, the extent of inundation estimated by the model configurations is not compared with observed flood inundation, and therefore, it is essential to note that the flood inundation maps presented here only provide a relative difference between the model configurations. From a watershed perspective, if the inflow and outflow from the watershed is predicted accurately, the extent of inundation will be a function of the resolution and vertical accuracy of topographic data.

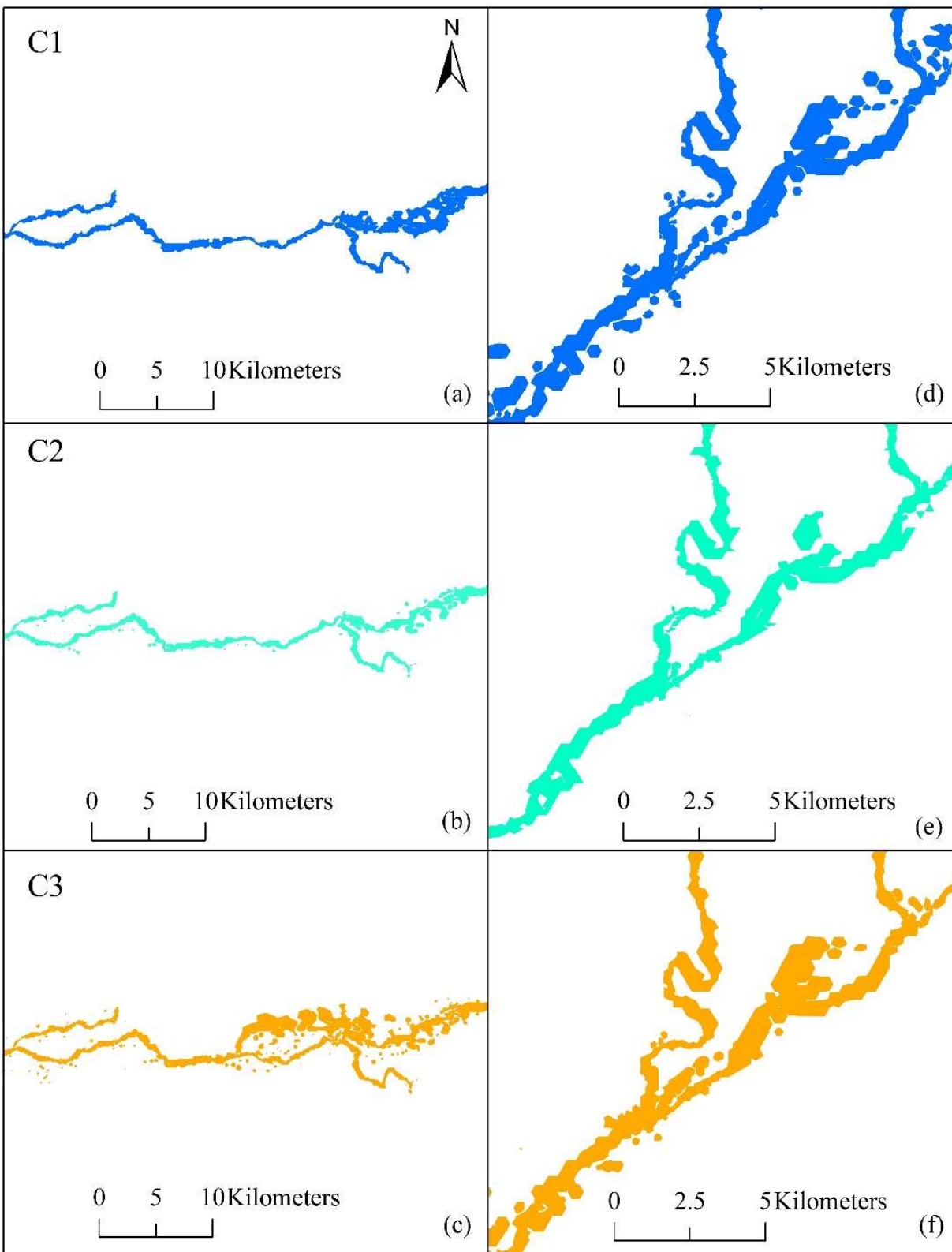


Fig. 2.6 Cross-sectional profiles for C1, C2 and C3 for (a) peak streamflow and (b) lowest streamflow

2.6.1.2 Statistical comparison of model performance

Fig. 2.5 suggests that C3 performs best when compared to observed flow, however, it is essential to evaluate model performance statistics to further validate these conclusions. Table 2.5 presents the statistical parameters for evaluating goodness of fit between the three models and observed data. The statistical performance of the models in estimating streamflow suggests that C3 ($R^2=0.95$) performs best, followed by C1 ($R^2=0.85$), and C2 ($R^2=0.80$). As mentioned earlier, the stage is evaluated by subtracting the bed elevation at the outlet from the WSE. The model performance in estimating stage suggests that C3 has a high R^2 value of 0.95, but both C1 and C2 have a diminished performance with R^2 values of 0.81 and 0.78 respectively. A very low NSE for C2 in estimating streamflow and stage indicates an unacceptable performance (Moriassi et al., 2007). Even though C1 and C3 have comparable R^2 values, high NSE values of 0.94 and 0.93 in estimating streamflow and stage clearly suggest that C3 has a very good performance when compared to observed data, based on the model evaluation guidelines by Moriassi et al. (2007).

While both C1 and C3 underpredict the rising limb of the hydrograph, the overall slope in comparison to the line $Y=X$ is close to 1 which indicates that neither of the models are consistently overpredicting or underpredicting the streamflow. Overall, C3 performs better statistically in estimating streamflow highlighted by a lower PBIAS (-6.0%) compared to C1 (-8.6%). Similarly, C3 also has a better performance in estimating stage as shown by a very low PBIAS (-3.2%) compared to C1 (-6.6%) and C2 (-22.4%). A low slope (0.77) for C2 indicates that the model underpredicts the streamflow consistently, even though the relative error in peak streamflow (Table 2.4) is very small (+2.2%). In addition, C3 has a lower RSR when compared to C1 and C2, which further highlights the improvement in model performance due to an accurate representation of physical processes.

Since an inaccurate SW mesh resolution can cause mass balance errors in the model, the performance of the three configurations is tested for two additional mesh resolutions, including one that is coarser and another that is finer than the one presented in this study. The overall conclusions do not change, but the degree of improvement compared to the observed data is different when using a different mesh resolution. For example, the reported R^2 values when using a coarser mesh resolution for C1, C2 and C3 are 0.59, 0.76 and 0.85 respectively. In this scenario, both C1 and C3 overpredict the streamflow and stage, but C3 performs better than both C1 and

C2. Using a SW mesh resolution finer than the one presented here results in an underprediction of the streamflow and stage instead of an overprediction, but the overall performance of C3 is more accurate in comparison to C1.

Table 2.5 Statistical analysis of model performance

Streamflow at Outlet					
Model	R ²	NSE	Slope	PBIAS	RSR
C1	0.85	0.77	0.96	-8.6	0.47
C2	0.80	0.50	0.77	-28.8	0.70
C3	0.95	0.94	0.95	-6.0	0.24
Stage at Outlet					
Model	R ²	NSE	Slope	PBIAS	RSR
C1	0.81	0.69	0.94	-6.6	0.56
C2	0.78	0.01	0.79	-22.4	0.99
C3	0.95	0.93	0.97	-3.2	0.26

2.6.2 Quantification of the relative contribution of watershed processes

The results in the previous section illustrate the importance of integrating rainfall and subsurface flow with surface water models for production of flood inundation maps. C3 is uncalibrated and yet the performance statistics suggest that this model predicts both the streamflow and stage accurately for the simulation period. In addition to reducing calibration uncertainty, it is also essential to quantify the contributions from different watershed processes during flood events. This analysis can help in highlighting which process plays a dominant role in exacerbating or attenuating the flood responses.

To quantify the relative contribution of different processes during a storm event, the volumetric contributions from hydraulic routing, vadose zone, and GW recharge, are evaluated for C3. Since estimating the exact flow paths for GW flow regimes is beyond the scope of this study and is less relevant in the context of flood simulation, the volumetric contribution divided by the watershed area (mm), is used as a metric for quantifying the relative contributions from different physical processes. Fig. 2.7a presents the streamflow hydrograph for C3, which is used as a metric to evaluate the volume of water leaving the watershed through the surface. Fig. 2.7b shows the ‘Stream Inflow’, which is the cumulative volumetric inflow into the model from all eight upstream

USGS gage stations for C3, and the ‘Stream Outflow’, which is the cumulative volume of water discharging or leaving the system from the model outlet, which is located at USGS gage 03335500, Wabash River at Lafayette. Fig. 2.7b also presents ‘ Δ Surface Storage’, which provides a cumulative estimate of the increase or decrease in the surface water volume in the river-floodplain system for the entire watershed. When flood responses are mapped without rainfall and subsurface integration, (for example, C1), the difference in ‘Stream Inflow’ and ‘Stream Outflow’ should represent the change in surface water inundation for the watershed. For C3 on the other hand, the ‘ Δ Surface Storage’ is also a function of rainfall excess and GW seepage.

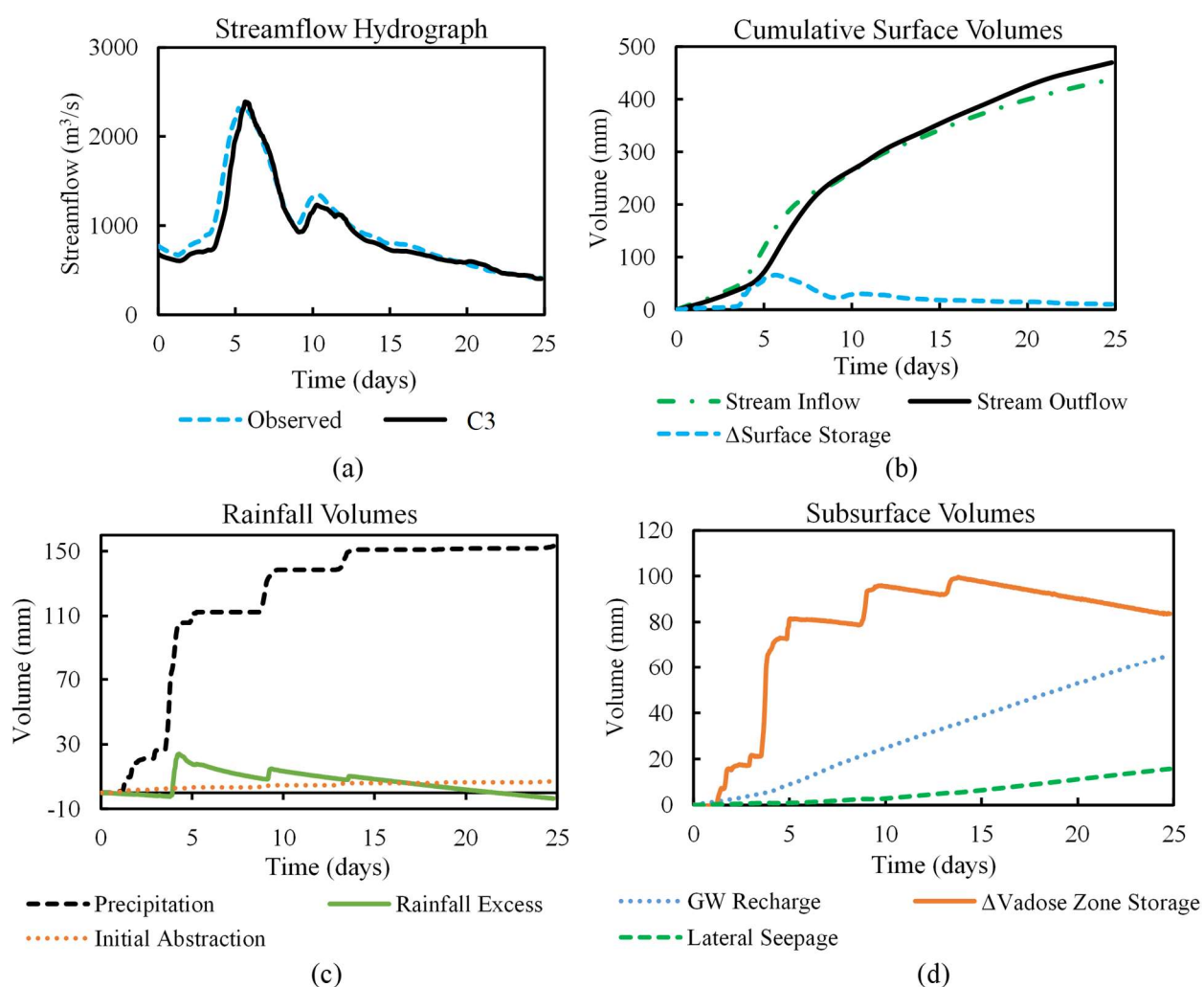


Fig. 2.7 (a) Streamflow hydrograph; (b) cumulative surface volumes; (c) volumetric contributions from rainfall; and (d) volumetric contributions from the subsurface for a 25-day simulation (April 16th to May 10th, 2013)

Fig. 2.7c shows ‘Precipitation’, which is the cumulative rainfall for the entire drainage area during the entire simulation period. The ‘Rainfall Excess’ (shown in Fig. 2.7c) represents the hourly excess rainfall volume which is delivered to the surface as runoff from the vadose zone, after evaluating infiltration and initial abstraction losses. Therefore, this represents the volume of runoff per hour that causes surficial ponding and subsequent inundation. The ‘GW Recharge’ (shown in Fig. 2.7d) represents the volume of water removed from the vadose zone due to downward percolation, which is delivered to the groundwater system as recharge. In addition, when the WT rises and intercepts the surface, the water is discharged to the surface system as ‘Lateral Seepage’, shown in Fig. 2.7d. Therefore, both ‘Rainfall Excess’ and ‘Lateral Seepage’ contribute additional volume to the surface system during flood events, thereby resulting in increased flood inundation, which is highlighted in Table 2.4 and Fig. 2.6.

The hydrograph in Fig. 2.7a highlights that C3 can capture streamflow variability throughout the simulation. On the other hand, in addition to the overprediction near the hydrograph peak, C1 underpredicts streamflow after a simulation time of 220 hours, as highlighted in Fig. 2.5a. As shown in Fig. 2.7d, the subsurface storage increases significantly during peak rainfall intensity, which accounts for reduction in overall surface storage, thereby producing a more accurate streamflow prediction during high flow conditions. After the rainfall event, the vadose zone storage recedes resulting in more GW recharge. This increase in potentiometric head in the surficial aquifer causes increased lateral seepage (Fig. 2.7d) from the subsurface into the river system. This lateral seepage volume results in a more accurate streamflow prediction during low flow conditions for C3 (after 400 hours, as shown in Fig. 2.7a) when compared to C1, which does not capture the increased streamflow due to GW seepage. Therefore, subsurface processes influence both the streamflow, and the surface water inundation, throughout the simulation.

These results further highlight the shortcomings of the current surface water models that route the streamflow solely based on roughness coefficients. While C1 overestimates the streamflow for this watershed, the absence of subsurface processes can lead to an underprediction of streamflow in GW-dominated watersheds. To rectify this overprediction/underprediction in streamflow, modelers calibrate the roughness coefficients for decreasing/increasing the flow velocities, thereby, changing the volume of water intercepted in the surface system. This practice of calibrating often improves the model results for specific events, however, without a true

representation of the streamflow attenuation or amplification caused by subsurface processes, these models can produce erroneous flood estimates for other events (Moore and Doherty, 2005).

2.6.3 Evaluating the effect of antecedent soil conditions on flood output

The results from the previous sections highlight the influence of subsurface processes on flood responses. The analysis in this section aims to evaluate the potential of existing vadose zone moisture content and WT location in controlling surface water inundation and streamflow generation. Therefore, only the subsurface component of C3 is modified in this step. The hypothesis is that the WT location determines the control of groundwater in redistributing soil moisture upwards in the vadose zone, which further impacts the land surface inundation. Three soil moisture scenarios are used to represent dry, moderate and wet conditions. For the dry scenario (D), the initial soil moisture in the vadose zone is near wilting point and the average depth of WT is approximately 6 m. Floods occurring during this scenario are synonymous to heavy rainfall occurring when dry conditions have existed for a long time before the event. Similarly, for the wet scenario (W), the vadose zone is very shallow (depth to WT < 0.5 m), and the degree of saturation in the vadose zone ranges from 0.90 to 0.95. Therefore, even a small amount of percolation can saturate the vadose zone as the initial soil moisture is very close to the porosity. Flooding in this scenario is synonymous to two extreme rainfall events occurring one after the other. The moderate scenario (M) represents the case where the soil moisture is at field capacity, and the WT is at an intermediate depth of 1.5 m from the surface, which also represents the NRCS's average vadose zone depth of 150 cm. The initial stage surface is imported from C3 using the stage outputs just before the 50-year storm event. The three scenarios (D, W and M) are run in an unsteady-state to simulate hourly flood inundation and streamflow outputs for the storm event and the comparisons are used to analyze the influence of existing subsurface conditions on flooding.

Table 2.6 Hydrologic and hydraulic outputs for multiple antecedent soil conditions

Variable	Moderate (M)	Dry (D)	Wet (W)
Peak Streamflow (m ³ /s)	2389.3	2302.1 (-3.7)	2647.8 (+10.8)
Lowest Streamflow (m ³ /s)	606.8	394.2 (-35.0)	607.0 (+0.03)
Average Streamflow (m ³ /s)	1204.6	997.5 (-17.2)	1294.7 (+7.5)
Peak Inundation Area (km ²)	188.2	165.2 (-12.2)	264.5 (+40.5)

*The values in parenthesis represent the relative difference (%) with respect to moderate (M) configuration

The results in Table 2.6 suggest that there is a significant difference in both the streamflow outputs and inundation area obtained using the three scenarios. The M scenario is considered as the base model to evaluate the relative difference when dry and wet conditions exist. Table 2.6 also shows that there is a 10.8% increase and a 3.7% decrease in peak streamflow for W and D respectively. In addition, the flood inundation area obtained using D is less severe (-12.2%) due to completely dry subsurface conditions, and more severe (+40.5%) due to completely saturated subsurface conditions for W as shown in Fig. 2.8. For the same amount of precipitation, the cumulative change in vadose zone storage (Fig. 2.8c) is highest for D, followed by M, and lowest for W. Since W has a nearly saturated vadose zone, a larger portion of the rainfall is redistributed to the surface as excess rainfall, which directly affects the peak inundation area (Table 2.6). Additionally, this also results in significantly higher GW recharge volumes throughout the simulation for W. Therefore, when the subsurface is saturated, the peak streamflow, cumulative outflow volume and GW recharge, increase substantially.

The flood inundation maps presented in Fig. 2.8e, 2.8f and 2.8g represent the extent of inundation across the three configurations at the exact instance of time when the peak streamflow is observed at the outlet. The flood inundation map shown in Fig. 2.8g suggests that the extent of inundation at peak streamflow also increases when saturated conditions (W) exist, as there is no infiltration into the subsurface, in addition to higher GW contributions due to lateral seepage when the WT interacts with the surface. It should be noted that these instantaneous maps do not show the maximum inundation in the watershed during the simulation period which can even occur before or after the peak streamflow is observed. As shown in Table 2.6, there is only a 3.7% difference in the peak streamflow for the dry and moderate conditions. Therefore, when the peak streamflow is observed, there is very small difference in the extent of inundation between the dry and moderate configurations as shown in Fig. 2.8e and 2.8f. However, Table 2.6 suggests that there is an overall difference of 12.2% in the maximum inundation area between the two configurations suggesting that the maximum inundation at specific locations may have occurred at different times. The results validate the hypothesis that the location of the WT and existing soil moisture influence the overall flood inundation outputs.

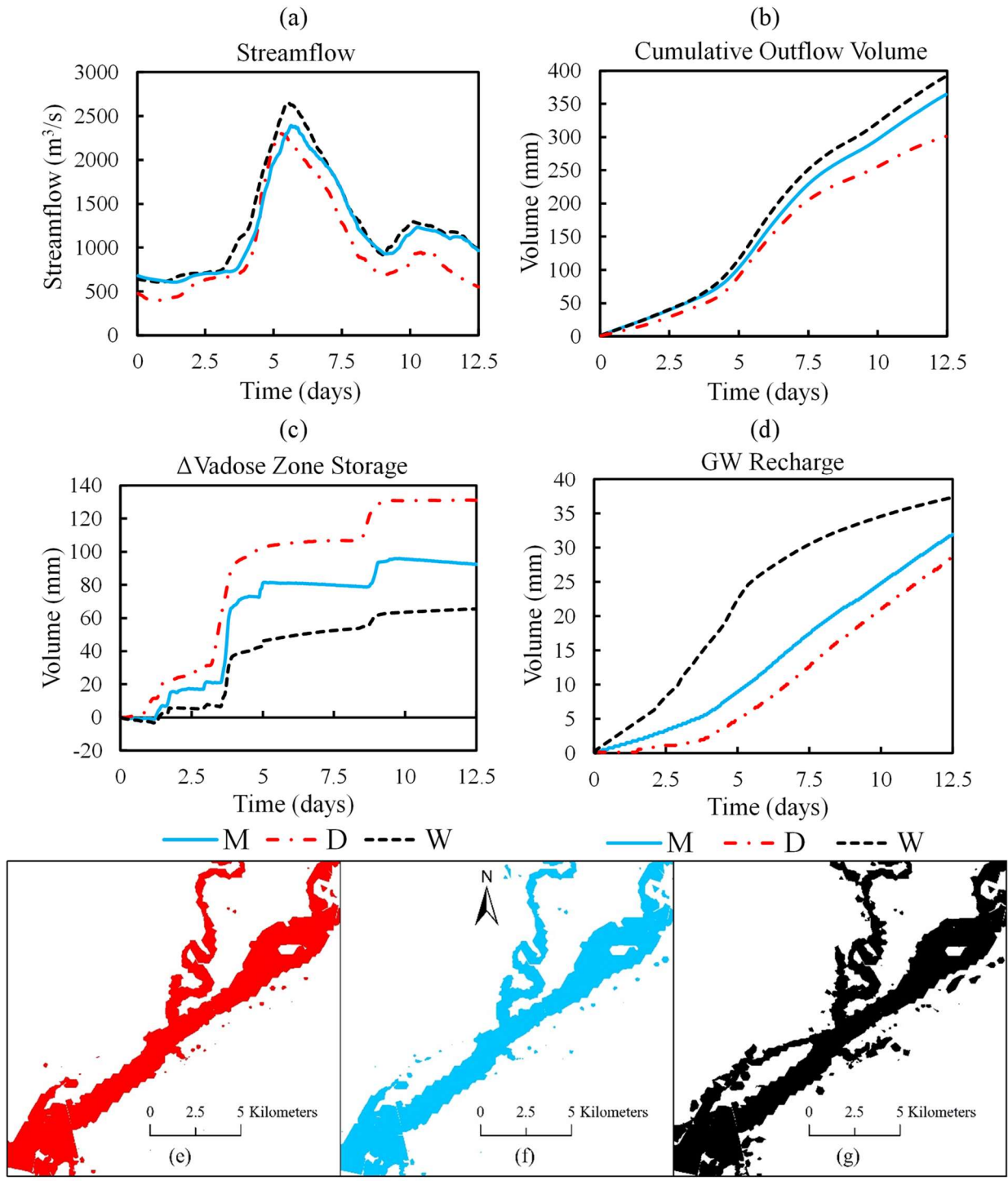


Fig. 2.8 (a) Streamflow at outlet; (b) cumulative outflow volume through the outlet; (c) cumulative change in vadose zone storage; (d) cumulative GW recharge; and flood inundation maps at peak flow for (e) dry (D); (f) moderate (M); and (g) wet (W) subsurface conditions for 12.5 day simulation (April 16th to April 28th, 2013)

The hypothetical phenomenon presented here using the W scenario highlights the potential of a fully saturated subsurface in increasing flood risk, which was observed during both Hurricane Frances and Hurricane Matthew (Weaver et al., 2016). Generally, floods corresponding to a specific return period have a standard map with a fixed extent of inundation, for example, 100-year FIRMs. However, due to existing saturated conditions, flooding from a 100-year flood event can be more severe than anticipated. Therefore, static flood maps should also be created based on antecedent soil moisture conditions as well as the WT location. For coastal aquifers that are prone to hurricane-induced rainfall, containing a shallow WT, and a higher antecedent soil moisture, these flood maps should be re-evaluated using integrated models so that the true flood risk can be estimated.

2.6.4 Further validation of C3 model

The results from the previous sections highlight the advantage of integrating hydraulic and hydrologic processes for simulating flood responses. To validate these findings, and further analyze the difference in the conventional flood modeling approach (C1) and the integrated modeling approach (C3), two models for the UWR basin (referred to as C1-UWR and C3-UWR) are simulated for a long-continuous three-month period from February 15th to May 15th, 2018, using the same model parameters. The first two days are used as warm-up period and the results are compared against observed data at the outlet (Wabash River at Lafayette) from February 17th to May 15th, 2018.

The results shown in Fig. 2.9 and Table 2.7 clearly highlight the advantage of using an integrated modeling approach for flood simulation. The hydrograph in Fig. 2.9c highlights that C3-UWR can capture streamflow variability throughout the simulation, which can be seen from the superior NSE (0.97), PBIAS (-4.2%) and peak flow error (-5.3%). On the other hand, C1-UWR (Fig. 2.9a) overpredicts the streamflow for high and moderate flows throughout the simulation, which is highlighted by the NSE (0.92), PBIAS (+12.1%), and peak flow error (+14.9%). Additionally, the results from Fig. 2.5 and 2.9 suggest that both C1 and C3 can capture the low flows accurately. The accurate performance of C1 during low flows in streamflow-dominated streams like the Wabash River highlights its applicability in conditions where the water remains inside the river channel and the volume of water exchanged between the river and subsurface is

insignificant in comparison to streamflow. Finally, the results also validate the applicability of the refined Green-Ampt method used in this study for continuous simulations.

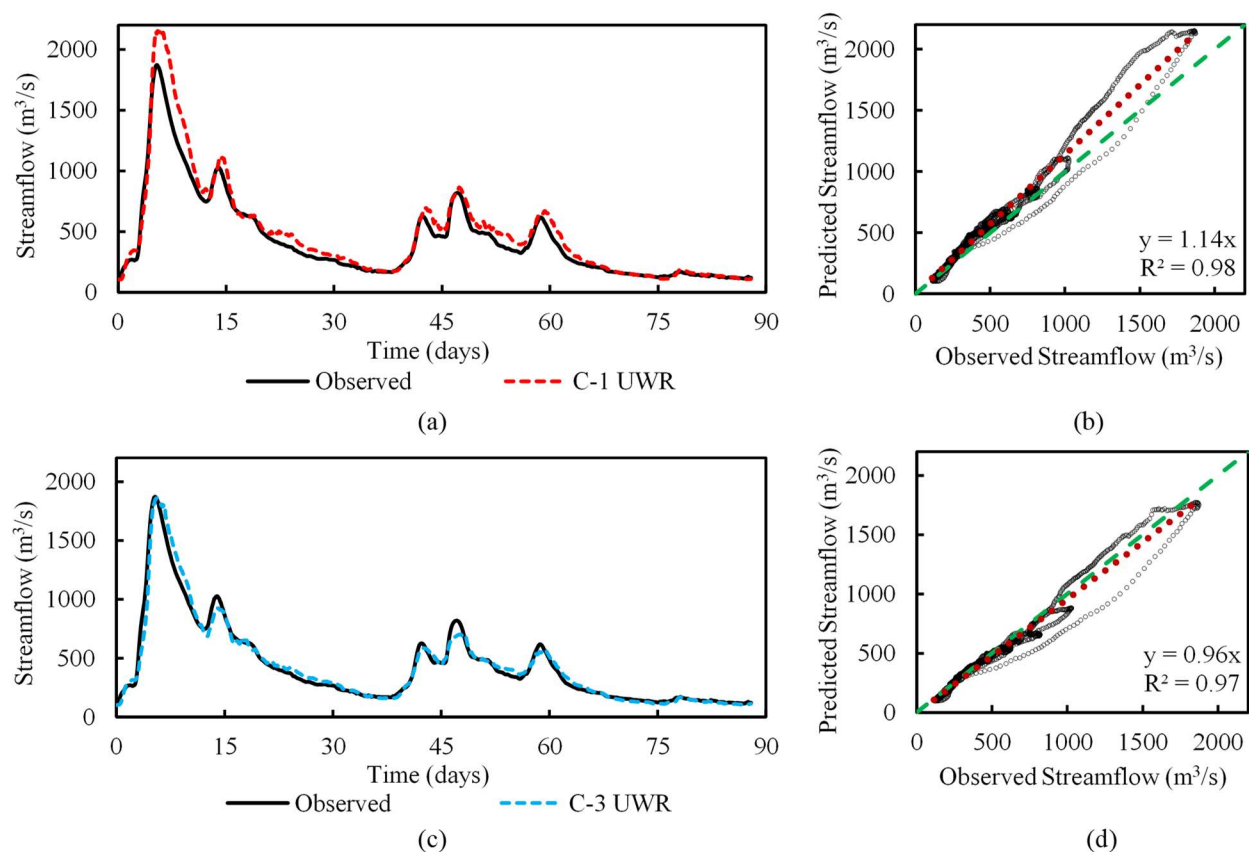


Fig. 2.9 Model comparison and validation for a three-month continuous simulation (February 17th to May 15th, 2018) for the UWR basin

To warrant a broader applicability of the integrated modeling approach, the C1 and C3 configurations are also tested for another watershed with significantly different physical characteristics from the UWR basin. Therefore, the East Branch Croton River (CR) basin with a drainage area of 210 km², situated in the state of New York, USA, is chosen as an additional validation site. As shown in Fig. 2.10, the land use for the CR basin is characterized by 56% forest cover, 23% developed, 11% agriculture, and 10% water. On the other hand, the land use for the UWR basin comprises of 7 % forest, 9% developed, 82% agriculture, and 2% water (Table 2.1), highlighting the difference in the physical characteristics between the two watersheds. Additionally, unlike the Wabash River, which is channel-flow dominated, the Croton River is a rainfall-runoff dominated stream surrounded by wetlands. The outlet of the CR basin is located at the USGS gage 01374505, East Branch Croton River at Brewster, NY as shown in Fig. 2.10. To

aid a more extensive validation, the performance of C1 and C3 is also compared against observed data inside the watershed at an additional USGS gage 0137449480, East Branch Croton River near Putnam Lake, NY. Using the same modeling approach as the UWR basin, two models for the CR basin (referred as C1-CR and C3-CR) are simulated for a continuous seven-month period from March 1st to September 30th, 2011. To provide a longer time for incorporating antecedent conditions in the integrated model, the first two months are used as warm-up period, and the results are compared with the observed data from May 1st to September 30th, 2011.

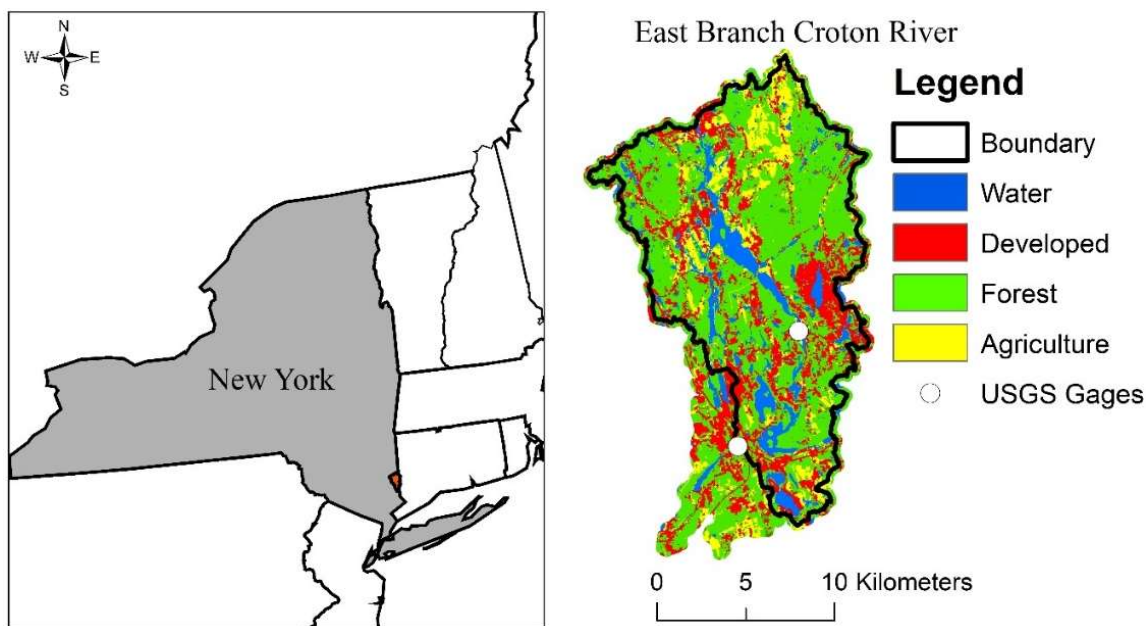


Fig. 2.10 Location map for East Branch Croton River Basin in New York

The results shown in Fig. 2.11 highlight the inability of C1-CR to capture streamflow variability in small rainfall-runoff dominated catchments, especially for low flows. As shown in Fig. 2.11c and Table 2.7, C1-CR overpredicts both the high and low flows at Brewster (NSE = 0.18, PBIAS = +86.3%, and Error Peak Flow = +23.4%). It is evident from Fig. 2.11d that C3-CR (NSE = 0.85, PBIAS = +4.2%, and Error Peak Flow = -21.1%) has a superior performance compared to C1-CR. The difference in the performance between the two configurations becomes wider during long-term continuous simulations, especially for small rainfall events. A possible explanation for this difference is the shallow channel conveyance and existence of wetlands around the Croton River, which can cause higher river-floodplain interactions even during low flows, resulting in streamflow attenuation during small events, which is evident from Fig. 2.11b and 2.11d.

When considering only the high flows which are more relevant to flood modeling, the performance of C1-CR is comparable to C3-CR at Brewster. The difference in performance is also observed at Putnam (inside the watershed), where C1-CR (NSE = 0.50, PBIAS = +64.8%, and Error Peak Flow = +41.6%) overpredicts the streamflow (Fig. 2.11a) during the continuous simulation, and C3-CR (NSE = 0.95, PBIAS = -6.1%, and Error Peak Flow = +12.1%) captures the hydrograph variability including the peak flows more accurately (Fig. 2.11b). The results from Fig. 2.11 and Table 2.7 highlight the broader applicability of the integrated modeling approach (C3) for watershed with distinct physical characteristics.

Table 2.7 Statistical analysis of streamflow prediction for model validation

Model	R²	NSE	Slope	PBIAS	RSR	Error Peak Flow (%)
C1-UWR	0.98	0.92	1.14	+12.1	0.28	+14.9
C3-UWR	0.97	0.97	0.96	-4.2	0.17	-5.3
C1-CR Putnam	0.74	0.50	1.26	+64.8	0.70	+41.6
C3-CR Putnam	0.95	0.95	0.99	-6.1	0.23	+12.1
C1-CR Brewster	0.68	0.18	1.38	+86.3	0.91	+23.4
C3-CR Brewster	0.85	0.85	0.95	+4.2	0.39	-21.1

As highlighted in Section 2.5.3, incorporating accurate antecedent conditions is essential in improving the predictive capacity of integrated models. This is also evident from the accurate performance of C3-CR, for which a sufficiently long warm-up period is chosen (2 months) to incorporate antecedent conditions more accurately. Therefore, during event-scale flood modeling, the rainfall distribution and streamflow patterns prior to the event should be carefully analyzed and saturated, dry or moderate soil moisture distribution should be used for characterizing initial conditions depending on the hydrologic time series preceding the flood events being simulated. While the performance of C3 is superior to C1 in both watersheds, this does not necessarily mean that the integrated models will obviously outperform the overland flow flood models across all watersheds. Since the physical processes involved in hydraulic and hydrologic modeling are scale-dependent, the application of integrated modeling may not achieve significant improvements compared to using simpler surface-water transport models at small spatial scales for channel flow dominated streams, when the influence of rainfall and subsurface processes is diminished.

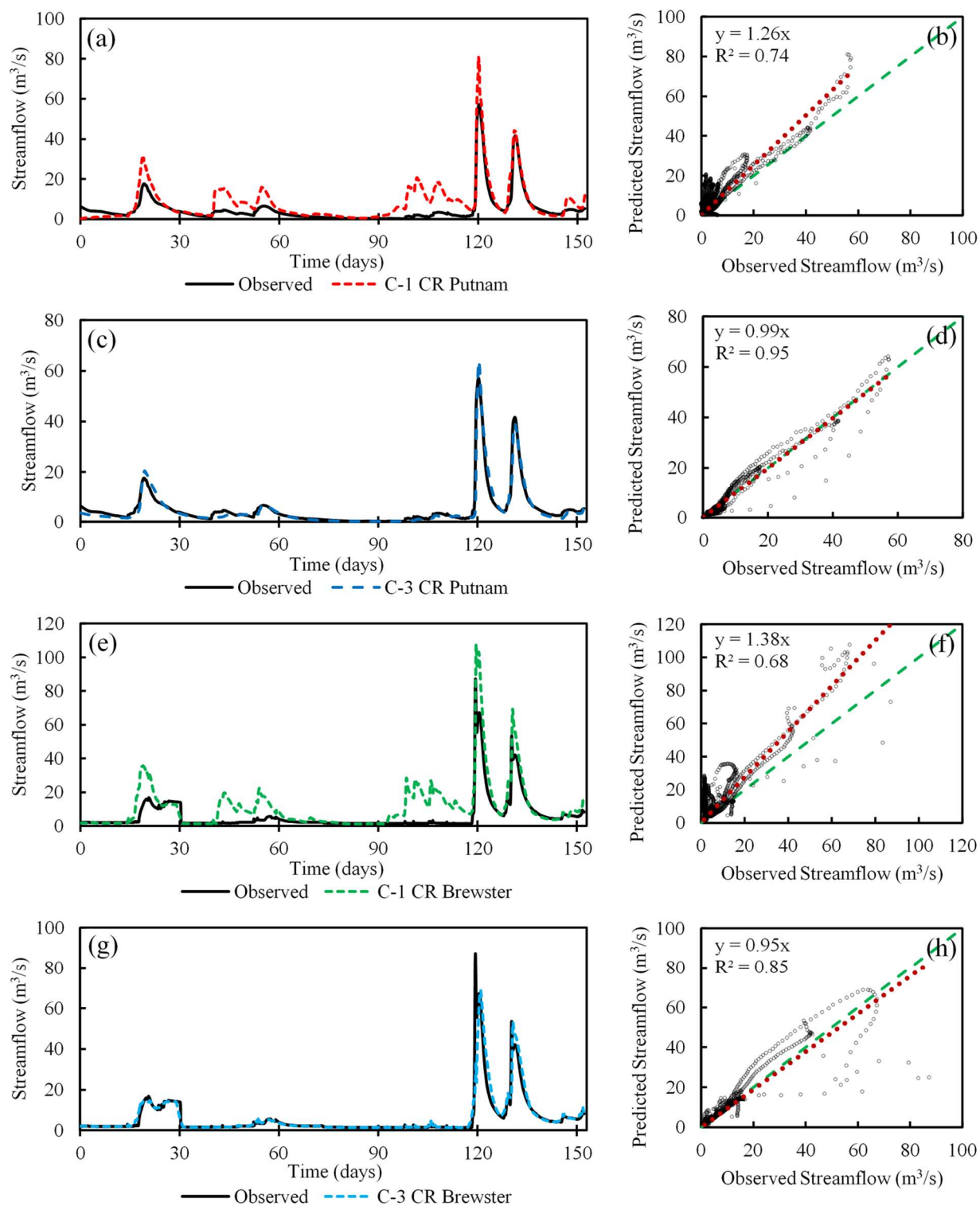


Fig. 2.11 Streamflow comparison against observed data across two gages for East Branch Croton River, NY for a five-month simulation (May 1st to September 30th, 2011)

2.7 Summary and Conclusion

Generally, hydrologic models are calibrated for streamflow while hydraulic models are calibrated for stage and extent of inundation. However, these three variables, streamflow, stage and extent of inundation are linked together, and are a function of multiple variables including topography, rainfall, soil type, land use, subsurface storage and evapotranspiration. This study highlights the discrepancies in simulating the river hydrodynamics when some of the underlying processes are not incorporated in the model. Specifically, the results from this study highlight the advantages of using integrated SW-GW models in simulating flood hydrodynamics. The following conclusions are drawn from this study:

1. A comparison of the model configurations shows that C1 produces the highest outflow volume since the change in storage is only dependent on topographic gradients and surface roughness, while C2 produces the smallest outflow volume since the water percolating below the vadose zone is lost from the water balance. The existence of a dynamic WT in C3 reduces the water lost from the system, and therefore, the outflow volume is higher than C2. Overall, C3 produces the highest NSE and lowest PBIAS in estimating streamflow and stage compared to observed data.
2. Looking at only the impact of streamflow in affecting the extent of inundation, the results from this study hint at an underprediction of the extent of inundation by using the conventional surface water modeling approach (C1 or C2) compared to C3. However, in the absence of observed extent of inundation, this conclusion needs further evaluation.
3. Most hydraulic models are calibrated by modifying the roughness coefficients but the results from this study show that an incorporation of the SW-GW dynamics within the river system (C3) can improve the performance of models in estimating streamflow and stage without any extensive calibration. This reinforces the notion that the dynamic river stage should be simulated by including SW-GW interactions in the model instead of only calibrating the roughness coefficient.
4. The existing WT location and antecedent soil moisture conditions can have a significant impact on the streamflow, stage and flood inundation area. The results suggest that saturated subsurface conditions (W) can severely increase the inundation area. On the other

hand, dry subsurface conditions (D) can reduce the overall impact of flood events. Incorporating accurate antecedent conditions is essential for predicting flood responses accurately, and therefore, adequate warm-up period should be chosen for integrated models depending on the spatial scale of the watershed and temporal scale of simulations.

5. The validation of C3 for an independent continuous 3-month simulation for the UWR basin, and for a 5-month simulation for the CR basin with different physical characteristics highlights the broad applicability of the integrated modeling approach.

It should be noted that the antecedent (initial) soil conditions are chosen at field capacity for all simulations of the integrated (C3) model. This is done as the exact soil moisture distribution is unknown at the beginning of the simulation. Similarly, the initial WT surface used in C3 is generated by simulating steady-state conditions for one month and assuming that the WT surface is in equilibrium. Further, this study uses contour maps for calculating the initial WT depths, but these maps are sparsely distributed and are not available for majority of the watersheds in the world. Therefore, it is possible that the superior performance of the C3 model is influenced by the choice of antecedent soil moisture distribution and the availability of accurate WT information for the UWR basin in Indiana. In the absence of such information, it is necessary to incorporate a substantially long warm-up period (e.g. two months for CR basin), which can help in balancing the soil moisture profile before the actual event is simulated. However, this warm-up period should be chosen depending on the scale of the watershed, magnitude of the event, and climatic conditions preceding the event for accurately incorporating the antecedent conditions (Berthet et al., 2009; Pathiraja et al., 2012; Zehe and Blöschl, 2004).

Similarly, the initial WT location for integrated modeling can be simulated by assuming that the WT is located at a fixed depth below the ground surface (e.g. 2 m for the CR basin), followed by a rebalancing of the WT hydraulic heads using a long steady-state simulation. This method is used to initialize the WT for the C3-CR model and the results presented here support its applicability. Another alternative to this approach is to start the model simulation during a dry season by assuming completely saturated subsurface conditions (WT = ground surface) and simulating the model for a period of more than three months to let the model obtain equilibrium before the onset of the rainy (wet) season. Regardless, these methods need to be validated across

several other watersheds with different physiological characteristics to justify a broader applicability.

Evapotranspiration is an important physical process that can impact river hydrodynamics and other hydrologic variables in the water cycle, especially during continuous simulations of several months. One of the limitations of this study is that ET is only incorporated in the 7-month simulation of the CR basin (Section 2.5.4). As shown in the results, the absence of ET does not affect the performance of C3 in estimating streamflow and stage for the UWR basin. This could be due to the large spatiotemporal scale of rainfall distribution, high relative humidity and cloud cover over many days in the simulation period. While the impact of ET may be less significant for the events in this study, the absence of ET may result in erroneous estimation of streamflow and stage during other events, and at other locations. Therefore, the effect of ET should be incorporated in future studies for long-term-continuous integrated modeling.

As mentioned in Section 2.6.1.2, two additional SW mesh resolutions, including one that is coarser, and another that is finer, are also used to evaluate the performance of C1, C2 and C3. The overall conclusions do not change, but the degree of overprediction or underprediction in comparison to the observed data is different when using a different SW mesh resolution. Considering that streamflow, stage and inundation extents are directly influenced by the SW mesh resolution, the performance of C1 or C2 may become comparable to observed data for a specific mesh resolution. While this is not evaluated in this study, it is expected that this would be specific to the event and watershed characteristics, and therefore, would be difficult to quantify. On the other hand, integrated modeling may provide a more reliable and consistent performance regardless of the SW mesh resolution and watershed characteristics. In this study, the SW mesh resolution of the models is chosen for maintaining a balance between the computational efficiency of the models and the desired resolution of the flood outputs. If computational efficiency is not a limiting factor, the SW mesh resolution should be increased to enhance the quality of the flood maps.

While it may be argued that the integrated model performance is specific to the watersheds used for the analysis, the broader goal here is to highlight the reduction in modeling uncertainties when SW-GW interactions are incorporated in modeling and mapping the flood inundation.

Watersheds with different physical characteristics react to rainfall events of similar magnitude and intensities differently. Similarly, the groundwater characteristics of the region control the amount of seepage, recharge, and WT fluctuations. Therefore, the integration of subsurface processes may achieve improvements of different degrees for watersheds depending on the physiographic and hydrogeologic characteristics. However, even a watershed with a completely different land use classification, aquifer characterization, and soil classification, can be modeled accurately, when the physical processes driving the hydrologic variability are incorporated. For example, a watershed with an urban land use, low infiltration capacity, and clayey aquifer will undergo diminished SW-GW interactions. While the GW recharge and vadose zone storage might reduce in such a scenario, excess rainfall contributions due to increased impervious cover and reduced infiltration will become more significant, and the inability of traditional streamflow driven flood models to account for excess rainfall in the watershed, may still result in poor performance. Alternatively, if excess rainfall and infiltration calculations are integrated with channel flow for such watersheds, it might yield a more realistic representation of the river-floodplain hydrodynamics, and therefore, the overall flood simulation would be more reliable. Therefore, future studies should incorporate the effect of antecedent atmospheric and subsurface conditions in flood models for more reliable flood determination.

3. ANALYZING THE INFLUENCE OF SPATIAL SCALE ON PHYSICAL PROCESS REPRESENTATION IN INTEGRATED MODELS FOR IMPROVED FLOOD SIMULATIONS

3.1 Abstract

As the flood intensity is expected to increase from urbanization and climate change, it is essential to improve the applicability of physically-based integrated models across large spatial scales for more reliable flood prediction. While the impact of spatial scale variability has been quantified for surface water (SW) and groundwater (GW) processes, there is a need to incorporate an optimal modeling structure for upscaling small scale processes, and to identify the optimal spatial resolution for quantifying surface-groundwater interactions at larger scales. This study aims to provide solutions to better characterize scale-dependent processes in integrated models by comparing two model structures across two spatial scales and analyzing the changes in flood responses. Using the Upper Wabash River Basin in Indiana, the Interconnected Channel and Pond Routing (ICPR) model is used for analyzing the scale-dependent behavior of physical processes such as overland flow, rainfall, infiltration, GW recharge, and seepage. The results indicate that since the characteristic length scales of GW processes are longer than SW processes, the intrinsic scales of GW sub-models should be coarser when compared to SW sub-models. The results also highlight the degradation of streamflow prediction using a single channel roughness when the stream length scales are increased. A distributed channel roughness variable along the stream length improves the modeled basin response. Further, the results highlight the ability of a dimensionless parameter η_L , representing the ratio of the reach length in the study region to maximum length of the single stream draining at that point, for identifying which streams may require a distributed channel roughness. Incorporating the modeling structure obtained from this analysis improves the flood prediction across two watersheds with distinct physical characteristics.

3.2 Introduction

Riverine flood modeling is affected by several uncertainties arising from streamflow estimation, quality of topographic data, spatiotemporal scale and resolution, model selection, calibration and parameterization, among others (Hall et al., 2005; Pappenberger et al., 2006;

Straatsma and Huthoff, 2011). For extreme events occurring across large watersheds, flood hydrodynamics is influenced by fundamental factors such as topography, channel bed-form, roughness distribution, rainfall distribution and intensity, groundwater (GW) seepage, infiltration, floodplain storage, and antecedent soil moisture conditions (Bloschl and Sivapalan, 1995; Hattermann et al., 2004; Hunter et al., 2007; Kim et al., 2012; Meire et al., 2010). Therefore, the existing assumptions driving flood modeling at reach scales may become invalid when applied for modeling flood events that occur across large watersheds, and integration of physical processes may be necessary to obtain reliable models for large watershed scale flood events (Gunduz and Aral, 2005; Hattermann et al., 2004; Liang et al., 2007; Maxwell et al., 2014; Saksena et al., 2019; Saleh et al., 2011).

In recent years, integrated models have been applied for several applications, including but not limited to, agriculture sustainability (Schoups et al., 2005), runoff generation (Kollet and Maxwell, 2006; VanderKwaak and Loague, 2001), stream-aquifer exchanges (Gunduz and Aral, 2005) and short-term forecasting and inundation mapping of natural hazards (Chen et al., 2017; Saksena et al., 2019; Saksena and Merwade, 2017a). Even though several studies at small scales conclude that integrated models perform more accurately than 2D hydrodynamic models, the use of integrated models is still in a nascent stage in large scale flood simulation (Jones et al., 2008; Maxwell et al., 2014; Rassam et al., 2013; Saksena et al., 2019). Since hydraulic-hydrologic-groundwater dynamics is formulated in a single system in integrated models, several degrees of complexities arise, including but not limited to, coupling mechanisms, spatiotemporal scaling, optimal numerical formulations, and computational efficiency (Atkinson et al., 2003; Ko et al., 2019; Paniconi and Putti, 2015; Patil and Stieglitz, 2015; Yu et al., 2014). There is an increasing global trend towards developing large scale integrated flood models to drive the future flood risk planning (Beven and Cloke, 2012; de Moel et al., 2015; Hattermann et al., 2004; Knebl et al., 2005; Schumann et al., 2014). However, before using integrated models for large scale flood simulation, there is a need to quantify and improve the characterization of scale-dependent physical processes affecting the watershed responses during flood events (Fatichi et al., 2016; Peters-Lidard et al., 2017).

One of the major issues in spatial extent scaling of integrated models is that the physical processes do not scale linearly from smaller to larger spatial scales as all physical processes exhibit

their own characteristic spatiotemporal scales. Hydrologic processes such as rainfall, GW recharge, lateral seepage and infiltration; and hydraulic processes such as channel flow routing, travel time and movement of hydraulic fluxes, are all influenced by spatial scaling to different extents (Goodrich et al., 1997; Muleta et al., 2007; Seyfried and Wilcox, 1995; Vivoni et al., 2007; Wood et al., 1988; Woods et al., 1997). Additionally, integrated models contain several sub-models for hydraulic routing, rainfall-runoff partitioning, and GW flow simulations. Therefore, the intrinsic sub-model scales (or resolution) needed to accurately simulate these processes may be different at small and large spatial scales.

Over the last few decades, several studies have evaluated the optimal spatial scaling of single processes or individual sub-models (Bloschl and Sivapalan, 1995). For example, Becker and Braun, 1999 suggested that a simple spatial scaling of Instantaneous Unit Hydrograph (IUH) for modeling lateral flows in basins can be obtained using drainage area and mean surface elevation (m.s.e.). Yu et al. (2014) investigated the effect of spatiotemporal grid scales of input data (precipitation and soil moisture) on the simulated discharge response. The study concluded that the intrinsic scale (or resolution) of the rainfall-runoff model is affected by the choice and resolution of its parameters. In a similar study evaluating the effect of simplifying the watershed geometry on basin runoff response, Lane and Woolhiser (1977) found a simplest kinematic cascade geometry that can preserve the runoff response of the watershed accurately. In terms of gridded models, this means that a maximum equivalent resolution exists for characterizing the overland flow region beyond which the simulated hydrograph becomes unreasonable. Additionally, Skøien et al. (2003) evaluated the characteristic space-time scales of precipitation, runoff, and GW flow using a variogram analysis.

One of the important studies in spatial scaling of integrated models by Vivoni et al. (2005) evaluated the spatial sensitivity of basin-averaged and distributed hydrologic response (water balance, runoff mechanisms, surface saturation, and GW flow) with respect to changes in topographic resolution. However, this study only analyzed the effect of modifying the spatial resolution of triangulated networks of the SW region (or intrinsic scale of the SW sub-model) and found that the near-stream resolution acts as a dominant control in affecting model performance. Considering that integrated models have both SW and GW sub-models, there is a need to quantify

the optimal intrinsic scales (or resolution) of both these sub-models relative to each other in a single system for improving the model performance across a range of spatial scales.

Another study by Wu et al. (1982) analyzed the effect of roughness distribution in the direction of flow in affecting the simulated discharge and concluded that a single (uniform) roughness can be used for a given reach length provided that the hydrographs obtained from both single and spatially variable roughness are identical. The study also concluded that the most important factors affecting the application of a uniform roughness for overland flow are the length and area (spatial extent) of the roughness domain. However, in case of larger watersheds that contain several streams of varying lengths (few to hundreds of kilometers) and geomorphological characteristics, it is difficult to identify which streams may be simulated using a single roughness and which streams may require a spatially distributed roughness. Therefore, it is essential to analyze the performance of reaches with different length scales within a large watershed to classify which reaches may need to be modeled using a distributed channel roughness and which reaches may be modeled accurately even with a single channel or uniform roughness.

The objective of this study is to improve the spatial extent scaling of integrated models through a better representation of the intrinsic scales of the physical processes and sub-models for providing a more realistic reproduction of overland flow characteristics not only at the outlet, but also within the watershed. This objective is accomplished through the following steps: (1) Analyzing the effect of spatial scaling of model extents on the SW-GW physical processes (e.g. rainfall, GW recharge and runoff) by quantifying the changes in basin response across a small and large sub-watershed for the same region; (2) Relating the change in the basin response using a single channel roughness to the stream length scales within a watershed; (3) Evaluating the effect of changing the intrinsic scale (or resolution) of the GW sub-model with respect to the SW sub-model by quantifying the change in streamflow prediction; and (4) Using the results from (1) – (3) to better capture the physical processes and improve integrated modeling at a larger spatial scale and across another watershed with distinct physical characteristics.

3.3 Study Area and Data

A portion of the Upper Wabash River (UWR) basin in Indiana, USA (shown in Fig. 3.1), is selected as the test site for this study. The UWR basin (4,385 km²) experiences significant SW-

GW interactions due to the existence of glacial till deposits, and shallow aquifers with a deep confining layer of shale. In addition, another watershed with distinct land cover but similar climatic conditions, is used as a validation site. Thus, a portion of the White River (WHR) basin with an area of 344 km², and encompassing the city of Indianapolis, Indiana, USA, is also chosen for this study. As shown in Fig. 3.1 and Table 3.1, the WHR basin is characterized by a significantly higher (86 %) proportion of developed (urban) region, when compared to the UWR basin (10 %), which has a predominantly agricultural land use. The average depth to water table for the UWR basin is 150 cm, while the WR basin has a relatively shallow water table with an average vadose zone depth of 65 cm. A 9-m resolution topographic dataset of high accuracy based on a LiDAR survey containing river channel bathymetry is used for both study areas.

The soil classification in Table 3.1 suggests a dominance of soil group ‘C’ for UWR basin, and an increase in percentage of soil group ‘D’ for the WHR basin. The average vadose zone depth from Table 3.1 suggests that the available storage in the unsaturated zone is higher for the UWR basin compared to the WHR basin. The NLDAS data is preferred over the National Oceanic and Atmospheric Administration’s (NOAA) Climate Data Online (CDO), often referred to as rainfall gage data, since NLDAS has higher spatial resolution compared to gage data, which is sparsely distributed. The outlet of the UWR basin (shown in Fig. 3.1) is located at the USGS gage 03335500 Wabash River at Lafayette, IN, (Latitude 40.422°N and Longitude 86.897°W) and the outlet for the WHR basin is located at the USGS gage 03353000, White River at Indianapolis, IN (Latitude 39.737°N and Longitude 86.169°W).

The type of data, the spatial or temporal resolution of data and the data sources are provided in Table 3.1. Several spatial datasets such as the land use, soil type, initial water table depth, impervious cover, shallow aquifer thickness and roughness are used in this study. In addition to the land use distribution, Fig. 3.1 also shows the location of the two study areas and the main hydrologic features such as the river networks, subbasins and outlet.

Table 3.1 Description of datasets and watershed characteristics

Description of Datasets		
Data	Spatial/Temporal Resolution	Source
Topographic Data (LiDAR DEM)	9 m Lidar	Indiana Spatial Data Portal (ISDP)
Land Use Data	30 m	2011 National Land Cover Database (NLCD): http://nationalmap.gov/viewer.html
Soil Type/Texture/Class/Properties	30 m	National Soil Conservation Service's (NRCS) Gridded Soil Survey Geographic database (gSSURGO)
Precipitation	~ 12 km / Hourly precipitation	North American Land Data Assimilation (NLDAS)
Streamflow	Hourly Streamflow	United States Geological Survey (https://waterdata.usgs.gov/nwis/sw)
Water Table (WT) Depth	30 m	Indiana Department of Natural Resources (IDNR) Potentiometric Surface Maps (http://www.in.gov/dnr/water/7256.htm)
Impervious Cover	30 m	Indiana Map Data Server (USGS, 2006)
Roughness Class	30 m	2011 National Land Cover Database (NLCD)
Shallow Aquifer Thickness	90 m	Indiana Geographic Information Council's (IGIC) Indiana Map server (http://maps.indiana.edu/index.html)
Watershed Characteristics		
Description	Upper Wabash River (UWR)	White River (WR)
Study Area, km ²	4,385	344
Landuse % (NLCD 2011)		
Agricultural	77	5
Forest	11	5
Open Water/Wetland	2	4
Developed	10	86
No. of USGS streamflow gages	9	5
Average vadose zone depth, cm	150	65
Soil Type % (NRCS gSSURGO)		
A	2	1
B	36	39
C	61	33
D	1	27

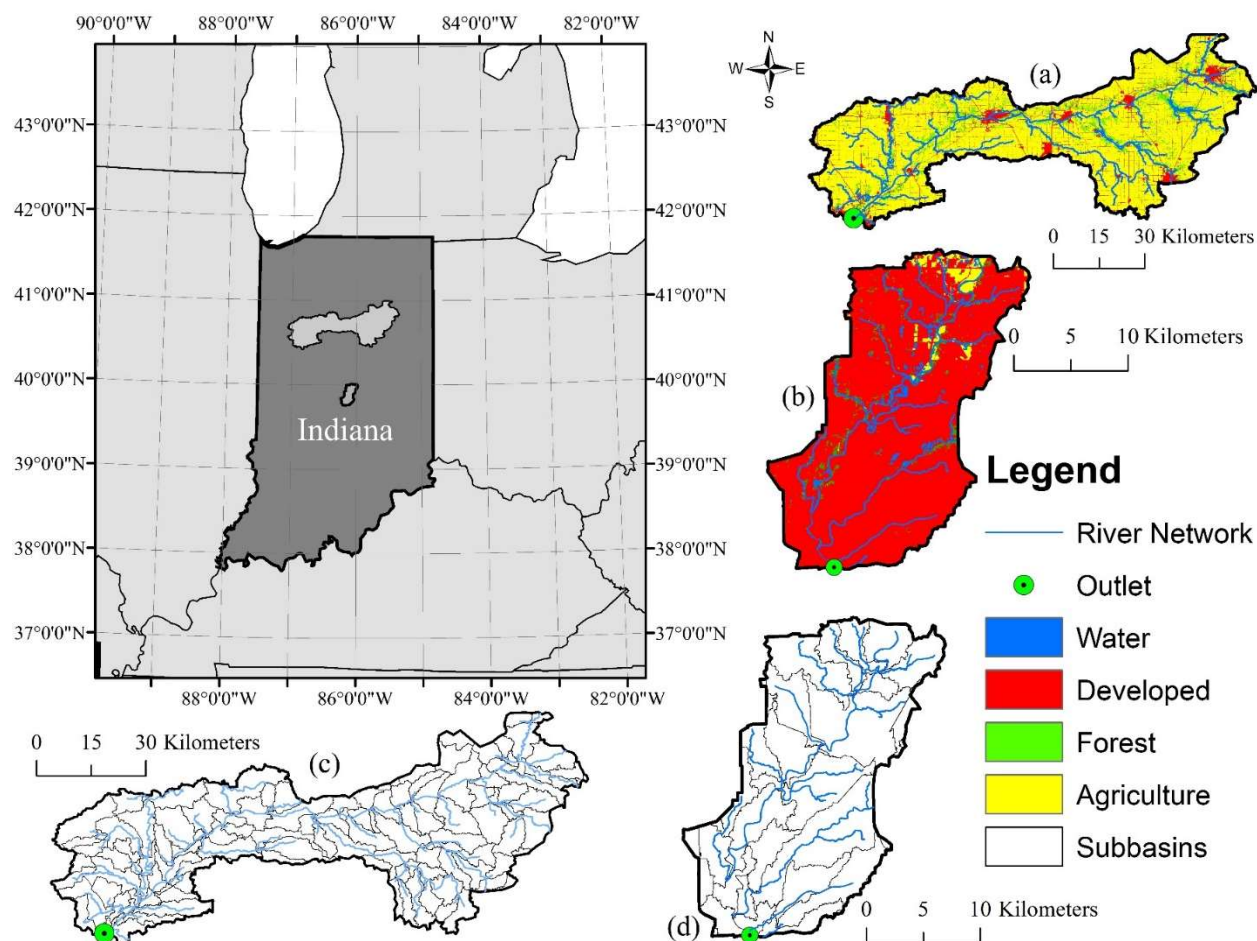


Fig. 3.1 Study area description for the UWR and WHR basin

3.4 Model Description

The Interconnected Channel and Pond Routing (ICPR) model, a physically-based, two-dimensional (2D) coupled SW-GW integrated model, is used for this study. The model description is divided into three sections (Sections 3.4.1 to 3.4.3) to describe the model characteristics, development and parameterization of the overland flow region, vadose zone and 2D GW region. A representation of the physical systems, processes and relevant model structure used for this study is presented in Fig. 3.2a.

3.4.1 Characteristics of surface and subsurface zones

3.4.1.1 Surface water zone or overland flow region

ICPR uses a finite volume approach for 2D overland flow based on a double mesh structure shown in Fig. 3.2c. Detailed description including relevant equations for overland flow routing are

presented in Appendix A. In ICPR, the momentum, energy or diffusive wave equations are lumped along the edges of a triangular mesh (Fig. 3.2c) for flow routing from one vertex to another and the mass balance equations are lumped at irregular-shaped polygons (referred to as ‘honeycombs’ in Fig. 3.2c) which are formed around the triangle vertices and are used to establish the local control volumes. Similarly, a diamond mesh is formed along triangle edges for roughness classification and extends from vertices to adjacent triangle centroids (referred to as ‘mid-nodes’ in Fig. 3.2c).

The 2D overland flow routing for this study is carried out using the diffusive wave formulations (Appendix A, Equations A.8 to A.10). A single roughness value is used for the river channels, while the land use information derived from NLCD dataset is used to determine roughness outside the river channels. The roughness outside the river channels is further characterized into a variable surface roughness based on an exponential decay function (presented in Appendix A, Equations A.12 and A.13) which is used for transitioning from shallow to deep channels (water depth > 1m) since the channel roughness changes over time when the depth of the water in the floodplain increases due to persistent flooding (Arcement Jr. and Schneider, 1984). Heterogeneities in topography, land cover and soil characteristics are incorporated into the model by intersecting the honeycomb mesh with the terrain surface and geospatial datasets (for example, soil and land use data in Fig. 3.2c) to form sub-polygons containing unique intersections of these datasets (Saksena et al., 2019; Streamline Technologies, 2018). These sub-polygons function as individual hydrologic units within a honeycomb, thereby, providing a high-resolution characterization of watershed properties.

3.4.1.2 Vadose zone characterization

The soil moisture accounting, and subsequent GW recharge in this study is computed using the ‘Vertical Layer Method’. In this method, the vadose zone is discretized into three vertical layers which are depicted in three shades in Fig. 3.2b which are bound by the ground surface and the water table. This discretization provides a non-homogeneous soil characterization in the vadose zone in which each of the three layers have distinct soil properties. Based on the gSSURGO database, each vertical layer in the vadose zone has an initial thickness of 50 cm, however, this thickness can change due to water table fluctuations during the simulation. This method is based on a non-iterative kinematic approach which distributes each of the three individual layers into

multiple cells (Fig. 3.2b) and tracks the fluxes through each individual cell in both upward and downward directions. In this study, a total of 30 cells (10 for each soil layer) are used to track the flow of water through the vadose zone. While all the cells in a single soil layer start with the same initial parameters, each unsaturated cell is wetted or dried individually during the simulation depending on the direction and magnitude of the hydraulic flux, available soil storage and unsaturated hydraulic conductivity.

Within the vadose zone, the water enters the soil column at the topmost cell and the hydraulic fluxes are calculated at the bottom of each cell based on the antecedent moisture content and the unsaturated vertical conductivity as estimated by the Brooks-Corey method (Appendix A, Equation A.13). Further, a mass balance is performed for each cell depending on the input flux minus the output flux and the moisture contents are updated based on these fluxes. Once the calculation reaches the bottommost cell of the vadose zone, the downward flux from this cell is removed from the vadose zone and delivered to appropriate groundwater node. After this step, the cells are rebalanced from the bottom to the surface while ensuring that the moisture content in each cell does not exceed saturation. In case any cell contains more moisture than the saturated moisture content, the excess is moved to the adjacent (upward) cell and delivered to the surface cell if the excess reaches the topmost cell. Based on the dynamic movement of the WT, the cells are 'fully wetted' as the WT moves upward or 'dried' to field capacity if the WT drops below the saturated cells.

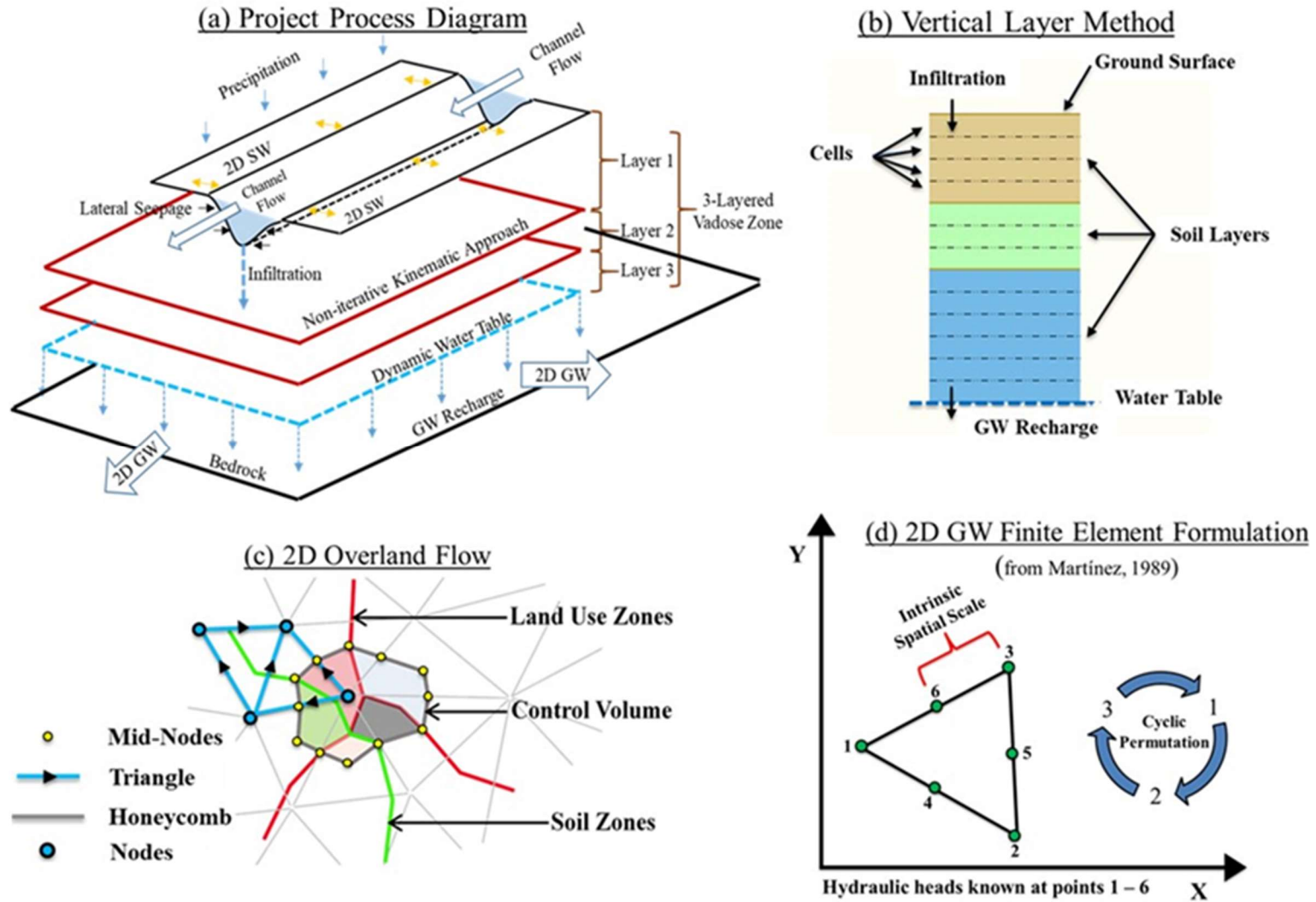


Fig. 3.2 (a) Conceptual model identifying the physical systems, processes, and model structure used for integrated modeling; (b) illustration of the vertical layer method for infiltration; (c) 2D overland flow routing and finite volume illustration; and (d) elemental description of finite element formulation used for 2D GW flow

3.4.1.3 Two-dimensional groundwater characterization

Within the surficial aquifer, the GW flow in ICPR is calculated using the 2D unsteady phreatic solution of the continuity equation using a finite element formulation. The water transport, storage variation, and external flows into the vadose zone and overland flow region are calculated by creating a six-point triangular element using a quadratic interpolation function dependent on a cyclic permutation (Fig. 3.2d), and the system of equations is solved using the Cholesky method (Kuiper, 1981; Martínez, 1989). Additionally, the change in water table location due to GW flow, and subsequent recharge from the vadose zone is dynamically tracked at each time step. The surficial aquifer is bounded by a spatially distributed bedrock layer with variable thickness, which is assumed to be impermeable. The relevant equations and their approximations used for GW flow in ICPR are provided in Appendix B.

Excess rainfall that does not enter the soil column is assigned to its respective surface node, and it routed from one surface node to another. Water that reaches the bottom of a given soil cylinder by crossing the interface between the vadose zone and the saturated zone is aggregated and delivered to its respective GW node as recharge. If the soil column in the vadose zone becomes saturated and there is inundated water on the surface, the vadose zone is bypassed and a known head condition is applied to the corresponding GW node based on the surface node stage. In this scenario, the seepage into or out of the groundwater system at that location is calculated by the GW model and removed from or delivered to the surface node based on Equation B.8 presented in Appendix B.

3.4.2 Mesh development for surface and GW zones

The 2-D mesh for both SW and GW is generated using only two features in ICPR, called ‘breakline’ and ‘breakpoint’ as shown in Fig. 3.3b. Therefore, both the SW and GW regions are discretized at the same mesh resolution. The ‘breakline’ feature is a polyline shapefile used to digitize the stream network using aerial imagery in GIS. Each point of the polyline ‘breakline’ feature is assigned a triangular vertex node in ICPR. Since more points are required to digitize river bends, the resultant mesh is denser along the river bends and at confluences.

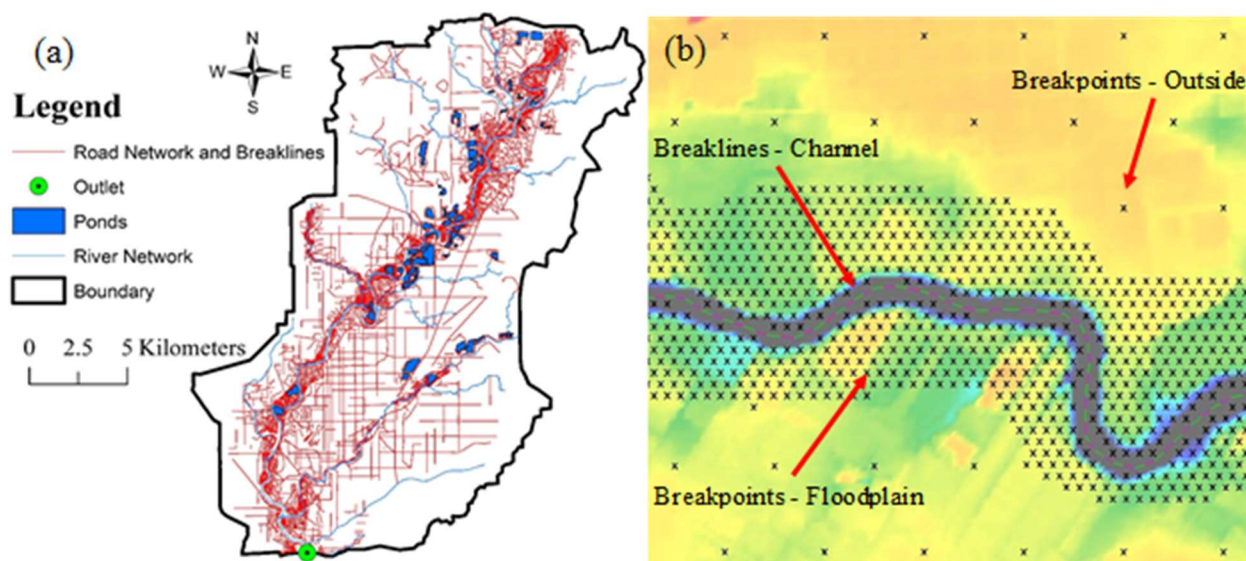


Fig. 3.3 (a) Road network and pond ingestion in ICPR for WHR region and (b) illustration of breaklines and breakpoints used for mesh generation

Across the entire length of the river networks, the ‘breakline’ feature is digitized such that the minimum distance between any two vertices is 9 m and the maximum edge length along straight channels is 27 m. Overall, the average triangular edge length in the river channels is 15 m. Triangle edges are guaranteed along a breakline and flow rates are computed along triangle edges in ICPR’s computational scheme. Based on the stream digitization in GIS, the ‘breakline’ shapefile is used to generate an average triangular mesh length of 15-m in the river channel. For mesh digitization outside the river channel, the ‘breakpoint’ feature, which is a point shapefile, is used to create the triangular mesh of consistent lengths. Triangular ‘breakpoint patterns’ with an edge length of 60-m are assigned in the river floodplains. Similarly, ‘breakpoint patterns’ with an edge length of 300-m are assigned outside the floodplain. This ensures the formation of a triangular mesh of average edge length 15-m in the river channels, 60-m in the floodplain, and 300-m outside the floodplain as illustrated in Fig. 3.3b and also presented in Table 3.3.

In addition, a 1D level-pool nodal representation of the ponds located throughout the watershed are integrated with the overland flow model. The 9-m LiDAR is used to extract stage-area rating curves, at a vertical resolution of 0.5 m, thereby ensuring that the wetted areas are calculated from the lowest elevation in the pond up to the pond control volume at every 0.5 m. A pond control volume is obtained by digitizing pond features in ArcGIS using aerial imagery as

shown in Fig. 3.3a. Since the WHR basin is located in a highly developed region, the road networks in the basin can play a significant role in routing the flow during extreme events. Therefore, the TIGER/Line® shapefile of road networks published by the U.S. Census Bureau is imported into ICPR (Fig. 3.3a) after simplifications to ensure that triangle edges are formed along the roadways thereby capturing important topographical features.

3.4.3 Model parameterization

The shallow and deep roughness values corresponding to the NLCD land use classes (Table 3.2) are directly obtained from the maximum and minimum roughness values from Chow, 1959. Table 3.2 presents the initial subsurface parameters used for the vadose zone and the GW region. The gSSURGO database contains spatially distributed hydrologic soil group classification based on runoff potential which includes variable parameters based on depth of soil. The four soil zones used in this study are based on this classification. From this dataset, the median values of the saturated vertical conductivity, moisture content at field capacity, and moisture content at wilting point (presented in Table 3.2) are extracted for the specific soil zones. The other parameters presented in Table 3.2 are extracted using the soil texture percentages (for example, percentage of sand and clay), which are also available from the gSSURGO database. These soil texture percentages are incorporated in the equations provided in Rawls, 2004 for estimating the other subsurface parameters such as pore size index, soil matric potential, and residual moisture content (Streamline Technologies, 2018).

For the GW zones, the map of the spatial distribution of different unconsolidated aquifer systems for Indiana is available from IGIC's Indiana Map Server (<http://maps.indiana.edu/index.html>). The aquifer properties for Wabash Valley are obtained from a study on the investigation of groundwater resources in Indiana (Pohlmann, 1987). Once these parameters are extracted, they are imported into the model. Since the modeling is dynamic, these parameters are used as initial or boundary conditions for the model and the actual values of moisture content, water table depth and hydraulic conductivity evolve with time based on the amount of water percolating into the subsurface.

Table 3.2 ICPR initial subsurface and surface roughness parameters

Subsurface parameters									
Vadose Zone	Soil Type	K_v (mm/hr)	Saturated MC	Residual MC	Initial MC	Field Capacity MC	Wilting Point MC	PSI	Ψ (cm)
Layer 1 50 cm	A	15.24	0.300	0.069	0.128	0.128	0.107	0.518	38.3
	B	6.20	0.540	0.061	0.200	0.200	0.138	0.620	25.5
	C	2.34	0.458	0.051	0.300	0.300	0.225	0.296	59.2
	D	1.40	0.620	0.053	0.240	0.240	0.118	0.161	197.9
Layer 2 50 cm	A	8.38	0.277	0.040	0.125	0.125	0.063	0.296	59.2
	B	3.10	0.280	0.070	0.170	0.170	0.135	0.316	67.5
	C	1.17	0.320	0.078	0.220	0.220	0.155	0.270	106.8
	D	0.80	0.360	0.080	0.200	0.200	0.090	0.161	197.9
Layer 3 50 cm	A	2.10	0.120	0.030	0.090	0.090	0.060	0.540	30.7
	B	0.77	0.200	0.040	0.100	0.100	0.040	0.226	99.8
	C	0.29	0.180	0.045	0.120	0.120	0.075	0.161	168.4
	D	0.20	0.190	0.045	0.090	0.090	0.060	0.161	197.9
GW Zone	Type	Effective Porosity, η_e		Hydraulic Conductivity, K (mm/hr)					
Aquifer	A	0.175		30.48					
	B	0.270		12.40					
	C	0.310		4.67					
	D	0.360		6.35					
Surface roughness parameters									
No.	Type of land use			Shallow	Deep				
1	Open Water			0.045	0.030				
2	Low Intensity Residential			0.020	0.011				
3	High Intensity Residential			0.015	0.011				
4	Commercial / Industrial			0.014	0.010				
5	Transportation			0.013	0.010				
6	Barren Land			0.100	0.050				
7	Deciduous Forest			0.198	0.184				
8	Evergreen Forest			0.198	0.184				
9	Mixed Forest			0.198	0.184				
10	Shrub/Scrub			0.200	0.100				
11	Grasslands			0.350	0.240				
12	Hay / Pasture			0.200	0.100				
13	Row Crops			0.180	0.100				
14	Woody Wetlands			0.060	0.045				
15	Herbaceous Wetlands			0.060	0.035				

3.5 Model Development and Numerical Simulation

3.5.1 Development of model configurations

3.5.1.1 Effect of spatial scaling of model extents

The 4,385 km² model of the unregulated UWR basin (shown in Fig. 3.4a), is characterized as the model with a larger spatial extent which is then reduced to a smaller model (Fig. 3.4a) with a spatial extent of 1,757 km². The spatial extents for the models are determined by the location of upstream USGS gages that act as boundary conditions for flow input (Fig. 3.4a). While the model with the smaller spatial extent (referred to as ‘*S*’) contains four upstream gages including the Wabash River, the model with the larger spatial extent (referred to as ‘*L*’) contains eight upstream gages (Fig. 3.4a). The USGS gage 03329000, Wabash River at Logansport, is used as the upstream boundary in the Wabash River for the ‘*S*’ model, and the USGS gage 03323500, Wabash River at Huntington, is used for the ‘*L*’ model. However, it is ensured that the outlet for both models is at the USGS gage 03335500, Wabash River at Lafayette (Fig. 3.4a). Table 3.3 provides a description of the model configurations used in this study.

3.5.1.2 Two model structures for analyzing the effect of spatial extent scaling

To identify which hydrologic outputs are affected by increasing the spatial extents of the model, the differences in surface and subsurface contributions across ‘*S*’ and ‘*L*’ models need to be quantified individually. Therefore, effect of spatial extent scaling is analyzed across two degrees of process-based complexities using two types of model structures, with and without subsurface connectivity. First, the 2D hydrodynamic modeling structure is created using the methodology described in Section 3.1.1. This model structure only incorporates the hydraulic processes, and thus, is based solely on SW routing governed by roughness characterization. The subsurface is assumed to be impervious in this structure. The models created using this structure for small and large spatial extents are referred to as ‘*S-1*’ and ‘*L-1*’ respectively. Second, a fully integrated modeling structure is developed following the procedure described in sections 3.1.1-3.1.3, which contains the SW, vadose zone and GW zones. The models created using the integrated modeling structure across small and large spatial extents are referred to as ‘*S-2*’ and ‘*L-2*’ respectively (Table 3.3).

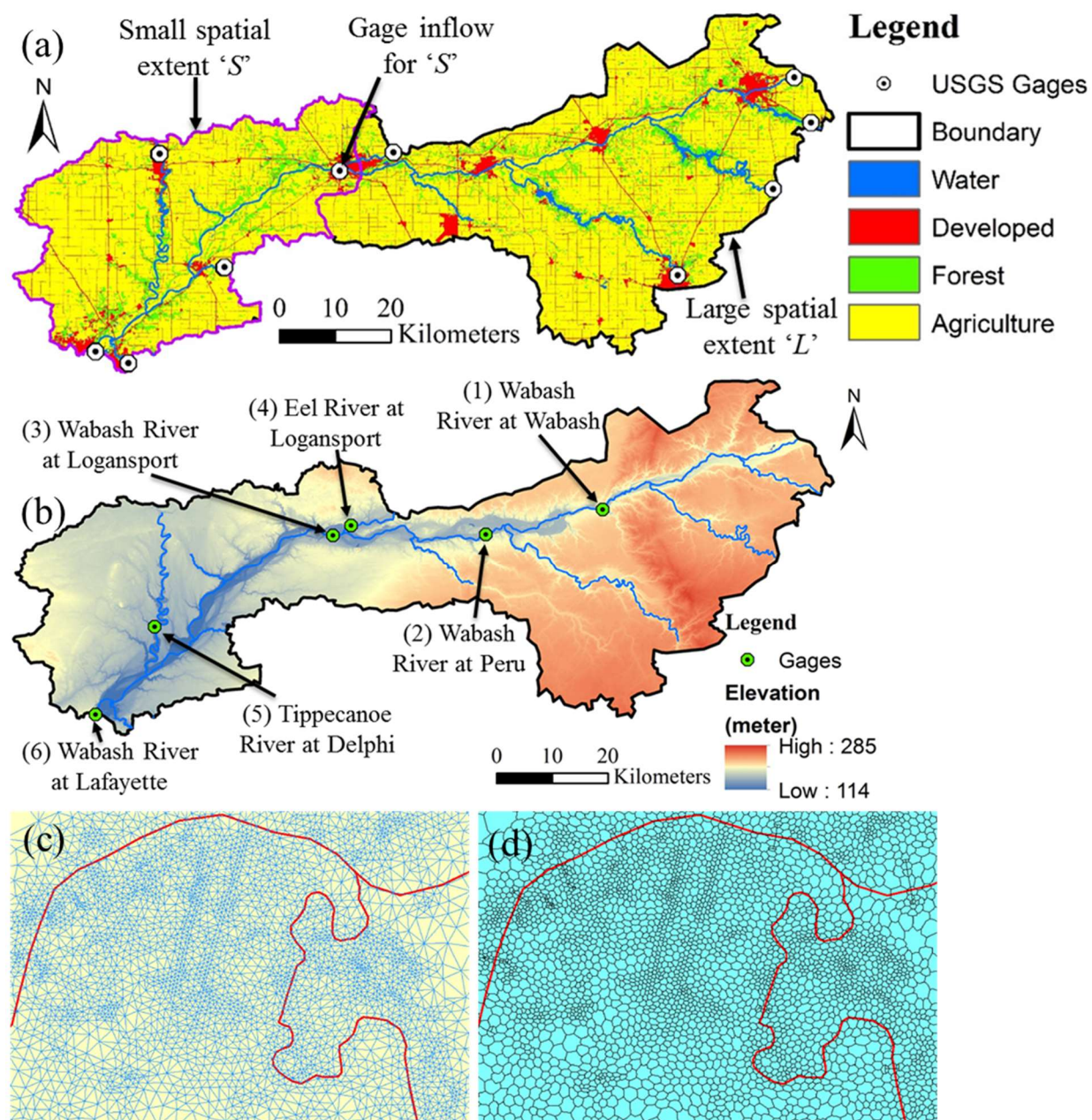


Fig. 3.4 Illustration of (a) two spatial extents used in this study with upstream USGS gages; (b) location of USGS gages used for testing the effect of spatial stream length scaling (c) fine resolution triangular mesh; and (d) fine resolution honeycomb mesh

The SW mesh resolution is the same for all four models (*S-1*, *S-2*, *L-1* and *L-2*) and is created using the methodology described in Section 3.2. There is no GW mesh for *S-1* and *L-1* but the GW mesh resolution for *S-2* and *L-2* is the same as the SW mesh resolution. For illustration, the triangular and honeycomb mesh structures generated near a confluence for the models are shown in Fig. 3.4c and 3.4d.

Table 3.3 Description of model configurations

Site Name	Model Name	Type	Area (km ²)	SW Resolution (m)*	GW Resolution (m)*	Channel Roughness
UWR	<i>S-1</i>	SW	1,760	15 (R) 60 (F) 300 (O)	-	Single (0.035)
	<i>S-2</i>	Integrated	1,760		15 (R) 60 (F) 300 (O)	Single (0.035)
	<i>L-1</i>	SW	4,385		-	Single (0.035)
	<i>L-2</i>	Integrated	4,385		15 (R) 60 (F) 300 (O)	Single (0.035)
	<i>S-3</i>	Integrated	1,760		45 (R) 180 (F) 900 (O)	Single (0.035)
	<i>S-4</i>	Integrated	1,760		75 (R) 300 (F) 1500 (O)	Single (0.035)
	<i>L-3</i>	Integrated	4,385		15 (R) 60 (F) 300 (O)	Variable (0.025 - 0.04)
	<i>L-4</i>	Integrated	4,385		75 (R) 300 (F) 1500 (O)	Variable (0.025 - 0.04)
WHR	<i>WHR 1</i>	Integrated	344	15 (R) 60 (F) 300 (O)	Single	
	<i>WHR 2</i>	Integrated	344	75 (R) 300 (F) 1500 (O)	Variable (0.025 - 0.04)	

*The values corresponding to the SW and GW resolution in the river (R), floodplain (F) and the overland region (O) outside the floodplain represent an average resolution or vertex spacing in these regions determined from the SW and GW meshes

After creating these configurations, SW mesh is overlain on the LiDAR DEM and the elevation of LiDAR cell (9 m resolution) directly intersecting with a specific triangular vertex is extracted and assigned to the vertex. Similarly, the GW mesh is overlain on the WT Depth raster (30m resolution) and the initial elevations are extracted. The spatial aggregation parameters for these meshes are calculated and presented in Table 3.3. Since the same SW mesh is used for *S-1* and *S-2*, and *L-1* and *L-2*, the number of triangles and the mean triangular area is the same, so only the parameters for *S-2* and *L-2* are reported. To compare the spatial resolution of triangulated irregular networks (TINs) with gridded DEMs, Vivoni et al., 2005 used two spatial aggregation parameters, the horizontal point density (d) and the equivalent cell size (r_e), which can be evaluated using Equations 3.1 and 3.2.

$$d = \frac{n_t}{n_g} \quad \text{Equation 3.1}$$

$$r_e = \sqrt{\frac{A}{n_t}} \quad \text{Equation 3.2}$$

Where, d = horizontal point density used to capture the degree of aggregation in a triangular mesh compared to a fixed grid model (Vivoni et al., 2005); n_t = number of triangular nodes; n_g = number of DEM nodes; r_e = equivalent cell size (or length scale); and A = basin area. The number of DEM nodes (n_g) are evaluated using the 9 m LiDAR for the SW region and the 30 m WT Depth raster for the GW region. The ' r_e ' values for the SW and GW meshes for *S-2* (114.6 m) and *L-2* (122.6 m) represent the equivalent spatial resolution of the TINs. Similarly, the ' d ' values provide a ratio of the number of computational elements used in the SW (*S-2* = 0.006 and *L-2* = 0.006) and GW (*S-2* = 0.057 and *L-2* = 0.050) meshes in comparison to the fixed-resolution gridded raster datasets. Table 3.4 also presents the average geometric characteristics of the model configurations. The total number of sub-polygons or soil-cylinders generated for the models are also shown in Table 3.4 which represent unique intersections of the land use, soil and rainfall datasets with the SW mesh (Section 3.2).

Table 3.4 Spatial aggregation and geometric characteristics for the integrated model configurations with different SW-GW mesh resolutions

Geometric Characteristics	<i>S-2</i>	<i>S-3</i>	<i>S-4</i>	<i>L-2</i>	<i>L-4</i>
No. of SW Triangles	213,040	213,040	213,040	466,842	466,842
No. of GW triangles	213,040	24,262	15,164	466,842	44,155
Mean SW Triangular Area (km ²)	0.008	0.008	0.008	0.009	0.009
Mean GW Triangular Area (km ²)	0.008	0.072	0.116	0.009	0.099
Percentage Triangles SW/GW (%)	100.0	11.4	7.1	100.0	9.5
Horizontal Point Density SW, d	0.006	0.006	0.006	0.006	0.006
Horizontal Point Density GW, d	0.057	0.007	0.004	0.050	0.005
Equivalent Cell Size SW, r_e (m)	114.6	114.6	114.6	122.6	122.6
Equivalent Cell Size GW, r_e (m)	114.6	339.7	429.7	122.6	398.5
No. of sub-polygons or soil cylinders	559,474	559,474	559,474	2,077,171	2,077,171

3.5.1.3 Effect of stream length scaling

Studies have highlighted that river channel roughness plays a key role in governing river hydrodynamics, since it determines the hydraulic variables such as magnitude, extent, and travel time of flows (Werner et al., 2005). The '*S*' and '*L*' models are initially developed using a single

channel roughness value of 0.035 (Table 3.3). In the first step, a sensitivity analysis of single channel roughness is carried out for *S-2* to quantify the change in streamflow and depth prediction when the channel roughness is varied assuming a constant reach length. Using the *S-2* integrated model, three values of river channel roughness ($n=0.025, 0.035$ and 0.045) are tested for the same stream length. In the second step, the reach length is varied, and the channel roughness is assumed to be constant. It is hypothesized that as the reach length and contributing area is increased, the uncertainty induced by assuming a single channel roughness should also increase. To test this, six reaches with different lengths are selected in the watershed based on the availability of USGS streamflow gages in the ‘*L-2*’ model domain.

$$\eta_L = \frac{L_R}{L_F} \quad \text{Equation 3.3}$$

$$L_F = 1.54 A^{0.6} \quad \text{Equation 3.4}$$

Table 3.5 presents the geomorphologic characteristics for the study reaches used for comparison of streamflow with observed data and Fig. 3.4b shows the locations of these USGS gages. Since *L-2* contains multiple river channels of varying reach length (L_R), width (W) and drainage area (A), it is also essential to define a standardized classification for determining small and large reaches within a watershed. Therefore, the ratio of the reach length in the study region to maximum length of the single stream draining at that point (η_L) is used as a classifier for identifying small and large reaches (Equation 3.3). Based on Hack’s Law (Hack, 1957), the stream length (L_F) and drainage area are interdependent quantities following a power law (Equation 3.4) function which holds true over large areas and a range of geologic conditions.

Using this relationship and the known drainage area at the points where the USGS gages are located in Fig. 3.4b, the full stream length (L_F) is calculated. Since the reach lengths are known for the streams in the study area, the ratio η_L can be calculated. It is evident from Table 3.5 that a lower value of η_L corresponds to a small reach and vice versa. This means that the reach length of a specific stream in the study area is small compared to the overall length of the stream in the full watershed. Since upstream USGS gages are chosen as boundary conditions (Fig. 3.4a), only a part of the stream (L_R) is incorporated in the model. For example, a low value of η_L for Eel River at Logansport and Tippecanoe River at Delphi suggest that the reach lengths are small in proportion

to the actual stream length of the watershed. Based on this classification, it is hypothesized that the model performance at these streams should be more accurate compared to other streams with higher η_L . This hypothesis is tested by comparing the streamflow prediction across these streams with the observed USGS gage data.

Table 3.5 Geomorphologic characteristics of study reaches used for analyzing the effect of stream length scaling on hydraulic outputs

Study Reach Name (USGS Gage Number)	Reach Length (L_R)	Average Width (W)	Daily Average Streamflow	Drainage Area (A)	L_F	η_L
	(km)	(m)	(m^3/s)	(km^2)	(km)	-
Wabash River at Wabash (USGS 03325000)	39	121	55.5	4379	235.7	0.17
Wabash River at Peru (USGS 03327500)	60	132	85.6	6957	311.1	0.19
Wabash River at Logansport (USGS 03329000)	90	179	121.2	9788	381.9	0.24
Eel River near Logansport (USGS 03328500)	12	117	24.7	2044	149.2	0.08
Tippecanoe River near Delphi (USGS 03333050)	23	76	59.2	4841	250.3	0.09
Wabash River at Lafayette (<i>L-2 Outlet</i> : USGS 03335500)	162	193	231.3	18822	565.4	0.29
Wabash River at Lafayette (<i>S-2 Outlet</i>)	72	211	231.3	18822	565.4	0.13

Finally, to test whether a distributed channel roughness improves the model performance by better accounting for spatial variability in longer streams, a variable channel roughness is applied to the *L-2* model. As recommended by Beven et al. (1979), the upstream roughness near the headwaters is increased to 0.04, and the channel roughness is reduced by 0.005 for every 40 km length of the Wabash River. Since the total reach length is about 160 km from the upstream boundary to the outlet, the roughness values incorporated in the river channel are 0.04, 0.035, 0.030 and 0.025. All the other constraints remain the same in the revised model, referred to as '*L-3*'. It should be noted that these values are only used as an illustration to evaluate the effect of roughness distribution in affecting model performance and may not represent the actual channel roughness.

3.5.1.4 Effect of changing the intrinsic scale (or resolution) of the GW sub-model

This section focuses on testing the effect of modifying the GW resolution or the intrinsic scale of the GW sub-model with respect to the SW sub-model. Initially, both the SW and GW regions are discretized at the same spatial resolution (Section 3.5.1.1), and hence the intrinsic scales of the SW and GW sub-models are assumed to be the same. It is hypothesized that a coarser spatial resolution of the GW sub-model relative to the SW sub-model can improve the process representation and subsequently, the model performance. To test this hypothesis, the GW resolution of *S-2* is modified to a coarser resolution and SW resolution is left unchanged. The *S-2* model is converted into two coarser resolution (3 and 5 times) models (referred here as *S-3* and *S-4*) by changing the average triangular vertex spacing of the GW sub-model, as shown in Table 3.3. The percentage of SW to GW triangles reduces significantly from a 100 % in *S-2* to 11.4 % in *S-3* and 7.1 % in *S-4* as shown in Table 3.4. Finally, a model with a coarser GW resolution is also generated for the larger spatial extent by modifying *L-3*, and the revised model is referred as *L-4*.

3.5.2 Numerical simulation and statistical analysis of watershed responses

The configurations (described in Table 3.3) for the UWR basin are used to simulate the 2013 summer floods of Indiana (1st April to 31st July 2013). During this period, multiple rainfall events of varying magnitude were observed in Indiana that also resulted in a peak streamflow corresponding to a 50-year return period in the Wabash River at Lafayette. A warm-up period of 100 hours is chosen for all simulations for all model reaches to be fully connected. The statistical analysis involves evaluating the goodness of fit between all the models and observed data and is carried out using the coefficient of determination (R^2), slope parameter (for comparison about the line $Y=X$), and the Nash-Sutcliffe Efficiency (NSE). The Percent Bias (PBIAS) is evaluated to compare the outflow volumes from the watershed with the observed data. This parameter also provides an estimate of the overprediction and underprediction of water storage in the system, as the inflow volumes for all models at a given scale are the same. Therefore, it is used as a representative parameter for comparing the overall water balance across models. Additionally, the scale-normalized-RMSE (RSR) is evaluated to estimate the root-mean-squared-error (RMSE) in prediction, scaled by the standard deviation of observed data. Finally, the model performance is also determined by the percentage of error in peak flow prediction (%Error Peak Flow), as the peak flow governs the maximum inundation extents due to flooding.

3.6 Results and Discussion

The results are presented in six parts: (i) validation of uncalibrated model parameters using *S-2*; (ii) analyzing the effect of scaling of spatial extents of the model; (iii) analyzing the effect of spatial stream length scaling; (iv) evaluating the effect of changing the intrinsic scale of the GW model; (v) scaling of model extents by modifying the intrinsic scales of sub-models; and (vi) validation of improved spatial scale representation at another watershed

3.6.1 Validation of uncalibrated model parameters for multiple events using *S-2*

This step is carried out to identify if the set of uncalibrated model parameters chosen a priori are physically feasible and justifiable, since the issues with modeling structure at larger spatial extents can only be analyzed if the parameters produce realistic and consistent predictions at smaller spatial extents (Beven, 2002; Wood et al., 1988). The validity of the model parameters is evaluated by simulating *S-2* across three independent events, a 4-month simulation from April 1st to July 31st 2013, a 3-month simulation from February 15th to May 15th 2018, and a relatively smaller storm event with a 10-year peak flow from May 5th to May 27th 2009. The streamflow and depth at the outlet (Wabash River at Lafayette) for the 4-month simulation is compared with observed data and shown in Fig. 3.5a and 3.5b. In addition to the outlet, the streamflow prediction at an additional gage inside the model domain (Tippecanoe River at Delphi) is also presented in Fig. 3.5c.

Since observed extents of inundation for these events are not available, the maximum flood extents in 2013 are compared with a reference dataset generated using a calibrated HEC-RAS model. The F-statistic (Equation 3.5) is used to quantify the difference in the maximum flood extents between the HEC-RAS model and the *S-2* model. An F-statistic value equal to 88.1 % suggests a high correlation between the extents of inundation obtained from the two models. Finally, the streamflow comparison for 2018 and 2009 is presented in Fig. 3.5e and 3.5f. The results from Fig. 3.5 suggest that the streamflow, depths and flood extents are predicted accurately, and hence, the model parameters used in this study are reasonable and reliable for spatial scale analysis. Further, the results also suggest that the model parameters used in this study are reliable and independent of the events chosen.

$$F - statistic = \frac{A_{OP}}{A_o + A_p - A_{OP}}$$

Equation 3.5

where, A_{OP} = intersection of the HEC-RAS and S-2 flood extents, and A_O = HEC-RAS flood extent, A_P = S-2 flood extents.

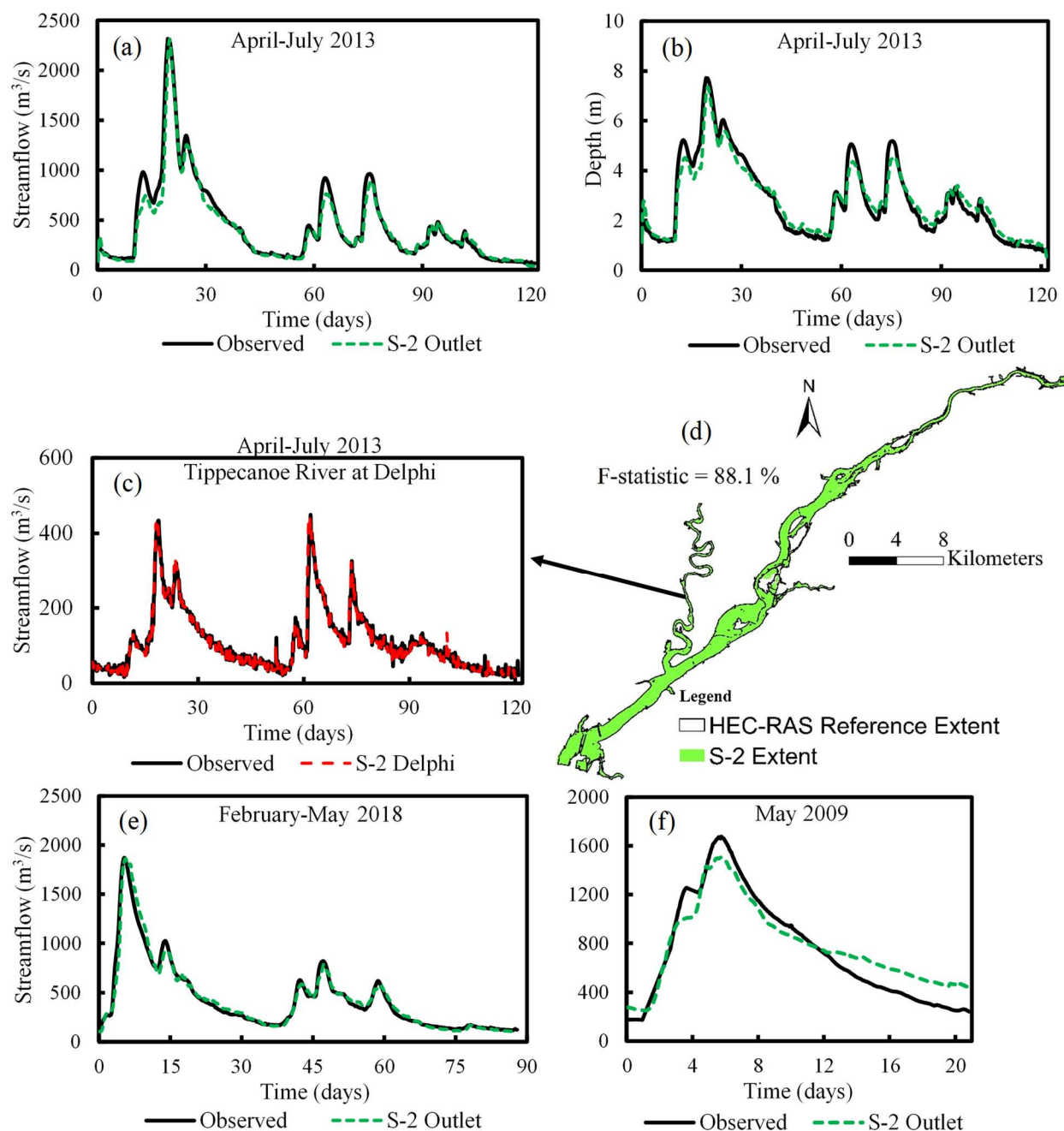


Fig. 3.5 Model validation using S-2 for (a) streamflow at outlet (April-July 2013); (b) depth at outlet (April-July 2013); (c) streamflow at Tippecanoe River (April-July 2013); (d) maximum flood extent comparison with reference map (HEC-RAS) for April-July 2013; (e) streamflow at outlet (February-May 2018); and (f) streamflow at outlet (May 2009)

3.6.2 Analyzing the effect of spatial extent scaling

3.6.2.1 Comparison of streamflow and flood extents

In this section, the 300-hour (or 12.5 day) period containing the storm event with the 50-year peak flow is compared across the four models (*S-1*, *S-2*, *L-1* and *L-2*). A smaller period is chosen to effectively delineate the effect of spatial scaling of model extents on streamflow and flood extents. The results shown in Table 3.6 suggest that *S-1* over-predicts the peak flow by 11.6 % compared to *S-2*, which over-predicts the peak flow by only 1.2 %. While there is some difference in peak flow, the overall hydrograph shape, PBIAS, and NSE for both models is similar (Fig. 3.6a), which suggests that for models with a small spatial extent and fine spatial resolution, there is no difference in the streamflow prediction with and without the inclusion of subsurface processes. In such cases, the role of rainfall and subsurface processes in influencing streamflow is diminished.

Table 3.6 Statistical comparison of streamflow hydrographs for small and large spatial extents

Model	R ²	NSE	PBIAS (%)	RSE	Slope	%Error Peak Flow
<i>S-1</i>	0.92	0.88	-6.91	0.34	0.95	+11.6
<i>S-2</i>	0.92	0.87	-8.55	0.36	0.92	+1.2
<i>L-1</i>	0.80	0.81	-7.45	0.44	0.89	-16.4
<i>L-2</i>	0.83	0.89	-1.60	0.33	0.95	-10.6

While the performance of *S-1* and *S-2* is similar, the results from Fig. 3.6b highlight the diminished performance of the two model structures at for *L-1* and *L-2*. Additionally, there are notable differences between *L-1* and *L-2*, which suggests that spatial scaling of model extents increases the influence of the contributions from subsurface processes. The PBIAS for *L-1* (-7.45 %) is significantly higher compared to *L-2* (-1.60 %), and error in peak flow is also higher for *L-1* (-16.4 %) compared to *L-2* (-10.6 %), indicating that the contributions from subsurface processes, which in-turn determine the water balance, change from *S-2* to *L-2*. A lower PBIAS for *L-2* also indicates that there is minimal mass balance error, however, this also means that more storage is trapped in the overland flow system, indicating that the inaccurate representation of the intrinsic scales (or resolution) of SW-GW sub-models may be the cause for peak flow underprediction.

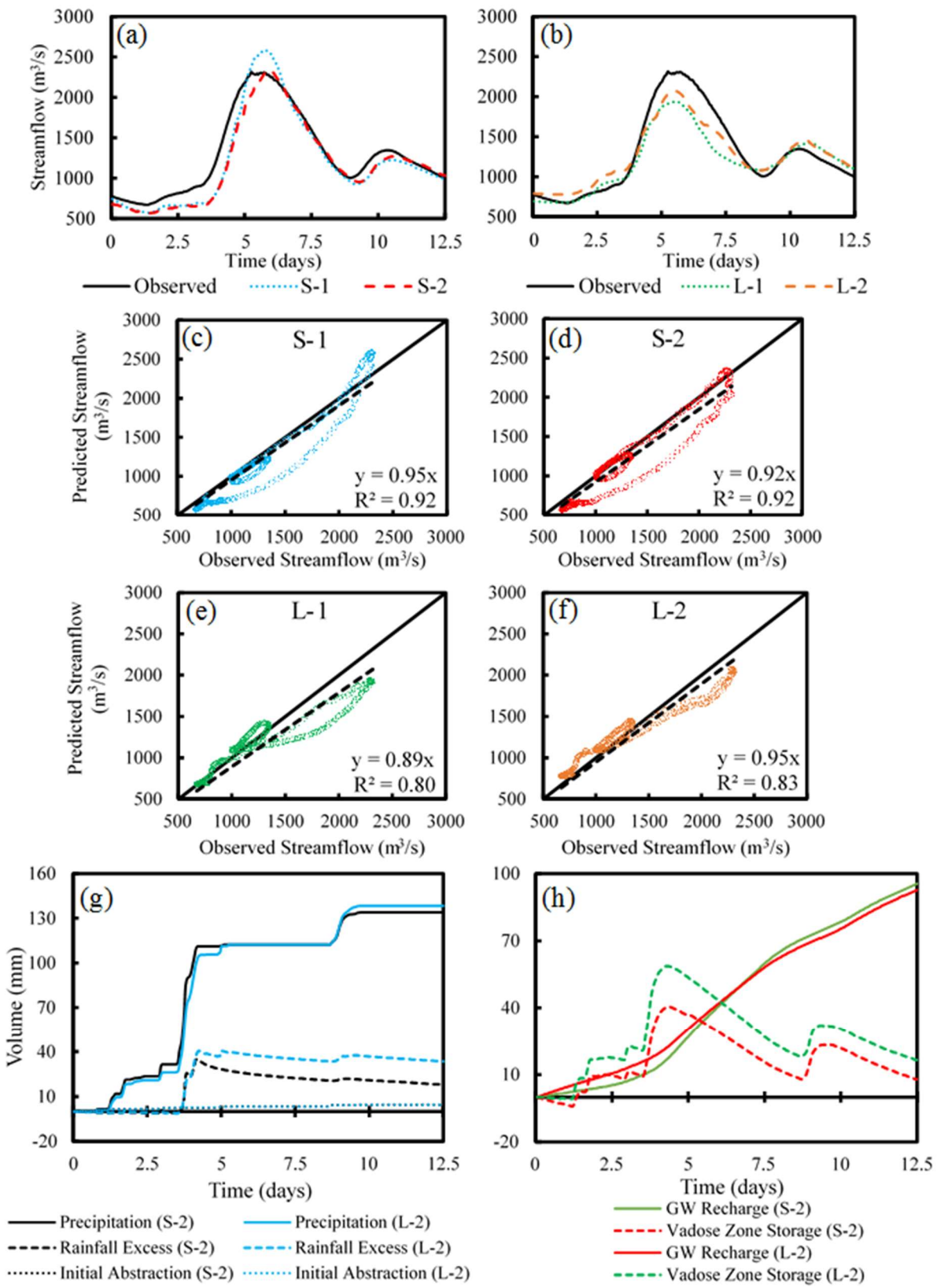


Fig. 3.6 (a) – (f) Effect of spatial extent scaling on streamflow hydrographs; and (g) – (h) evolution of subsurface processes at small (*S-2*) and large (*L-2*) spatial extents

The difference in the performance between $L-1$ and $L-2$ can be attributed to the increased significance of rainfall excess and subsurface flow at large spatial scales, which leads to increased contributions from lower order streams. At small scales, the upstream inflow dominates the flood hydrodynamics, but at larger scales, excess rainfall and lateral seepage contributions also influence riverine flow, as highlighted by the peak flood inundation extents in Fig. 3.7. At small scales, the difference in flood extents between $S-1$ and $S-2$ is not significant, however, at large scales ($L-1$ and $L-2$), the water contribution from headwater streams that have higher hydraulic conductivity and steeper valleys increases, thereby, increasing the overall water contributions into the main channels. However, the difference between the $S-1$ and $S-2$ can widen for other watersheds if the model domain has a higher drainage density with more low-order streams.

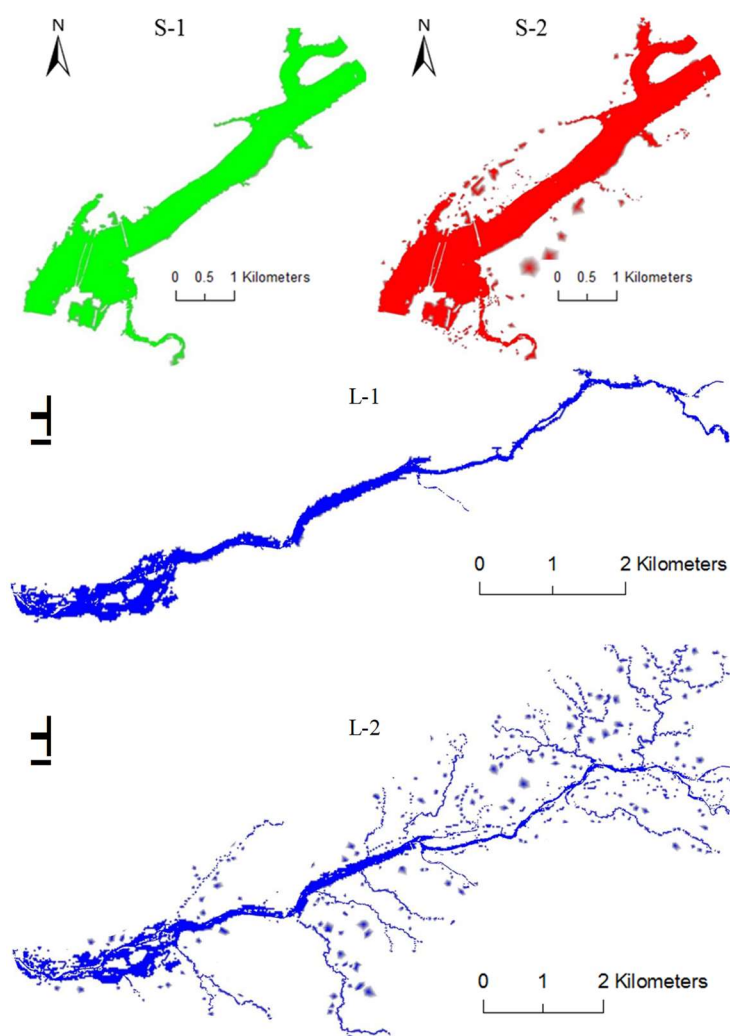


Fig. 3.7 Illustration of difference in extent of inundation when peak streamflow is observed at the outlet for $S-1$, $S-2$, $L-1$, and $L-2$

The flood extents also suggest that the integration of rainfall and subsurface hydrology with hydrodynamics becomes essential for watersheds with higher drainage density in the stream network as the volumetric contributions from lower-order streams increases at larger scales. While the flows generated from a purely hydrologic model can be applied as boundary conditions for ungaged streams, the overall performance can be affected by the uncertainty in the flow estimation, which can reduce the accuracy further.

3.6.2.2 Comparing volumetric contributions for ‘S-2’ and ‘L-2’

Fig. 3.6g and 3.6h present the volumetric contributions (in mm) from subsurface processes during the simulation for *S-2* and *L-2*, which are evaluated by dividing the total volume by the total watershed area. The precipitation values (Fig. 3.6g) indicate that there is a similar amount of rainfall occurring for *S-2* and *L-2*, which highlights the magnitude and extent of the 50-year flood event. Since rainfall characterization is influenced by the intrinsic scale of the input dataset, the consistency in rainfall volumes across two spatial extents in this study is also driven by characterizing rainfall variability using a relatively fine NLDAS rainfall forcing (12 km resolution). Considering that the characteristic length scale for hourly rainfall lies within 10-20 km (Skøien et al., 2003), the spatial aggregation of rainfall is more feasible using this dataset. It is expected that if a coarser intrinsic scale (or resolution) of rainfall dataset is used, for example, a sparsely distributed gage data, the difference in scaled rainfall volumes may change which can influence the streamflow hydrograph and hydrologic volumes. While the intrinsic scale of rainfall forcing is not considered as a factor in this study, it can play an important role for other watersheds and/or rainfall events.

While the rainfall aggregation across the two spatial extents is similar, the subsurface contributions change from *S-2* to *L-2*, as shown in Fig. 3.6g and 3.6h respectively. More specifically, the amount of vadose zone storage increases for *L-2* when compared to *S-2*. Similarly, the amount of rainfall excess (or surface runoff from rainfall) is higher for *L-2* when compared to *S-2*. This difference is expected as there is an increase in the impervious land cover in the floodplain of about 0.7 % from *S-2* to *L-2*, which increases rainfall excess. As excess water gradually re-enters the soil column in ponded areas over time, the rainfall excess reduces across both extents. The GW recharge (Fig. 3.6h) on the other hand, is similar for both *S-2* and *L-2*, which supports the argument that the GW recharge operates over larger characteristic length scales when

compared to overland region and vadose zone, and therefore, aggregates linearly and does not change significantly even after increasing the modeling extents (Bloschl and Sivapalan, 1995).

3.6.2.3 Temporal scale analysis of GW fluxes for *S-2*

While the overland flow dynamics may fluctuate depending on variation in hydrologic response due to a storm-event induced forcing, the subsurface response to this forcing may vary in both time and space depending on residence time distributions and hyporheic flow path lengths, which can have distinct implications on the lateral-seepage exchanges between the river channel and subsurface (Schmadel et al., 2016). In this section, the 4-month period from April to July 2013 (Fig. 3.5a) is used to quantify the lateral seepage exchanges between the rivers and groundwater using the *S-2* model.

Fig. 3.8 presents the volumetric lateral seepage inflow and outflow rates for *S-2* from all the river channels into the groundwater region. During flood events, as the water flows into the river channels, hyporheic exchanges intensify, as a positive head is created in the rivers with respect to the subsurface. This forces the lateral fluxes into the subsurface, thereby increasing the lateral GW seepage outflow from the river channels (as shown in Fig. 3.8), and subsequently increasing the subsurface storage. However, as the event recedes, the volume of water in the river channels decreases rapidly, since hydraulic routing occurs at a faster rate compared to the GW flow. This decrease in channel storage creates a negative head in the river with respect to the subsurface, which in turn causes the water stored in the subsurface to flow towards the river channel, resulting in an influx of lateral seepage. However, this inflow is significantly slower, and therefore, a longer duration is required to reduce the subsurface storage occurring due to lateral seepage. This inflow due to hyporheic exchange causes the tail of the recession curve in the streamflow hydrograph to be significantly longer, which is evident from Fig. 3.5a.

These results agree with several studies which conclude that in addition to larger characteristic length scales, subsurface processes operate over a longer time-scales when compared to overland flow routing, due to which, the influence of large flood events extends well beyond peak flows (Bloschl and Sivapalan, 1995; Salvatore et al., 2015). For example, the characteristic time-scales for subsurface processes ranges approximately between 1 day to 2 months as per the temporal scales for hydrologic processes presented in Bloschl and Sivapalan (1995). It should be

noted that these seepage rates presented here are governed primarily through rainfall and streamflow induced hyporheic exchanges, and therefore, these conclusions do not represent heterogeneous GW flow due to fracturing, preferential flow, or deep aquifer leakage induced seepage.

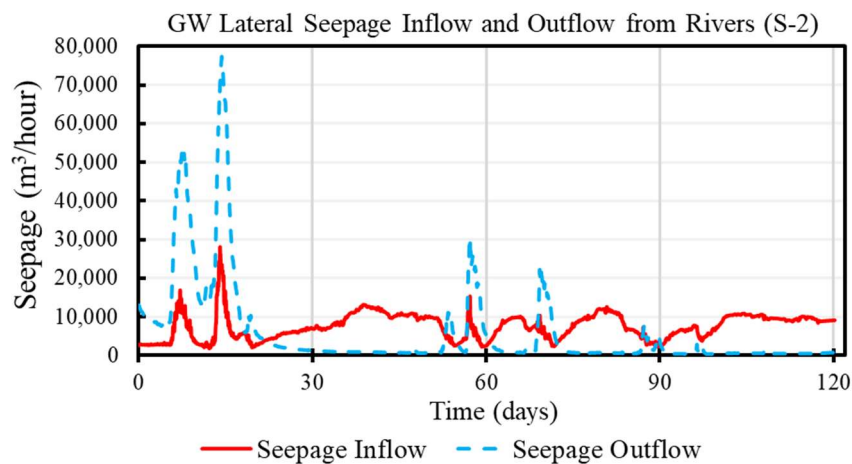


Fig. 3.8 Evolution of GW seepage fluxes over time for *S-2*

3.6.3 Analyzing the effect of spatial stream length scaling

3.6.3.1 Effect of modifying channel roughness for a fixed stream length for *S-2*

Using the *S-2* integrated model, three values of river channel roughness ($n=0.025$, 0.035 and 0.045) are used to run a 300-hour (or 12.5 day) period in April 2013 containing the storm event with a 50-year peak flow and the results are compared with observed flow and depth data. After simulating the flood outputs for three n -values, the observed streamflow at the outlet is compared with the simulated streamflow and the statistical parameters for evaluating goodness of fit are presented in Table 3.6. The sensitivity analysis for river channel roughness is carried out using a baseline value of 0.035 and the predicted peak flows are normalized with respect to the peak flow at 0.035 to aid a scale-independent comparison. A negative 28% variation (0.035 to 0.025) in n -value accounts for only 1.2% variation in the normalized peak flow at the outlet of the watershed. After further sensitivity analysis at $n=0.02$ and $n=0.04$ (not presented here), it is found that the normalized peak flow variability is low (less than $\pm 10\%$) for n -values ranging from 0.02 to 0.04 . The performance of *S-2* is negatively influenced only at n -value less than 0.02 or greater than 0.04 which are unrealistic roughness values for this watershed.

3.6.3.2 Effect of stream length scaling assuming a constant channel roughness

The results from Fig. 3.6 and Table 3.5 suggest that the total outflow volume is influenced for $L-1$ and $L-2$ when a single roughness value is used for routing. As the reach length and contributing area is increased in the case of $L-1$ and $L-2$, the uncertainty induced by assuming a single channel roughness, propagates for larger distances. Because the error induced by using a single channel roughness is large for both $L-1$ and $L-2$, the overall flow at the outlet is lower than the observed data, even when the overall water balance is maintained in the case of $L-2$. To test this further, reaches with different channel lengths are selected in the watershed, and the $L-2$ predicted streamflow is compared with observed USGS gage data at multiple locations within the watershed.

Initially, all the streams are characterized using a single channel roughness. The flow prediction statistics shown in Table 3.7 suggest that $L-2$ performs with high accuracy for both Eel River and Tippecanoe River. These results also suggest that for reaches with a low η_L (Equation 3.3), the uncertainty due to a single channel roughness has a smaller length to transpire, as the flows are routed for a shorter distance. Under this scenario, the overall error due to a single channel roughness during hydraulic routing is small, and therefore, the influence of a single roughness characterization on modeling of physical processes such as streamflow generation, lag time, shear stress, and movement of water through topographic gradients is minimal, which is also highlighted by near perfect flow hydrographs in Fig. 3.9a and 3.9b. From solely a hydraulic modeling perspective, the results show that when the reach lengths are small, and the channel flow is dominated by inflow boundary conditions, the spatial distribution of channel roughness may not be a dominant control.

However, the flow hydrographs in Fig. 3.9c, 3.9d and 3.9e signify the reduction in accuracy for streams with a higher η_L . It should also be noted that the streamflow prediction improves from upstream (Wabash River at Wabash) to downstream (Wabash River at Lafayette) even though the η_L values are higher for Wabash River at Lafayette (Fig. 3.9 and Table 3.7). This is because the streamflow prediction at Lafayette improves as the streams with small η_L values (and highly accurate streamflow prediction) drain into the Wabash River. Overall, higher η_L values indicate that the single channel roughness may not be suitable for accurate modeling of those streams.

Table 3.7 Effect of reach length and river channel roughness on hydraulic routing characterized by comparing streamflow hydrographs

Effect of modifying the channel roughness for a fixed stream length using S-2							
Streamflow at Outlet							
Model (S-2)	R²	NSE	PBIAS (%)	RSE	Slope	%Error Peak Flow	
0.025	0.98	0.91	-10.4	0.3	0.91	-0.07	
0.035	0.92	0.87	-8.55	0.36	0.92	+1.22	
0.045	0.79	0.59	+7.8	0.64	1.09	17.89	
Depth at Outlet							
0.025	0.96	0.78	-7.55	0.47	0.92	-7.58	
0.035	0.89	0.86	+4.57	0.37	1.04	+2.26	
0.045	0.78	-0.74	+21.85	1.32	1.21	+20.13	
Effect of stream length scaling on streamflow assuming a single channel roughness using L-2 (120-day simulation)							
Model	Reach Length (km)	R²	NSE	PBIAS (%)	RSE	Slope	%Error Peak Flow
Eel River near Logansport	12	0.99	0.99	+0.8	0.06	1.01	+1.5
Tippecanoe River near Delphi	23	0.95	0.95	-1.5	0.22	0.99	+3.2
Wabash River at Wabash	36	0.55	0.32	+79.6	0.82	1.33	-26.7
Wabash River at Peru	60	0.65	0.52	+55.6	0.66	1.26	-13.2
Wabash River at Logansport	90	0.56	0.69	+40.2	0.56	1.10	-30.9
L-2 Outlet (Wabash River at Lafayette)	162	0.84	0.90	+16.0	0.31	0.98	-10.6
Improvement in streamflow using a distributed channel roughness for Wabash River (300 hour or 12.5-day simulation*)							
L-3 (Wabash River at Logansport)	90	0.05 (-)	0.48 (0.11)	+15.4 (+18.8)	0.72 (0.97)	1.08 (1.07)	-17.1 (-30.9)
L-3 Outlet (Wabash River at Lafayette)	162	0.94	0.94	-2.9	0.25	0.95	-2.9

*values in parenthesis represent the results from a 12.5-day simulation using the L-2 model highlighting the degree of improvement from L-2 to L-3

The dimensionless ratio η_L also explains the high performance in streamflow prediction for S-2. The reach length for the Wabash River in S-2 is equal to 72 km. If the application of single or variable roughness is decided solely on reach length, then this reach is significantly longer compared to other smaller reaches (Tippecanoe River, 23 km) in the model domain. Therefore, a variable channel roughness would be used for this reach if the decision is made solely on reach length. However, considering that η_L is equal to 0.13 for this reach and another small stream with η_L equal to 0.09 (Tippecanoe River) drains into it, this reach can likely be modeled using only a

single channel roughness. This is validated by the accurate streamflow prediction shown in Fig. 3.5 for *S-2* using a single channel roughness.

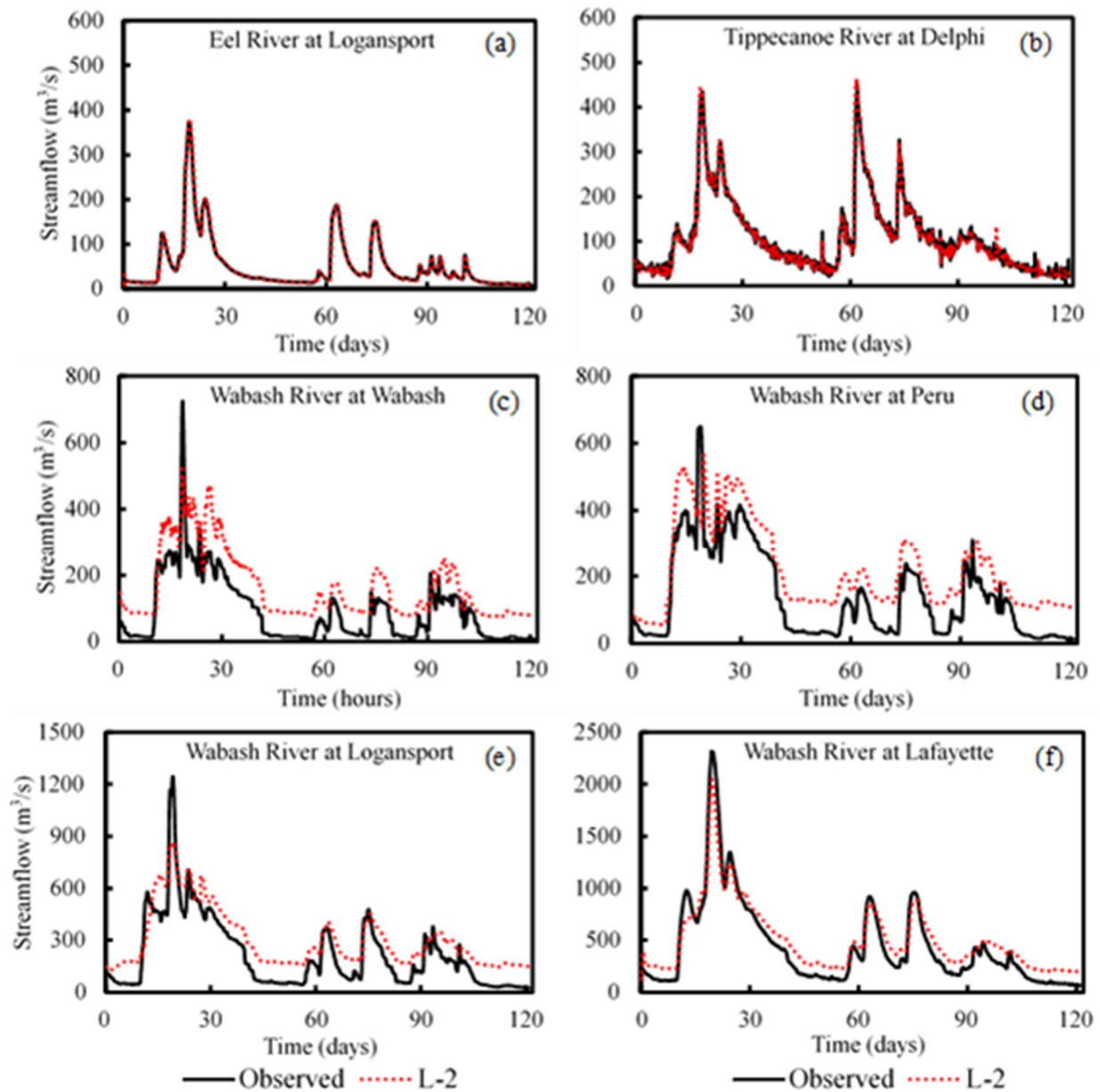


Fig. 3.9 Flow hydrographs using *L-2* model for (a) Eel River at Logansport; (b) Tippecanoe River at Delphi; and Wabash River at (c) Wabash; (d) Peru; (e) Logansport and (f) Lafayette

Geomorphic scaling laws for stream networks are characterized by continuous relationships dependent on drainage area that modify the stream features (channel length, width and depth) and the related physical processes from upstream to downstream. Therefore, the classification of reaches for single versus variable roughness distribution should not only depend

on the reach length, but also on where the reach (upstream to downstream) is located in the watershed. The results shown here highlight the effectiveness of a dimensionless metric like η_L in quantifying which streams are more likely to provide erroneous results using a single channel roughness. However, this needs more investigation across a broader range of stream characteristics and watershed scales.

3.6.3.3 Effect of variable roughness distribution on a fixed reach length

From the results presented in Section 3.6.2, it is evident that the accuracy of modeling is significantly influenced by the single channel roughness assumption, which is traditionally used for hydraulic routing across large stream lengths. For better representation of spatial variability in stream characteristics, a variable channel roughness may be used. The results for *L-3* (presented in Table 3.7) that contains a variable channel roughness suggest an overall improvement in the streamflow prediction at the outlet (Fig. 3.10b), as the NSE increases to 0.94 from 0.83, and the error in peak flow reduces to 2.9 % from 10.7 %. Additionally, the flow prediction for the Wabash River at Logansport (Fig. 3.10a) also improves, with an increase in NSE to 0.48 from 0.11, and a reduction in peak flow error from 30.1 % to 17.1 %. Since none of the other variables are changed between *L-2* and *L-3*, the improvement in the results is solely due to the addition of a variable channel roughness. These results suggest that a distributed roughness parameterization based on stream length scales and geomorphologic properties can help in improving streamflow prediction in integrated models.

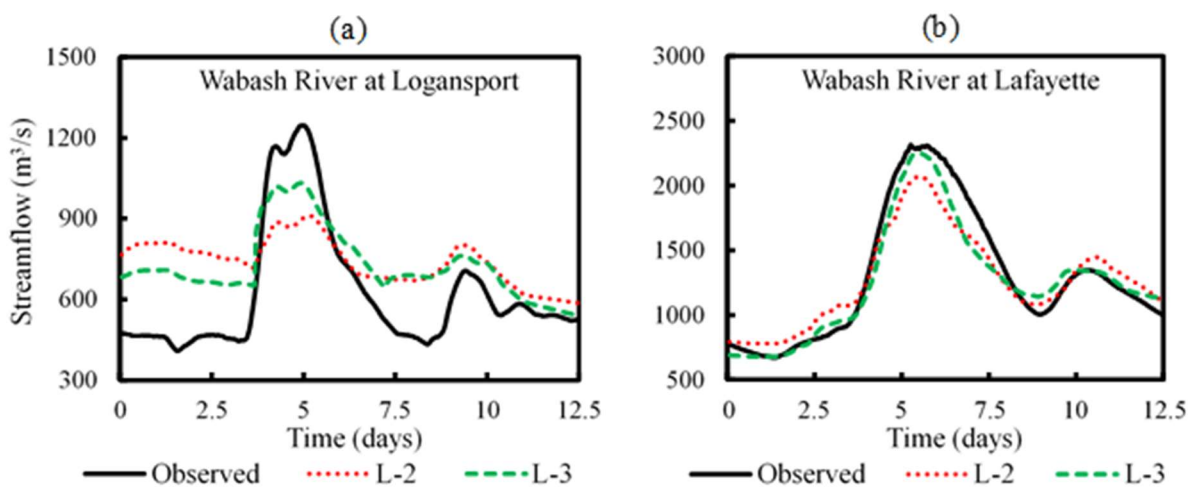


Fig. 3.10 Flow hydrographs for *L-3* at (a) Wabash River at Logansport; and (b) Wabash River at Lafayette

3.6.4 Evaluating the effect of changing the intrinsic scale of the GW sub-model

This section presents the results of increasing the intrinsic scale of the GW model or coarsening the GW resolution with respect to the SW resolution. As shown in Table 3.8 and Fig. 3.11a and 3.11b, the use of a coarser resolution GW mesh for both *S-3* and *S-4* improves the prediction of rising and falling limb of the hydrograph, lag-time, and hydrograph duration, when compared to *S-2*, which has a shorter hydrograph duration, and errors in the rising limb and lag-time (Fig. 3.6). This suggests that the subsurface contributions to streamflow are better represented using *S-3* and *S-4*. A thin-shaped ‘flashy’ hydrograph with a short duration for *S-2* suggests relatively less contribution from subsurface processes. The statistics provided in Table 3.8 suggest that the overall performance of *S-3* is comparable to *S-4*, however, the PBIAS comparison suggests that *S-4* (-0.1 %) has a slightly improved water balance compared to *S-3* (-3.59 %). By incorporating optimal GW resolution in *S-3* and *S-4*, the streamflow estimation improves significantly, highlighted by smaller error variance (RSE), higher NSE and R^2 values. Therefore, using a GW resolution which is approximately 3 to 5 times the SW resolution results in improved model prediction. The results suggest that the intrinsic scale (or resolution) of the GW sub-model should be larger than SW since the physical processes influencing subsurface flow operate over larger length and time scales. For example, the lateral seepage fluxes causing water table fluctuations change over larger length scales when compared to river-floodplain fluxes.

Table 3.8 Improvement in streamflow estimation using a distributed channel roughness and optimal process interaction scales

Model	R^2	NSE	PBIAS (%)	RSE	Slope	%Error Peak Flow
<i>S-3</i>	0.98	0.97	-3.59	0.18	0.96	-0.49
<i>S-4</i>	0.97	0.96	-0.10	0.19	1.01	+9.67
<i>L-4</i> (Wabash River at Wabash)	0.82	0.76	+32.8	0.49	1.14	-19.4
<i>L-4</i> (Wabash River at Peru)	0.89	0.90	+19.2	0.32	1.06	-10.2
<i>L-4</i> (Wabash River at Logansport)	0.88	0.90	+8.5	0.32	0.99	-17.1
<i>L-4 Outlet</i> (Wabash River at Lafayette)	0.97	0.97	-0.4	0.17	0.98	+10.5
<i>WHR 1</i>	0.84	0.71	+24.4	0.54	1.18	+15.5
<i>WHR 2</i>	0.96	0.94	-8.7	0.24	0.91	-4.8

The improvement in hydrograph characteristics by incorporating a coarser GW resolution can be related to the equivalent cell size of the GW zone (Table 3.4) and the characteristic length scales at which surficial GW flows operate. The equivalent GW cell size for *S-4* is approximately 430 m. This study incorporates a six-point cyclic finite element approximation for simulating GW flow where the distance between two GW nodes is equal to half the triangular edge length (centroid to triangle vertex). Therefore, the intrinsic scale (Fig. 3.2d), or the distance between two GW nodes with distinct hydraulic heads is approximately equal to 215 m for *S-4*. For an hourly time-scale, the typical characteristic lengths scales for shallow GW flows are much larger than overland or channel flow as per the spatiotemporal scales for hydrologic processes presented in Blöschl and Sivapalan (1995). If the time-scale at which SW-GW processes are quantified is fixed, the intrinsic GW sub-model scale should be larger than the SW sub-model. Therefore, the *S-4* model, with a coarser GW resolution, results in a better representation of the SW-GW interactions results in improved streamflow prediction. On the other hand, *S-2* has an intrinsic scale of approximately 57 m which results in less accurate prediction compared to *S-4*.

In addition to a better representation of the ratio between the characteristic length scales of SW-GW processes for a fixed time-scale, the performance likely improves due to the spatial aggregation of model parameters at a coarser resolution. Although the land use, WT depth and soil property datasets are available at a 30 m resolution, and the topography is available at a 9 m resolution (Table 3.1), the mesh extracts these parameters from fixed-grid raster datasets to a triangular mesh. It is possible that the coarsening of the GW mesh changes the spatial aggregation of the model parameters, which in-turn, provides a better depiction of the processes, thereby, improving the model prediction.

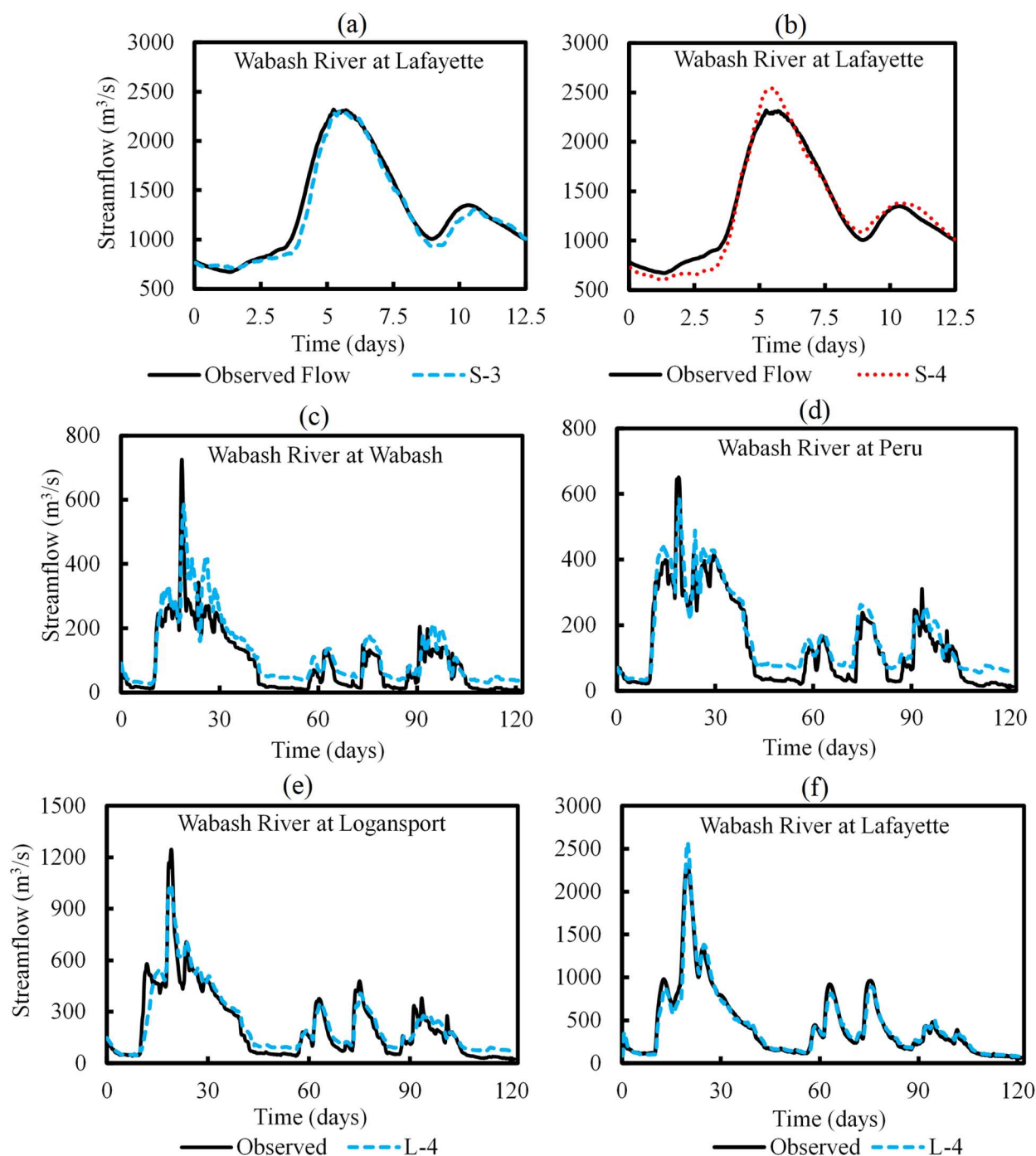


Fig. 3.11 Flow hydrographs for (a) *S-3* and (b) *S-4* at Lafayette; (c) *L-4* at Wabash; (d) *L-4* at Peru; (e) *L-4* at Logansport; and (f) *L-4* at Lafayette

3.6.5 Scaling of model extents by modifying the intrinsic scales of sub-models

Sections 3.6.3.1 and 3.6.3.2 suggest that a variable channel roughness is more suitable for reaches with higher η_L values. Additionally, modifying the intrinsic scale of the GW sub-model

with respect to the SW sub-model for a better representation of the characteristic length scales of SW-GW processes improves the streamflow prediction for the *S-4* model. In this section, both these modifications are applied to the *L-2* model to test if the overall streamflow prediction across different locations in the model domain improves or not. The results shown in Table 3.8 and Fig. 3.11 highlight the improvement from *L-2* to *L-4*, and therefore, suggest that using optimal intrinsic scales of SW-GW sub-models results in a better streamflow prediction even for larger spatial extents. The streamflow prediction across four USGS gages in the Wabash River improves significantly, for example, the NSE for Wabash River at Wabash increases from 0.32 for *L-2* to 0.76 for *L-4*. Additionally, the performance of *S-4* and *L-4* becomes comparable. For example, the PBIAS (*S-4* = -0.1 % and *L-4* = -0.4 %) and NSE (*S-4* = 0.96 and *L-4* = 0.97) for Wabash River at Lafayette are very close to each other suggesting that the model performance is not affected by increasing the spatial scale of model extents. On the other hand, there is a significant difference in the performance of *S-2* and *L-2* shown by the higher variability in PBIAS (*S-2* = 7.4 % and *L-2* = 16 %) and R^2 (*S-2* = 0.97 and *L-2* = 0.84). Therefore, modifying the intrinsic scales of the sub-models (SW through channel roughness and GW through spatial resolution) improves the spatial scalability of integrated models.

The difference in the model performance across four gages and six statistical parameters for *L-1*, *L-2*, and *L-4* is presented in Fig. 3.12. The results from Fig. 3.12 show that incorporating an integrated modeling structure in *L-2* instead of a purely hydrodynamic structure (impervious surface) in *L-1* improves the overall streamflow prediction in the watershed. Further, modifying the intrinsic scales of the sub-models in *L-4* results in a greater improvement in streamflow prediction than simply using an integrated model (*L-2*). The extent of improvement also varies from upstream to downstream with the upstream-most gage having the largest improvement (Wabash River at Wabash) and the downstream-most gage (Wabash River at Lafayette) having the smallest improvement. Hence, the degree of improvement also changes depending on the location of the reach in the watershed.

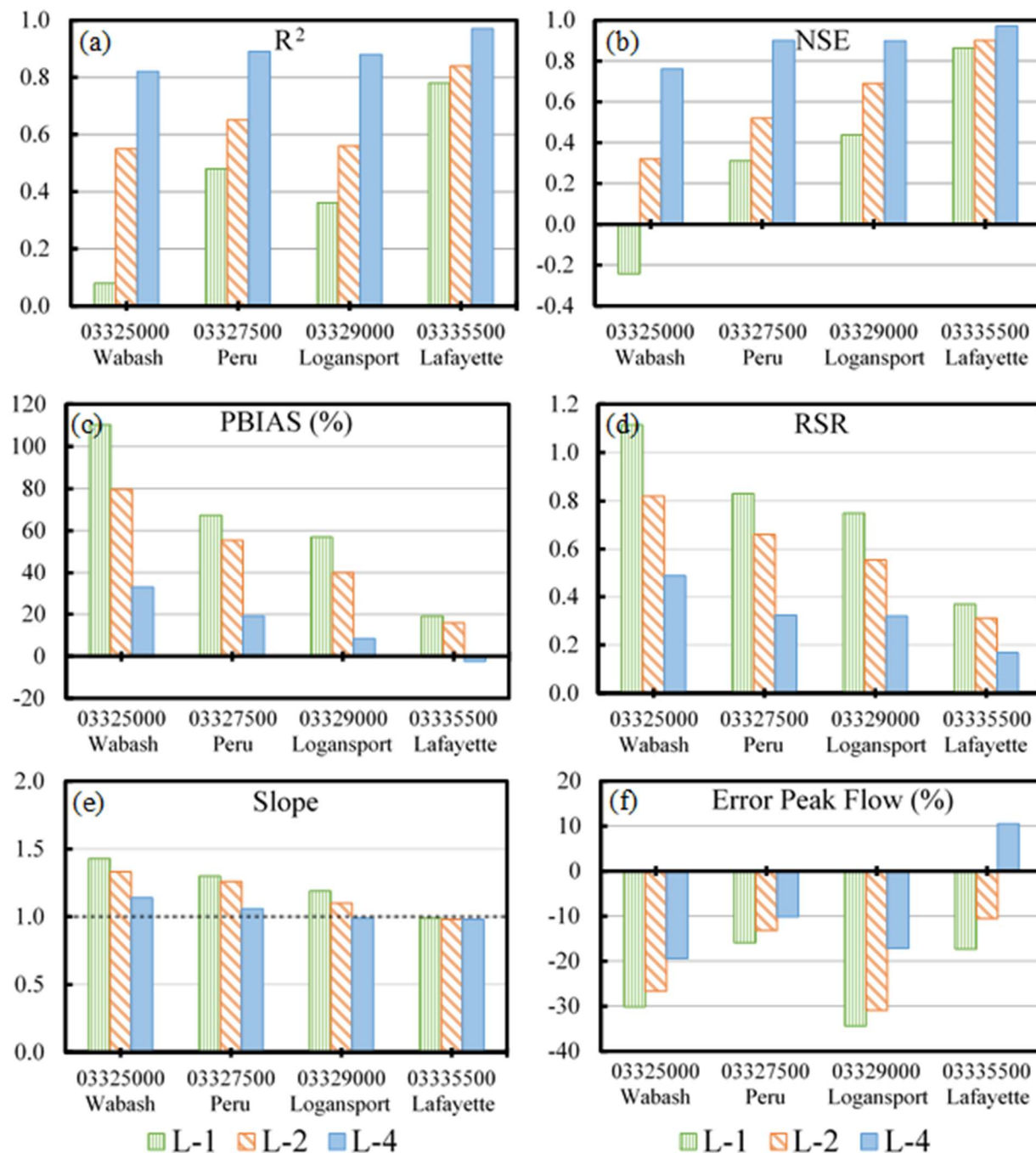


Fig. 3.12 Variation of statistical performance in streamflow prediction across four USGS gages using $L-1$, $L-2$ and $L-4$ model configurations

The results presented earlier highlight the improvement in streamflow prediction across the two spatial extents. As mentioned earlier (Section 3.5.2), the streamflow prediction, flood extents and hydrologic volumes predicted for $S-2$ and $L-2$ are significantly different highlighting the uncertainties in model performance when the intrinsic scales of underlying sub-models are not

considered and the same spatial resolution is used for SW and GW sub-models. In addition to streamflow, the subsurface variability in the prediction of $S-2$ and $L-2$ is also quantified by evaluating the difference (both positive and negative) in the median WT depth simulated during the 120 day (4-month) period. Similarly, this difference is evaluated between $S-4$ and $L-4$. Fig. 3.13 shows that the difference in the median WT depths predicted by $S-4$ and $L-4$ reduces when compared to the difference between $S-2$ and $L-2$. The region in ‘red’ denotes the locations where there is a difference between the median WT depth between $S-2$ and $L-2$ but not in case of $S-4$ and $L-4$ ($|S2 - L2| \setminus |S4 - L4|$). The region in ‘green’ denotes the intersection between these differences ($|S2 - L2| \cap |S4 - L4|$) identifying the locations where the median WT depth does not improve. The results show that the variability in WT depth reduces suggesting an optimal scaling of spatial extents when the intrinsic scales of the sub-models are incorporated accurately.

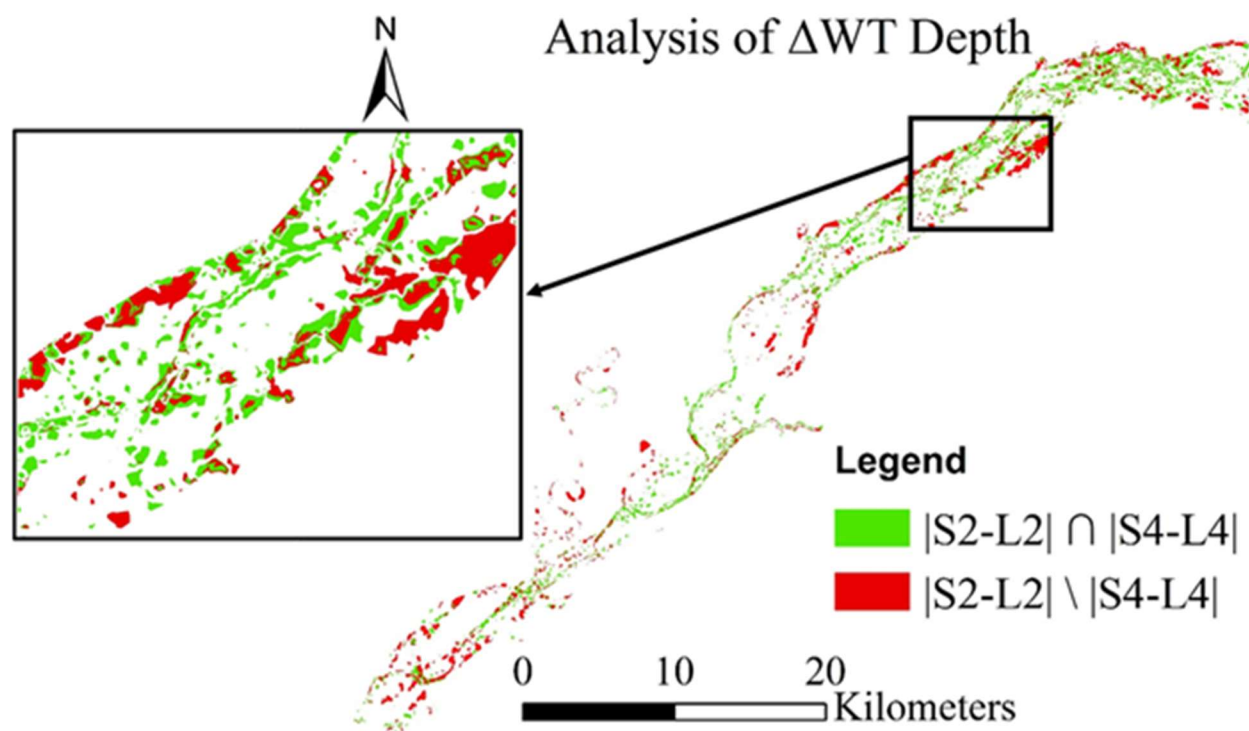


Fig. 3.13 Analysis of change in median water table depth during the 120-day simulation across the common region of small and large scale models

3.6.6 Validation of improved spatial scale representation at another watershed

To evaluate broader applicability of the results from this study across watersheds with different physical characteristics, the results from Section 3.6.5 are tested at the WHR basin. This

basin has a highly developed urban land use and a shallow water table (Table 3.1), in comparison to the UWR basin, which is an agricultural watershed with a deeper unsaturated zone. For the first model (referred to as *WHR 1*), the SW and GW resolution (intrinsic scales) are assumed to be the same and a single channel roughness is applied for the largest reach (White River at Indianapolis, reach length = 50 km). For the second model (referred to as *WHR 2*), a fine resolution SW region, a coarse resolution GW region with a mesh size equal to three times the SW mesh, and a variable channel roughness, is used.

The models (*WHR 1* and *WHR 2*) for the WHR basin are simulated for a 300-hour long simulation, for an event with a 50-year peak flow return period, after a warm-up period of 50 hours. These models require a smaller warm-up period due to a relatively smaller study area. It should be noted that these models are created using the same representative parameters for soil type, roughness, and aquifer properties as the *L-4* model. However, due to an increased impervious cover, land use variability may impact watershed hydraulics as the floodplain roughness reduces, as well as hydrologic processes such as rainfall excess and subsurface storage. Comparison of the two models (Fig. 3.14) clearly indicates that *WHR 2* has a superior performance (NSE = 0.94, PBIAS = -8.7 %, and Peak Flow Error = -4.8 %) compared to *WHR 1* (NSE = 0.71, PBIAS = +24.4 %, and Peak Flow Error = +15.5 %). Overall, *WHR 1* over-predicts the streamflow for both high and low flows (Fig. 3.14a) in addition to erroneous estimation of the recession limb of the hydrograph.

The results indicate that the incorporation of optimal intrinsic scales in integrated models results in an improved performance even for a watershed with variable land use characteristics. The hydrologic volumes for the *WHR 2* (shown in Fig. 3.14e and 3.14f) suggests a significant increase in rainfall excess, and subsequent decrease in vadose zone storage, and GW recharge, when compared to the UWR basin. The influence of urban land use on hydrologic process interactions has been evaluated by several studies (Lerner, 1990; Price, 2011; Schilling et al., 2008), and the results here validate the findings from these studies. Therefore, it can be concluded that the hydrologic processes are accurately represented using the modified model structure for the WHR basin.

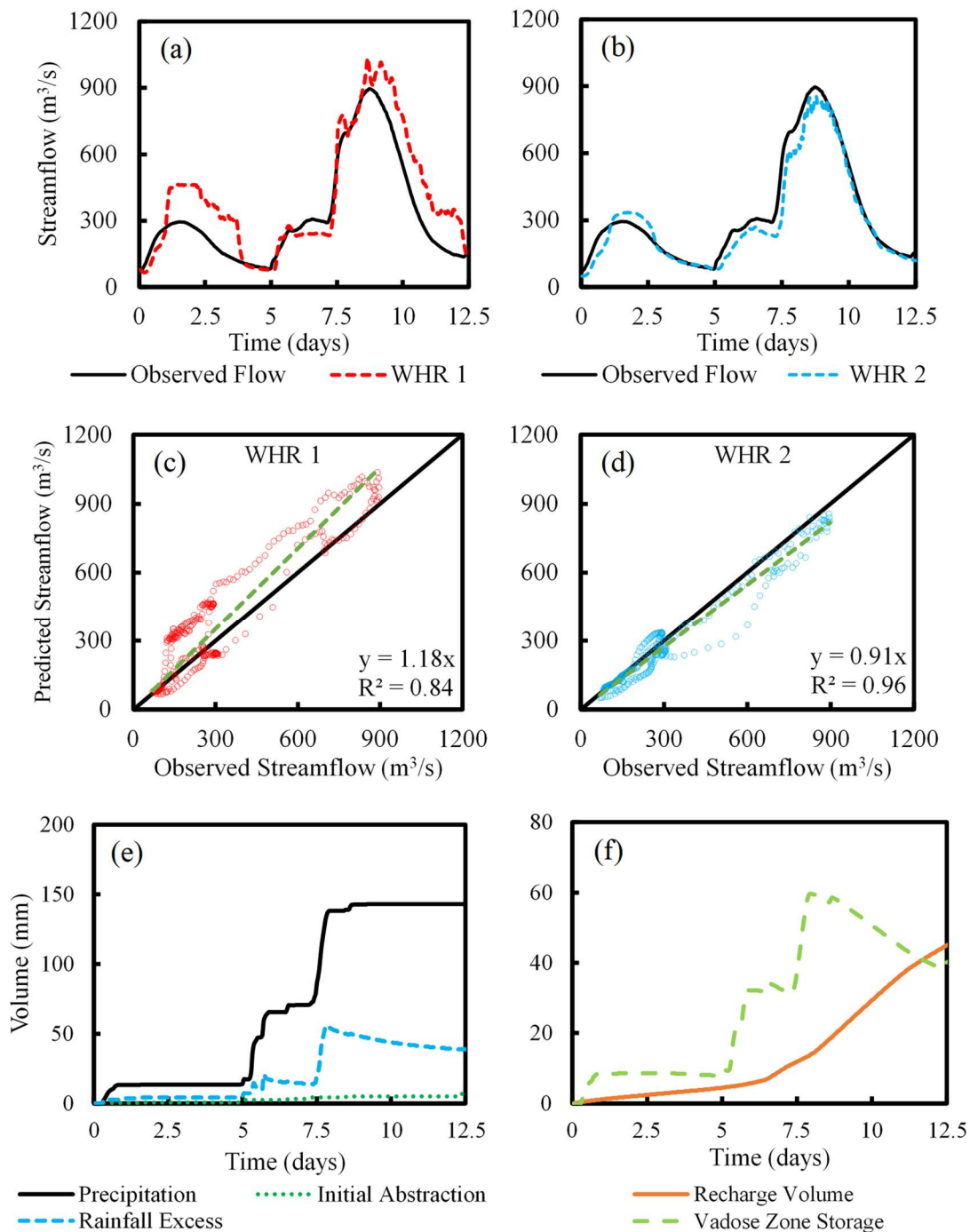


Fig. 3.14 (a) and (b) Streamflow hydrographs for *WHR 1* and *WHR 2*; (c) and (d) scatter plots at the outlet for *WHR 1* and *WHR 2*; (e) and (f) volumetric contributions from hydrologic processes for *WHR 2*

3.7 Summary and Conclusions

The physical processes governing flood responses function at different spatial and temporal scales. Some factors such as watershed topography and channel bed-form can influence flood responses locally, as well as at large scales. The overall influence of other processes changes with watershed scale, for example, rainfall, GW recharge, and seepage fluxes, may not influence watershed responses at small scales, but play an important role at large scales. Therefore, the assumptions related to characterizing these processes in models are only applicable over certain thresholds. This study improves the spatial extent scaling of integrated models through a better representation of the intrinsic scales of the physical processes and sub-models and provides a more realistic reproduction of basin and flood response. The following conclusions are drawn from this study:

1. At small scales, the role of rainfall and subsurface processes in influencing flood hydrodynamics is diminished as boundary inflows dominate. During floods with very low exceedance probabilities, flooding becomes streamflow dominated at small scales, and the influence of hydrologic processes is reduced.
2. The influence of hydrologic processes increases at large scales as excess rainfall and lateral seepage also influence riverine flow, implying an increased significance of headwater and lower order streams. The findings from this study support the argument that GW recharge operates at larger spatial scales, when compared to overland region and vadose zone.
3. The results highlight the ability of a dimensionless parameter η_L , representing the ratio of the reach length in the study region to maximum length of the single stream draining at that point, for identifying which streams may require a distributed channel roughness. Overall, higher η_L values indicate that the single channel roughness may not be suitable for accurate modeling of those streams. The classification of reaches for the application of single versus variable roughness distribution should not only depend on the reach length, but also on where the reach (upstream to downstream) is located in the watershed.
4. Considering that the typical characteristic lengths scales for shallow GW flows are much larger than overland or channel flow, the intrinsic scale (or resolution) of the GW sub-model should be larger than the SW sub-model. Application of a coarser GW sub-model

with respect to the SW sub-model improves the prediction of rising and falling limb of the hydrograph, lag-time, and hydrograph duration.

5. By applying a variable channel roughness and increasing the intrinsic scale of the GW sub-model with respect to the SW sub-model, the streamflow prediction improves not only at the outlet, but also across several locations inside the basin. The degree of improvement in streamflow prediction changes depending on the location of the reach in the watershed.
6. The difference in the median WT depth between the two models with different spatial extents reduces when the intrinsic scales of the sub-models are incorporated accurately.
7. By evaluating the effect of spatial scale variability on physical process characterization, an optimal modeling structure can be determined for any watershed. For example, even with an urban land use, a highly accurate water balance and flood estimation is achieved for the WHR basin by incorporating optimal intrinsic scales of the sub-models.

While this study focuses mainly on modeling process interactions across two spatial extents, the analysis approach, and subsequent application, are driven towards improving the performance of integrated models. It may be argued that the relative influence of spatial scale on physical processes may change for different watersheds. However, if these processes are characterized such that the conservation of mass holds across scales, these effects can be characterized for any system. As it is very difficult to estimate the exact flow paths for GW flow regimes, the overall volumetric contribution from different physical processes is a useful metric for large scale analysis. As an example, in this study, the change in the overall GW recharge between two watersheds with entirely different land use, highlights the broad applicability of this approach. Other important contributions from this study include disseminating the specific contributions from physical processes that contribute towards producing a flow hydrograph. For example, roughness distribution affects the lag time and surface storage, while groundwater flow controls the thickness of hydrograph limb, peak streamflow and water balance of the watershed. Similarly, future studies can include the effect of evapotranspiration in addition to subsurface processes and simulate the water balance for an entire watershed.

The results from this study suggest that using a variable channel roughness for reaches with higher η_L values improves the model performance. However, the roughness values in this study are linearly reduced for increasing downstream length, while studies have suggested that there is

a non-linear relationship between roughness and downstream length (Leopold and Maddock, 1953). Therefore, future studies should incorporate this relationship for large scale watersheds. Future studies should also incorporate the temporal-scale variability of rainfall for capturing the influence of rainfall at large watershed scales.

In conclusion, the hydrologic and geomorphic characteristics may or may not change in a watershed across two spatial scales, but the methods and schemes needed to characterize these processes in integrated models change at large scales. For example, a region with high impervious land use will result in increased rainfall excess. The existing model assumptions and structure can capture these effects at small scales. At large scales, the conclusions from this study including optimal roughness distribution and GW resolution can be used as a guide for integrated modeling of watersheds with distinct physical characteristics, while incorporating some site-specific information for more realistic event simulations. Such an analysis is especially vital with the increased focus on developing stream-network-based large flood models at regional or continental scales.

4. OBJECTIVE-ORIENTED HYBRID FLOOD MODELING BY COUPLING EMPIRICALLY-BASED AND PHYSICALLY-BASED MODEL FORMULATIONS IN A SINGLE SYSTEM

4.1 Abstract

Flood modeling across large watersheds is traditionally accomplished by loosely-coupling the streamflow predicted by an empirically-based hydrologic model to a hydrodynamic model for simulating the depth and extent of inundation. While the empirically-based hydrologic models have a high computational efficiency, their accuracy is limited by an overreliance on parameter calibration and lack of physicality. On the other hand, the relatively new and advanced integrated models simultaneously simulate watershed processes in a single system using physically-based equations and produce flood depths, extents, streamflow and water table depths. However, the complex numerical formulations for physical process characterization and the coupling mechanisms between SW-GW sub-models can cause a significant computational burden when using integrated models at large scales. This study presents an objective-oriented hybrid approach that incorporates the advantages of both loosely-coupled and integrated modeling approaches and allows user-flexibility in determining the level of process-based detail within a watershed. Using the Interconnected Channel and Pond Routing Model, the computational efficiency and accuracy of the proposed hybrid modeling approach is tested across three watersheds in Indiana using multiple flood events and comparing the results with fully-integrated models. The application of the hybrid model results in a 65% and 36% reduction in the number of computational elements, and a 53.3% and 67.7% reduction in the computation time for a one-month simulation at the UWR and WCC basins respectively, when compared to a fully-integrated model. A high F-statistic value of 94.1% for the UWR basin suggests that the reliability of the flood simulation does not reduce significantly when a hybrid modeling structure is incorporated instead of a fully-integrated model structure. Finally, the results also suggest that the hybrid models are able to accurately capture the basin response in large watersheds using only rainfall forcing, highlighting their applicability across ungaged basins.

4.2 Introduction

Hydrodynamic models such as LISFLOOD-FP, FLO-2D and HEC-RAS 2D (Bates and De Roo, 2000; Brunner, 2014; FLO-2D, 2018) do not simulate any hydrologic processes, so these models have to rely upon other hydrologic (rainfall-runoff) models (for example, HEC-HMS and SWAT) for generating streamflow, which is used as upstream boundary forcing to simulate flood maps. These hydrologic models are often based on the ‘top-down’ or ‘downward’ development approach that aims to predict the overall catchment response based on calibrating model parameters with observed data, and then use this information to estimate streamflow. Since these models are based on simple and parsimonious representations of physical processes, they are applicable across large watersheds and can be run for extended periods of time while maintaining computational efficiency. However, the simplicity of conceptualized processes, inability to capture heterogeneity, and scaling issues because of lack of physicality are major drawbacks of using these models (Fatichi et al. 2016; Sivapalan et al. 2003).

The loosely-coupled hydrologic-hydraulic modeling approach involves discretization of the watershed into several smaller units based on a user-defined threshold. These smaller units can be subbasins or hydrologic response units (HRUs) depending on the choice of model (e.g. HEC-HMS and SWAT). These smaller units act as individual basins and effective model parameters are calculated based on aggregation of geospatial datasets such as topography, soil, land use, impervious cover and rainfall. This is followed by rainfall-runoff partitioning using an empirical loss calculation (e.g. SCS Curve Number or HEC-2). The excess rainfall volumes are then aggregated and converted into streamflow using a simplistic transformation approach (e.g. NRCS Unit Hydrograph) followed by an empirical routing approach (e.g. Muskingham-Cunge). This streamflow at specific locations is transferred to a hydrodynamic model as upstream boundary forcing which is routed using roughness parameters to produce flood extents.

In case of ungaged basins, the uncertainty in flood simulation increases significantly as the empirically-based hydrologic models are required to predict the streamflow through optimal rainfall-runoff partitioning which cannot be accomplished without extensive calibration. (Salvadore et al., 2015). Further, the streamflow prediction is affected by the lack of accurate representation of antecedent conditions in empirically-based hydrologic models (Kim et al., 2012; Pfister et al., 2003). Therefore, recent studies have focused on simultaneous calibration of loosely-

coupled hydrologic-hydraulic models using remotely-sensed flood information (Montanari et al., 2008). However, these models are calibrated at a coarse resolution, hence, the subsequent conclusions across small scales are often unreliable. Due to the scaling issues, the effects of human-induced environmental changes that are critical to future flood risk estimation and planning cannot be captured accurately using these models (Fatichi et al. 2016). Moreover, the routing in empirically-based hydrologic models is based on simplistic methods such as Muskingum routing (Nash, 1959; Ponce, 1979), linear or nonlinear storage reservoir approximations (Mantilla et al., 2006). Using parameter calibration, the streamflow estimation using these routing methods is improved by modifying the storage-discharge relationships to approximate the flow dynamics of river networks in the watershed. However, these routing methods cannot capture the dynamic aspects of a flood wave propagation including river-floodplain hydrodynamics and backwater effects (Choi et al., 2015). Therefore, even if empirically-based approaches for streamflow prediction are used, the hydrologic routing needs to be improved significantly by incorporating a more robust and physically-based approach which is less dependent on calibration.

In recent years, several physically-based integrated models (for example, ParFlow, MIKE-SHE and GSSHA) have been applied for simulating hydrologic processes from reach to continental scales (Barthel and Banzhaf, 2016; Ebel et al., 2008; Kollet et al., 2017, 2010; Maxwell et al., 2015). Using these models, complex processes such as rainfall-runoff partitioning, unsaturated zone fluxes, GW recharge, and river-floodplain hydrodynamics can be represented more accurately. Traditionally, these models are based on the ‘bottom-up’ or ‘upward’ development approach that aims to model the catchment response by incorporating the variability in small scale processes and scale-up these responses to larger watersheds (Sivapalan et al. 2003). Over the last few decades, integrated models have evolved significantly from the earliest blueprint presented by Freeze and Harlan (1969) through advances in mathematical derivations of hydrologic processes that can capture non-homogeneity, anisotropy, and non-stationarity in physical processes (Fatichi et al., 2016). Further, the increasing availability and coverage of high resolution satellite-based topographic and hydrometeorological data for model parameterization, data assimilation and calibration has reduced input data uncertainties (Harris et al., 2014; Maidment, 2016).

However, the complex formulations in integrated models including the solution of dynamic wave routing, finite volume methods for estimating runoff volumes, and finite element

approximations for GW flow pose serious computational challenges when applied continuously over longer durations across large watersheds (Kim et al., 2012). Further, the coupling mechanisms between SW and GW sub-models (e.g. first-order coupling and simultaneous iterative coupling) require very small simulation time-steps to simultaneously solve all processes together which can create a great computational burden at large scales (Kampf and Burges, 2007).

While the empirical approximation of physical processes results in high computational efficiency, the accuracy of this approach is limited by its overreliance on calibration and lack of physicality. On the other hand, the integrated modeling approach combines several processes such as rainfall-runoff partitioning, unsaturated zone fluxes, GW recharge and river-floodplain hydrodynamics in a single system using physically-based equations to simulate the watershed response and produce flood extents, streamflow and water table depths simultaneously. While integrated modeling is highly accurate, it is sometimes unnecessary across the entire watershed domain and requires significant computation power for simulating floods across large watersheds. To illustrate the differences between the loosely-coupled and fully-integrated flood modeling approaches, process diagrams describing the model structure used in these approaches are presented in Fig. 4.1.

This study presents an alternative hybrid approach to incorporate the advantages of both loosely-coupled ('downward') and integrated ('upward') modeling approaches by coupling empirically-based and physically-based models within a watershed. This involves reducing the model complexity by simulating the river-floodplain hydrodynamics and subsurface flows using fully-integrated modeling only across specific user-defined regions inside the watersheds. A new procedure for hydrologic routing is adapted wherein an empirically-based hydrologic modeling approach is coupled with one-dimensional energy equation in the headwater and lower order streams to improve the streamflow prediction and subsequent flood simulation in the river-floodplain. Further, instead of using a simplistic rainfall-runoff partitioning method (e.g. Curve Number) across lower order streams, a physically-based infiltration method, coupled with a simplistic NRCS Unit Hydrograph method, is incorporated. The computational efficiency and accuracy of the proposed hybrid modeling approach is tested across three watersheds in Indiana using multiple flood events and comparing the results with fully-integrated models.

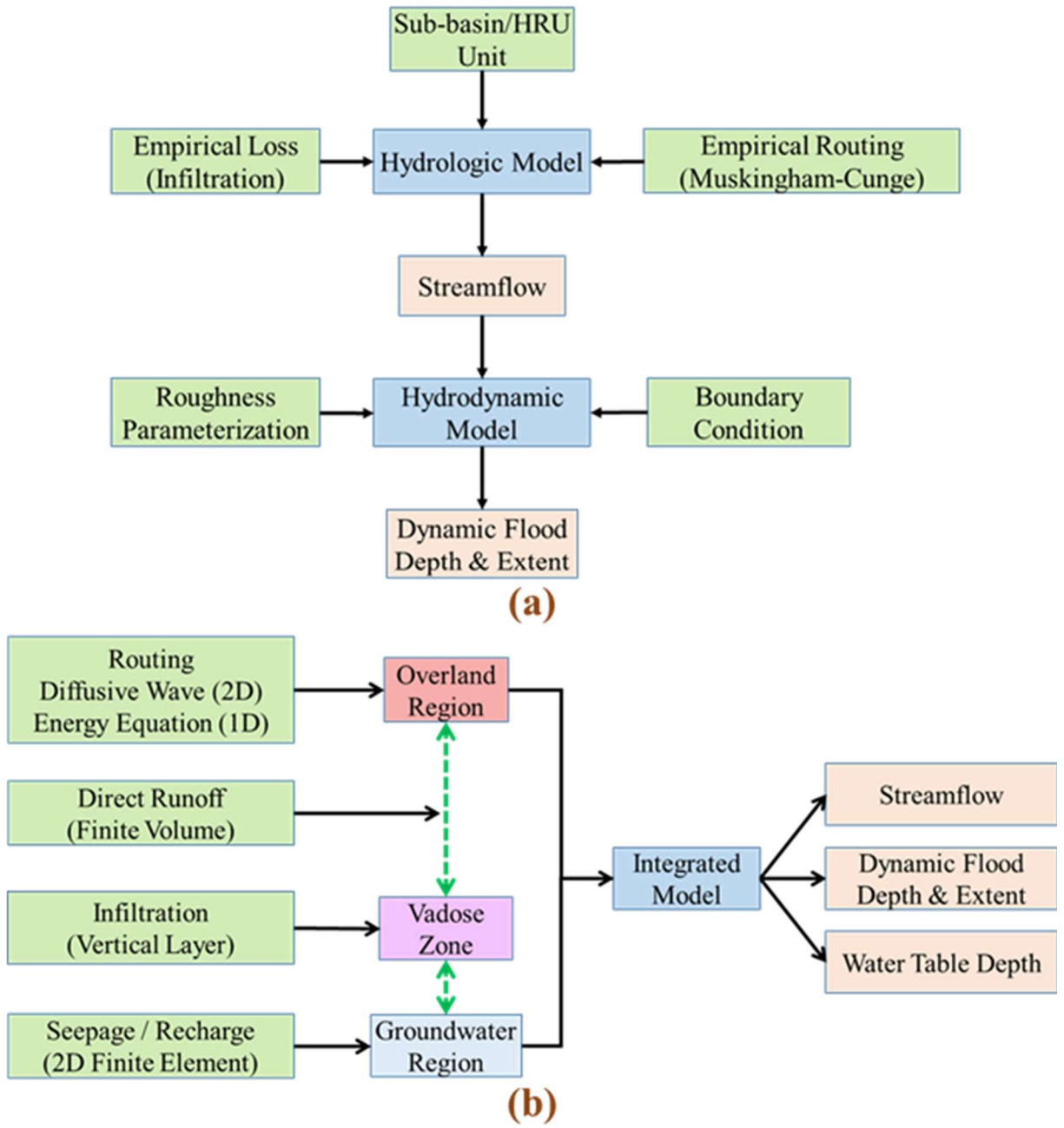


Fig. 4.1 (a) Flood modeling using loosely-coupled hydrologic-hydraulic models and (b) flood modeling using integrated models

Table 4.1 Description of watershed characteristics

Name	Upper Wabash River (UWR)	Wildcat Creek (WCC)	White River (WHR)
Study Area, km²	1,757	1,426	4,234
Land Use as per NLCD 2011 (%)			
Open Water	1.2	0.3	1.0
Low Intensity Residential	5.2	6.1	11.1
High Intensity Residential	3.2	3.3	8.6
Commercial / Industrial	0.5	1.1	3.5
Transportation	0.2	0.5	1.4
Barren	0.1	0.02	0.0
Deciduous Forest	10.7	6.0	5.4
Evergreen Forest	0.0	0.02	0.02
Mixed Forest	0.0	0.0	0.0
Shrubs	0.1	0.2	0.2
Grasslands	0.8	1.0	1.3
Hay / Pasture	4.1	1.3	3.0
Row Crops	73.4	79.5	64.0
Woody Wetlands	0.3	0.6	0.2
Herbaceous Wetlands	0.04	0.1	0.2
Soil Zone as per gSSURGO (%)			
A	11.6	2.8	0.1
A/D	8.5	1.3	0.1
B	19.9	5.8	5.8
B/D	9.5	27.8	42.0
C	40.5	14.8	19.2
C/D	7.3	46.2	25.4
D	2.6	1.3	7.4

4.3 Study Area and Data

As mentioned in the previous section, the hybrid modeling approach is evaluated across three study areas. The first area contains a portion of the Upper Wabash River Basin (referred to as UWR) with an area of 1,757 km². The outlet of UWR basin (shown in Fig. 4.2a) is located at the USGS gage 03335500, Wabash River at Lafayette, IN, (Latitude 40.422°N and Longitude 86.897°W). The second area is the Wildcat Creek basin (referred to as WCC) with a drainage area of 1,426 km². The outlet of WCC (shown in Fig. 4.2b) is located at the USGS gage 03335000,

Wildcat Creek near Lafayette, IN (Latitude 40.44°N and Longitude 86.83°W). The third area is the White River basin (referred to as WHR) which contains the city of Indianapolis, IN with a drainage area of 4,234 km². The outlet of WHR (shown in Fig. 4.2c) is located at the USGS gage 03353000, White River at Indianapolis, IN (Latitude 39.737°N and Longitude 86.169°W). Fig. 4.2 presents the location of the three sites in Indiana along with the land use distribution and outlet location. The WHR basin is used as a validation site for this section.

Table 4.1 presents the watershed characteristics of the three study areas used in this section. As shown in Fig. 4.2 and Table 4.1, the WHR basin is characterized by a higher (24.6%) proportion of developed (urban) region, when compared to the UWR basin (9.1%) and WCC basin (11%). The three basins have a high percentage of agricultural land use, especially row crops, which are distributed over 60% of the areas for all basins. The soil classification provided in Table 4.1 suggests a dominance of soil group 'C' for UWR basin, soil group 'C/D' for the WCC basin, and soil group 'B/D' for the WHR basin. The input data including topography, rainfall, streamflow, land use, soil type, impervious cover, roughness distribution and aquifer properties for all three watershed are extracted from the same data sources as described in Table 3.1 in Chapter 3. Therefore, a detailed description of these datasets is not provided in this section. A 9-m resolution LiDAR DEM containing river bathymetry is used for the three study areas to maintain consistency among the models.

For the empirical portion of the WCC and WHR basin, the subbasin extents were extracted using the HEC-GeoHMS toolbox in ArcGIS (Fleming and Doan, 2009). In case of the UWR basin, the subbasins were directly imported from the National Hydrography Dataset (NHD) using the Hydrologic Unit Code (HUC-12) subbasins. The parameters extracted from all the datasets are used as initial or boundary conditions. However, the actual values of moisture content, water table depth and hydraulic conductivity evolve with time based on the amount of water percolating into the subsurface only for the integrated portion of hybrid models. The parameters for the empirical modeling region do not change in time.

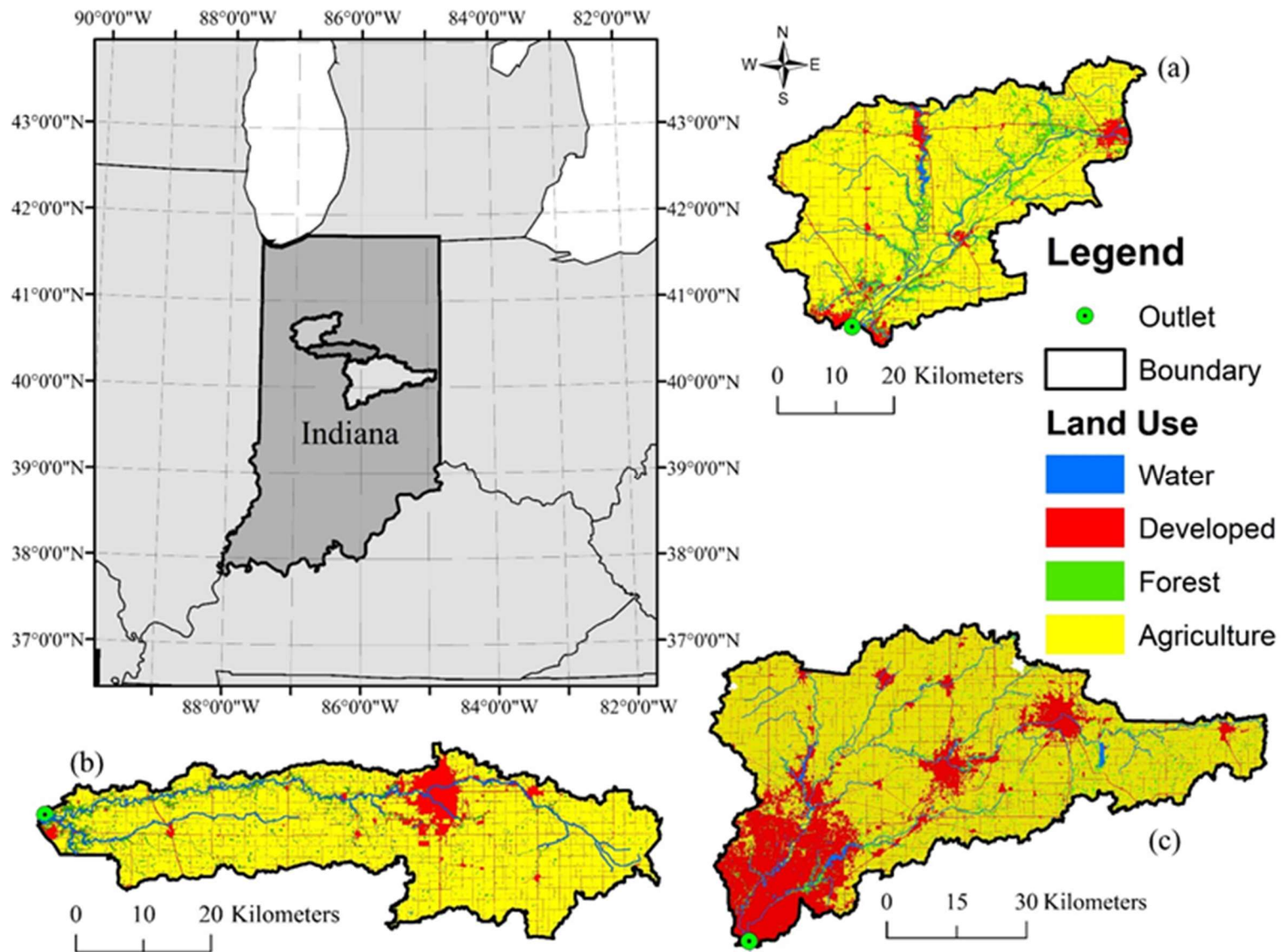


Fig. 4.2 Location and land use distribution of three study areas in Indiana (a) a portion of the Upper Wabash River (UWR) basin; (b) Wildcat Creek (WCC) basin; and (c) White River (WHR) basin

4.4 Development and illustration of the hybrid flood modeling approach

This section provides a description of the model development procedure and details about the hybrid structure across the three watersheds. To illustrate the applicability of the hybrid approach, the three study areas are designed differently.

4.4.1 Hybrid model structure for the SW system

In the first step, a layer defining the extents of integrated region is delineated inside the model (referred to as the ‘hybrid interface’). In the next step, the subbasin boundaries are imported into the model along with the stream network. The outlets of the streams draining into the hybrid interface are assigned as inflows into the integrated region. Inside the hybrid interface, the hydrodynamic modeling is carried out using a combination of 1D channels and a 2D overland flow region and a finite volume approach for surface flow calculation using unstructured mesh networks is used. Therefore, the diffusive wave equation in the 2D region is lumped along triangle edges, and the mass balance equations (Appendix A, Equations A.4 to A.7) are lumped at the triangle vertices where irregular shaped polygons (referred to as the honeycomb mesh) are formed establishing local control volumes. The triangular and honeycomb meshes are only created inside the hybrid interface and not inside the subbasins.

Heterogeneities in topography, land cover and soil characteristics are incorporated into the model by intersecting the honeycomb mesh with the terrain surface and geospatial datasets to form sub-polygons containing unique intersections of these datasets (Saksena et al., 2019; Streamline Technologies, 2018). These sub-polygons function as individual hydrologic units within a honeycomb, thereby, providing a high-resolution characterization of watershed properties. For more details, please refer to Section 3.4 and Fig. 3.2 in Chapter 3. Inside the 1D channels, the river geometry is defined using a node-link structure where the cross-sections are placed across the nodes, and the 1D region boundary is digitized using the river banks. Additionally, each node is assigned a ‘channel control volume’ which is used to assign elevations to the channel boundary and act as the linkage between the 1D-2D regions. Outside the channels, a triangular mesh with a fixed resolution of 60-m is embedded.

In addition to the 1D-2D coupling inside the hybrid interface, the streams inside all the subbasins are connected in a network of 1D nodes and links, where the subbasin outlets are assigned as 1D nodes. Channel cross-sections are then digitized for all the 1D nodes in the entire basin and the cross-section profiles are extracted from the 9-m DEM. The shallow and deep roughness values corresponding to the NLCD land use classes are directly obtained from the maximum and minimum roughness values recommended in Chow, 1959 (shown in Table 2.2). A variable channel roughness in the direction of flow (similar to $L-4$ in Chapter 2) is used for all the basins. The 1D channels across the entire basin are used for hydraulic routing using the energy equation and the 2D regions are solved using the diffusive wave equations (please see Appendix A for more details). This approach is superior to traditional empirical hydrologic models as the routing of water is not based on an empirical method like the Muskingham-Cunge routing. Instead, the water delivered to a subbasin outlet is routed using the fundamental solution of the 1D energy equation across the entire stream network.

4.4.2 Hybrid model structure for the vadose zone

The soil moisture accounting, and subsequent GW recharge across the entire basin is computed using the ‘Vertical Layer Method’ which is described in detail in Section 3.4 (Chapter 3). This method is not only used inside the hybrid interface, but also within individual subbasins. For example, inside any individual subbasin, the land use, impervious cover and soil characteristics are intersected to form unique combinations of sub-polygons with different properties. While these sub-polygons are not intersected with a honeycomb as it is only built for the region inside the hybrid interface, the runoff and infiltration volume for each sub-polygon is calculated individually, which is then aggregated and delivered to the 1D node at the outlet. This approach is analogous to creating HRUs in the SWAT hydrologic model, but instead of an empirical loss calculation (e.g. SCS Curve Number Method), a physically-based method is used. Additionally, the spatial discretization is at a very fine resolution when compared to HRUs as all unique intersections of geospatial datasets are formulated individually. In comparison to the empirical approach, not only does the hybrid model incorporate a physically-based infiltration method, but also calculates the hydrologic volumes at a higher resolution.

Although the routing and infiltration (loss) calculations in the subbasins are based on the 1D energy equation and the ‘Vertical Layer Method’, the transform method for delivering runoff

volumes to the subbasin outlet is based on a simplistic NRCS Unit Hydrograph method. This method requires an estimate of the time of concentration (T_c) for each individual subbasin. The time of concentration is the time required for a particle of water to travel from the most hydraulically-distant point in the subbasin to its outlet. The T_c values for individual subbasins are estimated using the HEC-GeoHMS toolbox in ArcGIS and are incorporated into the models without any modification. Using the NRCS Unit Hydrograph method, a complete hydrograph is generated at each time step based on the rainfall excess. Then, the individual hydrographs are added together through a convolution process forming a composite hydrograph for the subbasin. The simplistic transform method ensures that the runoff volumes can be delivered to the subbasin outlet without the need for 2D diffusive wave routing inside the entire subbasin. Even though the hydrologic calculations using the hybrid model structure are superior to the traditional empirical approach, the disadvantage of this approach compared to a fully-integrated model is that the spatially-distributed flood depths and extents cannot be generated outside the hybrid region.

4.4.3 Hybrid model structure for the GW region

A 2D GW region is incorporated across the entire model domain using the same initial parameters presented in Chapter 3. Although the 2D GW model is integrated into the entire basin, a dynamic water table (WT) is present only in the region inside the hybrid interface. This means that the lateral seepage due to WT fluctuations interacts with the overland flow region only inside the hybrid interface. Outside the hybrid interface, the GW honeycomb is intersected directly with the subbasins. Even though SW-GW interactions are not incorporated using the physically-based finite volume approach outside the hybrid interface, the advantage of integrating the 2D GW region across the entire basin is that the water that infiltrates into the subsurface from the subbasins is not lost from the system, but enters the GW region as recharge. If the WT exceeds the ground surface due to recharge, the excess seepage is delivered to the 1D channel node. Thus, even with empirical formulations outside the hybrid interface, the overall water balance in the system is maintained, which is a distinct advantage of this approach over traditional empirically-based hydrologic models.

4.4.4 Differences in model design across the three basins

In case of the UWR basin, the modeling is carried out for only a portion of a watershed using upstream streamflow as a boundary forcing. Therefore, four upstream gages (shown in Fig. 3.4a) including the USGS gage 03329000, Wabash River at Logansport, are used as the upstream boundaries for this model. The 2D GW region for the UWR basin has a mesh structure similar to the ‘*S-4*’ model described in Section 3.5.1.4 of Chapter 3. Fig. 4.3a provides an illustration of the hybrid model structure for the UWR basin. The hybrid interface for this basin encompasses the floodplain areas for all the major rivers. In case of the WCC basin, the modeling is carried out for an entire watershed without using streamflow information from USGS gages as boundary forcing. Rainfall obtained from the NLDAS dataset is directly used as the weather forcing and flood depths are generated solely from rainfall inputs. The WCC basin also contains a subbasin which is modeled as a fully-integrated region (Fig. 4.3b). The hybrid interface for the main channel (Wildcat Creek) is still delineated along the floodplain. This test case illustrates the flexibility of the hybrid modeling approach in discretizing the watershed hydrologic calculations based on user-defined specifications. Fig. 4.3b provides an illustration of the hybrid design for the WCC basin.

As mentioned earlier, the WHR basin is used as a validation site for testing the performance of the hybrid modeling approach at larger scales (4,234 km²). Additionally, the basin also contains the City of Indianapolis (highly developed region) near the outlet, and therefore, provides a different land use in comparison to the UWR and WCC basins which are primarily agricultural. The model development for this basin is solely driven by rainfall forcing, and hence, upstream gage inflow is not used. Fig. 4.4 provides an illustration of the hybrid design for the WHR basin. Since the basin contains more developed areas compared to the UWR and WCC basins, a hybrid interface extending beyond the floodplains and encompassing the developed regions is created for this basin. In addition to the hybrid models, fully-integrated models are also created for the UWR and WCC basins in order to evaluate the computational performance and accuracy of the hybrid models in comparison to a fully-integrated models. The integrated models for the two basins are created using the same design procedure as the *S-4* and *L-4* models used in Chapter 3.

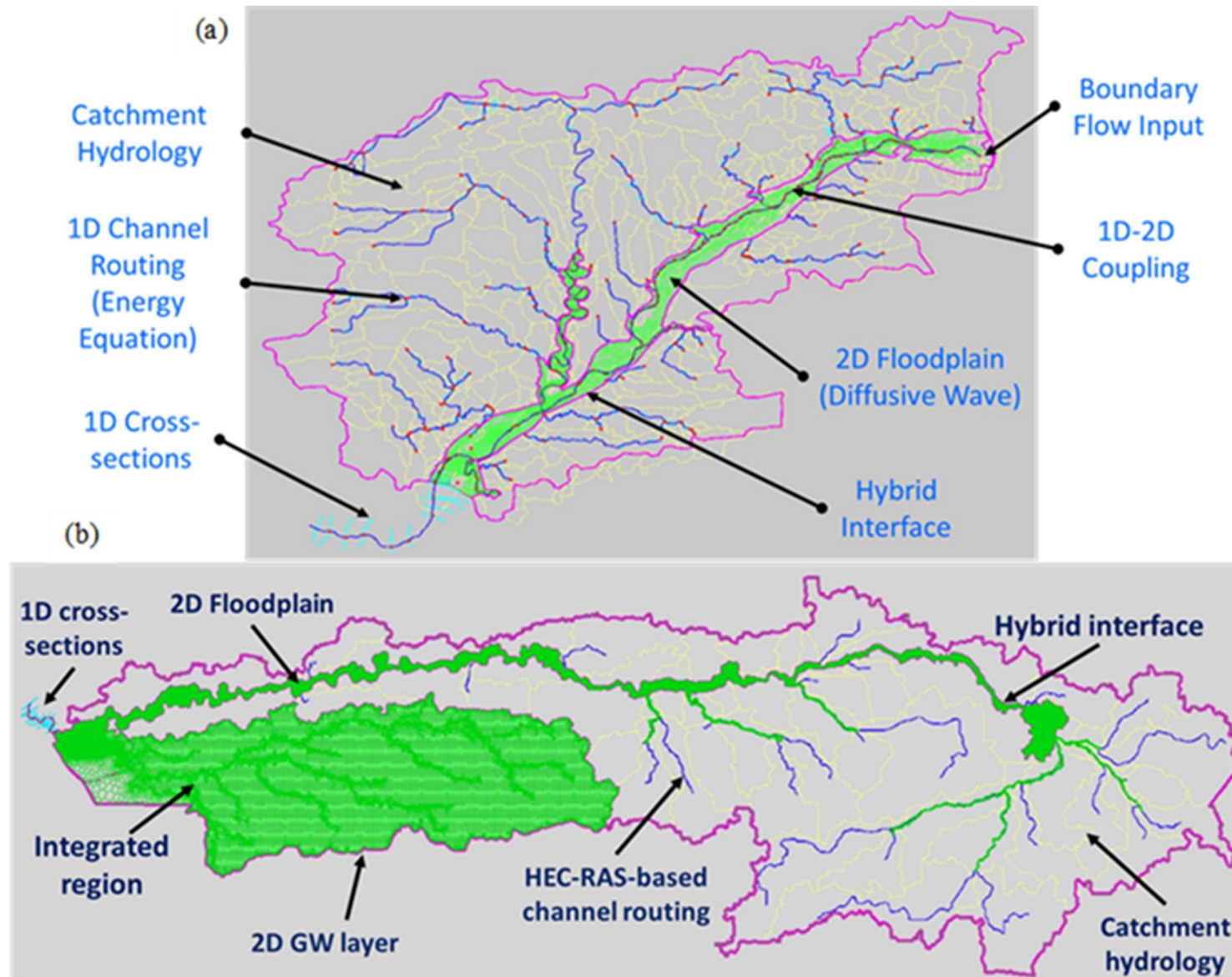


Fig. 4.3 Illustration of the hybrid modeling structure for (a) UWR and (b) WCC basin

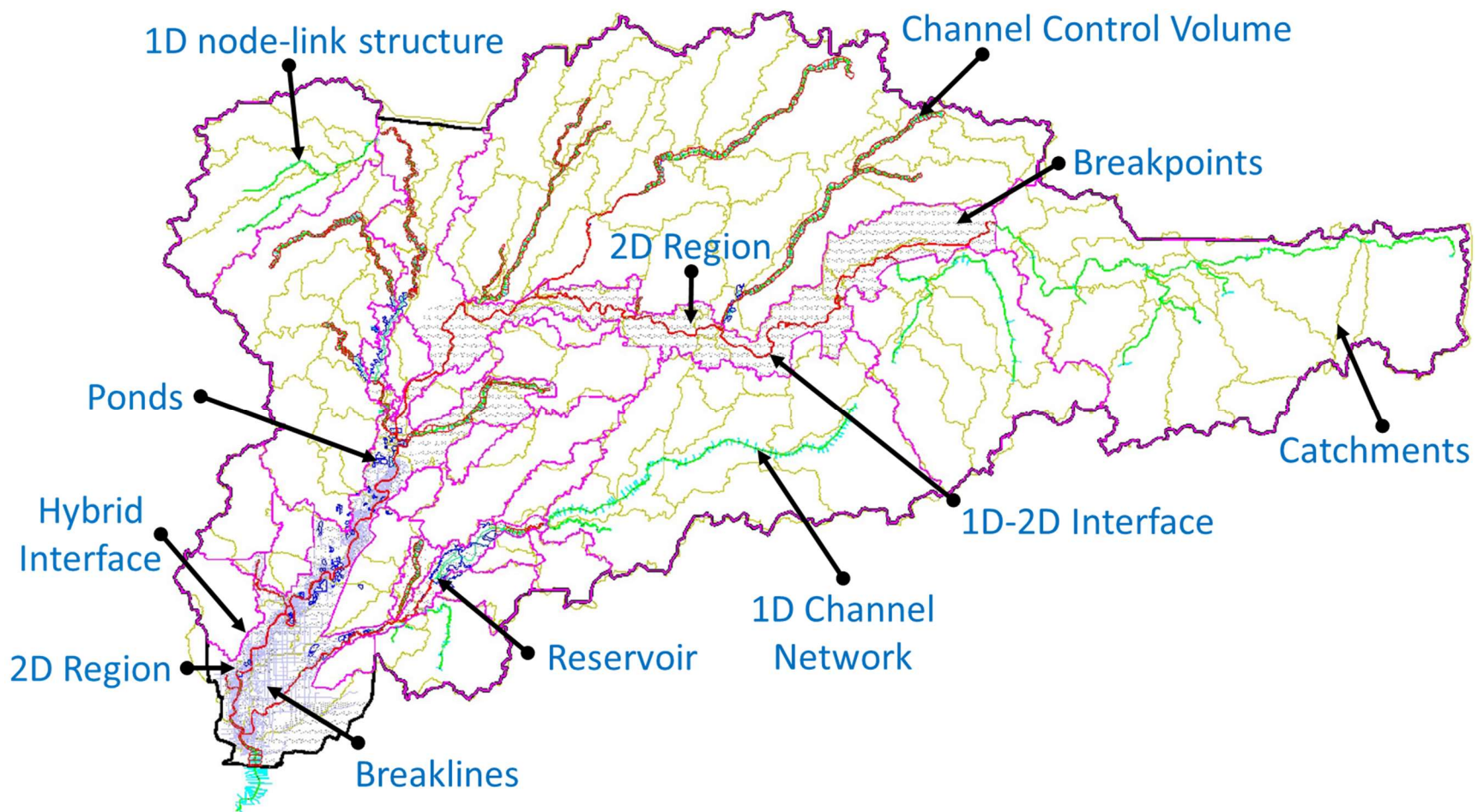


Fig. 4.4 Hybrid model for WHR basin used for validation

4.5 Spatial aggregation, computational parameters and numerical simulation

Table 4.2 presents the spatial aggregation and computational parameters for the three basins. As shown in Table 4.2, there is a 65% reduction in the number of triangles using the hybrid (*H*) model when compared to the fully-integrated (*I*) model for the UWR basin. The percent reduction in the number of triangles for the WCC basin is approximately 36%, which is less compared to the UWR basin as a fully-integrated region is incorporated for a subbasin (Fig. 4.4c) in the WCC basin. The number of sub-polygons outside the hybrid interface represent the total number of unique intersections of the geospatial datasets. As mentioned earlier, the runoff volumes are calculated for each of these sub-polygons highlighting the high spatial resolution even in the empirical region of the '*H*' models. The number of sub-polygons (both inside and outside the hybrid interface) are significantly higher for the WCC basin, which suggests that there is a larger spatial variability in the land use and soil characteristics in this basin. On the other hand, the WHR basin has a smaller variability in the geospatial characteristics, which may be because a large portion of the basin consists of a developed (urban) region.

The number of 1D hydraulic links represent the total number of connections between the 1D nodes in the stream network that are used for hydraulic routing inside the channels. The hydraulic routing time-interval is set between 0.01 to 5.12 seconds (ten time-steps), the hydrology is updated after every 300 seconds (5 minutes), and the groundwater flows, seepages and recharge rates are calculated at every hour (3600 seconds) for all the basins. The equivalent cell sizes for the '*H*' and '*I*' models are calculated using Equations 3.1 and 3.2 and the initial subsurface parameters for the three basins are adapted from Table 3.2 in Chapter 3.

All the models used in this study are simulated on Purdue University's Halstead cluster using only one computational node containing two 10-core Intel Xeon E5 processors (20 cores @ 2.6 GHz) to aid a consistent comparison. The triangular, diamond and honeycomb meshes for all models are built on a 4-core Intel i-7 system with a processing speed of 3.7 GHz. The model build process involves generation of the meshes required for simulation, intersection of all input datasets to extract model parameters, and assignment of nomenclature to mesh nodes and vertices. The build time for both the '*H*' and '*I*' models are comparable to each other for the UWR and WCC basins, although the '*H*' models have a relatively smaller build time.

The computational performance and accuracy of the ‘*H*’ models is compared with the ‘*I*’ models and observed data for both UWR and WCC basins. The ‘*H*’ and ‘*I*’ models for the UWR basin are simulated across two events, a 30-day period between April 11th to May 10th 2013 and a relatively longer 95-day period between February 10th to May 15th 2018. Similarly, the ‘*H*’ and ‘*I*’ models for the WCC basin are simulated across a 26-day period between March 31st to April 25th 2013. A relatively longer 50-day period between April 16th to June 4th 2016 is chosen for validating the performance of the ‘*H*’ model for the WCC basin. Finally, performance of the ‘*H*’ model of the WHR basin is validated across a 36-day period between April 2nd to May 7th 2013. The first 5 days are used as warm up period and all models are simulated at an hourly time-scale.

Table 4.2 Spatial aggregation and computational parameters for UWR, WCC and WHR basins

Computational Elements*	UWR	WCC	WHR
Model Area (km ²)	1,757	1,426	4,234
No. of triangles	119,190 (341,758)	225,482 (351,196)	334,202
No. of 1D hydraulic links	345 (-)	384 (-)	1,288
No. of 2D hydraulic links	122,646 (477,555)	219,531 (474,588)	260,110
No. of 2D sub-polygons	428,881 (596,333)	833,163 (2,108,195)	365,583
No. of sub-polygons outside the hybrid interface	157,580 (-)	713,908 (-)	210,951
No. of subbasins	573 (-)	55 (-)	203
Equivalent cell size (m)	58.7 (92.1)	66.6 (90.1)	71.1
Percent reduction in no. of triangles	65.1	35.8	-
Hydraulic simulation parameters	0.01 to 5.12 s (10 time-steps)	0.01 to 5.12 s (10 time-steps)	0.01 to 5.12 s (10 time-steps)
Model build time (hours)	2.8 (4.5)	9.0 (9.7)	14.3

*The values in parenthesis represent the parameters for the fully-integrated (*I*) models. Since fully-integrated models are only created for the UWR and WCC basins, only the hybrid model (*H*) parameters are reported for the WHR basin

The statistical analysis involves evaluating the goodness of fit between all the models and observed data and is carried out using the coefficient of determination (R^2), slope parameter (for comparison about the line $Y=X$), and the Nash-Sutcliffe Efficiency (NSE). The Percent Bias (PBIAS) is evaluated to compare the outflow volumes from the watershed with the observed data. This parameter also provides an estimate of the overprediction or underprediction of water storage

in the system, as the inflow volumes for all models at a given scale are the same. Therefore, it is used as a representative parameter for comparing the overall water balance across models. Additionally, the scale-normalized-RMSE (RSR) is evaluated to estimate the root-mean-squared-error (RMSE) in prediction, scaled by the standard deviation of observed data. Finally, the model performance is also determined by the percentage of error in peak flow prediction (%Error Peak Flow), as the peak flow governs the maximum inundation extents due to flooding.

4.6 Results and Discussion

4.6.1 Computational performance of ‘*H*’ and ‘*T*’ models

Table 4.3 presents the computation times for the ‘*H*’ and ‘*T*’ models for all the basins. The results highlight the improvement in computational efficiency of hybrid models in comparison to the fully-integrated models. For the UWR basin, the computation time reduces by 53.3% for a 30-day period and by 61.1% for a 95-day period when the ‘*H*’ model is used. The results also indicate that the percentage reduction in computation time increases as the simulation period is increased. A possible explanation for this is the increase in amount of time during which low flows exist in the basin during a longer simulation. It is expected that the ‘*H*’ models will be faster during periods of low flows in comparison to the ‘*T*’ models, thereby, decreasing the overall computation time. However, this increase may also be due to the difference in the event scales (50-year return period in 2013 compared to 25-year return period in 2018). Similarly, the computation time for a 26-day event in the WCC basin is reduced by 67.7% when the ‘*H*’ model is used. Additionally, Table 4.3 also presents the computation time ratio which represents the number of hours simulated by the model in one hour of actual time. This parameter provides an estimate of the forecasting ability of these models. Assuming that the weather forcing needed for forecasting is available, the ‘*H*’ model for WCC basin can provide an hourly forecast of streamflow and flood inundation upto 33 hours (1.38 days) in the future. This forecast duration can be increased to 3-7 days if 3-hourly or 6-hourly outputs are generated instead of an hourly forecast. Considering that the National Water Models’ (NWM) medium-range forecast weather forcing is available at a 3-hourly scale for upto 10 days, the WCC model can be effective for providing forecast flood simulations for upto 4 days using the hybrid approach, but this needs further testing.

Considering that the number of cores (20) used for the simulation are fixed across all models, a further increase in this number can improve the computation time for both ‘*H*’ and ‘*I*’ models. While this improvement can likely increase the overall forecasting ability of these models, the relative improvement using the ‘*H*’ models will still exist in this scenario. This is because the parallelization algorithm in ICPR is designed in a way that optimizes the distribution of the computational elements (or number of triangular nodes) across all cores. Therefore, an increase in the number of cores may scale the computation times across both models similarly. An analysis of the relative change in computational efficiency using a different number of cores was carried out by simulating the UWR basin using only 8 cores instead of 20 and the results (not reported here) scaled consistently across both ‘*H*’ and ‘*I*’ models.

Table 4.3 Simulation times for hybrid (*H*) and fully-integrated (*I*) models

UWR (1,757 km²)			
Model (Event)*	Simulation Period (days)	Total Computation Time (hours)	Computation Time Ratio
<i>H</i> (2013)	30	17.3 (53.3)	41.6
<i>I</i> (2013)	30	37.1	19.4
<i>H</i> (2018)	95	35.1 (61.1)	61.5
<i>I</i> (2018)	95	90.2	24.0
WCC (1,426 km²)			
Model (Event)	Simulation Period (days)	Total Computation Time (hours)	Computation Time Ratio
<i>H</i> (2013)	26	15.3 (67.7)	33.0
<i>I</i> (2013)	26	47.3	10.6
<i>H</i> (2016)	50	29.7	36.4
WHR (4,234 km²)			
Model (Event)	Simulation Period (days)	Total Computation Time (hours)	Computation Time Ratio
<i>H</i> (2013)	36	29.0	25.6

*The values in paranthesis represent the percentage reduction in the computation time when using the ‘*H*’ model instead of the ‘*I*’ model. The computation time ratio represents the number simulation hours the model can complete in one hour of actual time

4.6.2 Comparison of streamflow, hydrologic volumes and extent of inundation

In this section, the observed streamflow at the basin outlet is compared with the simulated streamflow using the ‘*H*’ and ‘*I*’ models. In addition to the streamflow hydrographs, scatter plots

comparing the observed and predicted streamflow are also created. Fig. 4.5 presents a comparison with observed streamflow for the ‘*H*’ and ‘*I*’ models of the UWR basin for the two events. As mentioned earlier, all models require a 5-day warm-up period, and therefore, the results for the warm-up period are excluded from the comparison. Fig. 4.5a – 4.5d suggest that both ‘*H*’ and ‘*I*’ models are able to predict the streamflow accurately for a 25-day period in 2013. Similarly, Fig. 4.5e – 4.5h show that the performance of the ‘*H*’ and ‘*I*’ models for the 90-day period in 2018 is comparable even though the computational efficiency of the ‘*H*’ model is significantly better.

Table 4.4 presents a statistical comparison of the model performance in streamflow prediction. In case of UWR basin, the high values of R^2 and NSE and low values of RSR for both ‘*I*’ and ‘*H*’ models for 2013 and 2018 further reinforce the performance of the ‘*H*’ model with respect to the ‘*I*’ model. Overall, the negligible difference between the performance statistics indicate that the ‘*H*’ model performance is similar to the ‘*I*’ model, although the PBIAS does indicate that the ‘*H*’ model has a tendency to slightly underpredict the streamflow when compared to the ‘*I*’ model, which might be a result of the empirical streamflow calculation in the ‘*H*’ model outside the hybrid interface.

Table 4.4 Statistical parameters for streamflow comparison

UWR						
Model (Event)	R^2	NSE	Slope	PBIAS (%)	RSR	Error Peak Flow (%)
<i>I</i> (2013)	0.98	0.98	0.96	-3.1	0.15	-0.5
<i>H</i> (2013)	0.98	0.97	0.96	-4.8	0.18	-1.5
<i>I</i> (2018)	0.97	0.96	1.01	-4.2	0.17	-5.3
<i>H</i> (2018)	0.99	0.97	0.92	-7.3	0.16	-3.4
WCC						
Model (Event)	R^2	NSE	Slope	PBIAS (%)	RSR	Error Peak Flow (%)
<i>I</i> (2013)	0.94	0.91	0.86	-16.4	0.29	-1.0
<i>H</i> (2013)	0.94	0.87	0.78	-24.6	0.36	-9.5
<i>H</i> (2016)	0.87	0.87	1.00	+1.9	0.36	-16.7
WHR						
Model (Event)	R^2	NSE	Slope	PBIAS (%)	RSR	Error Peak Flow (%)
<i>H</i> (2013)	0.94	0.92	1.09	+21.5	0.28	+4.3

The overall performance of both '*I*' and '*H*' models is less accurate for the WCC basin with more underprediction shown by the PBIAS (*H*: -24.6% and *I*: -16.4%) when compared to the UWR basin. This is expected as the WCC basin is a rainfall-driven model with no input streamflow as upstream boundary condition. However, considering that these results are based on uncalibrated model parameters, the overall performance is satisfactory. Table 4.4 shows that the '*H*' model underestimates the streamflow and that the overall performance for the 2013 event is less accurate compared to the '*I*' model. This reduction in the performance of '*H*' model is acceptable considering a significant increase in computational efficiency is achieved using this approach (Table 4.3). If the hybrid interface is expanded to cover a greater percentage of the basin, the performance may improve but this will also lead to an increase in the computational burden. This demonstrates that the choice of model structure depends on a tradeoff between accuracy and computational burden and that the effects may be more significant in a fully rainfall-driven model when compared to a model with input streamflow boundary condition.

To further validate the performance of '*H*' model on basins with only rainfall forcing, the streamflow hydrograph is compared for the WCC basin for the 2016 event and the WHR basin for the 2013 event. In case of the WCC basin (2016 event), the first hydrograph peak is underestimated but the subsequent peaks are captured accurately. Since this simulation results in a positive PBIAS compared to the 2013 event for the WCC basin (negative PBIAS), the overall performance suggests that there is no inherent bias in the model. Further, the simulation of WHR basin for the 2013 event shows that the model captures the peak flow accurately with an error of only 4.5%. While there is positive bias in the simulation, the high values of R^2 and NSE coupled with a low value of RSR and a slope nearly equal to one shows that the '*H*' model performance is acceptable for the WHR basin.

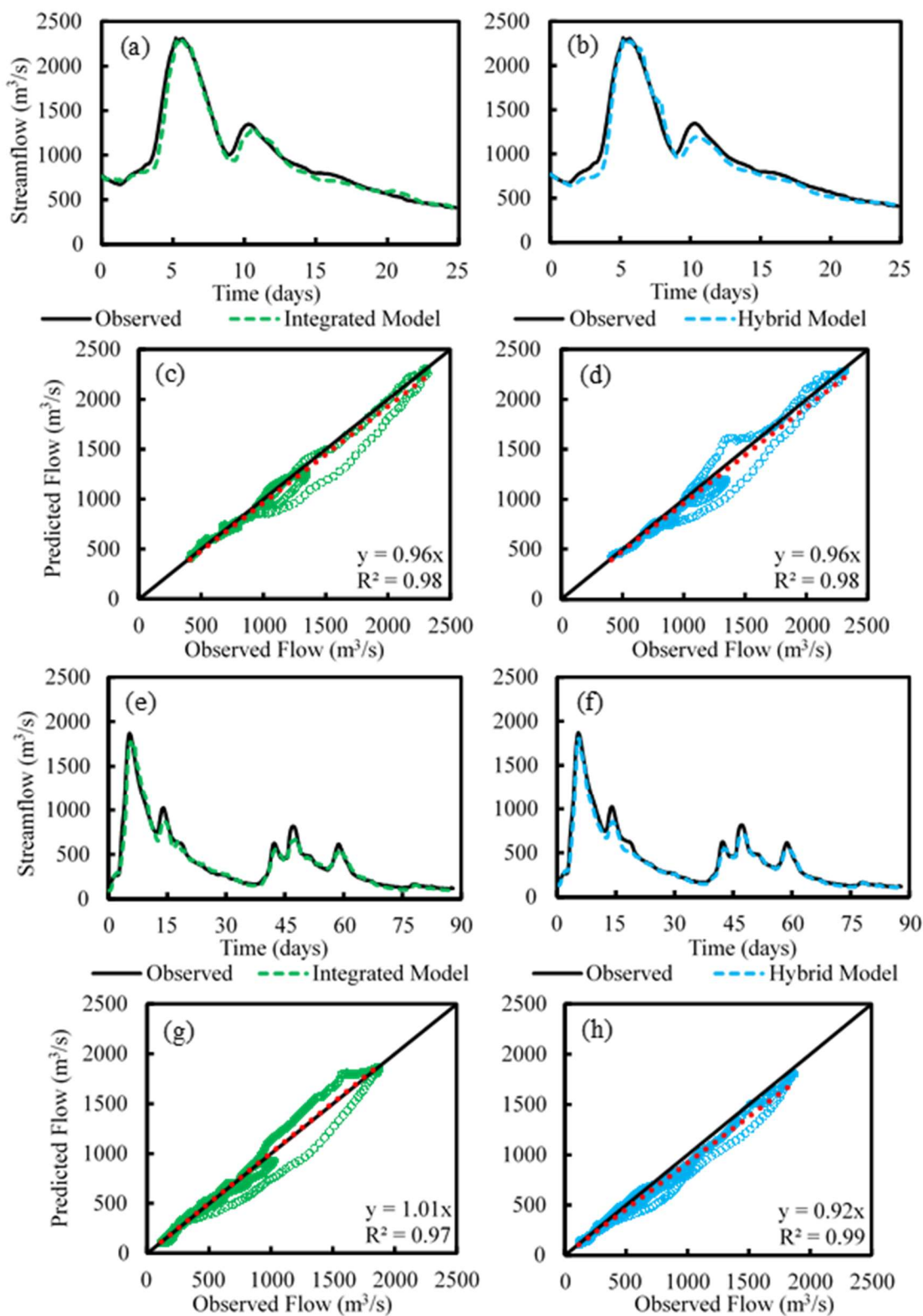


Fig. 4.5 Streamflow hydrographs and scatter plots showing the performance of integrated (*I*) and hybrid (*H*) models for (a) – (d) 25-day period from April 16th to May 9th 2013; and (e) – (h) 90-day period from February 15th to May 15th 2018

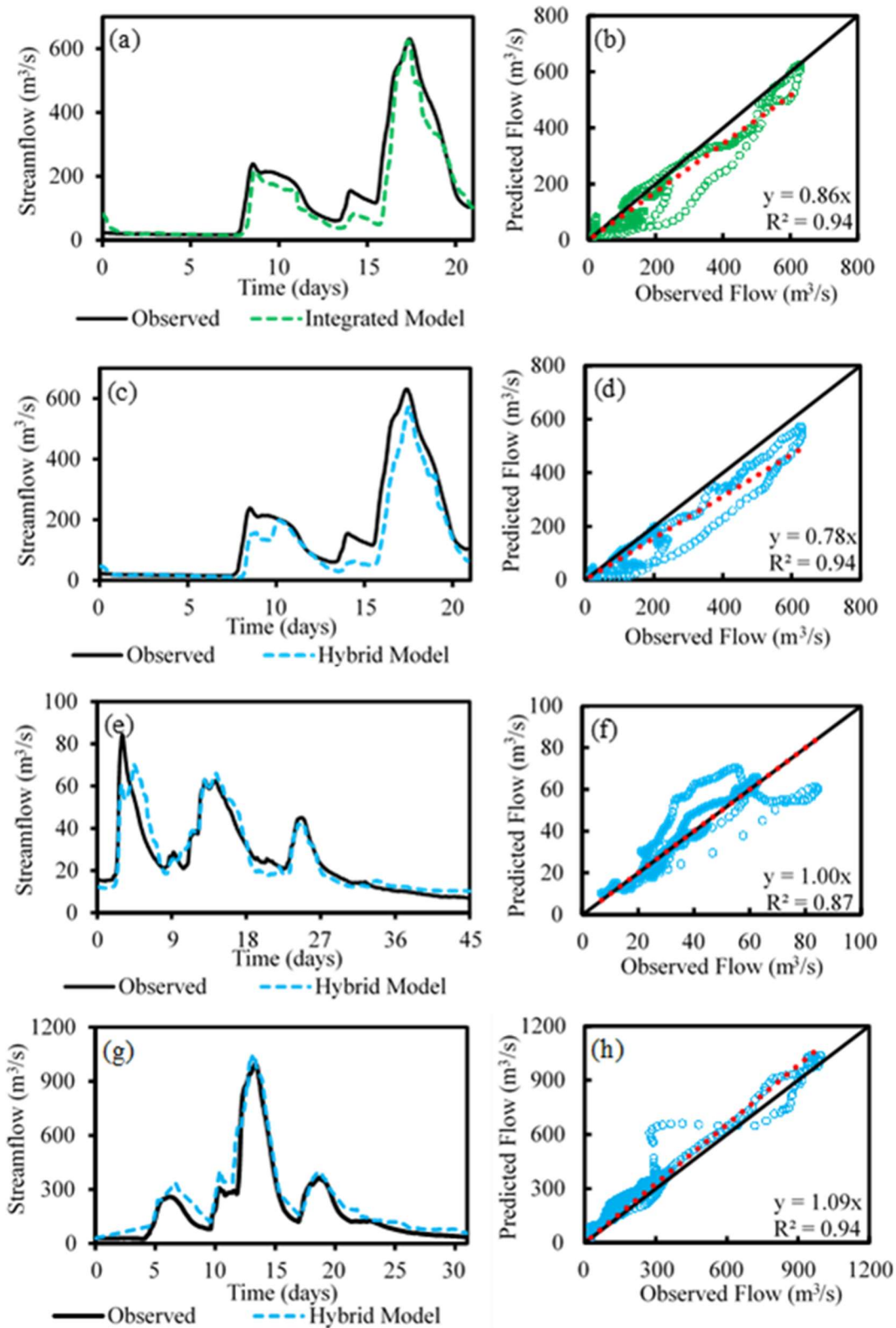


Fig. 4.6 Streamflow hydrographs and scatter plots for (a) – (d) 21-day period for the WCC basin from April 5th to April 25th 2013; (e) – (f) 45-day period for the WCC basin from April 20th to June 4th 2016; (g) – (h) 31-day period for the WHR basin from April 7th to May 7th 2013

The overall comparable performance in streamflow estimation between the ‘ T ’ and ‘ H ’ models for the WCC basin also highlights the utility of incorporating a fully-integrated region for more reliable modeling of ungaged subbasins. Additionally, the capability of including such a hybrid design also provides flexibility to the modeler to create models based on the objective-at-hand. For example, if an urban area exists outside of the floodplain in some part of the basin where estimating the extent of inundation is essential, a fully-integrated region encompassing the urban area can be embedded inside the basin. This type of flexibility is highly beneficial when modeling relatively large basins as there can be several urban areas outside the floodplain. While the WHR basin contains an urban area (City of Indianapolis), this region is located along the major stream (White River), therefore, the city is already embedded inside the hybrid interface.

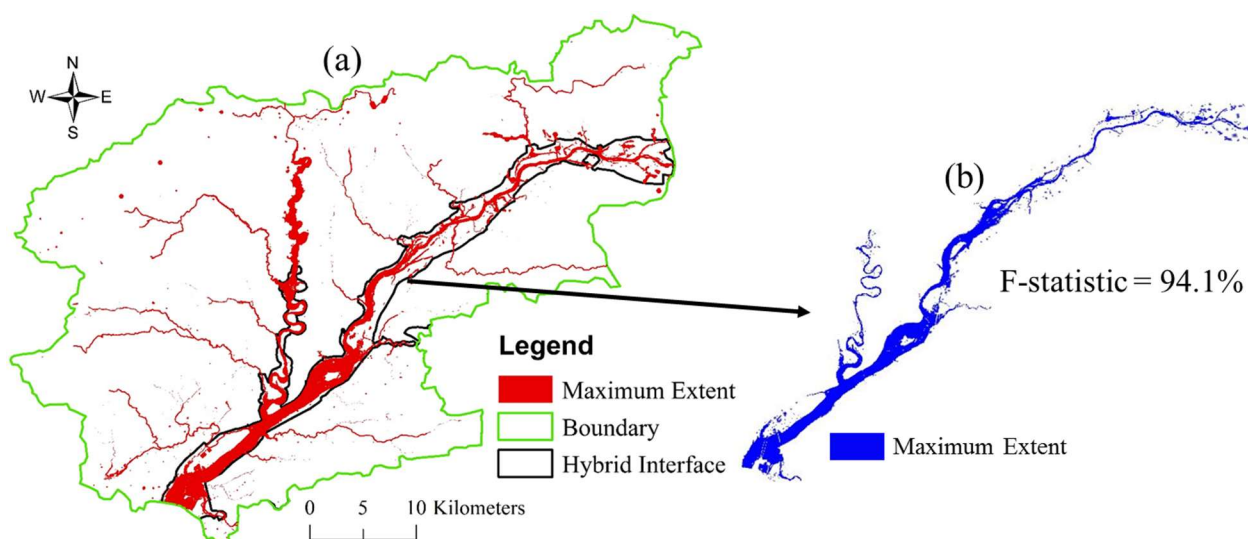


Fig. 4.7 Maximum extent of inundation (2013) for (a) fully-integrated model (T) and (b) hybrid model (H) for the UWR basin

Fig. 4.7 presents a comparison between the maximum extents of inundation obtained from the ‘ H ’ and ‘ T ’ models for the UWR basin for the 25-day period in 2013. Since the ‘ H ’ model only provides inundation information inside the hybrid interface, the performance of the ‘ H ’ model is evaluated by extracting the extent of inundation predicted by the ‘ T ’ model inside the hybrid interface. The two extents are compared and an F-statistic (Equation 3.5, Chapter 3) of 94.1% is obtained for the ‘ H ’ model relative to the ‘ T ’ model. This suggests that in addition to a similar streamflow prediction, the maximum extent of inundation for the ‘ H ’ model is also acceptable. Therefore, the hybrid modeling approach results in a performance comparable to a fully-integrated

approach but at a much higher computational efficiency. The disadvantage of the hybrid approach is the absence of predicted flood extents anywhere outside the hybrid interface.

Similarly, Fig. 4.8 presents the maximum extents of inundation for the WCC basin (2013) using the ' H ' and ' T ' models. As shown in Fig. 4.8, the flood extents are predicted only inside the hybrid interface and for the subbasin which is modeled using the fully-integrated approach. On the other hand, the ' T ' model provides an estimate of the maximum extent of inundation for the entire stream network. However, the hybrid interface can be redesigned to include any stream in the basin depending as per the user specifications. This flexibility is another advantage of the hybrid approach. Regardless, the streamflow and simulated flood extents clearly suggest that this approach offers an intermediate solution to flood modeling where the overreliance on loosely-coupled empirical hydrologic-hydraulic models is reduced and a higher computational efficiency is achieved in comparison to a fully-integrated approach.

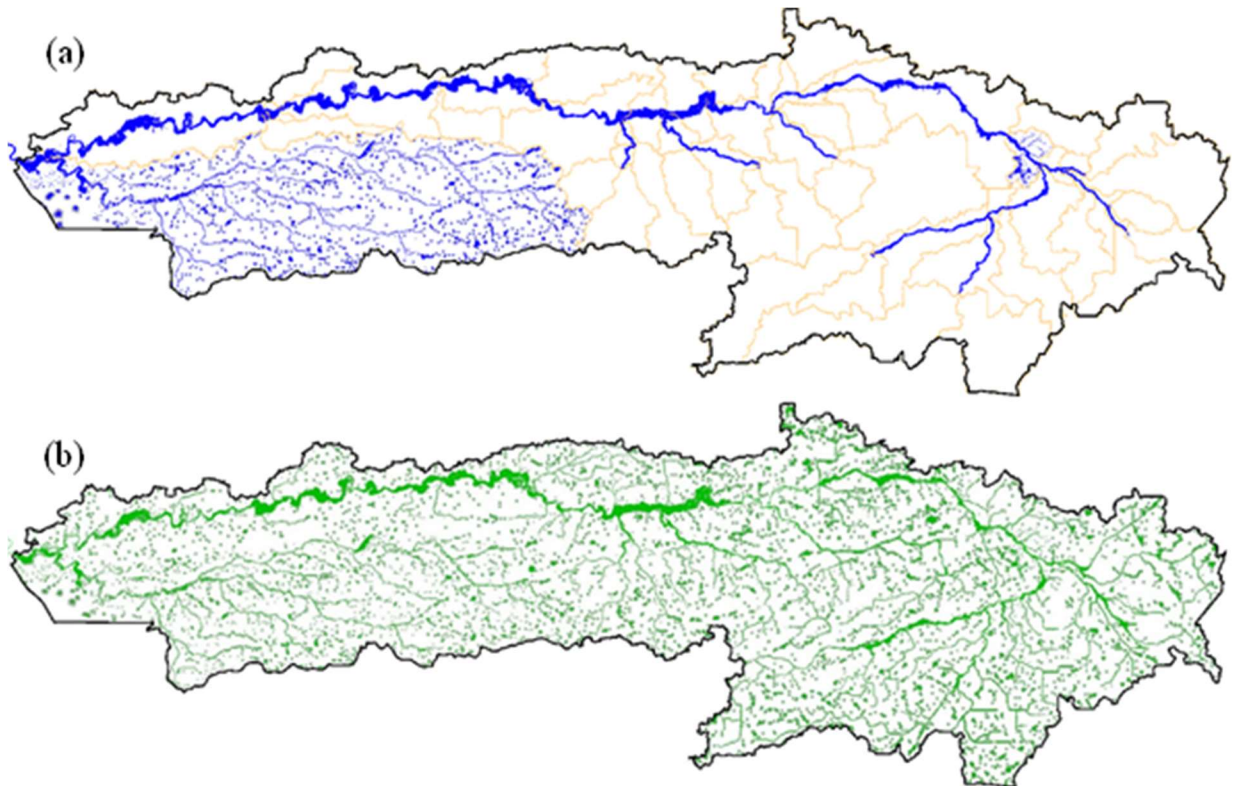


Fig. 4.8 Maximum extent of inundation (April 2013) for (a) hybrid (H) model and (b) fully-integrated model (I) for the WCC basin

Fig. 4.9 presents a comparison of the volumetric contributions from hydrologic processes between the ‘*H*’ and ‘*I*’ models of the WCC basin. The volumetric contribution divided by the watershed area (mm), is used as a metric for quantifying the relative contributions from different physical processes. It should be noted that these calculations are only quantified for the physically-based region of the ‘*H*’ model. For the WCC basin, this region includes the region inside the hybrid interface and the subbasin where fully-integrated modeling is carried out. Fig. 4.9a suggests that the precipitation for both ‘*I*’ and ‘*H*’ models is similar. The rainfall excess for the ‘*H*’ model is higher than the ‘*I*’ model. Considering this rainfall excess is calculated inside the river-floodplain region (inside the hybrid interface) for the ‘*H*’ model, highly saturated conditions exist during the flood simulation which increase the scaled-rainfall excess (with respect to the area) in comparison to the ‘*I*’ model in which the rainfall excess is calculated across the entire basin. This effect is also highlighted by the relatively higher vadose zone storage for the ‘*I*’ model when compared to the ‘*H*’ model. The amount of infiltration is expected to be higher away from the streams where unsaturated conditions exist, and therefore, the vadose zone storage is higher for the ‘*I*’ model. The relative difference between these hydrologic volumes can increase further if the fully-integrated region (subbasin) is removed from the comparisons.

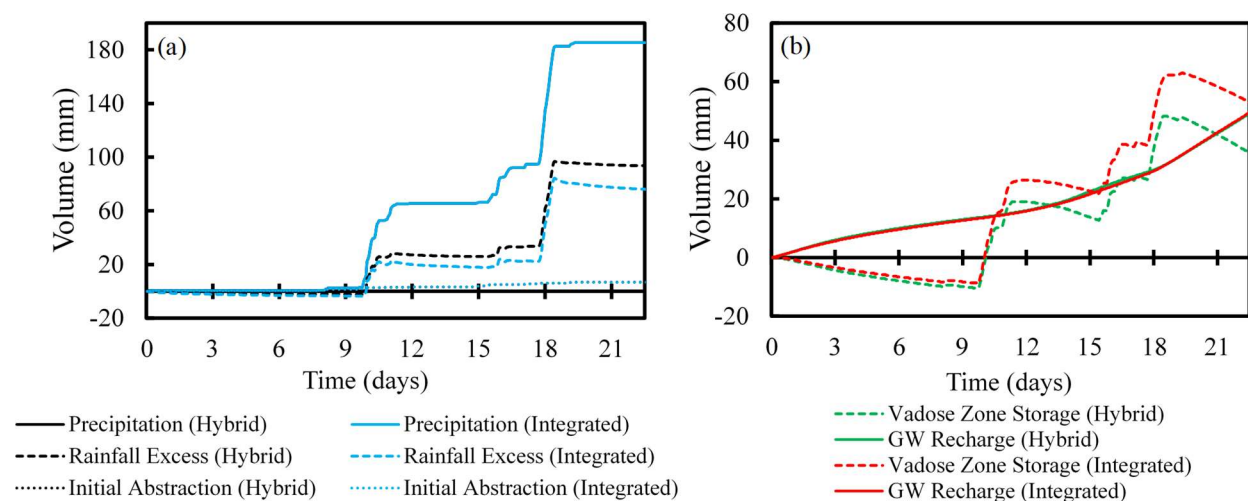


Fig. 4.9 Volumetric contributions from hydrologic processes for the hybrid (*H*) and fully-integrated (*I*) models for the WCC basin

4.7 Summary and Conclusions

Traditionally, flood modeling is dependent upon the availability of streamflow forcing to drive a hydrodynamic model and produce flood inundation. Since hydrodynamic models do not simulate any hydrologic processes, these models have to rely upon empirically-based hydrologic (rainfall-runoff) models for estimating streamflow, which is used as a boundary forcing. Alternatively, physically-based integrated models can be used to directly simulate physical processes such as rainfall-runoff partitioning, unsaturated zone fluxes, GW recharge, and river-floodplain hydrodynamics in a single system to generate flood extents. The analysis presented in Chapters 2 and 3 provides a pathway for flood simulation using integrated models. However, integrated models require complex numerical formulations to simultaneously simulate complex physical processes, which can increase the computational resources exponentially (Chen et al., 2017).

This study provides an alternative objective-oriented hybrid approach to flood modeling that incorporates the advantages of both empirically-based and physically-based models within a single system. This is accomplished by reducing the overall model complexity by simulating the river-floodplain hydrodynamics and subsurface flows using fully-integrated modeling based on user-defined specifications either along higher order streams where flood extents are needed, or along lower order ungaged subbasins, or inside regions of high flooding potential (urban areas). The other regions inside the watershed are modeled using relatively simple and conceptual representations of hydrologic processes. The computational efficiency and accuracy of this approach is tested across three watersheds in Indiana using multiple flood events. Following are the conclusions drawn from this study:

1. The application of the hybrid modeling approach results in a 65% reduction in the number of computational elements when compared to a fully-integrated modeling approach for the UWR basin and a 36% reduction for the WCC basin.
2. The hybrid model for the UWR basin reduces the computation time by 53.3% for a 30-day period and by 61.1% for a 95-day period when compared to a fully-integrated model. Similarly, the computation time for a 26-day event simulated at an hourly time-scale for the WCC basin reduces by 67.7% using the hybrid model.

3. Streamflow prediction across three basins (UWR, WCC and WHR) using five continuous simulation periods containing several flood events suggests that the hybrid models are capable of estimating the streamflow for the basins accurately. The degree of reduction in the accuracy when compared to a fully-integrated model is dependent upon the hybrid model design and the availability of upstream streamflow forcing. The results also suggest that the hybrid models are able to simulate streamflow accurately for large watersheds using only rainfall forcing. This highlights the applicability of the hybrid modeling approach for ungaged basins.
4. The comparison between the maximum extents of inundation obtained from the hybrid and fully-integrated models suggest that the spatial distribution of the flood extents does not change significantly using the hybrid approach. Therefore, the reliability of the flood simulation does not reduce significantly when a hybrid modeling structure is incorporated instead of a fully-integrated model structure. This is highlighted by a high F-statistic value of 94.1% for the UWR basin. The disadvantage of the hybrid modeling approach is that the flood extents cannot be predicted across all the streams in the basin, but only inside user-defined regions where fully-integrated modeling is carried out.
5. The results also highlight the capability of the hybrid design in providing flexibility to the modeler in changing the model structure based on the objective-at-hand. The regions for application of the empirically- and physically-based formulations can be modified anywhere inside the watershed depending on the required accuracy, level of process-based detail, and target computational efficiency.
6. Overall, the hybrid modeling approach results in a performance comparable to a fully-integrated approach but at a much higher computational efficiency while providing objective-oriented flexibility to the modeler.

5. A COMPUTATIONALLY-EFFICIENT FLOOD MODELING APPROACH FOR SIMULATING THE HYDRODYNAMICS OF UNPRECEDENTED EVENTS IN COMPLEX URBAN SYSTEMS

5.1 Abstract

Recent unprecedented events have highlighted that the conventional approach to managing flood risk is inadequate for complex urban systems because of its overreliance on simplistic methods at coarse resolution-large scales, lack of model physicality using loose hydrologic-hydraulic coupling, and absence of urban water infrastructure at large scales. Integrated models are a potential alternative as they can capture the complex nature of these unprecedented events through simultaneous tracking of hydrologic and hydrodynamic processes. However, their application to large scale flood mapping and forecasting remains challenging without compromising on spatiotemporal resolution, spatial scale, model accuracy, and local-scale hydrodynamics. Therefore, it is essential to develop techniques that can address these issues in urban systems while maximizing computational efficiency and maintaining accuracy at large scales. This study presents a physically-based but computationally-efficient approach for large scale (area $> 10^3$ km²) flood modeling of unprecedented events using an integrated model called ICPR (Interconnected Channel and Pond Routing). The performance of the proposed approach is compared with a hyper-resolution-fixed-mesh model at 60 m resolution. Application of the proposed approach reduces the number of computational elements by 80%, and the simulation time for Hurricane Harvey by approximately 4.5 times when compared to the fixed-resolution model. The results show that the proposed approach can simulate the flood stages and depths across multiple gages with a high accuracy ($R^2 > 0.8$). Comparison with FEMA building damage assessment data shows a correlation greater than 95% in predicting spatially-distributed flooded locations. Finally, the proposed approach can estimate flood stages directly from rainfall for ungaged streams.

5.2 Introduction

Over the last few decades, an increasing population trend towards the cities has resulted in rapid urbanization causing significant shifts in land use patterns in already flood-prone regions,

increasing exposure and intensifying future flood risk (IPCC, 2014; Johnson et al., 2018; Michel-Kerjan and Kunreuther, 2011). In addition to an increased impervious surface due to land use change, human-induced climate change has resulted in uncharacteristic weather patterns that have resulted in several unprecedented events (> 500 -year return period) along the coastal regions of the United States in 2017 and 2018 alone. These events have highlighted the importance of large scale flood risk assessment for aiding decision makers in developing mitigation and planning strategies (Berg and Sudicky, 2018; Dottori et al., 2016).

Flooding in complex urban systems is affected by several physical factors interacting together at different spatiotemporal scales, including but not limited to, rainfall intensity and magnitude, land use variability, storm surge in coastal regions, reservoir storage and release, riverine flow, infiltration induced by surface-subsurface interactions, longitudinal and lateral movement of river-floodplain fluxes, water entrapment through topographic gradients, and levee overtopping (Fletcher et al., 2013; Hattermann et al., 2004; Peters-Lidard et al., 2017; Salvadore et al., 2015; Sulis et al., 2010; Vivoni et al., 2007). With the increasing intensity and spatial influence of unprecedented flood events, the question that the research community needs to address is whether the existing techniques for flood simulation can capture the dynamic and compound nature of these events using the existing computational tools.

Static flood inundation maps provided by the Federal Emergency Management Agency (FEMA) for 100- and 500-year events are available for a majority of the United States. However, the dynamic aspects of flooding such as the timing and magnitude of inundation at specific locations, and inland flooding due to excess overland flow are critical elements needed for accurate evacuation and planning which are missing from the conventional flood models (Brody et al., 2013). While tools such as the National Water Model (NWM) that can forecast both rainfall and streamflow nationally are useful for decision-making and response-relief operations, they provide flooding information only along the streams at a relatively coarse resolution. Additionally, complex two-dimensional (2D) hydrodynamic models such as LISFLOOD-FP, FLO-2D and HEC-RAS 2D (Bates and De Roo, 2000; Brunner, 2014; FLO-2D, 2018) do not simulate any hydrologic processes so these models have to rely upon other hydrologic (rainfall-runoff) models for generating streamflow, which is used as upstream boundary forcing to simulate flood maps. Additionally, due to the reliance of upstream streamflow forcing in simulating flood maps, the

rainfall falling downstream of input flow locations causing lateral inflows is neglected. Further, extreme flood events that impact multiple watershed systems simultaneously may be difficult to capture using loosely-coupled hydrologic-hydraulic models as there can be inter-watershed flows due to significant rainfall, levee overtopping, and saturated subsurface conditions. Therefore, there is a need to incorporate multiple hydro-system components affecting flood hydrodynamics and build models that can simulate atmospheric, land, and subsurface processes accurately in a single system (Highfield et al., 2013; Hwang et al., 2019; Salvatore et al., 2015; Viero et al., 2014).

In recent years, several physically-based integrated models (for example, ParFlow, MIKE-SHE and GSSHA) have been applied for simulating hydrologic processes from reach to continental scales (Barthel and Banzhaf, 2016; Ebel et al., 2008; Kollet et al., 2017, 2010; Maxwell et al., 2015). Using these models, complex processes such as rainfall-runoff partitioning, unsaturated zone fluxes, GW recharge, and river-floodplain hydrodynamics can be represented accurately. However, integrated models not only require complex formulations to simulate multiple physical processes, but also need a fine spatial resolution to capture large scale flood hydrodynamics, which can increase the computational resources exponentially (Chen et al., 2017). Accurate simulation of flood hydrodynamics in complex systems may also require incorporation of more detailed and localized hydraulic information at a finer resolution. For example, square-grid or fixed-mesh integrated models have the potential of providing high resolution flood outputs, however, a fixed-resolution mesh structure in an integrated model can result in an extremely high number of computational elements, in addition to not being able to capture topographic variability in essential locations without reducing the overall mesh size substantially. Similarly, surface, subsurface, and atmospheric processes function at different time-scales, hence the iterative time-steps and temporal resolution of integrated models needs to be adjusted accordingly. For example, accurate flood hydrodynamics requires estimating the flow of water from one location to the other at very small time-steps (milliseconds to a few seconds), even though hydrologic processes can be simulated much faster due to the larger time-scales (minutes to days). This is required to ensure model accuracy and stability especially when simulating extreme events as the hydraulic gradients are often steep and conveyance volumes are very high. Therefore, the temporal resolution required for large scale flood modeling further decreases the computational efficiency making it impractical to use integrated models (Melsen et al., 2015).

These issues have restricted the application of integrated models to either small scale-fine resolution or large scale-coarse resolution (> 1 km), which significantly affects the accuracy and limits the efficacy of these models for modeling extreme flood events at large scales (Chen et al., 2017; Kauffeldt et al., 2016; Stisen et al., 2008). Therefore, to address the issues highlighted above, the computational efficiency of integrated models needs to be improved significantly while also implementing parallelization and cluster computing for modeling large scale flood events. In summary, the existing tools available for modeling large scale extreme events are all affected by one or more of the following issues: (1) overreliance on simplistic methods in coarse-resolution-large scale models such as the NWM; (2) lack of model physicality in 2D hydrodynamic models using loose hydrologic-hydraulic coupling; (3) computational inefficiency of integrated models at large scales; and (4) lack of innovative solutions for incorporating urban features and hydro-systems. Due to these issues, the existing tools may not be useful in simulating the complex hydrology and hydrodynamics of unprecedented flood events (> 500 -year return period) across urban systems that include several managed systems, man-made channels, canals, reservoirs, riverine-coastal interactions and spatial heterogeneity in land use.

This study proposes a modeling approach to address these four issues in a systematic manner for simulating the hydrology and hydrodynamics of unprecedented events in complex urban systems at large scales by: (1) integration of physical processes including river-floodplain and surface-subsurface interactions; (2) flexible spatiotemporal structure for computational efficiency; and (3) incorporation of artificial systems such as weirs, bridges, man-made channels, road networks and levees. The efficacy of this approach in capturing the flood hydrodynamics of unprecedented flood events at large scales is evaluated by using Hurricane Harvey as the test case. Using the principle of incorporating detail, only where needed, this approach aims to enable large scale-fine resolution simulation of flood hydrodynamics across multiple watersheds using a flexible spatiotemporal structure while performing minimal calibration (limited number of trial runs). The applicability of this approach is evaluated across two spatial scales, first, for a smaller area with a fine resolution spatial mesh, an open downstream boundary, and a fine-scale variable hydraulic time-step; and second, for a larger area with a coarser resolution spatial mesh, a coastal surge as the downstream boundary, and a coarser hydraulic time-step. Finally, the accuracy in flood simulation and reduction in the computational burden is tested by comparing the proposed approach with a hyper-resolution-fixed-mesh integrated model.

5.3 Study Area and Data

5.3.1 Study area description and history

Since the section focuses on developing a large scale computationally efficient integrated modeling approach for simulating unprecedented events, a portion of the Harris County region in Texas (TX), USA, which was affected by Hurricane Harvey in 2017, is chosen (Fig. 5.1a). The City of Houston, one of the most populous cities in the United States, is also situated inside the study area (Gao, 2017). The entire region is characterized by flat topography, clayey soils, mild slopes, and shallow and wide floodplains (Sebastian et al., 2017). Fig. 5.1b shows the land use distribution map for the region according to the 2011 National Land Cover Database (NLCD 2011: <http://nationalmap.gov/viewer.html>). As seen in the figure, this region has a high percentage of developed land use (56 %). In fact, this region has witnessed a 22 % increase in land development between 1996 and 2010, which has resulted in an increased impervious area, causing lesser infiltration and groundwater (GW) storage. Therefore, the amount of runoff generation from rainfall has increased substantially in the last two decades even though the annual rainfall has not changed significantly from its average of 1264 mm in any given year. Harris County contains two major watersheds, the San Jacinto River Basin and the Buffalo Bayou, and several other watersheds, including both, natural and man-made system of streams. The majority of these streams flow into the Houston Ship Channel (HSC) as shown in Fig. 5.2b, which drains into the Galveston Bay.

In the natural state without any development, the Harris County region would be dominated by wetlands/coastal prairies, which can provide higher evapotranspiration volumes, larger floodplain storages and increased GW recharge (Schaper, 2017). However, due to the significant development in the region, most rivers are rainfall-runoff dominated, and are not influenced by groundwater flow. In addition, the flow exiting from the Buffalo Bayou and other watersheds is influenced by tidal effects and storm surge, especially through Galveston Bay. At present, there is no regional levee protection system against storm surges across the Galveston Bay. Further, the Galveston Bay water levels are higher than the HSC during flood events which reduces the amount of water exiting the region. Upstream of Houston, two main reservoirs for flood control were built by the Harris County Flood Control District (HCFCD) and the US Army Corps of Engineers (USACE) called Addicks and Barker in 1945 and 1948 respectively. The Addicks and Barker

reservoirs (Fig. 5.1b) have levees enclosing an area of 37 km² and 34 km², respectively, and contain flood gates for water release into the Buffalo Bayou. Additionally, the Lake Houston reservoir (Fig. 5.1b) controls the inflow of water from the San Jacinto River Basin into the HSC.

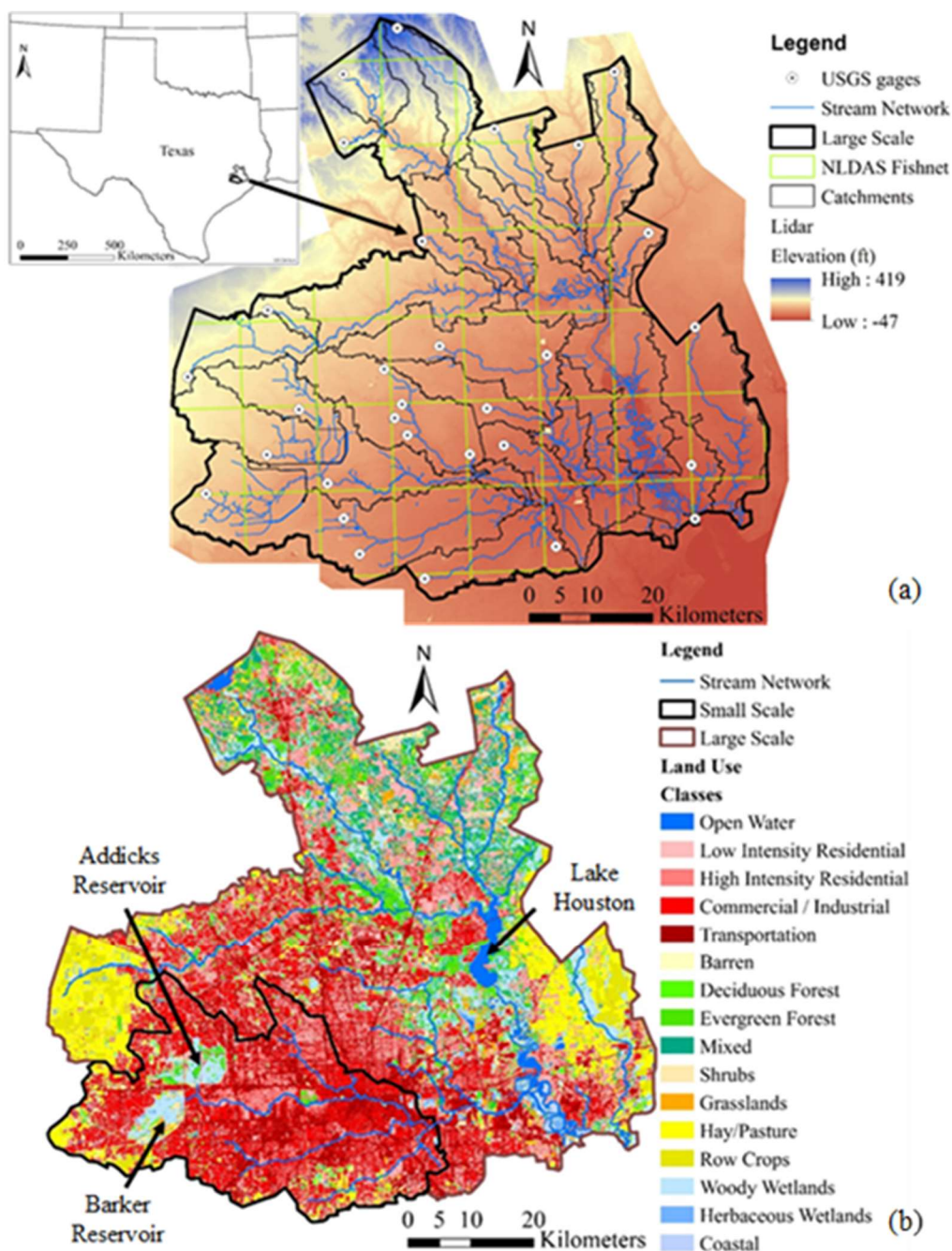


Fig. 5.1 (a) Study area location, USGS gage locations, drainage network and NLDAS fishnet for a portion of the Harris County, TX (b) land use distribution, reservoir location and extents of 'small' and 'large' models

5.3.2 Description of Hurricane Harvey

On August 25th, 2017, Hurricane Harvey made landfall near Rockport, TX as a Category 4 hurricane and caused record breaking rainfall across the state over six days (August 25-31, 2017). The rainfall from Harvey was exacerbated due to its slow-moving path or ‘stall’, helping it gain moisture while causing heavy rains through its outer bands. Additionally, it changed course and returned back into the Gulf, thereby gaining more moisture, and eventually making a second landfall in Louisiana on August 30th 2017 (van Oldenborgh et al., 2018). During this period, the Harris County region suffered the highest amount of hurricane-induced rainfall (shown in Fig. 5.2a) ever recorded in U.S. history which exceeded the 1000-year return periods in certain locations (Emanuel, 2017; Lindner and Fitzgerald, 2018). The rainfall magnitude (>1200 mm) and intensity (531 mm in 12 hours) exceeded record levels in the region and caused widespread flooding as a majority of the streams in the county overflowed, including the ones that were protected by levees (Lindner and Fitzgerald, 2018; Sebastian et al., 2017). The levee system constructed along the streams in the city, for example, Buffalo Bayou, White Oaks Bayou, and Brays Bayou, were only capable of handling 100-year flows, however, the majority of the residential flooding occurred outside the flood zones due to the large spatial influence of Harvey (City of Houston, 2018). The lack of localized near-real time information resulted in significant damages including over 80 fatalities, primarily due to drowning, and economic losses greater than \$150 billion in the region (Halverson, 2018; Sarkar et al., 2018; Sebastian et al., 2017).

5.3.3 Study area delineation

Two spatial extents are delineated in this study to test the computational efficiency and applicability of the modeling approach across these spatial scales. The first model, referred to as the ‘*large*’ model (5,342 km²), is delineated by selecting all the streams draining into the HSC, up to the city of Morgan’s Point, situated on the shores of Galveston Bay, which is also where the HSC drains into the bay and forms the downstream coastal boundary. The second model, referred to as the ‘*small*’ model (1,459 km²), encompassing the City of Houston, has an open downstream boundary allowing all the water flowing into the HSC to leave the system, therefore, this model does not incorporate the influence of coastal storm surges from the Galveston Bay. The two spatial extents are also chosen to evaluate the effect of different spatial resolution and hydraulic time-stepping in affecting the performance of the modeling approach. Therefore, in addition to the

difference in spatial scale, the two models are designed in a way that the ‘*small*’ model has a finer spatial resolution and smaller hydraulic time-steps, while the ‘*large*’ model has a coarser resolution and larger hydraulic time-steps. More information on the spatial resolution and hydraulic time-steps is provided in Section 5.5.1.

To delineate the extents of these models, first, watershed boundaries are located using the Hydrologic Unit Code-8 (HUC-8) catchments. Second, the United States Geological Survey’s (USGS) stream gage locations are overlaid on top the HUC-8 catchments. The model extents are then delineated using the gage locations as upstream boundary and the entire catchment downstream of the gage location is included in the model domain. This is done to capture flows from all possible streams draining into the HSC, as well as including all watersheds for potential inter-basin flows due to the high rainfall magnitude during Hurricane Harvey and the flat terrain in the region. Fig. 5.1a shows the USGS gage locations and HUC-8 catchment boundaries, while Fig. 5.1b shows the resultant study areas and their land use distributions. The extents of the ‘*large*’ model completely encompass the extents of the ‘*small*’ model. The USGS gage 08067650, downstream of the reservoir at Lake Conroe, is used as the upstream boundary for the ‘*large*’ model. For all the ungaged streams inside the study areas downstream of the USGS gages, the flow and subsequent inundation is also calculated based on distributed modeling of rainfall. The land use for the area inside the ‘*small*’ model is highly developed (82 %), while the ‘*large*’ model also contains regions with a higher percentage of forest and agricultural land use (as shown in Table 5.1) mainly inside the San Jacinto River Basin above Lake Houston (Fig. 5.1b). Therefore, the overall developed percentage reduces to 56 % for the ‘*large*’ model.

5.3.4 Data acquisition

The modeling approach used in this study is data intensive and requires integration of several public domain datasets for extracting surface properties such as topography, land use, and surface roughness (Manning’s n); climatic variables such as rainfall and streamflow; and subsurface datasets for determining the soil properties. The land use data for the study are obtained from the NLCD 2011 database. Impervious cover data in the form of a raster grid is downloaded from USGS’s The National Map Viewer (<https://viewer.nationalmap.gov/basic/>). For the subsurface part, vadose zone properties such as moisture content, vertical conductivity, and soil type are characterized using information from the National Resource Conservation Services’

(NRCS) Gridded Soil Survey Geographic (gSSURGO) Database. The soil zones shown in Table 5.1 suggest a higher percentage of Hydrologic Soil Groups (HSG) ‘C/D’ and ‘D’ highlighting the reduced infiltration capacity of the soils in this region. The rainfall data for the region is obtained from the North American Land Data Assimilation System (NLDAS) that provides hourly precipitation at a spatial resolution of one-eighth-degree (shown in Fig. 5.1a).

The NLDAS data is preferred over the National Oceanic and Atmospheric Administration’s (NOAA) Climate Data Online (CDO) rainfall gage data, since NLDAS has higher spatial resolution compared to gage data, which is sparsely distributed. The rainfall during Hurricane Harvey is represented using an isohyetal raster map as shown in Fig. 5.2a. Instantaneous streamflow and gage height data for 30 stations (Fig. 5.1a) are obtained from the USGS National Water Information System (<http://waterdata.usgs.gov/nwis/rt>). Depending on the availability of data, either stage elevations or streamflow data obtained from USGS gages are used as upstream boundary forcing for the locations highlighted in Fig. 5.1a. The coastal boundary acts as the downstream control for the ‘*large*’ model, and dynamic wave information is obtained from NOAA’s Tides and Currents (<https://tidesandcurrents.noaa.gov>) gage 8770613 at Morgan’s Point, Barbours Cut, TX.

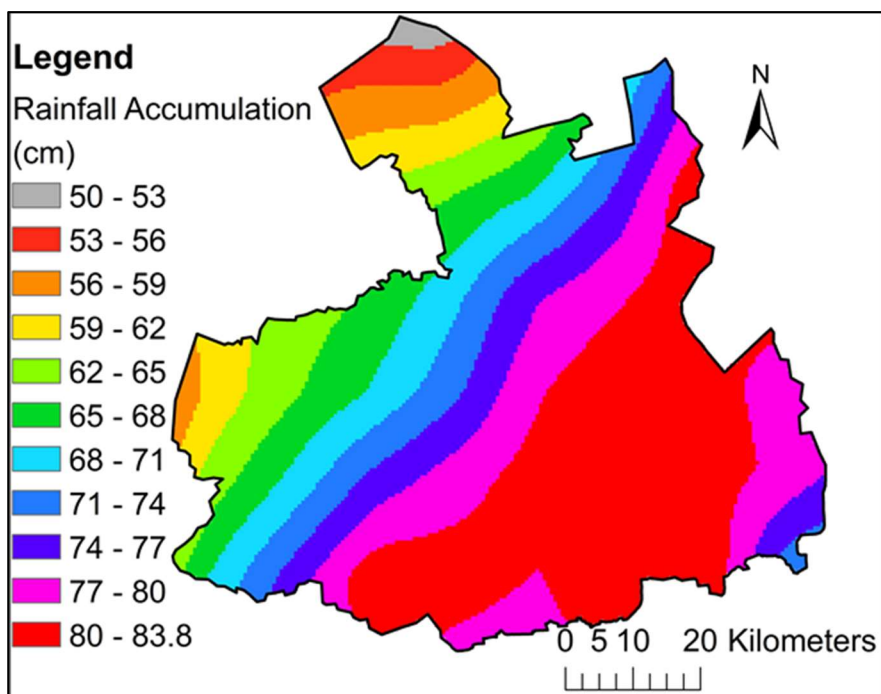


Fig. 5.2 Isohyetal map of rainfall distribution during Hurricane Harvey

Table 5.1 Watershed characteristics for the ‘*large*’ and ‘*small*’ model

Name	<i>Large Model</i>	<i>Small Model</i>
Study Area, km²	5,342	1,459
Land Use as per NLCD 2011 (%)		
Open Water	2.6	0.7
Low Intensity Residential	13.1	10.5
High Intensity Residential	15.2	18.7
Commercial / Industrial	19.1	34.5
Transportation	8.6	18.3
Barren	0.8	0.7
Deciduous Forest	1.7	1.3
Evergreen Forest	5.9	1.3
Mixed Forest	6.4	0.3
Shrubs	3.4	1.7
Grasslands	3.5	1.5
Hay / Pasture	7.5	4.3
Row Crops	2.5	1.3
Woody Wetlands	8.3	4.2
Herbaceous Wetlands	1.2	0.5
Coastal	0.2	0.0
No. of USGS gages	30	13
No. of NLDAS rainfall grids	51	17
Soil Zone as per gSSURGO (%)		
B	10.8	0.0
C	17.2	1.2
C/D	28.9	38.7
D	43.0	60.1

5.4 Methodology

The proposed approach is tested using the ICPR model, a detailed description of which is provided in Section 2.4. Fig. 5.3 provides a 2D illustration of the physical processes incorporated in the model. Although the model includes a 3-layered vadose zone, the soil surface is assumed to be impervious after 180 cm and the models in this section do not include a 2D GW system since the aim is to evaluate the accuracy and computational efficiency of a flexible spatial structure in the surface system when compared to a fixed resolution model. Details on the model structure,

including the steps involved in creating and simulating the models for Hurricane Harvey are provided below.

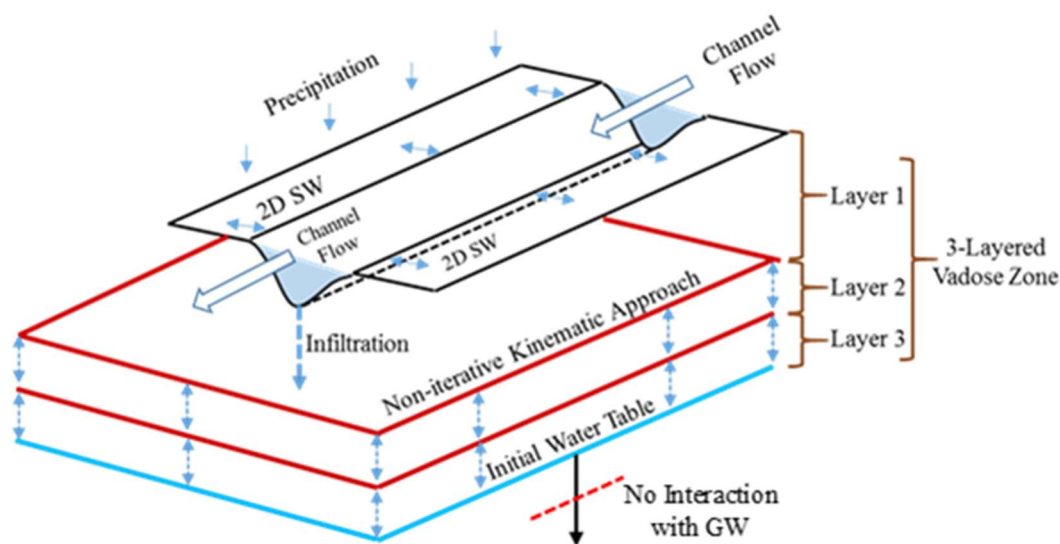


Fig. 5.3 Conceptual illustration of physical processes using ICPR

5.4.1 Incorporating a computationally-efficient model structure

The model structure is designed to obtain maximum efficiency while maintaining accuracy. The elements used to build the model structure are shown in Fig. 5.4. The hydrodynamic modeling involves the combination of 1D channels and a 2D overland flow region. The river geometry is defined using a node-link structure where the cross-sections are placed across the nodes, and the 1D region boundary is digitized using the levees built along the channels. Additionally, each node is assigned a ‘channel control volume’ which is used to assign elevations to the channel boundary and act as the linkage between the 1D-2D regions. Outside the channel, a flexible triangular mesh structure is used, such that it is dense in the river floodplain (as shown in Fig. 5.4a and 5.4c), and coarser for the land surface away from the floodplain to reduce computation time.

The features inside the 2D overland flow region are generated using the ‘breakline’ and ‘breakpoint’ features in ICPR. The ‘breakline’ feature is a polyline shapefile generated by digitizing the smaller streams, instream barriers, and road networks in the study area using aerial imagery and LiDAR data. Each point used to create the polyline ‘breakline’ feature is assigned a triangular vertex node in the model and the triangle edges are formed along the polyline. Therefore, flow rates are computed along the triangle edges within the ICPR computational scheme. The

TIGER/Line[®] shapefile of road networks published by the U.S. Census Bureau is used to extract major road networks which are imported into the model as ‘breaklines’ (Fig. 5.4a) after vertex simplifications to ensure that triangle edges are formed along the roadways thereby capturing important topographical features.

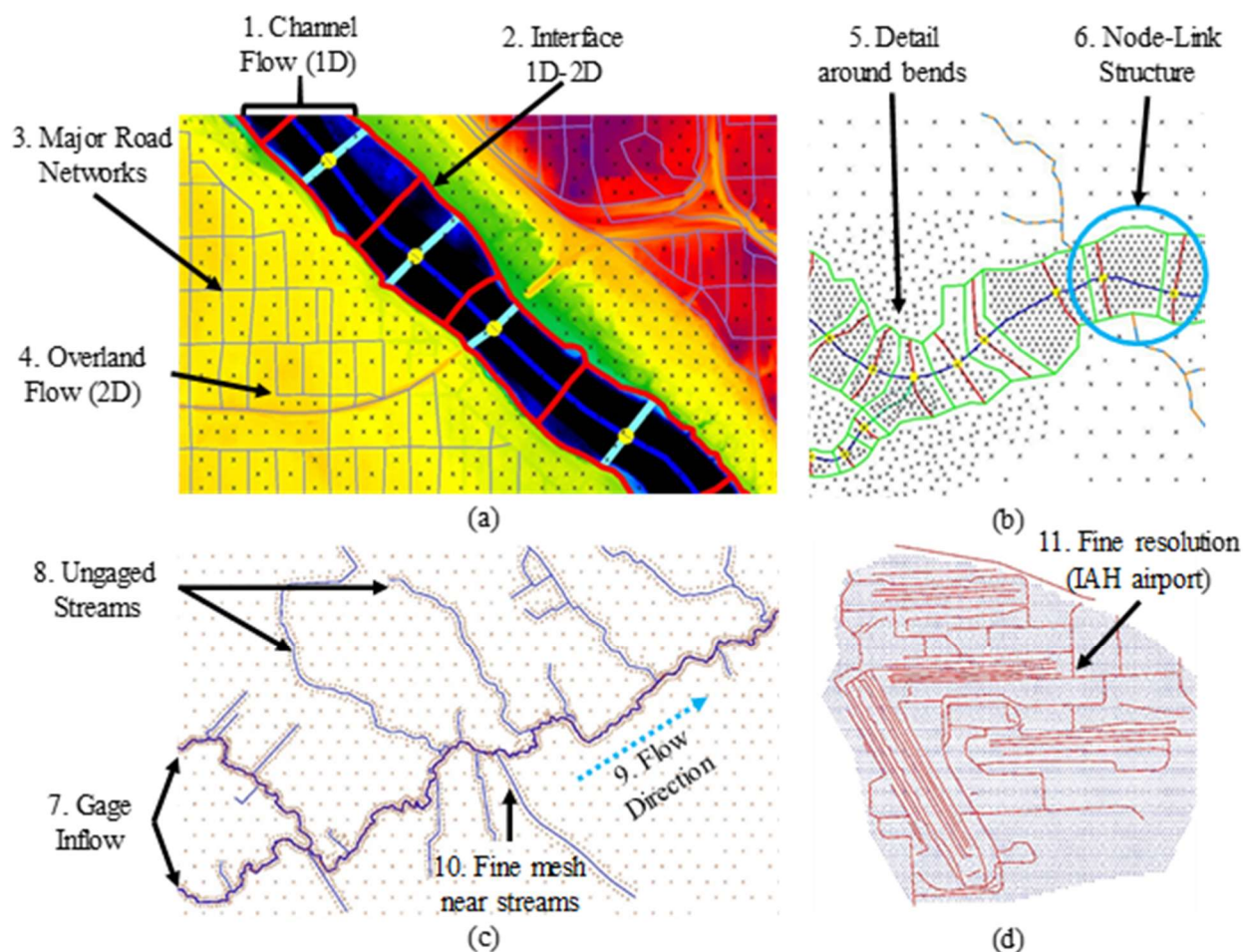


Fig. 5.4 Computationally-efficient model structure (1): 1D flow region inside the stream; (2) Interface between 1D and 2D regions usually along the levees; (3) road networks delineated as ‘breaklines’ to establish important topographic variations; (4) 2D overland flow region solved using diffusive wave equation; (5) location denotes example of flexible mesh structure where more vertices are placed near bends and confluences; (6) 1D node-link structure and cross sections along nodes denoting locations where energy equation is applied; (7) locations where USGS stream gage inflow is used as boundary condition; (8) ungaged streams inside subbasins where no gage information is available; (9) location denoting the direction of flow in the stream; (10) location denoting fine resolution mesh around the streams and coarser elsewhere; and (11) fine resolution (15-m) delineation of important features such as George Bush Intercontinental Airport (IAH) in Houston, TX

Additionally, essential features, both hydraulic and non-hydraulic are digitized for generating the mesh using a combination of the ‘breakline’ and ‘breakpoint’ features. Every ‘breakpoint’ is assigned a triangular vertex in the mesh as shown in Fig. 5.4. For example, the George Bush Intercontinental Airport (IAH) is located inside the model domain where the mesh resolution is refined to 15 m. Similarly, the mesh is refined around river bends and confluences where complex river-floodplain exchanges may take place during high flow conditions. After digitizing all essential features inside the model domain, the mesh resolution is further refined by applying an edge-length buffer for ensuring that the maximum edge-length is 457 m (1500 feet) inside the ‘*large*’ model, and approximately 229 m (750 feet) inside the ‘*small*’ model. Further, the mesh around the City of Houston (as shown in Fig. 5.5) for the ‘*small*’ model is further densified to enable a maximum edge length of 122 m (400 feet) in this region. While the mesh structure used in Chapters 2 – 4 contains a fixed resolution mesh in the floodplain (60-m) and outside the floodplain (300-m), the mesh structure in this study is completely flexible everywhere, and only a maximum triangular edge length is specified to ensure a minimum resolution.

In order to evaluate the performance of the proposed modeling approach in comparison to the traditional fixed mesh model, a third model, referred to as the ‘*small-fixed*’ model, with a constant edge length of 60 m, is created. The comparison with a fixed mesh resolution is only carried out with the ‘*small*’ model. While the 1D portion is unchanged for this model, a fixed resolution 2D overland flow region is used. Since these models are physically-based distributed models, mesh refinements not only result in finer resolution when simulating hydrodynamic fluxes, but also improve the resolution of hydrologic analysis by refining the honeycomb mesh, which reduces the individual surface area of the node where the mass balance equations are lumped. Fig. 5.5 presents the honeycomb mesh structure of the ‘*small*’ and ‘*large*’ model. Each polygon in the mesh acts as a hydrologic basin and the water is routed using the 2D diffusive wave equations in the overland flow region, while the 1D energy equation is used inside the streams. Fig. 5.5b also shows the cross-sections embedded inside the honeycomb mesh along the streams that are used for directing water from one node to the other.

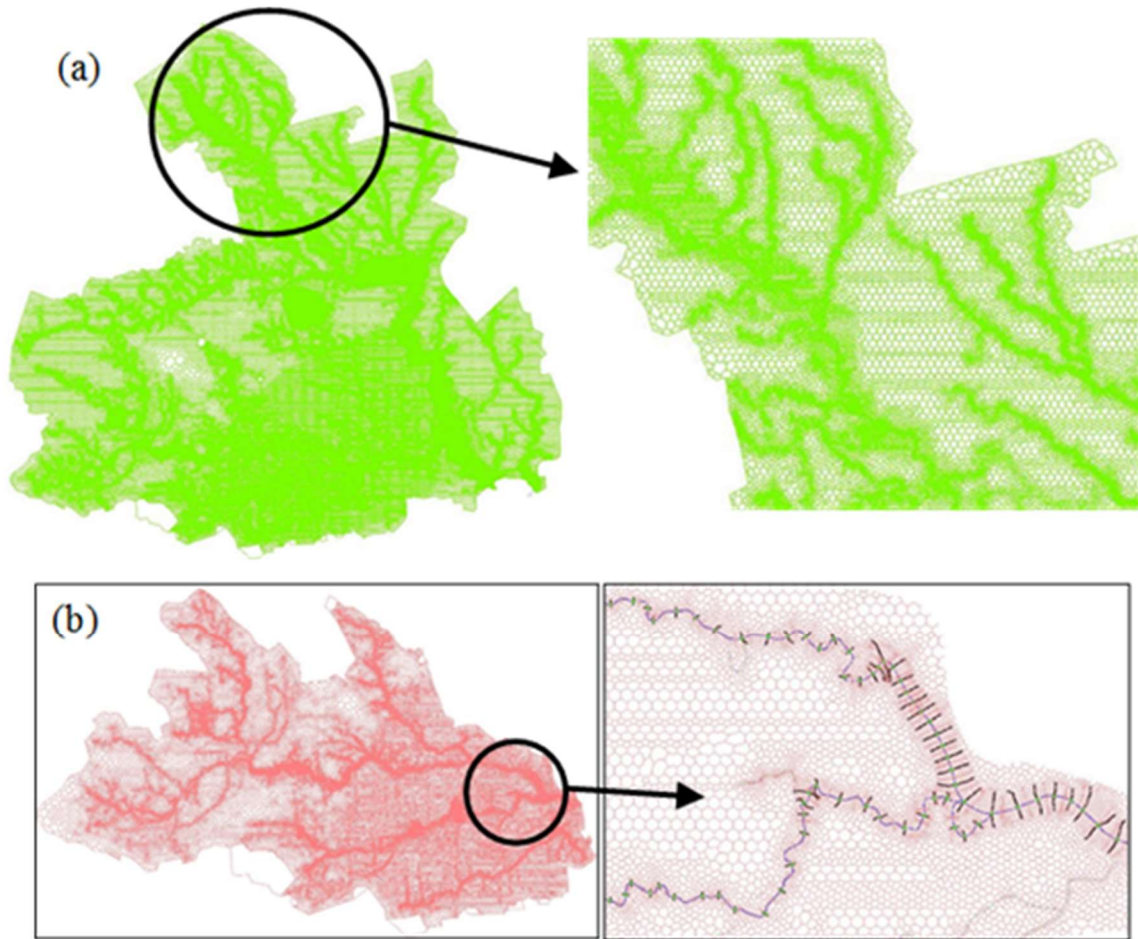


Fig. 5.5 Honeycomb mesh resolution across (a) *large* model and (b) *small* model

5.4.2 Model parameterization and numerical simulation

Table 5.2 presents the initial values of subsurface parameters that are classified based on soil zones. The gSSURGO database contains spatially distributed hydrologic soil group classification based on runoff potential and the four soil zones used in this study are based on this classification. The saturated vertical conductivity, moisture content at field capacity, and at wilting point (presented in Table 5.2) reflect the median values corresponding to the specific soil zones in the gSSURGO database. The other parameters require information on the soil texture percentages, which are also available from the gSSURGO database. Using the soil texture percentages, and the equations provided in Rawls (2004), the other subsurface parameters such as pore size index, soil matric potential, and residual moisture content are evaluated (Streamline Technologies, 2018). The initial values of Manning's roughness corresponding to the eleven land use classes in NLCD are adapted from Chow (1959).

All the models used in this study are simulated on Purdue University’s Halstead cluster using only one computational node containing two 10-core Intel Xeon E5 processors (20 cores @ 2.6 GHz) to aid a consistent comparison. The triangular, diamond and honeycomb meshes for all models are built on a 4-core Intel i-7 system with a processing speed of 3.7 GHz. Both the models are simulated for a continuous twenty-day period from 17th August 2017 to 5th September 2017. To provide a longer time for incorporating antecedent conditions in the models, the first six days are used as warm-up period, and the results are compared with the observed data from 23rd August to 5th September 2017.

Table 5.2 Initial values of subsurface parameters using in ICPR

Vadose Zone*	Soil Type	K _v (mm/hr)	Saturated MC	Residual MC	Initial MC	Field Capacity MC	Wilting Point MC	PSI	Ψ (cm)
Layer 1 90 cm (15 cells)	B	11.18	0.501	0.015	0.338	0.338	0.138	0.234	26.4
	C	6.28	0.458	0.051	0.300	0.300	0.225	0.296	59.2
	C/D	8.42	0.620	0.078	0.310	0.310	0.155	0.270	106.8
	D	4.14	0.430	0.109	0.339	0.339	0.239	0.161	197.9
Layer 2 60 cm (10 cells)	B	8.38	0.277	0.070	0.195	0.195	0.135	0.296	59.1
	C	4.98	0.398	0.068	0.255	0.255	0.148	0.271	106.8
	C/D	5.47	0.300	0.057	0.240	0.240	0.141	0.270	146.8
	D	3.34	0.330	0.045	0.120	0.120	0.090	0.161	197.9
Layer 3 30 cm (5 cells)	B	5.85	0.220	0.030	0.100	0.100	0.080	0.226	99.8
	C	1.57	0.180	0.040	0.110	0.110	0.110	0.161	197.9
	C/D	3.94	0.260	0.055	0.220	0.220	0.141	0.270	168.4
	D	1.48	0.170	0.040	0.090	0.090	0.080	0.161	197.9

The time-marching method for hydrodynamic iterations used in this study is based on a second order Runge-Kutta technique (modified Euler method) that varies the time step not only in time, but also spatially (Domingues et al., 2008). This method, referred to as the “FIREBALL” method in ICPR, involves establishing a set of time step levels at the beginning of a simulation based on the minimum and the maximum calculation times, with each successive level doubling in duration (Streamline Technologies, 2018). For more information, please refer to Appendix C. Table 5.3 presents the hydraulic simulation parameters for the models in this study. As mentioned earlier, a finer hydraulic time-stepping is used for the ‘*small*’ model comprising of a total of ten (10) time steps varying between 0.01 to 5.12 s while seven (7) time steps varying between 0.1 to

6.4 s are chosen for the ‘*large*’ model. The same hydraulic time steps are used for the ‘*small*’ and ‘*small-fixed*’ models as shown in Table 5.3. The hydrologic time steps are static and set to five minutes (300 seconds) for all models which means that the hydrology runoff rates are simulated at the beginning and end of every 5 minutes and delivered to the appropriate surface node.

Since this study aims to simulate accurate flood hydrodynamics through minimal parameter calibration, the initial hydrologic parameters are not calibrated across simulation trials. For the first iteration, the channel roughness across all channels is assumed to be 0.035, and no hydraulic structures are incorporated in the model. For the second iteration, hydraulic structures such as weir overflows, drop structures, lakes and ponds are incorporated in the model. Since channel roughness varies with distance from upstream to downstream in natural streams, in the third iteration, channel roughness is varied from 0.045 to 0.025 using a fixed interval of 0.005 from the upstream to downstream in the natural channels. Finally, in the fourth iteration, the channel roughness across artificial streams is modified depending on the overprediction and underprediction of peak flood stage and time-of-peak. Even in this case, the channel roughness lies within the 0.025-0.045 range but is spatially variable across different subbasins in the model domain. Although it is possible to improve the results further using more iterations, only four parameter iterations are used in this study to maintain the computational efficiency of the modeling approach and produce optimal results without significant parameter optimization.

5.5 Results and Discussion

5.5.1 Evaluation of the computational efficiency of the proposed approach

Table 5.3 presents information on the computational parameters and simulation times for the ‘*small*’, ‘*large*’ and ‘*small-fixed*’ models. The model build process involves generation of the meshes required for simulation, intersection of all input datasets to extract model parameters, and assignment of nomenclature to mesh nodes and vertices, which is followed by the simulation of Hurricane Harvey. The model build time increases exponentially as the number of triangular increases from 221,807 for the ‘*small*’ model, followed by the ‘*large*’ (729,007), and ‘*small-fixed*’ (1,002,064). Although the ‘*large*’ model requires longer build time (19 hours) compared to the ‘*small*’ model (2 hours), the computation time for a 20-day simulation for the ‘*large*’ model is only 55 % more than the ‘*small*’ model even though the number of computational elements (mesh nodes)

is almost three times greater in the ‘*large*’ model. This is largely due to the relatively coarser spatial resolution and a larger time step range (0.1 s to 6.4 s) for hydraulic simulation in the ‘*large*’ model compared to the ‘*small*’ model (0.01 s to 5.12 s) although a smaller time step may lead to a higher accuracy, which is discussed in the next section.

Table 5.3 Computational elements and performance for ‘*small*’, ‘*large*’, and ‘*small-fixed*’ models

Computational Elements*	‘ <i>Small</i> ’ Model	‘ <i>Large</i> ’ Model	‘ <i>Small-Fixed</i> ’ Model
Model Area	1,459 km ²	5,342 km ²	1,459 km ²
No. of triangles in the mesh	221,807	729,007	1,002,064 3,319,546 (<i>large</i>)*
No. of 1D hydraulic links	463	2,424	463
No. of 2D hydraulic links	294,041	929,072	1,449,859
No. of hydrologic basin sub-polygons	263,259	921,494	930,093
Spatial resolution	9 m to 229 m	9 m to 457 m	60 m
Percent reduction in no. of triangles	77.8 %	78.0 % *	-
Hydraulic simulation parameters	0.01 to 5.12 s (10 time-steps)	0.1 to 6.4 s (7 time-steps)	0.01 to 5.12 s (10 time-steps)
Model build time	2.0 hours	19.0 hours	26.2 hours
Model simulation time (20-day run)	49.3 hours	76.3 hours	217.9 hours

*Based on the drainage area and the mesh structure, the number of nodes for the fixed-mesh ‘*large*’ model at 60-m resolution are estimated to be over 3.3 million, and therefore, the percentage reduction in the number of nodes using the flexible mesh approach for the ‘*large*’ model is 78 %. It should be noted that these values are hypothetical and the fixed-mesh ‘*large*’ model is not built in this study.

The number of triangles required to build the ‘*small-fixed*’ model at a 60-m edge length is approximately five times the number of triangles in the ‘*small*’ model. Considering the hydraulic time-steps are the same for both models, the simulation times for the ‘*small-fixed*’ model are approximately 4.5 times greater than the ‘*small*’ model, highlighting the increase in computational-efficiency using the proposed approach. Similarly, the number of triangles required for the ‘*large*’ model following a fixed mesh structure are estimated (hypothetically) to be five times the number

of triangles using the proposed approach, enabling a reduction of 78 % in the number of triangles and improving computational efficiency. In addition to the reduction in the number of computational elements, a flexible mesh structure also enables more detail (9-m minimum edge length) in essential locations compared to a fixed mesh (60-m edge length everywhere).

5.5.2 Comparison of modeled stages across scales

The HCFCD provides instantaneous daily stage measurements across several gages located inside the modeling domain, which are used to compare the performance of the models. It should be noted that the comparisons with observed data are not only made at watershed outlets but, unlike previous studies, the model performance is evaluated at multiple locations inside the study area, thereby, providing a more realistic spatial outlook on the model performance, which is crucial for accurate flood simulation. As mentioned in the Section 5.4.2, the predicted stages result from only four model iterations. The comparisons with observed stage are carried across 16 gages located inside the ‘*small*’ model domain (1,459 km²) and the results for the performance of both the ‘*small*’ and ‘*large*’ model are presented for six (6) out of sixteen (16) gages in Fig. 5.6. In the case of the ‘*large*’ model, comparisons were made across 14 additional gages and the results for 10 out of 14 of those gages are presented in Fig. 5.7 and 5.8. Therefore, stage comparisons are made for a total of 30 gages inside the ‘*large*’ model (5,342 km²). The modeled stage versus observed stage across all other gages (not reported here) for both models can be found in the Appendix D.

The modeled stage comparisons with observed data (Fig. 5.6) show that the performance of the ‘*small*’ model across all gages is accurate, except for the slight underprediction at the Buffalo Bayou at San Felipe Drive. In this case, the gage is located downstream of two highly sinuous river bends, which may have resulted in reduced performance. The overprediction during the recession limb of the hydrograph at Brays Bayou and Sims Bayou for the ‘*large*’ model (Fig. 5.6) may be caused by the inaccuracies in simulating the hydraulic interactions at the confluence of these streams with the HSC. Therefore, the difference in the performance between the ‘*small*’ and ‘*large*’ model can be attributed to the difference in the minimum time step for hydraulic simulation (0.01 s for ‘*small*’ versus 0.1 s for ‘*large*’). Since the geometry of these streams is relatively small and the change in conveyance is significant during Harvey, the prediction at these locations can be improved using a higher spatial resolution and finer hydraulic time-steps. Although a larger time step improves the computational time for the ‘*large*’ model, it can reduce the accuracy, especially

at confluences, where a smaller time step may be more suitable for capturing the flood hydrodynamics accurately. However, considering that the peak stage is predicted accurately across 5 of the 6 gages, the overall performance of the ‘*large*’ model is satisfactory. Further downstream, the performance of the ‘*large*’ model across deeper and wider streams such as the Hunting Bayou, Halls Bayou and Greens Bayou (Fig. 5.7b) is more accurate compared to the Sims Bayou (Fig. 5.6). Since these streams have a relatively larger channel geometry, they are affected by change in conveyance to a lesser extent compared to smaller streams like Sims Bayou, resulting in a better prediction even with a large hydraulic time-step.

The overall performance from Fig. 5.6 and 5.7b suggests that the proposed modeling approach used in this study produces robust estimates of flood stage even for unprecedented (1000-year) flood events. However, the performance of the ‘*large*’ model upstream of the Lake Houston reservoir at Luce Bayou (Fig. 5.7a) is less accurate as shown by the overprediction of stage. The overprediction at Luce Bayou, which is draining directly into Lake Houston is caused due to the lack of operational data on the outfall structure of the reservoir resulting in an incorrect estimation of the weir overflow from Lake Houston. The performance of the ‘*large*’ model upstream of the Lake Houston reservoir can be improved by accurately modeling the reservoir operations, which is a location-specific issue, and beyond the scope of this study. Alternatively, the lack of knowledge about the reservoir operation can be addressed by incorporating boundary conditioning through 1D nodes upstream and downstream of the reservoir, which has recently been tested by Hwang et al. (2019). The upstream boundary condition node can be used to remove the weir overflow from the reservoir by providing an infinite sink and the downstream node can be used as an input to downstream model domain using gage inflow.

The results presented in Fig. 5.8 show that it is possible to simulate accurate flood stage for ungaged streams without any known upstream boundary inflow using an integrated modeling approach. The stage comparisons are made at the downstream end of these streams and flood hydrodynamics is simulated using only rainfall as an input. The hydrologic parameters for these subbasins are uncalibrated and obtained directly from freely available data sources. The performance at ungaged basins can be further improved by modifying the hydrologic parameters, which would require additional simulations.

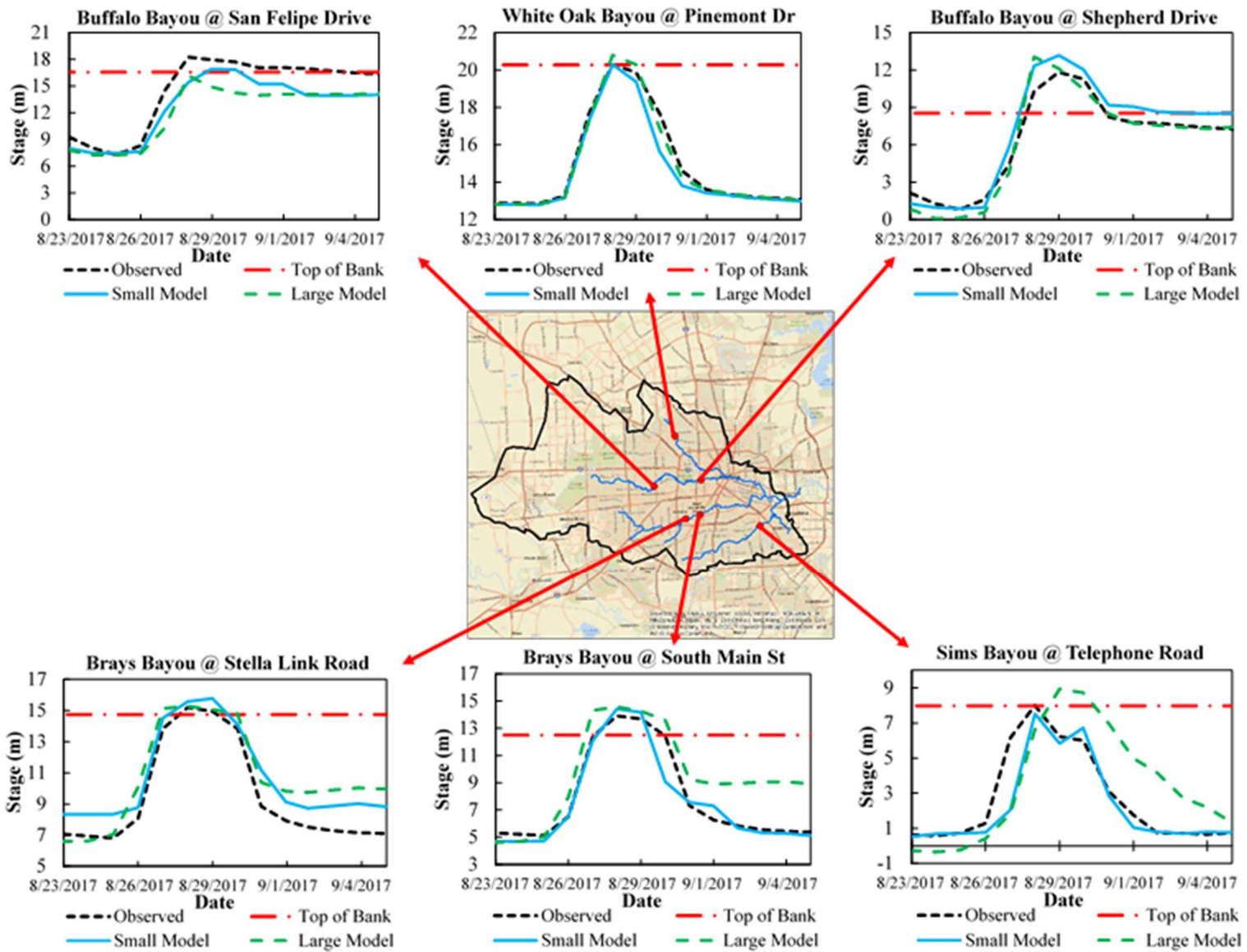


Fig. 5.6 Stage comparisons with observed data for *small* and *large* model across HCFCD gages

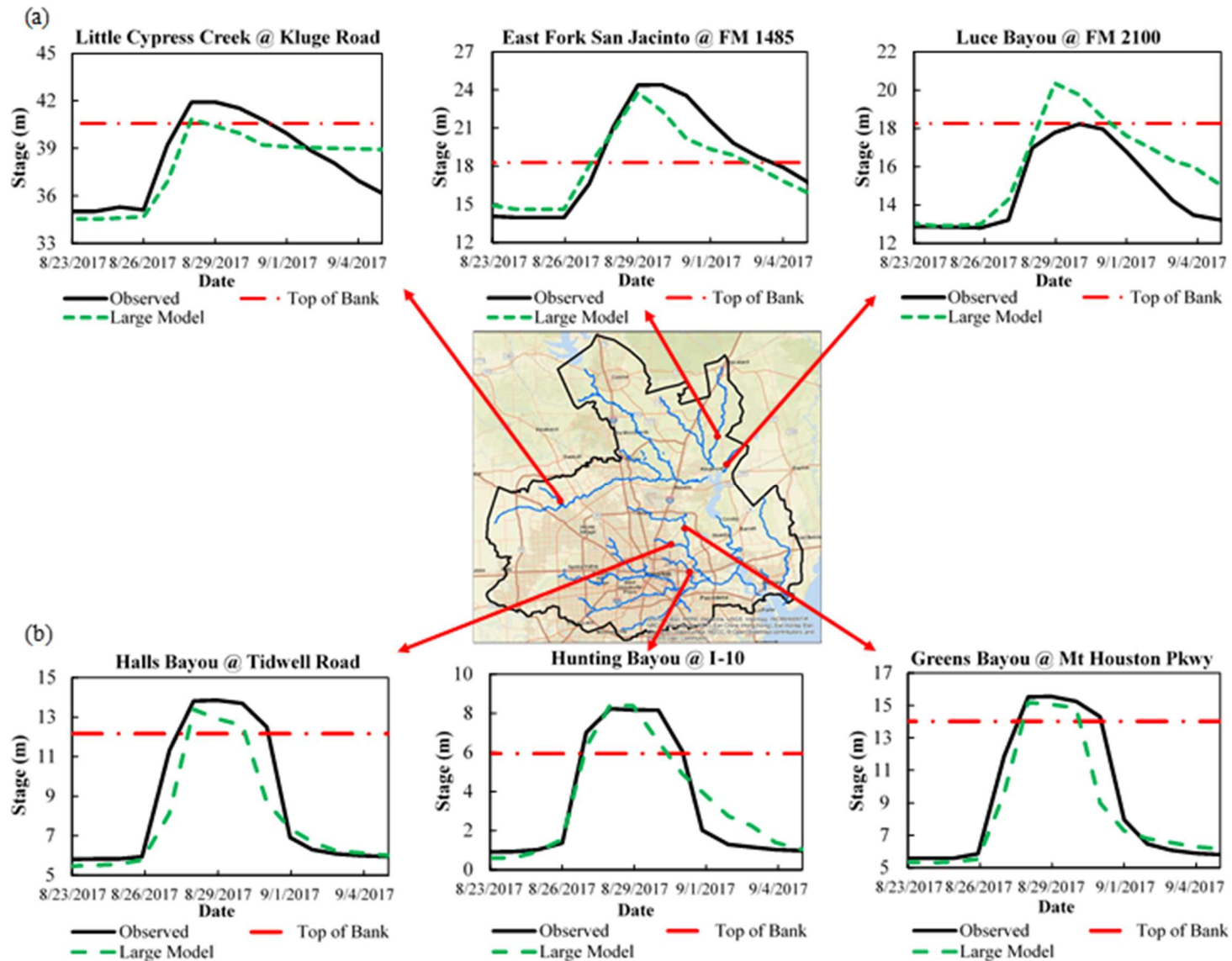


Fig. 5.7 (a) Stage comparisons at gages upstream of Lake Houston; (b) stage comparisons for streams draining into the HSC for *large* model

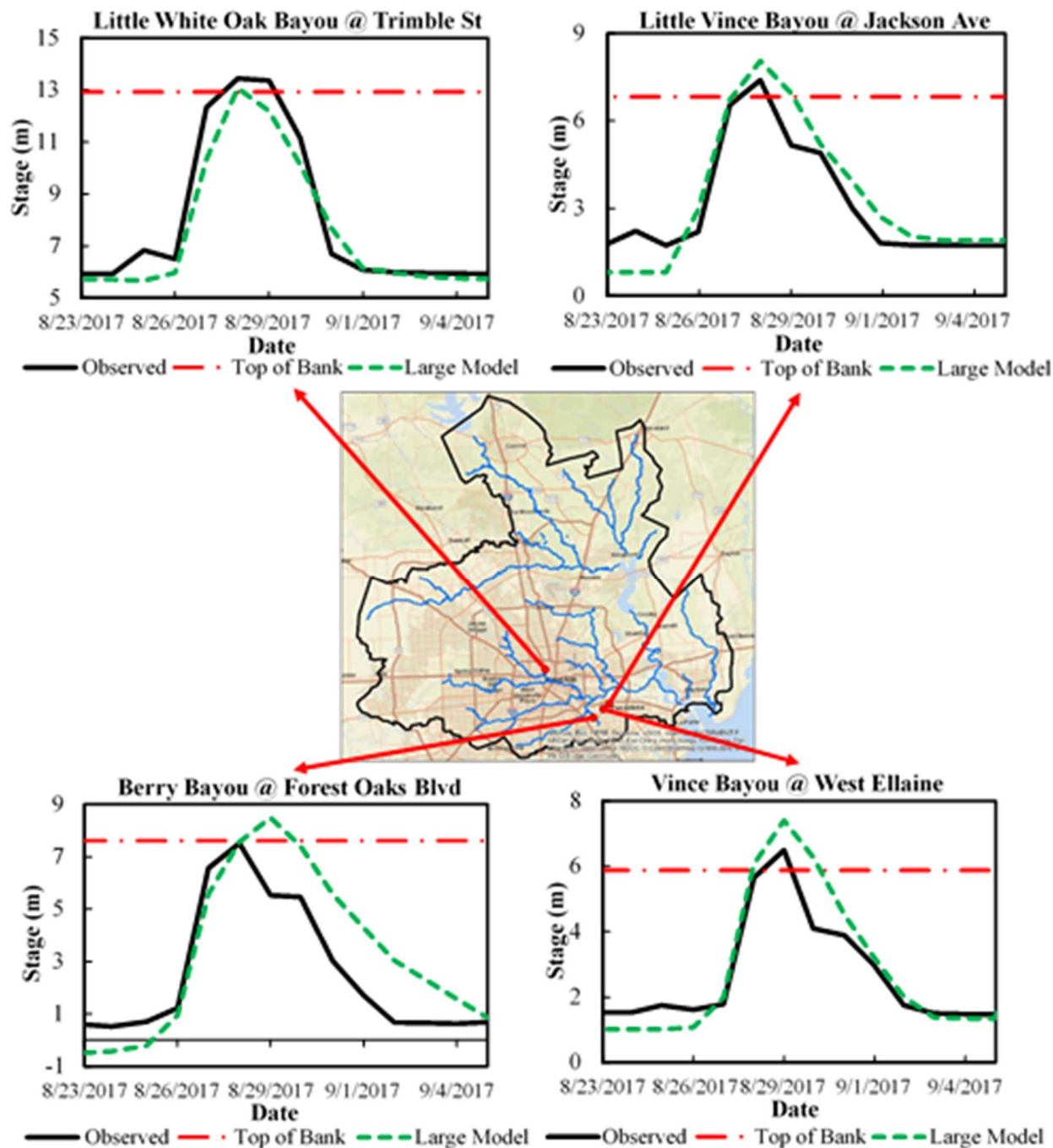


Fig. 5.8 Stage comparisons at streams without upstream gage inflow (fully-distributed rainfall-runoff-routing)

5.5.3 Statistical evaluation of model performance

Fig. 5.9a to 5.9d present the scatter plots highlighting the overall performance of the ‘small’ and ‘large’ models across all locations. In order to evaluate the goodness of fit between the two models and HCFC D gage data, the coefficient of determination (R^2) is calculated across all

locations. While R^2 is used as a measure of linear trend, the slope parameter, which provides a measure of overprediction or underprediction of model outputs with increasing magnitude, is also evaluated. The slope about the line $Y=X$ for the water surface elevation (WSE) across both ‘*small*’ (0.96) and ‘*large*’ (0.98) indicates that there is minimal underprediction. The slope for the predicted depths for ‘*small*’ (0.90) and ‘*large*’ (0.95) indicates more severe underprediction in depths.

The R^2 for the ‘*small*’ model for both WSE (0.96) and depth (0.87) indicates highly accurate performance for flood simulation using the proposed approach for unprecedented (1000-year) flood events. While the R^2 for WSE (0.96) suggests a high accuracy for the ‘*large*’ model, the WSE is a scale-dependent parameter, and therefore, it is affected by the higher performance at the upper extremities for the ‘*large*’ model. The R^2 is lower for depth (0.79) highlighting the issue of inaccurate representation of reservoir storage and overflow through the Lake Houston reservoir resulting in a higher degree of variability in the depth estimates. The overall results highlight the applicability of the proposed approach across multiple spatial scales. Even with a coarser spatial resolution and larger hydraulic time-steps, the results are promising for simulating large scale flood events provided that accurate topographic information is available throughout the modeling domain.

Table 5.4 Median values of model performance statistics across all gages

Hydraulic Variable	Model	NSE	PBIAS (%)	RSR	Error in Peak Stage (%)
<i>WSE</i>	<i>small</i>	0.84	-2.1	0.39	-0.2
	<i>large</i>	0.75	+1.7	0.48	+2.4
	<i>small-fixed</i>	0.68	+0.3	0.54	-1.6
<i>Depth</i>	<i>small</i>	0.84	-6.9	0.39	-0.6
	<i>large</i>	0.75	+4.6	0.48	+4.9
	<i>small-fixed</i>	0.52	+0.4	0.67	-7.5

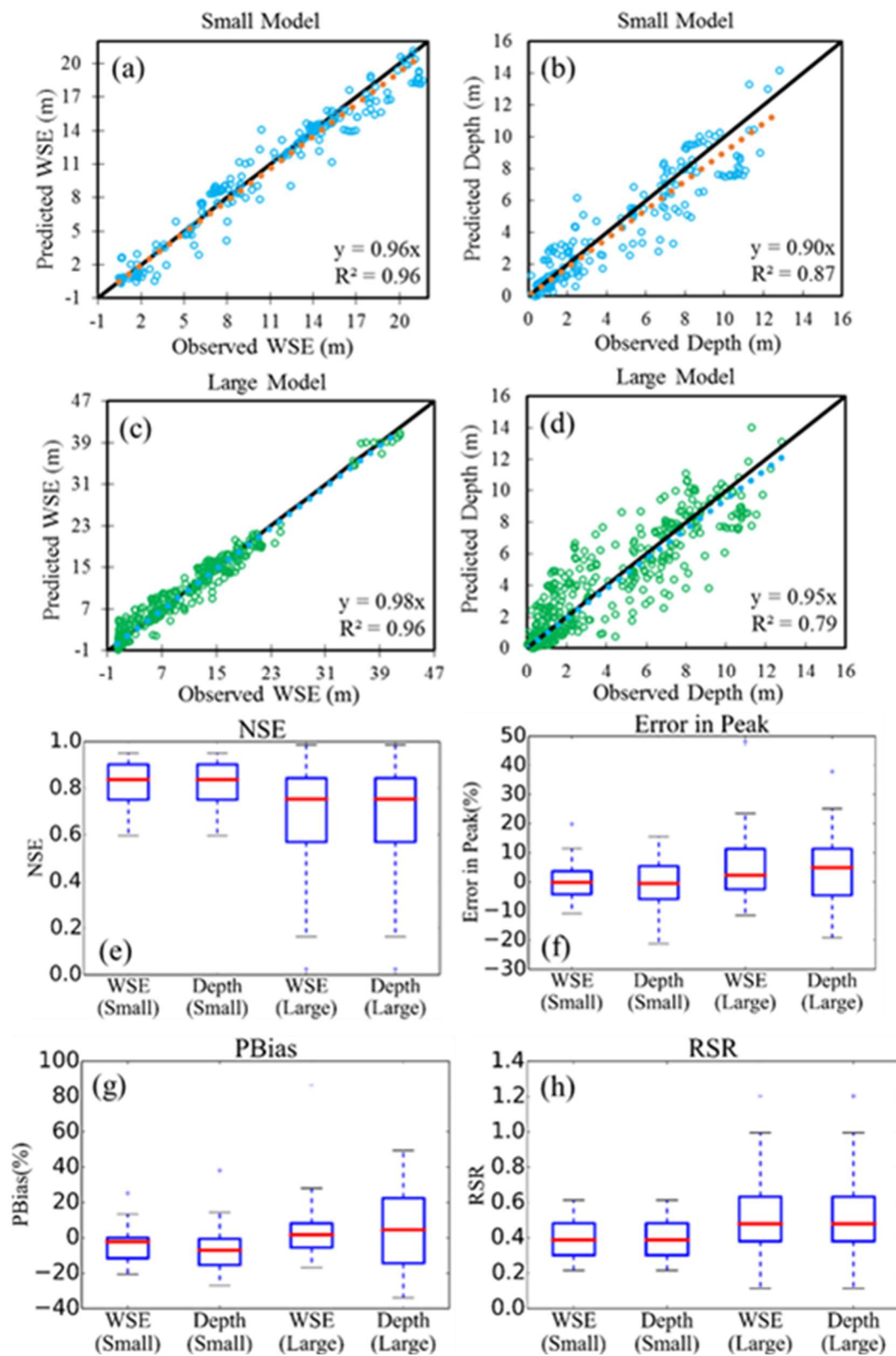


Fig. 5.9 Scatter plots of observed versus predicted WSE and depth for *small* and *large* model; and box plots showing the variability in model performance statistics across all gages

Similarly, the Nash-Sutcliffe Efficiency (NSE, Nash and Sutcliffe, 1970) which reflects the overall fit of a hydrograph, is also evaluated, and is represented by a box plot (Fig. 5.9e) highlighting its distribution across sites for WSE and depth. It is evident from Fig. 5.9e that barring a few outliers, the overall NSE distribution across locations is higher than 0.60 for a majority of gages in the ‘*large*’ model, with a median NSE of 0.75 as shown in Table 5.4. The NSE distribution and median value (0.84) suggests a higher accuracy across gage locations for the ‘*small*’ model. The Percent Bias (PBIAS, Sorooshian et al., 1993), a statistic used to measure if the average tendency of simulated data is larger or smaller than observed data (Gupta et al., 1999), also shows the high accuracy in simulating flood stages for both the ‘*small*’ and ‘*large*’ model. Even with a larger spread in the NSE distribution, the PBIAS for the ‘*large*’ model WSE is very small, indicating an overall acceptable performance with no systemic bias.

Further, the performance is also quantified by the percentage of error in peak stage prediction (Error in Peak Stage shown in Fig. 5.9f), as the peak stage governs the maximum inundation extents due to flooding. The small variability in the distribution of the error in peak stage and a median value of less than 5 % across both models indicate that the modeling approach is useful in predicting peak flood stages at multiple spatial scales. Finally, the RMSE-observations standard deviation ratio (RSR), which is a scaled-normalized parameter, is evaluated to estimate the variation in model residuals, and is represented in Fig. 5.9h and Table 5.4. The RSR values for both models show that the overall performance is satisfactory, however, the variability in performance across gages for the ‘*large*’ model is higher than the ‘*small*’ model.

5.5.4 Comparison of the proposed approach with a fixed-resolution approach

The stage comparisons across four gages presented in Fig. 5.10a to 5.10d suggest that the overall performance of the ‘*small-fixed*’ model is less accurate compared to the ‘*small*’ model, even though the overall build and simulation times (Table 5.3) are significantly higher. Although the overall spatial resolution for ‘*small-fixed*’ is finer (60 m) than ‘*small*’, a fixed resolution results in less detail at river bends and confluences, resulting in diminished performance across several gage locations, especially in Brays Bayou. The scatter plots (Fig. 5.10e and 5.10f) show the comparison with observed WSE and depths across all 16 gages and suggest a reduction in model performance using a fixed resolution. Except for the improved performance at the Buffalo Bayou

at West Beltway 8 (Fig. 5.10b), all other gages show severe overprediction or underprediction, especially during the receding limb of the stage hydrographs.

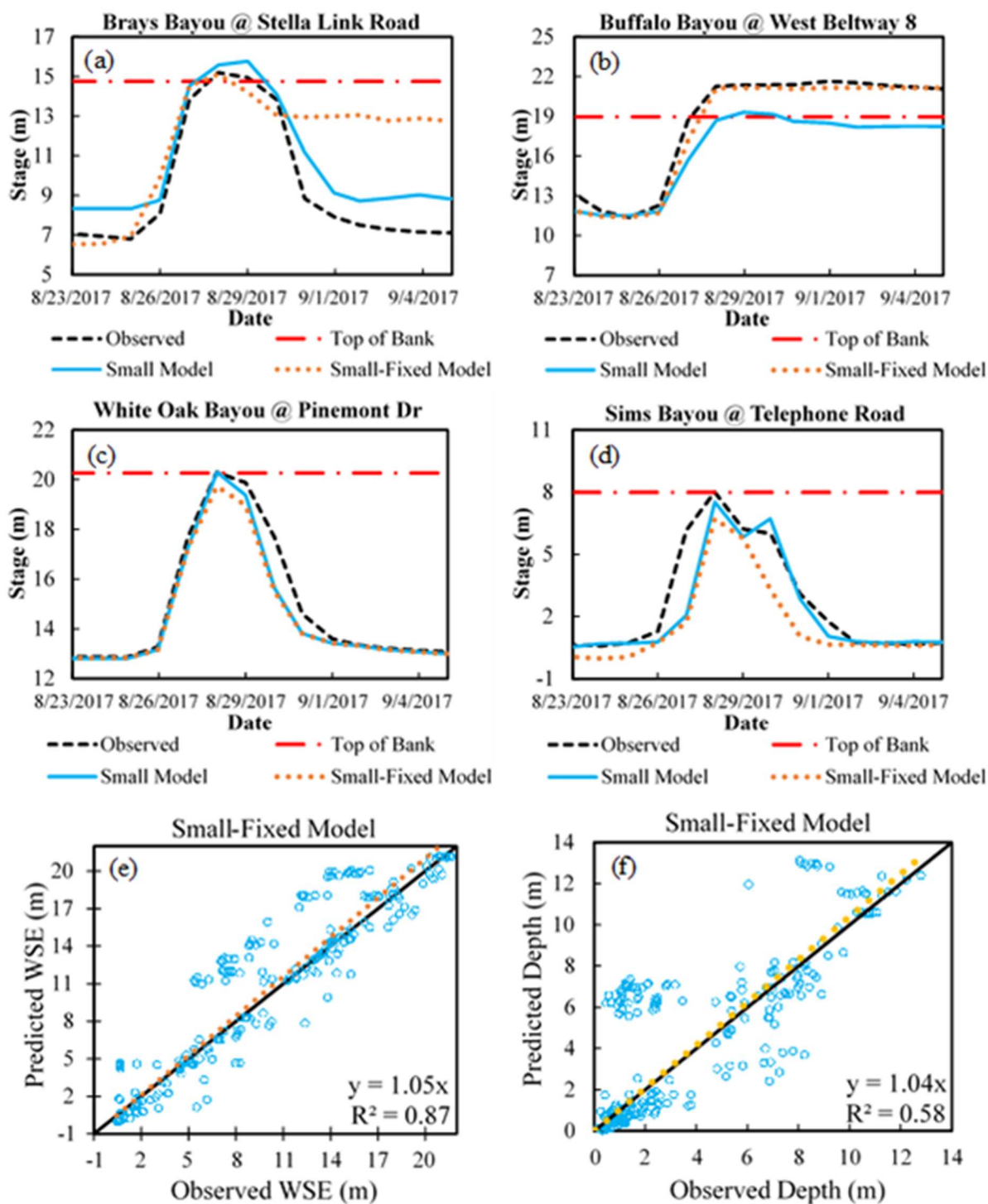


Fig. 5.10 Scatter plots showing the performance of the ‘*small-fixed*’ model in predicting WSE and depth

The variability in the percent bias across gages reduces the median bias for WSE (0.3 %) and depth (0.4 %), and results in slope values closer to one for WSE (1.05) and depth (1.04). However, the low R^2 of 0.58 (Fig. 5.10f) and median values of NSE (0.52) and error in peak stage (-7.5 %) for the depths (Table 5.3) across all gages highlight the reduction in performance using a fixed resolution approach. In order to improve the results across gages, the resolution needs to be reduced significantly, thereby, increasing both the build and simulation time further, which is infeasible for large scale flood modeling. While a fixed-resolution mesh is easier to construct, it is often developed using an automated algorithm without analyzing how it can affect interdependent physical processes. In these cases, important flow paths are often blocked off, and therefore, even an integrated hydrologic model at a fine resolution is unable to capture the actual hydrodynamics of the system. Since the flexible computational mesh provides the ability to control the mesh development, the important physical and hydraulic features can be incorporated in the model.

5.5.5 Assessment of flood inundation volumes and extents

The relative contribution from different hydrologic processes during Hurricane Harvey for the ‘*large*’ model is evaluated by dividing the volumetric contributions from individual processes by the watershed area (cm). Fig. 5.11a shows ‘*Precipitation*’, which is the cumulative rainfall for the entire area during the entire simulation period. A total of 76.2 cm of rainfall is estimated from the NLDAS rainfall data during the simulation, which is in addition to the streamflow through upstream gages at the boundary of the modeled area. The ‘*Subsurface Storage*’ is the stored volume inside the vadose zone during the simulation, with a maximum volume of 20.3 cm, which is approximately 26.6 % of the total rainfall. The ‘*Excess Rainfall*’ (shown in Fig. 5.11a) represents the hourly excess rainfall volume or direct runoff which is the amount of water that does not infiltrate into the vadose zone because of saturated conditions or impervious areas. Therefore, this represents the volume of runoff per hour that causes surface ponding and subsequent inundation. The maximum excess rainfall is simulated to be 55.7 cm which is approximately 73.1 % of the total rainfall. A high percentage of excess rainfall is resultant of a high percentage of impervious cover and the high intensity of rainfall during Harvey. The hydrologic volumes for the ‘*small*’ model are similar to the ‘*large*’ model, and hence, are not reported here.

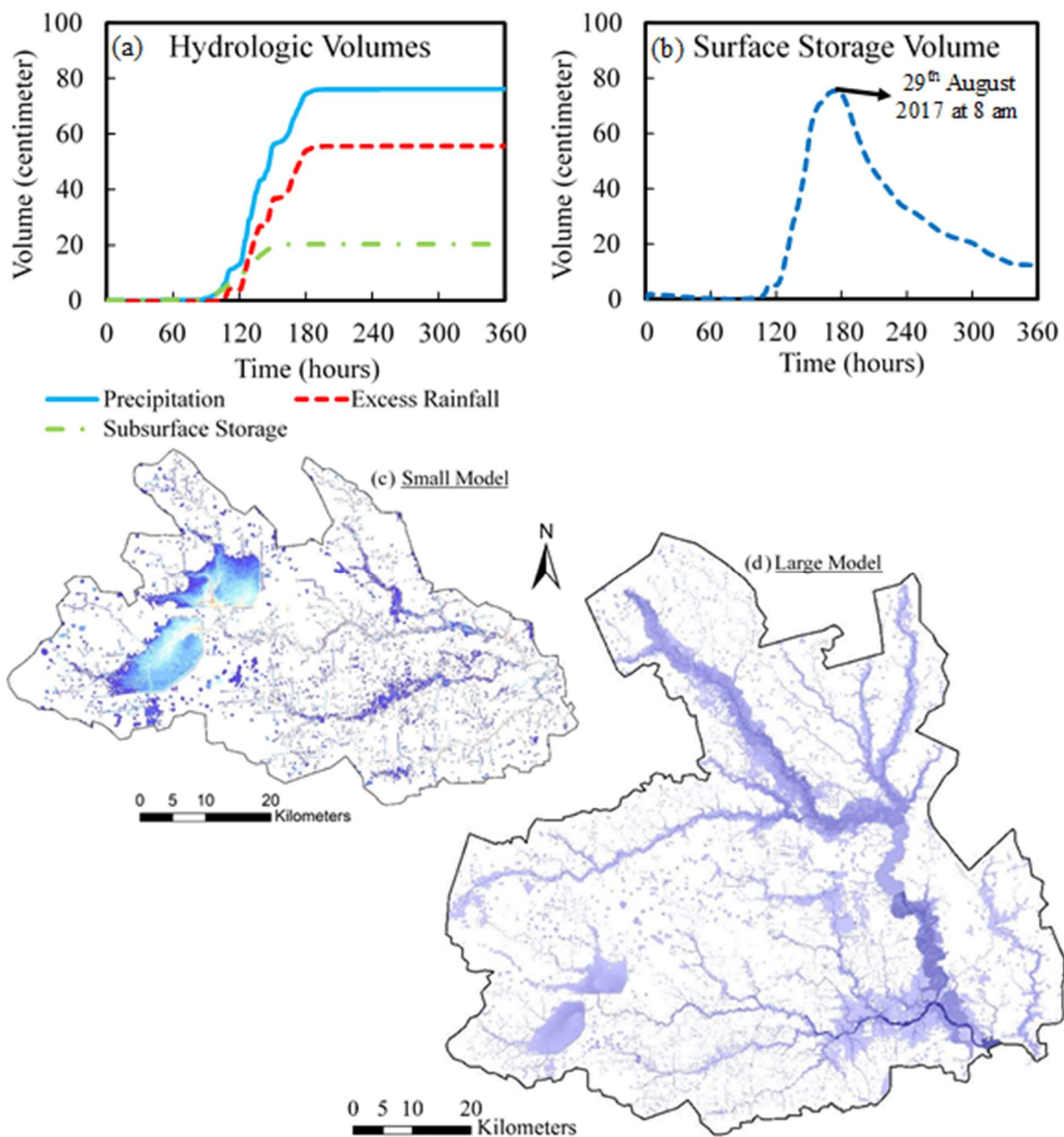


Fig. 5.11 Volumetric contributions from watershed processes scaled with respect to total area for (a) subsurface and (b) surface; and flood extent at peak surface storage volume for (c) *small* model and (d) *large* model

A high percentage of excess rainfall also signifies the importance of integrating rainfall-runoff (hydrology) with hydraulic modeling in the same system, as these effects cannot be accurately captured using loosely-coupled models. Additionally, the subsurface storage saturates within the first 40 hours of rainfall across the surface highlighting the intensity of the event. The

‘*Surface Storage Volume*’ provides an estimate of the increase or decrease in the surface water volume in the river-floodplain system for the entire model domain. The initial volume is assumed to be zero and the resultant peak surface volume (75.6 cm) is estimated on 29th August 2017 at 8 am (Fig. 5.11b) during the simulation.

Fig. 5.11c and 5.11d also present the peak flood extents across the two models at the instant of the peak surface volume. The flood extents are generated using a minimum inundation buffer of approximately 15 cm (6 inches), such that all regions with a minimum inundation of 15 cm are marked as flooded. Based on the flood extents and the stage results reported earlier (Fig. 5.6 and 5.7), it is evident that there is an overprediction in the floodplain of the HSC, which is likely due to the lack of operational data on the outfall structure of the reservoir causing an incorrect estimation of the weir overflow from Lake Houston. The simulated flood extents highlight the advantage of the proposed modeling approach as the flooding is predicted not only in the river-floodplain, but throughout the entire model domain. Therefore, in addition to the riverine flooding, subsurface saturation-induced surficial ponding and inundation across road networks is also predicted.

The flood extents generated from the ‘*large*’ model are also compared against observed aerial images during Hurricane Harvey to identify if the model can reasonably predict flooding in these locations. Fig. 5.12 presents the predicted flood extents overlaid on aerial imagery (Source: ESRI World Imagery) on the left, and images showing observed inundation during Hurricane Harvey on the right. The arrows marked in red, yellow or green across both images represent the same location. For example, the location in Fig. 5.12c marked in red represents bridge overtopping as the depth gradient in the flood map changes. The location marked in yellow in Fig. 5.12c shows the inundation at the West District WWTP which is also inundated in the aerial image observed during Hurricane Harvey. Finally, the location marked in green in Fig. 5.12c shows inundation below the bridge. This is not shown in the aerial imagery as it is below the bridge, while in the model prediction, the DEM is hydro-burned and predicts inundation below the bridge. The results (Fig. 5.12b) also suggest that the predicted flood maps can capture the inundation in the river floodplain and across road networks.

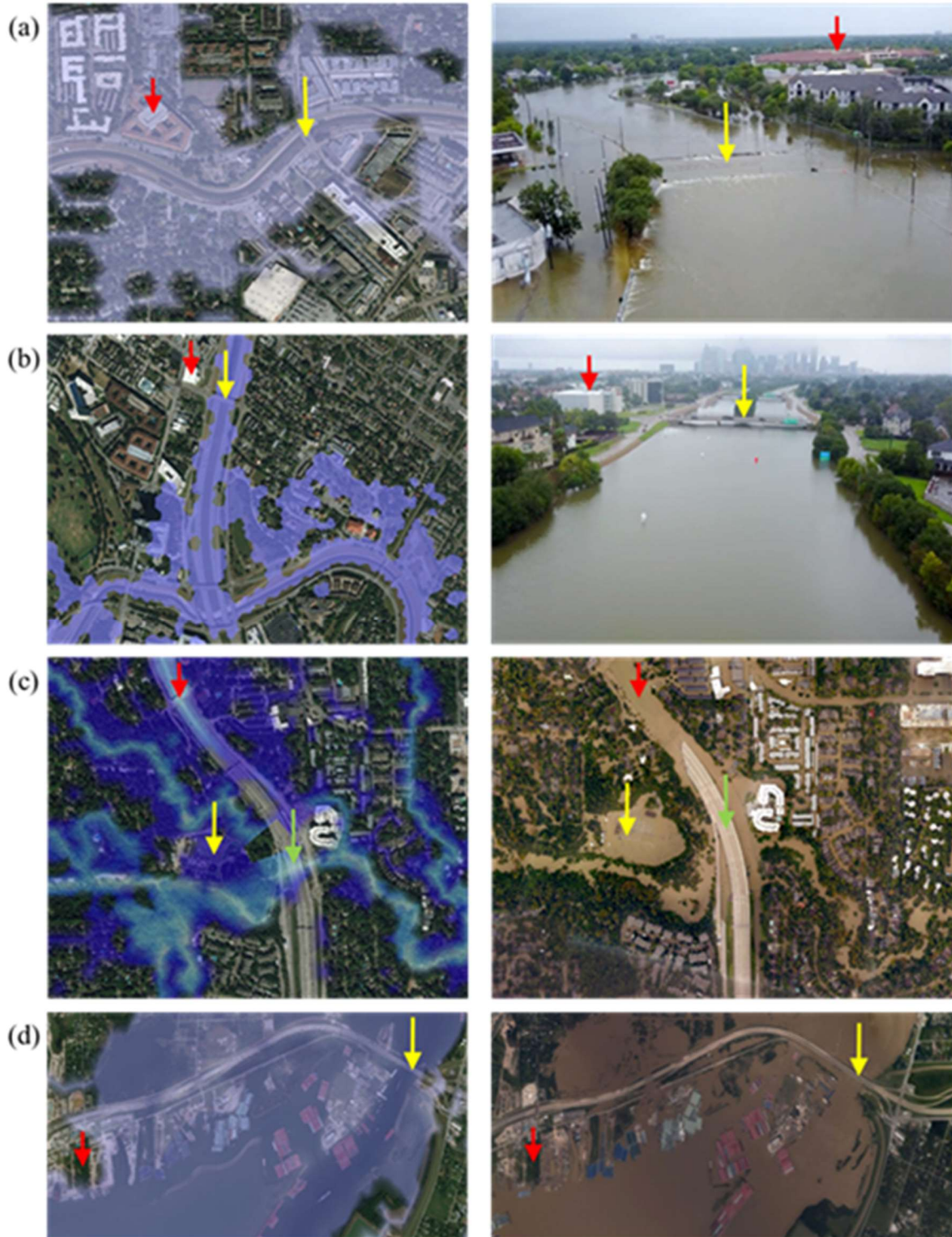


Fig. 5.12 Qualitative assessment of predicted flood inundation extents across four locations: (a) North Braeswood Boulevard, Houston, TX ; (b) South Freeway towards downtown Houston; (c) West District Waste Water Treatment Plant (WWTP); and (d) San Jacinto River – Houston Shipping Channel Confluence at Lynchburg, TX (Image source: Fig. 5.12a and 5.12b: <https://www.washingtonpost.com/graphics/2017/national/harvey-photos-before-after/> and Fig. 5.12c and 5.12d: <https://storms.ngs.noaa.gov/storms/harvey/index.html>)

Since a quantitative assessment of the flood extents using aerial imagery across the entire domain is not possible due to the unavailability of observed flood extents for such a large region, the flood depths and extents are validated by comparing the modeled extents with observed data at specific locations as shown in Table 5.5 and Fig. 5.13. The observed flood locations are determined by the FEMA Building Damage Assessment dataset which provides depth of inundation across residential and manufacturing structures located throughout the modeled area. The flood depths and extents are compared with this dataset for both the ‘*small*’ and ‘*large*’ model. The performance of modeled flood extents is evaluated by measuring whether the models predict flooding at locations where the FEMA-derived dataset reports inundation. Therefore, the performance is measured as a percentage of total inundated locations (points) where flooding is observed as shown in Table 5.5. Further, the flood depths obtained from both the models are compared with observed depths at these locations and the performance is evaluated as the error in depth prediction (m) and a histogram is created showing the distribution of error in depth prediction (m) across all locations as shown in Fig. 5.13.

Table 5.5 Quantitative assessment of flood extents with the FEMA Damage Assessment dataset

Model*	Total Number of Points	Percentage of total points		
		True Positive	False Positive	False Negative
<i>Small</i>	23,142	95.5	0.7	3.8
<i>Large</i>	66,786	97.1	0.7	2.2

*True positive means that the location is marked as flooded by both model and reference dataset. False positive means that the model predicts flooding where the reference data shows no flooding. Finally, false negative means model predicts no inundation at a location which is flooded in the reference dataset

The flood extent assessment from Table 5.5 shows a high correlation between the inundated points for both ‘*small*’ (95.5 %) and ‘*large*’ (97.1 %) when compared to observed inundation. This suggests that the models are able to capture flooding across several discrete points accurately. In addition to flood extents, the ability to predict depth of inundation accurately is crucial as it determines the risk of structural damage due to flooding. Fig. 5.13 suggests that there is severe overprediction (error in depth > 3.5 m) in depth estimates for 6.8 % points across the ‘*small*’ model and 6.4 % points across the ‘*large*’ model. However, both models provide satisfactory performance (-1.5 m < error in depth < 1.5 m) across 82.2 % (‘*small*’) and 79.4 %

(‘large’) points in estimating flood depths. Therefore, in addition to accurately predicting flood inundation across a majority of the locations, the models are also able to provide a reasonable performance in capturing the depth of inundation.

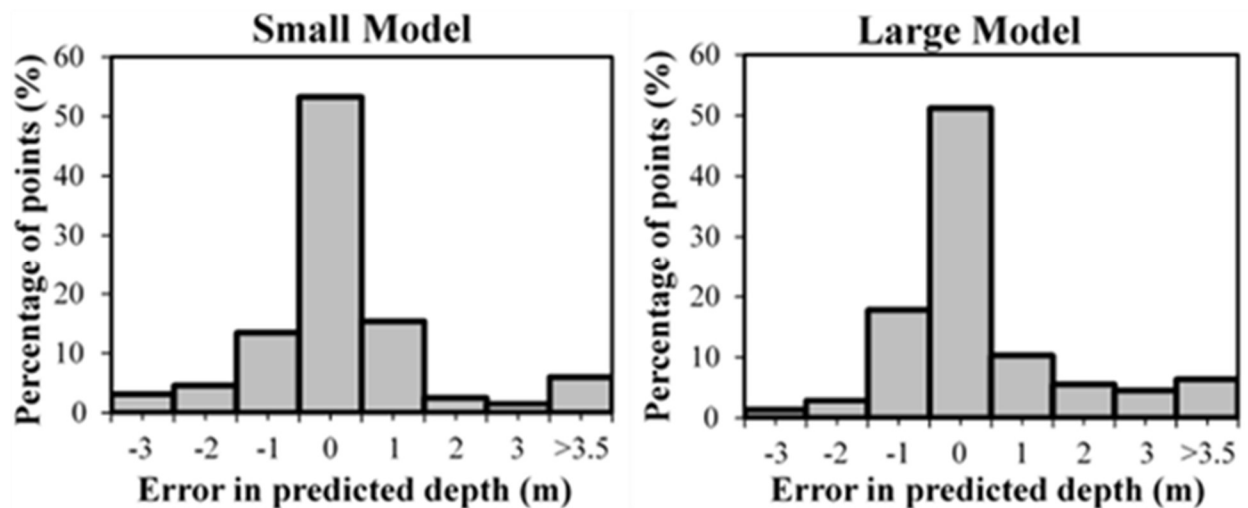


Fig. 5.13 Histogram depicting the percentage of points against the error in predicted depth for *small* and *large* model

5.5.6 Importance of inclusion of local hydraulics of urban systems

As mentioned in Section 5.4.2, the first model iteration is carried out without incorporating hydraulic structures, therefore, local hydraulic effects within a large scale system are ignored. The links shown in Fig. 5.14 are color coded in the aerial image identifying their location and direction of flow from the Brays Bayou. Links 1, 2 and 3 show the inflow and outflow from a location along the Brays Bayou when the lake is modeled as a 2D region and the weir overflow from the detention pond is ignored. When local hydraulic effects of urban systems such as river-lake fluxes, levee overtopping, and weir overflow are not incorporated accurately, the flow from the channel enters the lake through ‘*Link 1*’, exits the lake, and moves back into the channel through ‘*Link 2*’. This causes negative flow along the channel and the resultant flow (‘*Link 3*’) is significantly lower than expected.

However, when the lake is represented as a level-pool, the levee along the channel is delineated and used as the 1D-2D channel boundary, and the overflow from the detention pond is modeled as a broad-crested weir overflow, the resultant flow (‘*Improved Flow*’) at ‘*Link 3*’ is much more accurate. The improved flow results in accurate stage prediction downstream of this location

as shown in Fig. 5.6 at the gage, Brays Bayou at Stella Link Road. This result suggests that accurate representation of local hydraulics is essential even for 1000-year flood events, and these hydraulic effects are usually ignored when implementing only 2D flood modeling using a grid-based model structure.

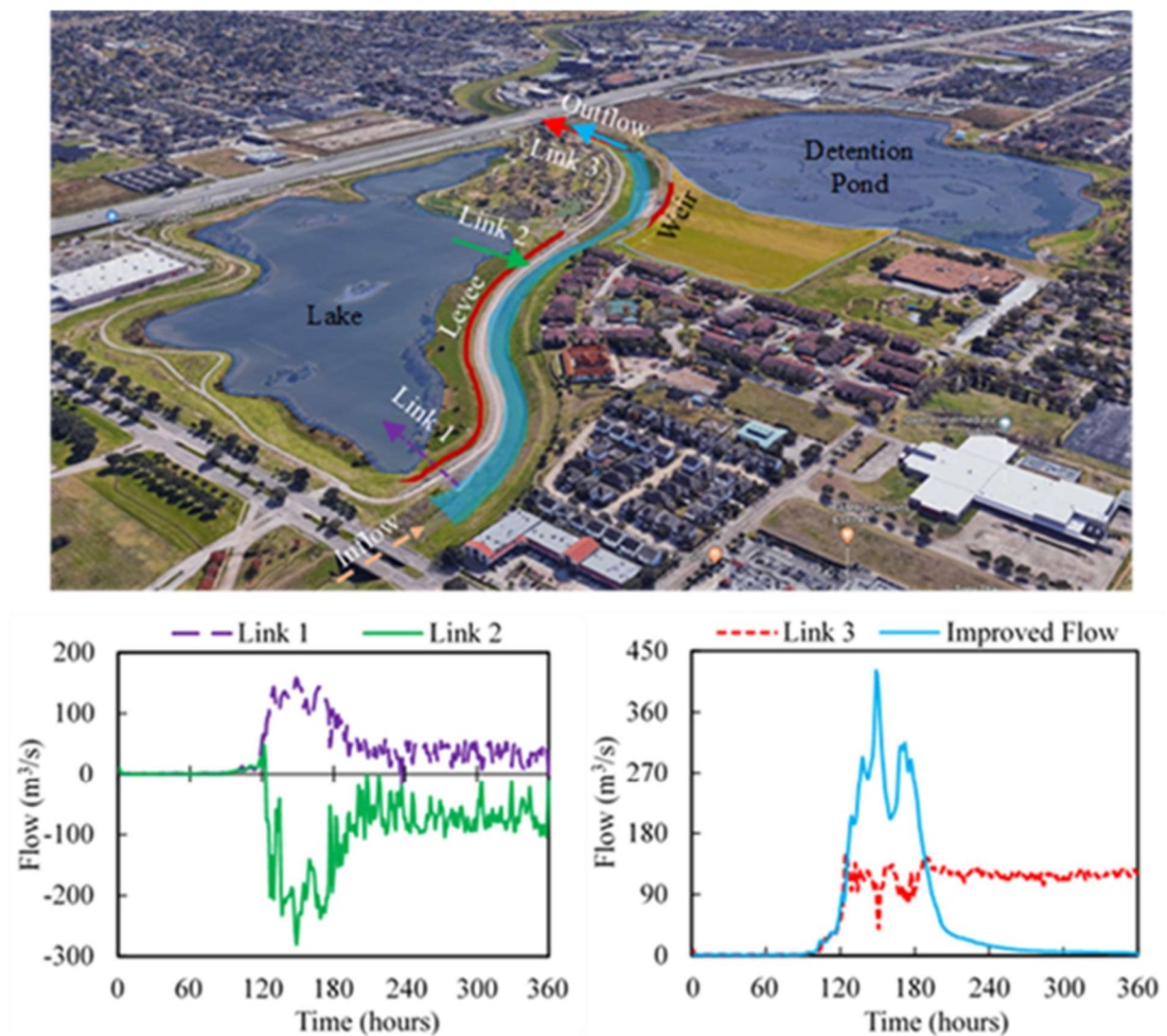


Fig. 5.14 Illustration of the effect of local hydraulics along the Brays Bayou (Image source: <https://www.google.com/maps>)

5.6 Summary and Conclusions

The existing methods for simulating the hydrology and hydrodynamics of large scale unprecedented events across complex urban systems are affected by a range of issues including the balance between spatial scale vs resolution, integration of physical processes and their

interactions in a single system, large scale computational inefficiency, and incorporation of essential hydraulic and non-hydraulic features. Due to these issues, the traditional tools may not be useful in simulating the complex hydrology and hydrodynamics of urban systems that include several managed systems, man-made channels, canals, reservoirs, riverine-coastal interactions and spatial heterogeneity in land use. While integrated models that can capture the hydrology and hydrodynamics in a single system are promising in simulating these complex processes, their application to large scale flood mapping and forecasting remains challenging without compromising on spatiotemporal resolution, spatial scale, model accuracy, and local-scale hydrodynamics.

For capturing the flood hydrodynamics of unprecedented events (> 500 -year return period) at large scales using integrated models, it is essential to develop techniques that can address these issues while maintaining computational efficiency. This study presents a physically-based but computationally-efficient approach for modeling unprecedented flood events at large scales in complex urban systems. The application of the proposed approach results in accurate simulation of large scale flood hydrodynamics which is shown using Hurricane Harvey as the test case. The results also suggest that the ability to control the mesh development using the proposed flexible model structure for incorporating important physical and hydraulic features is as important as integration of distributed hydrology and hydrodynamics. Following are the conclusions drawn from this study:

1. The application of the flexible-mesh structure, 1D channel and 2D overland flow, efficient study area delineation, and incorporation of urban hydraulic and non-hydraulic features results in approximately eighty percent (80 %) reduction in the number of computational triangles (*'small'* and *'large'*) compared to a fixed resolution model at 60 m edge length (*'small-fixed'*). This, in-turn, reduces the simulation times for Hurricane Harvey by approximately 4.5 times even when the hydraulic time-steps (0.01 to 5.12 s) are unchanged. Therefore, the proposed approach results in significant improvement in the computational efficiency for large scale models.
2. A statistical comparison with observed data across several gage locations for both *'small'* and *'large'* models signifies the ability of the proposed approach in providing optimal flood simulation at multiple spatial scales. For example, the median error of less than 5 % in predicting peak stage and depth across both *'small'* and *'large'* models highlights the

accuracy in performance. Further, the evaluation of model performance is not only carried out for WSE (stage), but also for flood depth, which is crucial in identifying the degree of risk and damage during large scale events, thereby, providing a more robust comparison with observed data.

3. The relatively higher accuracy obtained for the '*small*' model (finer resolution and smaller hydraulic time-steps) compared to the '*large*' model (coarser resolution and larger hydraulic time-steps) highlights the importance of a finer spatial resolution at river confluences and a finer hydraulic time-stepping for accurately modeling the recession limbs of the hydrographs. The results also validate the application of a variable hydraulic time-stepping for improving computational efficiency.
4. The optimal prediction across four ungaged streams highlights the applicability of the proposed modeling approach in estimating accurate flood stages directly from rainfall with minimal calibration when streamflow information is not available.
5. A quantitative assessment of flood extents with the FEMA Damage Assessment dataset suggests that both '*small*' (95.5 %) and '*large*' (97.1 %) models are able to capture flood inundation across spatially distributed building locations accurately. Further, both models provide satisfactory performance ($-1.5 \text{ m} < \text{error in depth} < 1.5 \text{ m}$) across 82.2 % ('*small*') and 79.4 % ('*large*') locations in estimating flood depths.
6. The improvement in flow characterization after incorporating urban hydraulic effects as illustrated on Brays Bayou highlights the impact of local hydraulics in influencing flood hydrodynamics even for unprecedented events. While these hydraulic effects are usually ignored in large scale 2D flood modeling, using the proposed model structure enables accurate representation of these effects as more detail is incorporated at these locations without reducing the overall computational efficiency.
7. Comparison of the computationally-efficient '*small*' model with the '*small-fixed*' model in predicting flood stages suggests that a fixed-resolution model cannot capture the hydrodynamic variability of unprecedented events in complex urban systems without increasing the spatial resolution, and subsequently, increasing the computational burden significantly.

6. SYNTHESIS

6.1 Summary

One of the earliest blueprints on physical process integration in models by Freeze and Harlan (1969) highlighted five major issues: (1) accurate representation of physical processes through mathematical formulations; (2) accurate estimation of hydrologic parameters at high spatial resolution; (3) continuous simulation of processes and their relationships within the system represented by the models; (4) spatiotemporal scalability of models and applicability across a range of hydrological and geographic conditions; and (5) computational efficiency for simulating large scale process dynamics. Over the last 50 years, integrated modeling has evolved significantly through advances in mathematical formulations, satellite-based remote sensing products for model parameterization, optimization tools for model calibration, and availability of high-resolution topographic data. The science of flood prediction, on the other hand, has evolved computationally, but not physically, and the integrated approach for capturing the complex nature of flood events has not been utilized to its potential. This dissertation takes a step in this direction by providing a pathway for large scale integrated flood modeling. As the way forward, this dissertation provides insights into the factors that need to be considered for accurate and efficient integrated flood modeling.

In the first objective, the advantage of using a process-based integrated approach for flood modeling is quantified and validated by increasing the level of process-based detail in flood models. This comparison shows that the incorporation of physical processes affecting the watershed response during flood events provides a more realistic simulation of flood hydrodynamics for different antecedent soil conditions. An important contribution from this research is the reduced dependency on model calibration for flood simulation when process-based details are increased. Overall, the findings suggest that the current practice of simulating floods which assumes an impervious surface may not be providing realistic estimates of flood inundation, and that an integrated approach incorporating all the hydrologic and hydraulic processes in the river system must be adopted.

The analysis presented in the second objective is especially important as more and more researchers are looking to accurately predict flood responses across large watershed scales. With increasing process-based model complexity and spatial scale, accurate representation of scale-dependent processes in integrated flood models becomes essential. The analysis shows that modifying the intrinsic scales of SW-GW sub-models to better represent the characteristic length scales of SW-GW processes reduces model uncertainties at large scales. The results also highlight the degradation of streamflow prediction using a single channel roughness when the stream length scales are increased. Using an example of a variable roughness distribution along the stream length, the results quantify the improvement in the basin response. Overall, the spatial extent scalability of integrated models is improved by incorporating the findings from this research.

The third objective bridges the gap between the computational requirements of physically-based models and the modeling uncertainties of faster and simpler empirically-based models. While the primary focus is maximizing the computational efficiency, the hybrid modeling approach incorporates the learnings from the first two objectives towards developing flood models for ungaged basins. Overall, the hybrid modeling approach results in a performance comparable to a fully-integrated approach but at a much higher computational efficiency while providing objective-oriented flexibility to the modeler.

Hurricane-induced flooding poses a significant risk to both life and property especially across urbanized regions with a highly dense population. In this regard, there are no studies till date that can capture the complex hydrodynamics and quantify the compound nature of Hurricane-induced inland flooding at large scales. Therefore, the fourth objective proposes a physically-based but computationally-efficient approach for modeling unprecedented flood events at large scales in complex urban systems. The application of the proposed approach results in accurate simulation of large scale flood hydrodynamics which is shown using Hurricane Harvey as the test case. The results also suggest that the ability to control the mesh development using the proposed flexible model structure for incorporating important physical and hydraulic features is as important as integration of distributed hydrology and hydrodynamics.

6.2 Limitations and Future Work

Although the results from this dissertation are promising, some of the modeling components can be further improved to enhance the findings. For example, the soil redistribution in the vadose zone and subsequent GW recharge is computed using a non-iterative kinematic approach, and hence, the models do not incorporate lateral flows in the vadose zone. This assumption works well for large flood events with a high intensity of rainfall, as the soil moisture profile closely resembles a sharp wetting front (cylinder). However, infiltration does not occur cylindrically, instead, percolates through the soil system in three dimensions. Lateral flows can not only influence the volume and location of GW recharge, but also the magnitude of streamflow, although the residence time may be large (Hughes, 2010). For a more realistic estimation of the soil moisture redistribution during continuous simulations, numerical solution of the 3D Richards' equation using finite element formulations can be used. However, obtaining adequate data to parameterize a 3D model of unsaturated flow is very difficult. Additionally, when dealing with large watersheds, representing the vadose zone using the 3D form of Richard's equation becomes computationally expensive and impractical for the purpose of flood modeling. In this regard, models such as ParFlow and HydroGeoSphere, which offer a fully integrated 3D solution of unsaturated and saturated subsurface flow aided by high performance computing can be incorporated in future studies (Brunner and Simmons, 2012). Similarly, the effect of preferential flows is also neglected in the models used in this dissertation. Preferential flow through macropores can bypass the entire unsaturated soil column and accelerate the transport of water into the streams (Alaoui et al., 2011). Therefore, preferential flow through the soil matrix should be incorporated in regions where the soil properties are conducive for its existence, although obtaining accurate data to characterize the preferential flow paths is very challenging.

Since the hybrid flood modeling approach using a flexible spatiotemporal mesh structure is relatively more comprehensive than simply using a fixed-resolution 2D model, future work involves developing tools for automating processes such as road-network incorporation, 1D-2D interface development, network-scale bathymetry integration, and delineation of rivers, banks and cross-sections. It is envisioned that this automation would enable the application of integrated modeling for evaluating multiple futuristic (what-if?) scenarios that can help in large scale planning and allocation of resources for protection against future flood risk. All the datasets used

in this dissertation are open access, highlighting the spatial transferability of the modeling approach to other large scale watersheds.

One of the limitations of the models developed as a part of this dissertation is the absence of stormwater drainage system, especially for developed regions inside large watersheds. The water discharging into the open channels from the storm drains can influence the magnitude of peak streamflow, time-of-peak, and duration of inundation in urban areas. However, studies on distributed modeling of urban areas have shown that the impact of stormwater drainage in affecting streamflow is diminished during extreme events as the conveyance in the open channels is significantly higher than stormwater drains (Ogden et al., 2011). Regardless, storm drains can increase flood peaks in the river channels during small to moderate rainfall events, and therefore, should be included in future studies especially during continuous simulations containing multiple rainfall events. The incorporation of stormwater infrastructure in urban watersheds within an integrated modeling framework can help in quantifying the relative contributions of stormwater flow during moderate to high flood events. This may also help in identifying which locations can be targeted for application of green infrastructure for flood protection.

In addition to improving flood modeling, it is essential to evaluate the applicability of forecast tools such as the National Water Model (NWM) that can forecast both the rainfall and streamflow nationally and use this information in estimating flood responses to prevent future catastrophes. While the NWM is a tremendous undertaking, its application in forecasting flood responses from climate forcing data prior to events is still limited and needs further testing before it can be directly used in planning and evacuation for future extreme events. Therefore, future work will also involve testing the efficacy of NWM forecast data in predicting flood events. Even if the forecast data is not entirely accurate, it can help in providing insights on the flooding potential of storm events in advance. The scientific knowledge obtained from this dissertation will be used for creating large scale integrated flood forecasting tools which will predict flood inundation directly from forecast precipitation data. In addition to short-term flood forecasting, future work will also involve evaluating the effect of climate and land use in exacerbating future flood risk.

APPENDIX

APPENDIX A

This section provides supplementary information on the overland flow processes including the relevant equations and numerical formulations that are used in this dissertation. The basic computational framework for both 1D and 2D surface is based on the node-link concept using a finite volume approach that allows for a single fully-integrated system of equations to be developed and solved simultaneously. Therefore, the 1D and 2D surface hydraulics do not have to be coupled. Nodes are specific locations in the modeling domain where WSE are calculated. Links are used to connect and move water from one node to another. The surface flows are calculated along the links based on the WSE values at the connecting nodes. Some of the examples of 1D links include, pipes, weirs, channel segments, bridges and pump stations.

A flexible triangular computational mesh is used for 2D overland flow and is generated automatically based on the various graphical features developed by the modeler. The vertices of the triangles are treated as nodes and the sides of the triangles become overland flow links. The control volumes are formed around the vertices and extend to the midpoints of the triangle sides and to the geometric center of the triangle as shown in Fig. A.1 (a). The control volumes become the catchment areas for the rainfall-runoff processes. The collection of control volumes is referred to as the “honeycomb” mesh which intersects with the soils and land use maps forming a system of sub-polygons (see Fig. A.1 (b)). Rainfall is applied to each sub-polygon and any water that does not percolate into the soil is aggregated by the respective control volume and delivered to the corresponding 2D surface node.

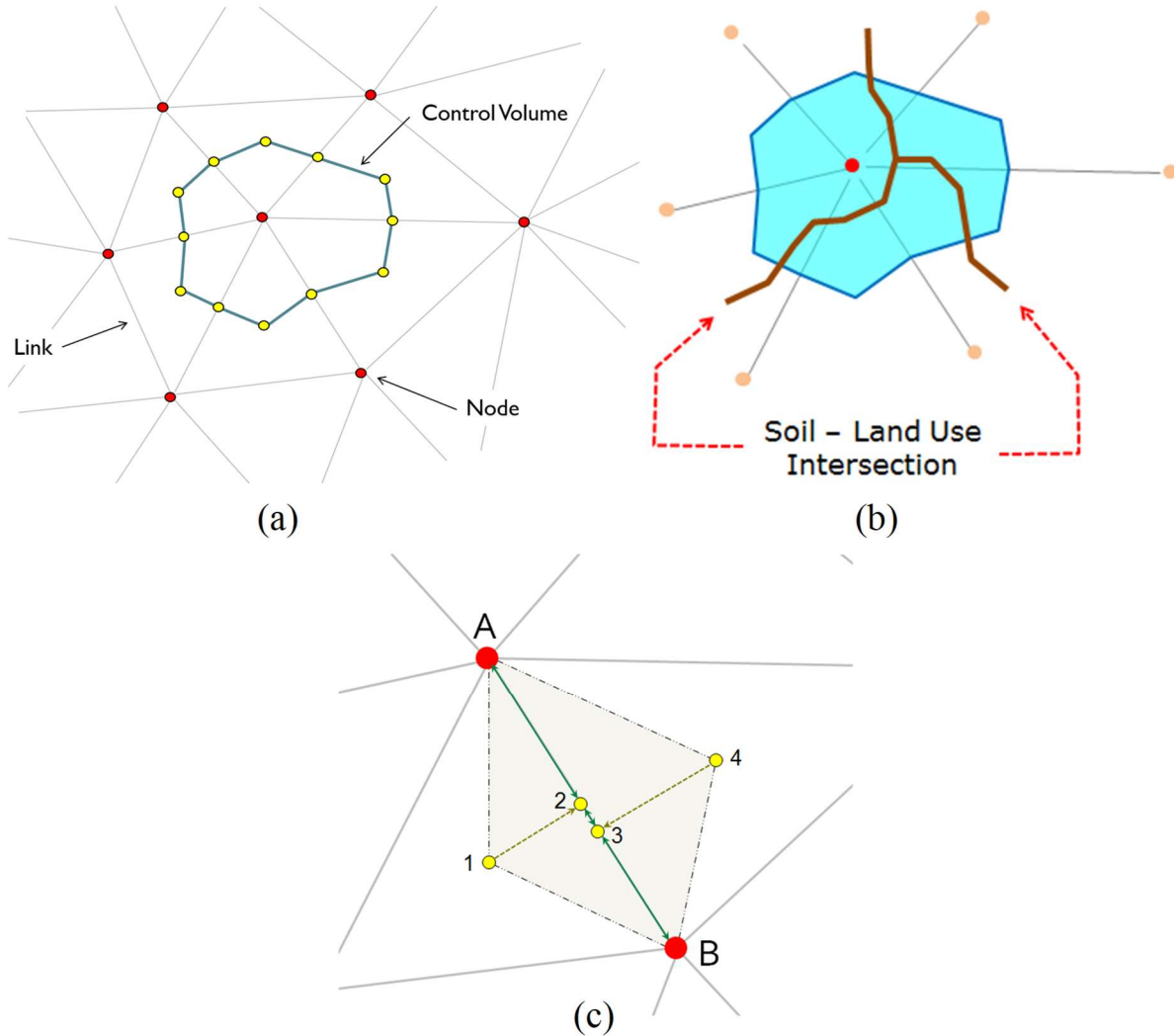


Fig. A.1 (a) Link, node and control volume development in a flexible triangular mesh; (b) Control volume intersection with soils and land use map layers; and (c) Overland flow link (triangle edge) development

A diamond mesh as depicted in Fig. A.1 (c) is simultaneously formed along the triangle edges (i.e. 2D overland flow links) and is used to develop the edge properties. The diamond mesh is intersected with a roughness zone map layer to determine the average roughness characteristics for each triangle edge. Each triangle edge is idealized into an equivalent rectangle for maximizing the computational efficiency. Edge properties are calculated using Equations A.1 to A.3 and Fig. A.1 (c).

$$L = \left(\frac{2}{3}\right)L_{A-B} \quad \text{Equation A.1}$$

$$W = A_{diamond}/L \quad \text{Equation A.2}$$

$$S_{2D} = [S_{A-B}^2 + (S_{1-2} + S_{3-4})^2]^{1/2} \quad \text{Equation A.3}$$

where, L = equivalent rectangular length; L_{A-B} = the length from vertex A to vertex B; W = equivalent width; $A_{diamond}$ = the area of the diamond along a triangle edge; S_{2D} = average two-dimensional ground slope along a triangular edge; S_{A-B} = the longitudinal ground slope between vertex A and vertex B; S_{1-2} = the ground cross-slope between the points 1 and 2; and S_{3-4} = the ground cross-slope between points 3 and 4.

The mass balance equations used in ICPR for every time-step are presented in Equations A.4 to A.7. These equations are applied at each node and at every time-step to evaluate the volume of water from individual processes such as seepage, direct runoff (rainfall excess) and link flow generation. These equations apply to both 1D and 2D surface hydraulics.

$$dz = \left(\frac{Q_{in} - Q_{out}}{A_{surface}} \right) dt \quad \text{Equation A.4}$$

$$Z_{t+dt} = Z_t + dz \quad \text{Equation A.5}$$

$$Q_{in} = \sum Q_{link_{in}} + \sum Q_{excess} + \sum Q_{external} + \sum Q_{seepage} \quad \text{Equation A.6}$$

$$Q_{out} = \sum Q_{link_{out}} + \sum Q_{irrigation} \quad \text{Equation A.7}$$

where, dz = incremental change in stage; dt = computational time-step; Q_{in} = total inflow rate; Q_{out} = total outflow rate; $A_{surface}$ = wet surface area; Z_{t+dt} = new WSE; Z_t = WSE at previous time-step; $\sum Q_{link_{in}}$ = sum of all link flow rates entering a control volume; $\sum Q_{link_{out}}$ = sum of all link flow rates leaving the control volume; $\sum Q_{excess}$ = sum of rainfall excess rates for polygons in control volume; $\sum Q_{external}$ = sum of all inflows from external sources such as streamflow gages; $\sum Q_{seepage}$ = sum of lateral seepage inflow from groundwater model; $\sum Q_{irrigation}$ = sum of water pulled out of the system for irrigation.

The ICPR model includes three solution options for 2D overland flow: (1) the one-dimensional St. Venant equation; (2) the energy equation; and (3) the diffusive wave equation. The diffusive wave equation is used in the overland flow region for maintaining computational efficiency. The flow volumes are evaluated using either the energy equation for 1D flow or diffusive wave for 2D flow or a combination of both and the relevant formulations are presented in Equations A.8 to A.10. The channel conveyance across two cross-sections (1D flow) or two

links (2D flow) is calculated for each depth using Manning's roughness. To evaluate the discharge along two cross-sections in the 1D flow region, the average friction slope is used (Equation A.11). ICPR uses several different methods for averaging the friction slope including the average conveyance (Equation A.11), average friction slope, geometric mean friction slope and harmonic mean friction slope. These methods are automatically used in ICPR based on the flow regimes, and the choice of the method is based on the information on friction slope provided in French, 1985.

$$K = \sum_{i=1,p} \left[\frac{CR_i^{2/3} A_i}{n_i} \right] \quad \text{Equation A.8}$$

$$Q = \left(\frac{Z_1 - Z_2}{\frac{1}{2g} \left[\frac{1}{A_2^2} - \frac{1}{A_1^2} \right] + \Delta x S_{f_{avg}}} \right)^{\frac{1}{2}} \quad \text{Equation A.9}$$

$$Q = \left(\frac{Z_1 - Z_2}{\Delta x S_{f_{avg}}} \right)^{\frac{1}{2}} \quad \text{Equation A.10}$$

$$S_{f_{avg}} = \frac{4Q^2}{(K_1 + K_2)^2} \quad \text{Equation A.11}$$

where, Q = channel discharge or flow rate (L^3T^{-1}); A = cross-sectional area (L^2); t = time (T); g = acceleration due to gravity (LT^{-2}); z = gravitational head (L); x = distance in direction of flow (L); $S_{f_{avg}}$ = average friction slope across two cross-sections; K_1 and K_2 = channel conveyance (L^3T^{-1}) at two cross-sections; p = number of segments with unique Manning's roughness; n_i = Manning's roughness for segment i ; A_i = cross-sectional area of i^{th} segment (L^2); R_i = hydraulic radius of the i^{th} segment (L); Δx = distance between adjacent cross-sections; C = unit conversion constant which is equal to 1.486 in US customary units and equal to 1 in SI units.

ICPR uses an exponential decay function (shown in Equations A.12 and A.13) dependent on surface depth to incorporate the variability in surface roughness (Arcement Jr. and Schneider, 1984).

$$n = n_{shall} e^{(k)(d)} \quad \text{Equation A.12}$$

$$k = \frac{\ln\left(\frac{n_{deep}}{n_{shallow}}\right)}{d_{max}} \quad \text{Equation A.13}$$

where, n = Manning's roughness at depth d ; n_{shall} = Manning's roughness at ground surface; n_{deep} = Manning's roughness at depth $\geq d_{max}$; k = exponential decay factor; d = depth of flow; d_{max} = user specified maximum depth (0.91 m or 3 feet) for transitioning to n_{deep} .

The Brooks-Corey soil water retention–hydraulic conductivity relationship (Rawls and Brakensiek, 1982), shown in Equation A.14, is used to determine unsaturated conductivities based on initial soil moisture contents.

$$\frac{K(\theta)}{K_s} = \left(\frac{\theta - \theta_r}{\phi - \theta_r} \right)^n \quad \text{Equation A.14}$$

where, θ = current moisture content; θ_r = residual moisture content; ϕ = saturated moisture content; $K(\theta)$ = unsaturated vertical conductivity at θ ; K_s = saturated vertical conductivity; $n = 3 + \frac{2}{\lambda}$; and λ = pore size index.

The reference evapotranspiration rates are evaluated using the Penman-Monteith Equation (shown in Equation A.15) as described in Allen et al., 1998.

$$RET = \frac{0.408 \Delta (R_n - G) + \gamma \frac{900}{T + 273} u_2 (e_s - e_a)}{\Delta + \gamma (1 + 0.34 u_2)} \quad \text{Equation A.15}$$

where, RET = reference evapotranspiration (mm day^{-1}); R_n = net radiation at crop surface ($\text{MJ m}^{-2} \text{day}^{-1}$); G = soil heat flux density ($\text{MJ m}^{-2} \text{day}^{-1}$); T = air temperature at 2 m height ($^{\circ}\text{C}$); u_2 = wind speed at 2 m height (m s^{-1}); e_s = saturation vapor pressure (kPa); e_a = actual vapor pressure (kPa); Δ = slope vapor pressure curve ($\text{kPa } ^{\circ}\text{C}^{-1}$); and γ = psychrometric constant ($\text{kPa } ^{\circ}\text{C}^{-1}$). To evaluate the coefficients in A.16 and subsequently, RET , the empirical equations provided in Allen et al., 1998, are used in conjunction with meteorological data. The meteorological data for calculating RET in ICPR includes observations of daily maximum and minimum temperature, dew point temperature, cloud cover percentage, wind speed and altitude.

APPENDIX B

Detailed Description of the 2D GW Flow Finite Element Formulation used in ICPR (modified from Martínez, 1989; Streamline Technologies, 2018) is provided in this section.

The continuity equation for unsteady phreatic 2D GW flow is given below:

$$n \frac{\partial h}{\partial t} = -\frac{\partial(uh)}{\partial x} - \frac{\partial(vh)}{\partial y} \quad \text{Equation B.1}$$

where, n is the fillable porosity (or specific yield); h is the GW elevation (piezometric head); u , v are the velocity vector components; t is time; and x , y are the Cartesian coordinates. Additionally, the velocity vectors for an isotropic porous media are expressed using the following equation:

$$u = -K \cdot \frac{\partial h}{\partial x}; \text{ and, } v = -K \cdot \frac{\partial h}{\partial y} \quad \text{Equation B.2}$$

where, K is the permeability (conductivity) of the porous media. On substituting equation B.2 in B.1, and adding an external flow f , representing the total flow coming into GW region in the form of seepage and recharge, the following equation is obtained:

$$f + n \frac{\partial h}{\partial t} = \frac{\partial(Kh \cdot h_x)}{\partial x} + \frac{\partial(Kh \cdot h_y)}{\partial y} \quad \text{Equation B.3}$$

Here, h_x and h_y are partial derivative notations. Since the GW region is divided into a triangular mesh network, the total aquifer area is the sum of partial areas of the all the triangles in the mesh network. Equation B.3 is then expressed as a summation function of each individual triangle using a Galerkin approximation, and the resultant equation is shown below:

$$\iint_R N_i \cdot I \cdot dx dy = \sum_{j=1}^{N_e} \iint_{e_j} N_i \cdot I \cdot dx dy = \{0\} \quad \text{Equation B.4}$$

where, $I = \frac{\partial(Kh \cdot h_x)}{\partial x} + \frac{\partial(Kh \cdot h_y)}{\partial y} - \left(f + n \frac{\partial h}{\partial t}\right)$; $N_i = \phi_i(x, y)$, the dimensionless shape function for any node i of the triangle; e_j is any triangular element j ; N_e is the total number of elements in the aquifer region; R is the total aquifer region; $\{0\}$ is the null vector with the number of components equal to the total number of nodes. On applying integration by parts and Green's Theorem over the integration of an individual element e_j , the following equation is obtained:

$$\iint_{e_j} N_i \cdot I \cdot dx dy = \iint_{e_j} I_1 \cdot dx dy + \iint_{e_j} I_2 \cdot dx dy - \int_{C_{e_j}} I_3 \cdot dL = 0 \quad \text{Equation B.5}$$

where, $I_1 = Kh \left\{ \frac{\partial N_i}{\partial x} \cdot h_x + \frac{\partial h}{\partial y} \cdot h_y \right\}$; $I_2 = N_i \left(f + n \frac{\partial h}{\partial t} \right)$; $I_3 = N_i (Kh) \cdot h_s$; h_x , h_y , and h_s are notations for partial derivatives; s is the flow direction; C_{e_j} is the boundary of the element e_j ; dL is the differential length along the boundary such that $h_s dL = h_x dy - h_y dx$. Within ICPR, Equation B.5 is expressed and solved for six nodes, which are formed using three triangle vertices and three mid-side points, and the solution is approximated using finite element formulations for each individual triangle over the entire mesh network. Overall, the variation of head (h) for each triangle is expressed using the following equation:

$$h = Ax^2 + By^2 + Cxy + Dx + Ey + F \quad \text{Equation B.6}$$

The shape function N_i is defined for each one the six nodes using six equations so that the overall head (h) anywhere inside the triangle is a linear combination of the head (h) at the six nodes, which gives:

$$h = \sum_{k=1}^6 N_k h_k \quad \text{Equation B.7}$$

Using a cyclic permutation involving calculation of six shape functions that are compatible with Equations B.7 and calculating the head (h) derivatives from Equation B.6, the three integrals in Equation B.5 are evaluated at each time-step for the entire mesh network. Finally, the seepage rates along a sloping ground surface, river bank or seepage faces on a hill are calculated using Equation B.8:

$$Q_{seepage} = \frac{(h_1 - h_2) \times (A) \times \varphi_b}{dt_{gw}} \quad \text{Equation B.8}$$

where, $Q_{seepage}$ = seepage rate (L^3T^{-1}); h_1 = calculated WT elevation (L); h_2 = ground surface elevation at node (L); A = groundwater control volume surface area (L^2); φ_b = below ground fillable porosity; and dt_{gw} = groundwater computational time increment (T).

APPENDIX C

This section provides information on the time-stepping mechanism used in ICPR. The coupling sequence between the vadose zone and the surface hydraulics is as follows: (1) Increment

hydrology clock (vadose zone); and (2) Increment surface hydraulics clock until it catches up to the hydrology clock. The hydrology (vadose zone) time increments are static. The hydrology time increment is usually several minutes in duration whereas the hydrodynamic time increments are typically in seconds or fractions of seconds in duration and operate between a user-specified minimum and maximum time increment. Hydrology runoff rates are saved at the beginning and end of a hydrology time increment and delivered to the appropriate surface node. There are two (2) time marching options in ICPR. The first is a Successive Approximation technique with Over-Relaxation (SAOR). This is an iterative solution that solves for heads at nodes and flow rates along triangle edges. It has an adaptive time step and changes between user-specified minimum and maximum time increments. However, a constant time step is used throughout the computational mesh at a given point in time. Consequently, the time step is typically driven by the node with the least amount of storage. The second method (used here) is based on a second order Runge-Kutta technique (modified Euler method) that varies the time step not only in time, but also spatially. The time-marching method, referred to as the “FIREBALL” method in ICPR, involves establishing a set of time step levels at the beginning of a simulation based on the minimum and the maximum calculation times, with each successive level doubling in duration.

For example, if the minimum and maximum calculation times are set to 0.01 and 5.12 seconds, respectively, then ten (10) time step levels are established, and routing calculations are based on these time step levels. In this case, the inner-most level is calculated 512 times compared to the outer-most level, but the neighboring cells do not increase by more than one level. A maximum allowable time step is then determined for each node based on inflows, outflows, and available storage, such that the change in stage does not exceed the user specified change in stage tolerance, which is typically set such that the mass-balance error is minimal. The time steps are rounded down to the closest time step level, following which, a pass is made through the entire network, beginning at nodes with the lowest time step level, to ensure that the neighboring nodes do not increase more than one time step level. An example is shown in Fig. C.2 (adapted from Streamline Technologies, 2018) with a total of thirteen (13) time step levels. The inner-most level in this example must be calculated 4096 times compared to the outer-most level, but the neighboring cells do not increase by more than one level. Once all cells on all time step levels have been calculated, the maximum allowable time steps for all the nodes are re-evaluated and the process is repeated.

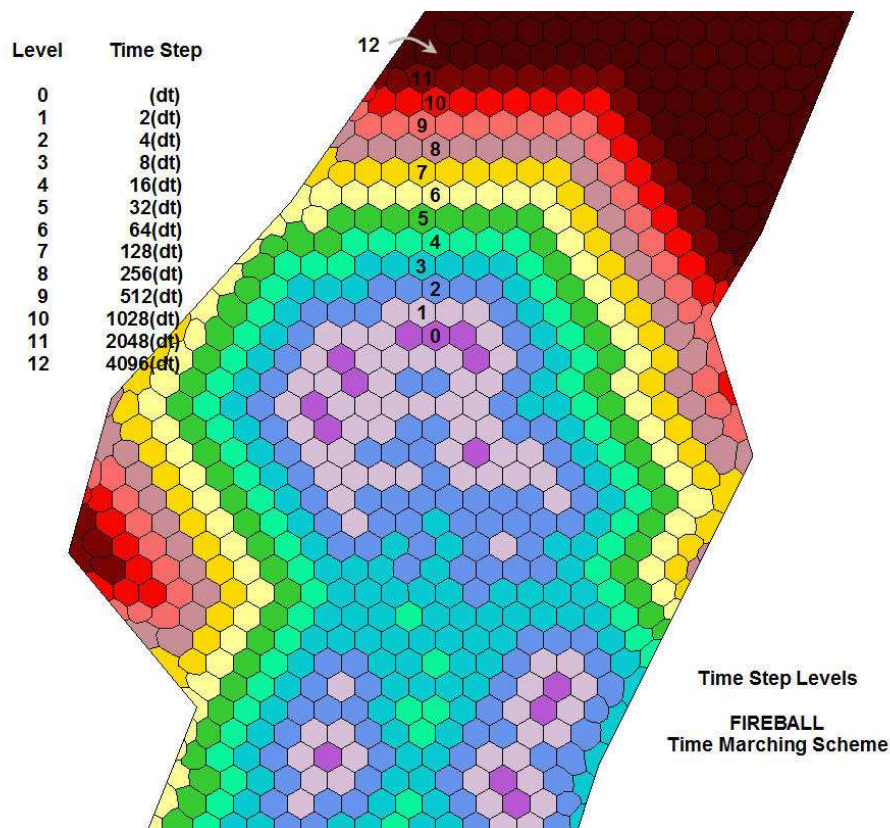


Fig. C.1 FIREBALL time marching scheme in ICPR (adapted from Streamline Technologies, 2018)

APPENDIX D

This section provides additional validation for the computationally-efficient model structure used to model Hurricane Harvey which is described in Section 5.5.4. Fig. D.1 and D.2 present the stage comparisons for the ‘*small*’ and ‘*large*’ model at ten (10) HCFCD gages located within the ‘*small*’ model domain.

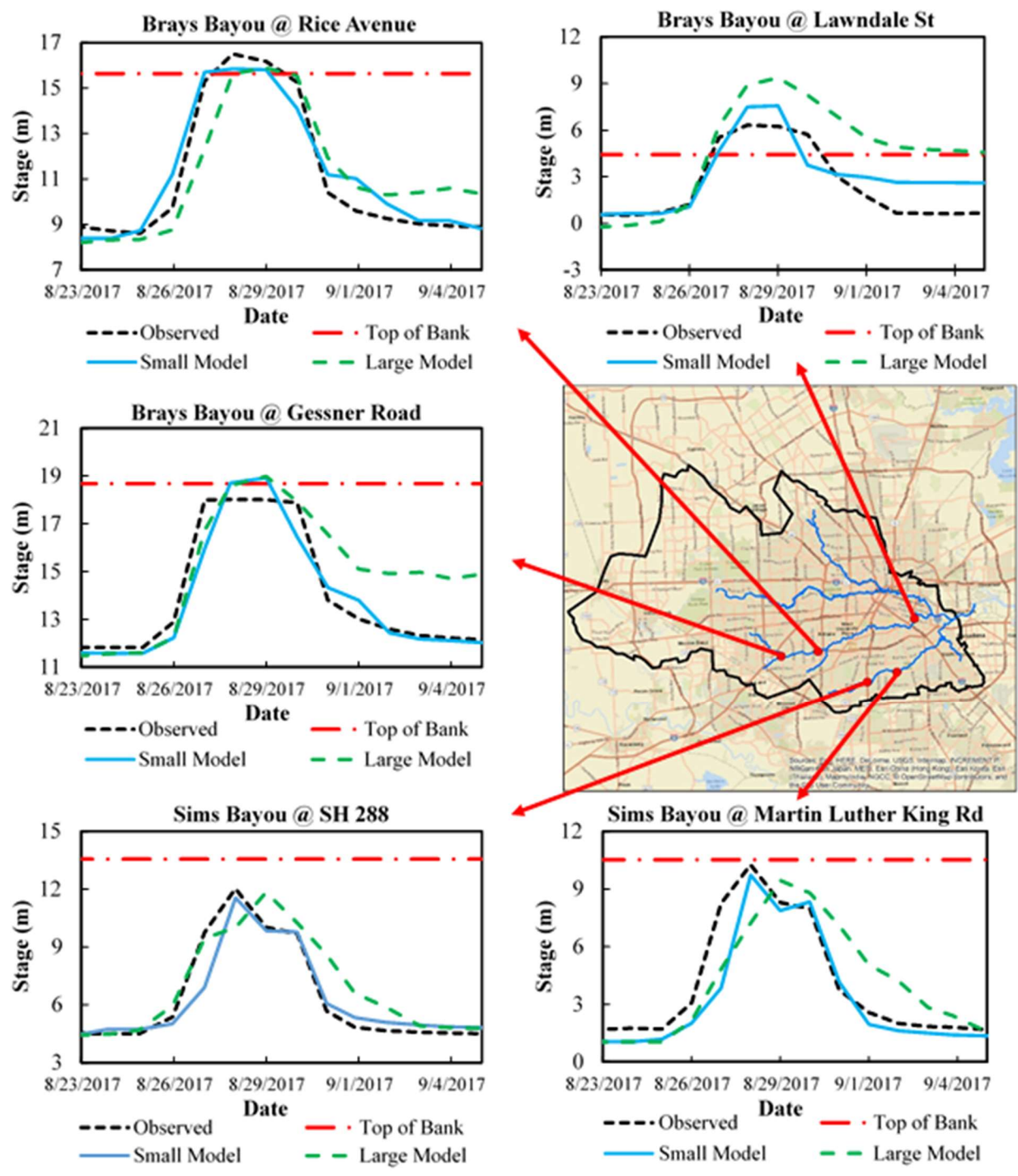


Fig. D.1 Stage comparisons with observed data across five locations inside the 'small' model domain

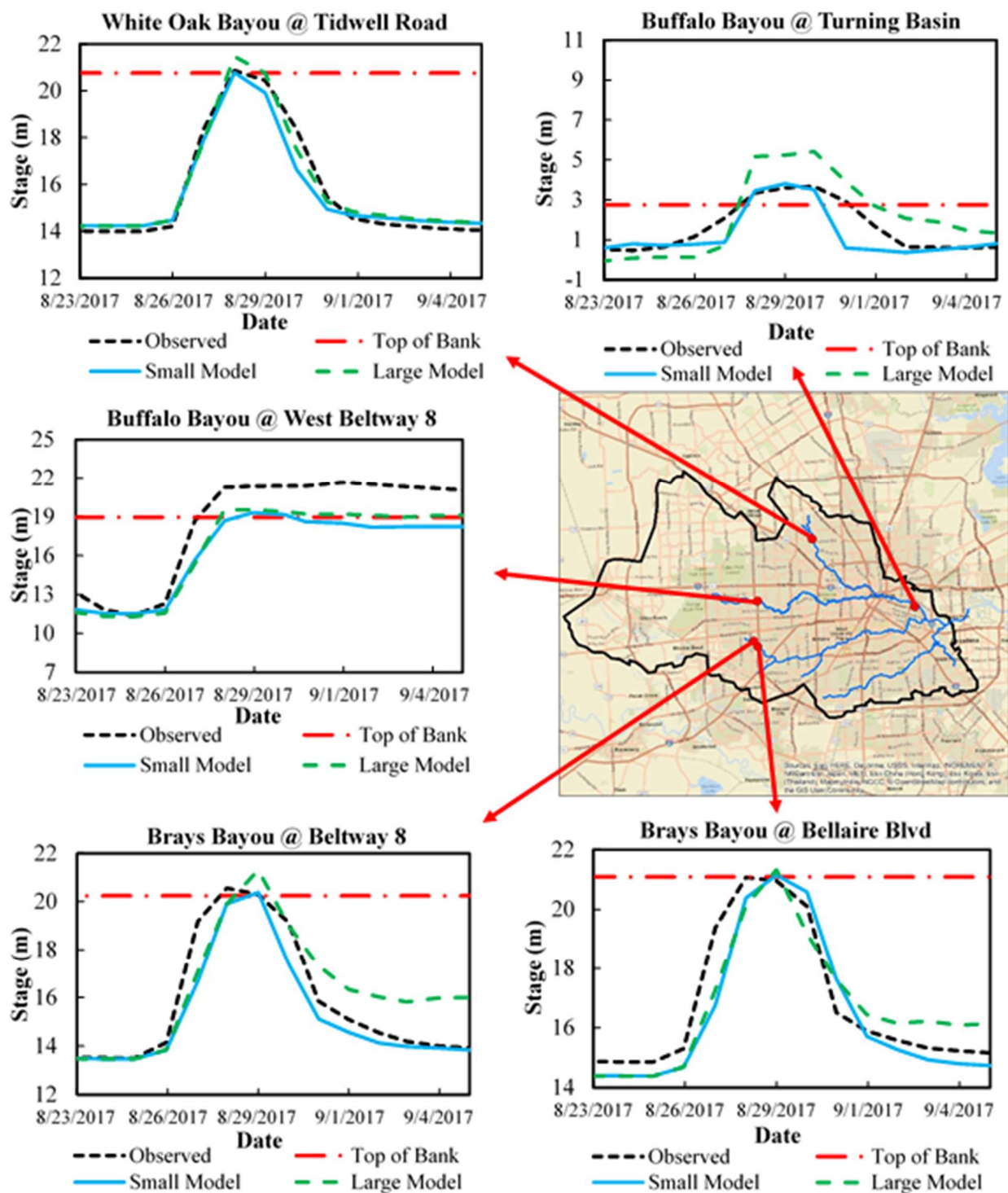


Fig. D.2 Stage comparisons with observed HCFCD data across several locations for both models inside the ‘small’ model domain

Fig. D.3 presents the stage comparisons at four (4) HCFCD gages for streams draining into the Houston Shipping Channel (HSC) inside the ‘large’ model domain.

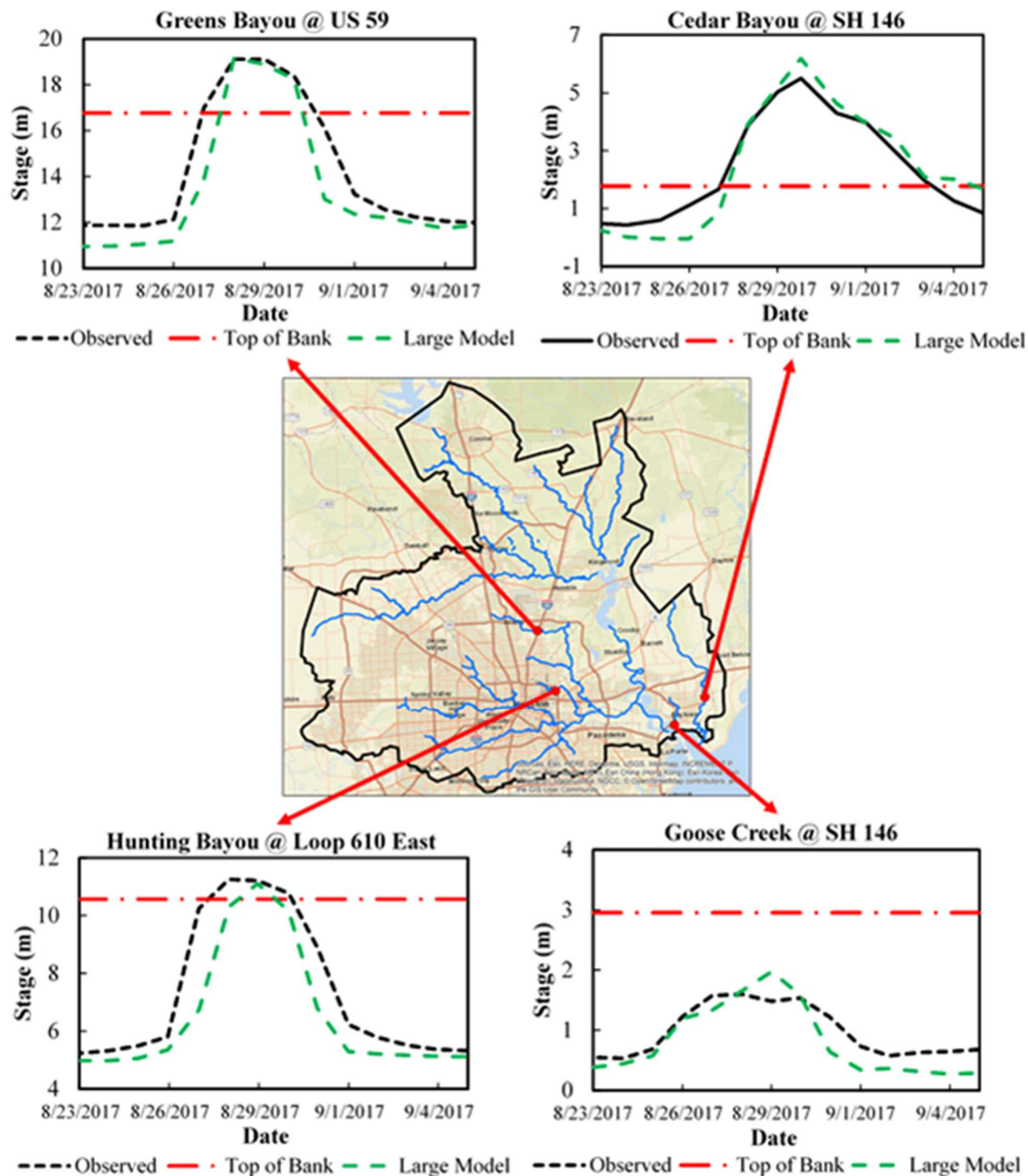


Fig. D.3 Stage comparisons with observed HCFCD gage data for the 'large' model at four locations

Fig. D.4 presents hourly stage comparisons across four (4) USGS gages located within the extents of the City of Houston for the ‘*small*’ model. Majority of the USGS gages in the model domain either have no information or missing information during the model simulation period. Therefore, only the gages with accurate and complete observed stage information are shown below.

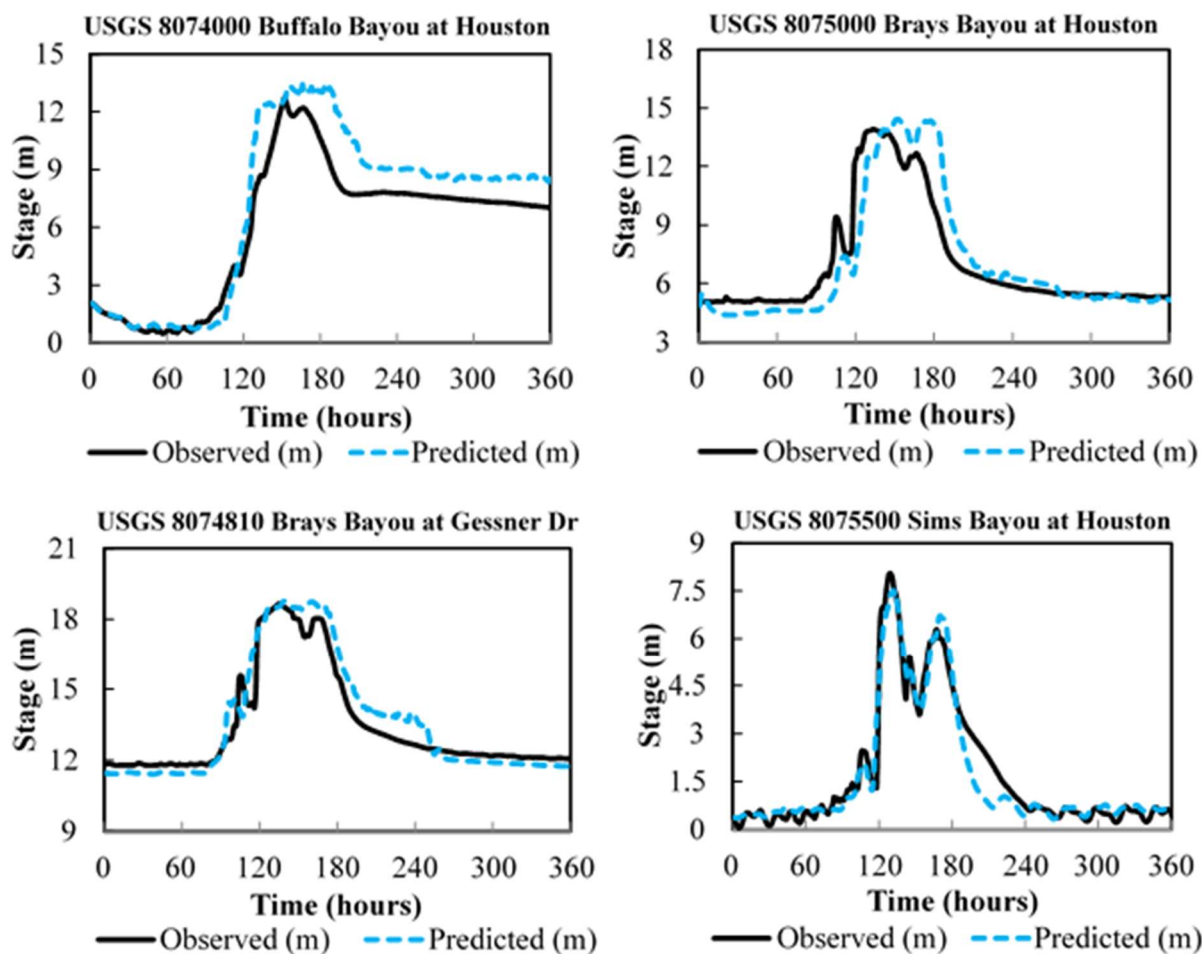


Fig. D.4 Hourly stage comparisons with USGS gages in the City of Houston for the ‘*small*’ model

The results shown in Fig. D.4 highlight the overall accuracy of the modeling approach not only across daily time-scale, but also across an hourly time-scale. Further, the tidal and storm surge induced stage is also captured across the gages located near the HSC as shown by the results at USGS gage 8075500, Sims Bayou at Houston, TX. The statistical metrics for evaluating model performance presented in Table D.1 further validate the performance of the modeling approach across the USGS gages. Even at an hourly time-scale, the overall error in peak stage is minimal, with NSE values higher than 0.75 in all case. However, there is significant overprediction along

the receding limb of the USGS gage 8074000, Buffalo Bayou at Houston, as shown in Fig. D.4. This overprediction results in a high PBIAS (18.1 %) at this gage. Since this gage is located just upstream of the confluence of the Buffalo Bayou and White Oaks Bayou, it is possible that this over-prediction during the receding limb is due to the inaccuracy in capturing the flows around the confluence.

Table D.1 Hourly stage performance statistics across USGS gages in the City of Houston for 'small' model

Gage Name	NSE	PBIAS (%)	RSR	% Error in Peak Stage
USGS 8074000 Buffalo Bayou at Houston	0.82	+18.1	0.43	+5.5
USGS 8075000 Brays Bayou at Houston	0.76	-0.03	0.49	+3.7
USGS 8074810 Brays Bayou at Gessner Dr	0.90	+1.22	0.32	+0.6
USGS 8075500 Sims Bayou at Houston	0.94	-5.07	0.25	-6.6

REFERENCES

- Ahmad, H., Miller, J.W., George, R.D., 2014. Minimizing pond size using an off-site pond in a closed basin: A storm flow mitigation design and evaluation. *Int. J. Sustain. Dev. Plan.* 9, 211–224. <https://doi.org/10.2495/SDP-V9-N2-211-224>
- Alaoui, A., Caduff, U., Gerke, H.H., Weingartner, R., 2011. Preferential Flow Effects on Infiltration and Runoff in Grassland and Forest Soils. *Vadose Zo. J.* 10, 367. <https://doi.org/10.2136/vzj2010.0076>
- Allen, R.G., Luis, S.P., Raes, D., Smith, M., 1998. Crop Evapotranspiration: Guidelines for Computing Crop Water Requirements. FAO Irrig. Drain. Pap. No. 56., Food Agric. Organ. L. Water, Rome, Italy. <https://doi.org/10.1016/j.eja.2010.12.001>
- Arcement Jr., G.J., Schneider, V.R., 1984. Guide for Selecting Manning's Roughness Coefficients for Natural Channels. Fed. Highw. Adm. FHWA-TS-84, 68.
- Arnold, J.G., Moriasi, D.N., Gassman, P.W., Abbaspour, K.C., White, M.J., Srinivasan, R., Santhi, C., Harmel, R.D., Griensven, a. Van, VanLiew, M.W., Kannan, N., Jha, M.K., 2012. Swat: Model Use, Calibration, and Validation. *Trans. ASABE* 55, 1491–1508.
- Atkinson, S.E., Sivapalan, M., Woods, R.A., Viney, N.R., 2003. Dominant physical controls on hourly flow predictions and the role of spatial variability: Mahurangi catchment, New Zealand. *Adv. Water Resour.* 26, 219–235. [https://doi.org/10.1016/S0309-1708\(02\)00183-5](https://doi.org/10.1016/S0309-1708(02)00183-5)
- Bales, J.D., Wagner, C.R., 2009. Sources of uncertainty in flood inundation maps. *J. Flood Risk Manag.* 2, 139–147. <https://doi.org/10.1111/j.1753-318X.2009.01029.x>
- Barthel, R., Banzhaf, S., 2016. Groundwater and Surface Water Interaction at the Regional-scale – A Review with Focus on Regional Integrated Models. *Water Resour. Manag.* 30, 1–32. <https://doi.org/10.1007/s11269-015-1163-z>
- Bates, P., De Roo, A., 2000. A simple raster-based model for flood inundation simulation. *J. Hydrol.* 236, 54–77. [https://doi.org/10.1016/S0022-1694\(00\)00278-X](https://doi.org/10.1016/S0022-1694(00)00278-X)
- Becker, A., Braun, P., 1999. Disaggregation, aggregation and spatial scaling in hydrological modelling. *J. Hydrol.* 217, 239–252. [https://doi.org/10.1016/S0022-1694\(98\)00291-1](https://doi.org/10.1016/S0022-1694(98)00291-1)
- Bednarek, A.T., 2001. Undamming rivers: A review of the ecological impacts of dam removal. *Environ. Manage.* 27, 803–814. <https://doi.org/10.1007/s002670010189>
- Begnudelli, L., Sanders, B.F., 2006. Unstructured grid finite volume algorithm for shallow-water flow and transport with wetting and drying. *J. Hydraul. Eng.* 132, 371–384.
- Berg, S.J., Sudicky, E.A., 2018. Toward Large-Scale Integrated Surface and Subsurface Modeling. *Groundwater* 57, 1–2. <https://doi.org/10.1111/gwat.12844>
- Berthet, L., Andréassian, V., Perrin, C., Javelle, P., 2009. How crucial is it to account for the antecedent moisture conditions in flood forecasting? Comparison of event-based and continuous approaches on 178 catchments. *Hydrol. Earth Syst. Sci.* 13, 819–831. <https://doi.org/10.5194/hess-13-819-2009>
- Beven, K., 2002. Towards an alternative blueprint for a physically based digitally simulated hydrologic response modelling system. *Hydrol. Process.* 16, 189–206. <https://doi.org/10.1002/hyp.343>
- Beven, K., 1993. Prophecy, reality and uncertainty in distributed hydrological modelling. *Adv. Water Resour.* 16, 41–51. [https://doi.org/10.1016/0309-1708\(93\)90028-E](https://doi.org/10.1016/0309-1708(93)90028-E)
- Beven, K., Gilman, K., Newson, M., 1979. Flow and flow routing in upland channel networks. *Hydrol. Sci. Bull.* 24, 303–325. <https://doi.org/10.1080/02626667909491869>

- Beven, K.J., Cloke, H.L., 2012. Comment on “hyperresolution global land surface modeling: Meeting a grand challenge for monitoring Earth’s terrestrial water” by Eric F. Wood et al. *Water Resour. Res.* 48, 1–10. <https://doi.org/10.1029/2010WR010090>
- Bhuyian, N.M., Kalyanapu, A.J., Nardi, F., 2015. Approach to Digital Elevation Model Correction by Improving Channel Conveyance. *J. Hydrol. Eng. ASCE* 20, 1–10. [https://doi.org/10.1061/\(ASCE\)HE.1943-5584.0001020](https://doi.org/10.1061/(ASCE)HE.1943-5584.0001020).
- Bixio, A.C., Gambolati, G., Paniconi, C., Putti, M., Shestopalov, V.M., Bublías, V.N., Bohuslavsky, A.S., Kasteltseva, N.B., Rudenko, Y.F., 2002. Modeling groundwater-surface water interactions including effects of morphogenetic depressions in the Chernobyl exclusion zone. *Environ. Geol.* 42, 162–177. <https://doi.org/10.1007/s00254-001-0486-7>
- Bloschl, G., Sivapalan, M., 1995. Scale Issues in Hydrological Modelling: A Review. *Hydrol. Process.* 9, 251–290.
- Booker, A.S., 2006. Modeling the 100-Year Flood Using GIS: A Flood Analysis in the Avon Park Watershed, Master’s Thesis. University of South Florida.
- Brody, S.D., Blessing, R., Sebastian, A., Bedient, P., 2013. Delineating the Reality of Flood Risk and Loss in Southeast Texas. *Nat. Hazards Rev.* 14, 89–97. [https://doi.org/10.1061/\(ASCE\)NH.1527-6996.0000091](https://doi.org/10.1061/(ASCE)NH.1527-6996.0000091)
- Brody, S.D., Zahran, S., Highfield, W.E., Grover, H., Vedlitz, A., 2008. Identifying the impact of the built environment on flood damage in Texas. *Disasters* 32, 1–18. <https://doi.org/10.1111/j.1467-7717.2007.01024.x>
- Brunner, G. 2010. HEC-RAS, River Analysis System Hydraulic Reference Manual.
- Brunner, G.W., 2014. Combined 1D and 2D Modeling with HEC-RAS. US Army Corps Eng. 1–130.
- Brunner, P., Simmons, C.T., 2012. HydroGeoSphere: A Fully Integrated, Physically Based Hydrological Model. *Ground Water* 50, 170–176. <https://doi.org/10.1111/j.1745-6584.2011.00882.x>
- Bunya, S., Dietrich, J.C., Westerink, J.J., Ebersole, B.A., Smith, J.M., Atkinson, J.H., Jensen, R., Resio, D.T., Luettich, R.A., Dawson, C., Cardone, V.J., Cox, A.T., Powell, M.D., Westerink, H.J., Roberts, H.J., 2010. A High-Resolution Coupled Riverine Flow, Tide, Wind, Wind Wave, and Storm Surge Model for Southern Louisiana and Mississippi. Part I: Model Development and Validation. *Mon. Weather Rev.* 138, 345–377. <https://doi.org/10.1175/2009MWR2907.1>
- Castillo, V.M., Gómez-Plaza, A., Martínez-Mena, M., 2003. The role of antecedent soil water content in the runoff response of semiarid catchments: A simulation approach. *J. Hydrol.* 284, 114–130. [https://doi.org/10.1016/S0022-1694\(03\)00264-6](https://doi.org/10.1016/S0022-1694(03)00264-6)
- Chen, Y., Li, J., Wang, H., Qin, J., Dong, L., 2017. Large-watershed flood forecasting with high-resolution distributed hydrological model. *Hydrol. Earth Syst. Sci.* 21, 735–749. <https://doi.org/10.5194/hess-21-735-2017>
- Choi, C.C., Constantinescu, G., Mantilla, R., 2015. Implementation of a Hydraulic Routing Model for Dendritic Networks with Offline Coupling to a Distributed Hydrological Model. *J. Hydrol. Eng.* 20. [https://doi.org/10.1061/\(ASCE\)HE.1943-5584.0001152](https://doi.org/10.1061/(ASCE)HE.1943-5584.0001152).
- Chow, V. Te, 1959. *Open Channel Hydraulics*. McGraw-Hill B. Company, Inc. <https://doi.org/10.1016/B978-0-7506-6857-6.X5000-0>
- City of Houston, 2018. Local Housing Needs Assessment- Hurricane Harvey Housing Recovery. City Houston, Hous. Community Dev.

- Cohen, S., Brakenridge, G.R., Kettner, A., Bates, B., Nelson, J., McDonald, R., Huang, Y.-F., Munasinghe, D., Zhang, J., 2018. Estimating Floodwater Depths from Flood Inundation Maps and Topography. *JAWRA J. Am. Water Resour. Assoc.* 54, 847–858. <https://doi.org/10.1111/1752-1688.12609>
- Cook, A., Merwade, V., 2009. Effect of topographic data, geometric configuration and modeling approach on flood inundation mapping. *J. Hydrol.* 377, 131–142. <https://doi.org/10.1016/j.jhydrol.2009.08.015>
- Cooper, H.H.J., Rorabaugh, M.I., 1963. Ground-water movements and bank storage due to flood stages in surface streams. *U. S. Geol. Surv. Water-Supply Pap.* 1536-J, 343–366. <https://doi.org/Water-Supply Paper 1536-J>
- David, C.H., Habets, F., Maidment, D.R., Yang, Z.L., 2011a. RAPID applied to the SIM-France model. *Hydrol. Process.* 25, 3412–3425. <https://doi.org/10.1002/hyp.8070>
- David, C.H., Maidment, D.R., Niu, G.-Y., Yang, Z.-L., Habets, F., Eijkhout, V., 2011b. River Network Routing on the NHDPlus Dataset. *J. Hydrometeorol.* 12, 913–934. <https://doi.org/10.1175/2011JHM1345.1>
- de Moel, H., Jongman, B., Kreibich, H., Merz, B., Penning-Rowsell, E., Ward, P.J., 2015. Flood risk assessments at different spatial scales. *Mitig. Adapt. Strateg. Glob. Chang.* 20, 865–890. <https://doi.org/10.1007/s11027-015-9654-z>
- Dey, S., 2016. Role of River Bathymetry in Hydraulic Modeling of River Channels. Open Access Theses, Purdue Univ. West Lafayette, Indiana 940.
- Dey, S., Saksena, S., Merwade, V., 2019. Assessing the effect of different bathymetric models on hydraulic simulation of rivers in data sparse regions. *J. Hydrol.* 575, 838–851. <https://doi.org/10.1016/j.jhydrol.2019.05.085>
- Di Baldassarre, G., Schumann, G., Bates, P.D., 2009. A technique for the calibration of hydraulic models using uncertain satellite observations of flood extent. *J. Hydrol.* 367, 276–282. <https://doi.org/10.1016/j.jhydrol.2009.01.020>
- Dimitriadis, P., Tegos, A., Oikonomou, A., Pagana, V., Koukouvinos, A., Mamassis, N., Koutsoyiannis, D., Efstratiadis, A., 2016. Comparative evaluation of 1D and quasi-2D hydraulic models based on benchmark and real-world applications for uncertainty assessment in flood mapping. *J. Hydrol.* 534, 478–492. <https://doi.org/10.1016/j.jhydrol.2016.01.020>
- Domingues, M.O., Gomes, S.M., Roussel, O., Schneider, K., 2008. An adaptive multiresolution scheme with local time stepping for evolutionary PDEs. *J. Comput. Phys.* 227, 3758–3780. <https://doi.org/10.1016/j.jcp.2007.11.046>
- Dottori, F., Salamon, P., Bianchi, A., Alfieri, L., Hirpa, F.A., Feyen, L., 2016. Development and evaluation of a framework for global flood hazard mapping. *Adv. Water Resour.* 94, 87–102. <https://doi.org/10.1016/j.advwatres.2016.05.002>
- Downer, C.W., Ogden, F.L., 2006. Gridded Surface Subsurface Hydrologic Analysis (GSSHA) User's Manual, Version 1.43 for Watershed Modeling System 6.1. US Army Corps Eng. Eng. Res. Dev. Cent.
- Downer, C.W., Ogden, F.L., Martin, W.D., Harmon, R.S., 2002. Theory, development, and applicability of the surface water hydrologic model CASC2D. *Hydrol. Process.* 16, 255–275. <https://doi.org/10.1002/hyp.338>
- Ebel, B.A., Loague, K., Montgomery, D.R., Dietrich, W.E., 2008. Physics-based continuous simulation of long-term near-surface hydrologic response for the Coos Bay experimental catchment. *Water Resour. Res.* 44, 1–23. <https://doi.org/10.1029/2007WR006442>

- Emanuel, K., 2017. Assessing the present and future probability of Hurricane Harvey's rainfall. *Proc. Natl. Acad. Sci.* 0, 201716222. <https://doi.org/10.1073/pnas.1716222114>
- Fatichi, S., Vivoni, E.R., Ogden, F.L., Ivanov, V.Y., Mirus, B., Gochis, D., Downer, C.W., Camporese, M., Davison, J.H., Ebel, B., Jones, N., Kim, J., Mascaro, G., Niswonger, R., Restrepo, P., Rigon, R., Shen, C., Sulis, M., Tarboton, D., 2016. An overview of current applications, challenges, and future trends in distributed process-based models in hydrology. *J. Hydrol.* 537, 45–60. <https://doi.org/10.1016/j.jhydrol.2016.03.026>
- Faulkner, B.R., Renée Brooks, J., Forshay, K.J., Cline, S.P., 2012. Hyporheic flow patterns in relation to large river floodplain attributes. *J. Hydrol.* 448–449, 161–173. <https://doi.org/10.1016/j.jhydrol.2012.04.039>
- Fleckenstein, J.H., Krause, S., Hannah, D.M., Boano, F., 2010. Groundwater-surface water interactions: New methods and models to improve understanding of processes and dynamics. *Adv. Water Resour.* 33, 1291–1295. <https://doi.org/10.1016/j.advwatres.2010.09.011>
- Fleming, M.J., Doan, J.H., 2009. HEC-GeoHMS Geospatial Hydrologic Modelling Extension: User's Manual Version 4.2. US Army Corps Eng. Hydrol. Eng. Cent. CPD-77, 193.
- Fletcher, T.D., Andrieu, H., Hamel, P., 2013. Understanding, management and modelling of urban hydrology and its consequences for receiving waters: A state of the art. *Adv. Water Resour.* 51, 261–279. <https://doi.org/10.1016/j.advwatres.2012.09.001>
- FLO-2D, 2018. FLO-2D Reference Manual. FLO-2D Software, Inc. Nutr. AZ.
- Follum, M.L., Tavakoly, A.A., Niemann, J.D., Snow, A.D., 2016. AutoRAPID: A Model for Prompt Streamflow Estimation and Flood Inundation Mapping over Regional to Continental Extents. *J. Am. Water Resour. Assoc.* 80523, 1–20. <https://doi.org/10.1111/1752-1688.12476>
- Freeze, R.A., Harlan, R.L., 1969. Blueprint for a physically-based digitally-simulated hydrologic response model. *J. Hydrol.* 9, 237–258.
- French, R.H., 1985. *Open Channel Hydraulics*. McGraw-Hill, New York.
- Frisbee, M.D., Meyers, Z.P., Stewart-Maddox, N.S., Caffee, M.W., Bogeholz, P., Hughes, M.N., 2017. What is the source of baseflow in agriculturally fragmented catchments? Complex groundwater/surface-water interactions in three tributary catchments of the Wabash River, Indiana, USA. *Hydrol. Process.* 31, 4019–4038. <https://doi.org/10.1002/hyp.11345>
- Gao, Y., 2017. *Assess the Risk of Extreme Floods: Case Study: Houston, Texas*. The University of Texas at Austin.
- Gleeson, T., Manning, A.H., 2008. Regional groundwater flow in mountainous terrain: Three-dimensional simulations of topographic and hydrogeologic controls. *Water Resour. Res.* 44. <https://doi.org/10.1029/2008WR006848>
- Goodrich, D.C., Lane, L.J., Shillito, R.M., Miller, S.N., Woolhiser, A., 1997. Linearity of basin response as a function of scale in a semiarid watershed. *Water Resour. Res.* 33, 2951–2965.
- Govindaraju, R.S., Kavvas, M.L., 1991. Dynamics of Moving Boundary Overland Flows Over Infiltrating Surfaces at Hillslopes. *Water Resour. Res.* 27, 1885–1898. <https://doi.org/10.1029/91WR00689>
- Grimaldi, S., Petroselli, A., Arcangeletti, E., Nardi, F., 2013. Flood mapping in ungauged basins using fully continuous hydrologic-hydraulic modeling. *J. Hydrol.* 487, 39–47. <https://doi.org/10.1016/j.jhydrol.2013.02.023>
- Gunduz, O., Aral, M.M., 2005. River networks and groundwater flow: A simultaneous solution of a coupled system. *J. Hydrol.* 301, 216–234. <https://doi.org/10.1016/j.jhydrol.2004.06.034>

- Gupta, H.V., Sorooshian, S., Yapo, O.P., 1999. Status of Automatic Calibration for Hydrologic Models: Comparison with Multilevel Expert Calibration. *J. Hydrol. Eng.* 4, 135–143. <https://doi.org/10.1002/fut.20174>
- Hack, J.T., 1957. Studies of Longitudinal Stream Profiles in Virginia and Maryland. *Geol. Surv. Prof. Pap.* 294-B. <https://doi.org/10.3133/pp294B>
- Hall, J., Sayers, P., Dawson, R., 2005. National-scale assessment of current and future flood risk in England and Wales. *Nat. Hazards* 36, 147–164. <https://doi.org/10.1007/s11069-004-4546-7>
- Halverson, J.B., 2018. The Costliest Hurricane Season in U.S. History. *Weatherwise* 71, 20–27. <https://doi.org/10.1080/00431672.2018.1416862>
- Harris, I., Jones, P.D., Osborn, T.J., Lister, D.H., 2014. Updated high-resolution grids of monthly climatic observations - the CRU TS3.10 Dataset. *Int. J. Climatol.* 34, 623–642. <https://doi.org/10.1002/joc.3711>
- Hattermann, F., Krysanova, V., Wechsung, F., Wattenbach, M., 2004. Integrating groundwater dynamics in regional hydrological modelling. *Environ. Model. Softw.* 19, 1039–1051. <https://doi.org/10.1016/j.envsoft.2003.11.007>
- Highfield, W.E., Norman, S. a., Brody, S.D., 2013. Examining the 100-Year Floodplain as a Metric of Risk, Loss, and Household Adjustment. *Risk Anal.* 33, 186–191. <https://doi.org/10.1111/j.1539-6924.2012.01840.x>
- Hughes, A.G., Vounaki, T., Peach, D.W., Ireson, A.M., Jackson, C.R., Butler, A.P., Bloomfield, J.P., Finch, J., Wheater, H.S., 2011. Flood risk from groundwater: Examples from a Chalk catchment in southern England. *J. Flood Risk Manag.* 4, 143–155. <https://doi.org/10.1111/j.1753-318X.2011.01095.x>
- Hughes, D.A., 2010. Unsaturated zone fracture flow contributions to stream flow: Evidence for the process in South Africa and its importance. *Hydrol. Process.* 24, 767–774. <https://doi.org/10.1002/hyp.7521>
- Hughes, J.D., Liu, J., 2008. MIKE SHE: Software for integrated surface water/ground water modeling. *Ground Water* 46, 797–802. <https://doi.org/10.1111/j.1745-6584.2008.00500.x>
- Hunter, N.M., Bates, P.D., Horritt, M.S., Wilson, M.D., 2007. Simple spatially-distributed models for predicting flood inundation: A review. *Geomorphology* 90, 208–225. <https://doi.org/10.1016/j.geomorph.2006.10.021>
- Hutchins, M.G., McGrane, S.J., Miller, J.D., Hagen-Zanker, A., Kjeldsen, T.R., Dadson, S.J., Rowland, C.S., 2017. Integrated modeling in urban hydrology: reviewing the role of monitoring technology in overcoming the issue of ‘big data’ requirements. *Wiley Interdiscip. Rev. Water* 4, e1177. <https://doi.org/10.1002/wat2.1177>
- Hwang, H.-T., Park, Y.-J., Frey, S.K., Callaghan, M. V., Berg, S.J., Lapen, D.R., Sudicky, E.A., 2019. Efficient Numerical Incorporation of Water Management Operations in Integrated Hydrosystem Models: Application to Tile Drainage and Reservoir Operating Systems, *Journal of Hydrology*. Elsevier B.V. <https://doi.org/10.1016/j.jhydrol.2019.03.098>
- IPCC, 2014. Climate Change 2014: Synthesis Report. Contribution of Working Groups I, II and III to the Fifth Assessment Report of the Intergovernmental Panel on Climate Change [Core Writing Team, R.K. Pachauri and L.A. Meyer (eds.)]. IPCC, Geneva, Switz. 151. <https://doi.org/10.1046/j.1365-2559.2002.1340a.x>
- Ivanov, V.Y., Vivoni, E.R., Bras, R.L., Entekhabi, D., 2004. Catchment hydrologic response with a fully distributed triangulated irregular network model. *Water Resour. Res.* 40, 1–23. <https://doi.org/10.1029/2004WR003218>

- Ivkovic, K.M., Letcher, R. A., Croke, B.F.W., 2009. Use of a simple surface–groundwater interaction model to inform water management. *Aust. J. Earth Sci.* 56, 71–80. <https://doi.org/10.1080/08120090802541945>
- Jackson, S.R., Maidment, D.R., 2014. RiverML: A Harmonized Transfer Language for River Hydraulic Models, CRWR Online Report 14-5. Cent. Res. Water Resour. Univ. Texas Austin.
- Johnson, K.A., Smith, A.M., Fargione, J., Bates, P.D., Morefield, P., Wing, O.E.J., Sampson, C.C., 2018. Estimates of present and future flood risk in the conterminous United States. *Environ. Res. Lett.* 13, 034023. <https://doi.org/10.1088/1748-9326/aaac65>
- Jones, J.P., Sudicky, E.A., McLaren, R.G., 2008. Application of a fully-integrated surface-subsurface flow model at the watershed-scale: A case study. *Water Resour. Res.* 44, 1–13. <https://doi.org/10.1029/2006WR005603>
- Joyce, J., Chang, N. Bin, Harji, R., Ruppert, T., Singhofen, P., 2017. Cascade impact of hurricane movement, storm tidal surge, sea level rise and precipitation variability on flood assessment in a coastal urban watershed. *Clim. Dyn.* 0, 1–27. <https://doi.org/10.1007/s00382-017-3930-4>
- Kampf, S.K., Burges, S.J., 2007. A framework for classifying and comparing distributed hillslope and catchment hydrologic models. *Water Resour. Res.* 43. <https://doi.org/10.1029/2006WR005370>
- Kaser, D., Graf, T., Cochand, F., McLaren, R., Therrien, R., Brunner, P., 2014. Channel Representation in Physically Based Models Coupling Groundwater and Surface Water: Pitfalls and How to Avoid Them. *Groundwater* 52, 827–836. <https://doi.org/10.1111/gwat.12143>
- Kauffeldt, A., Wetterhall, F., Pappenberger, F., Salamon, P., Thielen, J., 2016. Technical review of large-scale hydrological models for implementation in operational flood forecasting schemes on continental level. *Environ. Model. Softw.* 75, 68–76. <https://doi.org/10.1016/j.envsoft.2015.09.009>
- Kidmose, J., Troldborg, L., Refsgaard, J.C., Bischoff, N., 2015. Coupling of a distributed hydrological model with an urban storm water model for impact analysis of forced infiltration. *J. Hydrol.* 525, 506–520. <https://doi.org/10.1016/j.jhydrol.2015.04.007>
- Kim, J., Warnock, A., Ivanov, V.Y., Katopodes, N.D., 2012. Coupled modeling of hydrologic and hydrodynamic processes including overland and channel flow. *Adv. Water Resour.* 37, 104–126. <https://doi.org/10.1016/j.advwatres.2011.11.009>
- Knebl, M.R., Yang, Z.-L., Hutchison, K., Maidment, D.R., 2005. Regional scale flood modeling using NEXRAD rainfall, GIS, and HEC-HMS/RAS: a case study for the San Antonio River Basin Summer 2002 storm event. *J. Environ. Manage.* 75, 325–36. <https://doi.org/10.1016/j.jenvman.2004.11.024>
- Ko, A., Mascaro, G., Vivoni, E.R., 2019. Strategies to Improve and Evaluate Physics-Based Hyperresolution Hydrologic Simulations at Regional Basin Scales. *Water Resour. Res.* 55, 1129–1152. <https://doi.org/10.1029/2018WR023521>
- Kollet, S., Sulis, M., Maxwell, R.M., Paniconi, C., Putti, M., Bertoldi, G., Coon, E.T., Cordano, E., Endrizzi, S., Kikinzon, E., Mouche, E., Mügler, C., Park, Y.-J., Refsgaard, J.C., Stisen, S., Sudicky, E., 2017. The integrated hydrologic model intercomparison project, IH-MIP2: A second set of benchmark results to diagnose integrated hydrology and feedbacks. *Water Resour. Res.* 53, 867–890. <https://doi.org/10.1002/2016WR019191>

- Kollet, S.J., Maxwell, R.M., 2008. Capturing the influence of groundwater dynamics on land surface processes using an integrated, distributed watershed model. *Water Resour. Res.* 44. <https://doi.org/10.1029/2007WR006004>
- Kollet, S.J., Maxwell, R.M., Woodward, C.S., Smith, S., Vanderborght, J., Vereecken, H., Simmer, C., 2010. Proof of concept of regional scale hydrologic simulations at hydrologic resolution utilizing massively parallel computer resources. *Water Resour. Res.* 46, 1–7. <https://doi.org/10.1029/2009WR008730>
- Kollet, S.S.J., Maxwell, R.R.M., 2006. Integrated surface – groundwater flow modeling : A free-surface overland flow boundary condition in a parallel groundwater flow model. *Adv. Water Resour.* 29, 945–958. <https://doi.org/10.1016/j.advwatres.2005.08.006>
- Kossin, J.P., 2018. A global slowdown of tropical-cyclone translation speed. *Nature* 558, 104–107. <https://doi.org/10.1038/s41586-018-0158-3>
- Kuiper, L.K., 1981. A comparison of the incomplete Cholesky-Conjugate Gradient Method with the strongly implicit method as applied to the solution of two-dimensional groundwater flow equations. *Water Resour. Res.* 17, 1082–1086. <https://doi.org/https://doi.org/10.1029/WR017i004p01082>
- Kundzewicz, Z.W., 2002. Non-structural Flood Protection and Sustainability. *Water Int.* 27, 3–13. <https://doi.org/10.1080/02508060208686972>
- Lane, L.J., Woolhiser, D.A., 1977. Simplifications of Watershed Geometry Affecting Simulation of Surface Runoff. *J. Hydrol.* 35, 173–190.
- Legleiter, C.J., Kyriakidis, P.C., McDonald, R.R., Nelson, J.M., 2011. Effects of uncertain topographic input data on two-dimensional flow modeling in a gravel-bed river. *Water Resour. Res.* 47, 1–24. <https://doi.org/10.1029/2010WR009618>
- Leopold, L.B., Maddock, T.J., 1953. The Hydraulic Geometry of Stream Channels and Some Physiographic Implications. *Geol. Surv. Prof. Pap.* 252, 57.
- Lerner, D.N., 1990. Groundwater recharge in urban areas. *Atmos. Environ.* 24B, 29–33. [https://doi.org/10.1016/0957-1272\(90\)90006-G](https://doi.org/10.1016/0957-1272(90)90006-G)
- Liang, D., Falconer, R.A., Lin, B., 2007. Coupling surface and subsurface flows in a depth averaged flood wave model. *J. Hydrol.* 337, 147–158. <https://doi.org/10.1016/j.jhydrol.2007.01.045>
- Liew, M.W. Van, Arnold, J.G., Bosch, D.D., 2005. Problems and Potential of Autocalibrating a Hydrologic Model. *Trans. ASAE* 48, 1025–1040.
- Lindner, J., Fitzgerald, S., 2018. Immediate Report – Final Hurricane Harvey - Storm and Flood Information. Harris Cty. Flood Control Dist. Houston, TX.
- Liu, G., Schwartz, F.W., Tseng, K.-H., Shum, C.K., 2015. Discharge and water-depth estimates for ungauged rivers: Combining hydrologic, hydraulic, and inverse modeling with stage and water-area measurements from satellites. *Water Resour. Res.* 51, 6017–6035. <https://doi.org/10.1002/2014WR016259>
- Maidment, D.R., 2016. Open Water Data in Space and Time. *J. Am. Water Resour. Assoc.* 52, 816–824. <https://doi.org/10.1111/1752-1688.12436>
- Mantilla, R., Gupta, V.K., J. Mesa, O., 2006. Role of coupled flow dynamics and real network structures on Hortonian scaling of peak flows. *J. Hydrol.* 322, 155–167. <https://doi.org/10.1016/j.jhydrol.2005.03.022>
- Martinez, J.B., 1989. Simulación Matemática de Cuencas Subterráneas, Flujo Impermanente Bidimensional. CIH, ISPJAE, Ciudad La Habana.

- Maxwell, R.M., Condon, L.E., Kollet, S.J., 2015. A high-resolution simulation of groundwater and surface water over most of the continental US with the integrated hydrologic model ParFlow v3. *Geosci. Model Dev.* 8, 923–937. <https://doi.org/10.5194/gmd-8-923-2015>
- Maxwell, R.M., Putti, M., Meyerhoff, S., Delfs, J.-O., Ferguson, I.M., Ivanov, V., Kim, J., Kolditz, O., Kollet, S.J., Kumar, M., Lopez, S., Niu, J., Paniconi, C., Park, Y.-J., Phanikumar, M.S., Shen, C., Sudicky, E.A., Sulis, M., 2014. Surface-subsurface model intercomparison: A first set of benchmark results to diagnose integrated hydrology and feedbacks. *Water Resour. Res.* 50, 1531–1549. <https://doi.org/10.1002/2013WR013725>
- McMillan, S.K., Noe, G.B., 2017. Increasing floodplain connectivity through urban stream restoration increases nutrient and sediment retention. *Ecol. Eng.* 108, 284–295. <https://doi.org/10.1016/j.ecoleng.2017.08.006>
- Meire, D., Doncker, L., Declercq, F., Buis, K., Troch, P., Verhoeven, R., 2010. Modelling river-floodplain interaction during flood propagation. *Nat. Hazards* 55, 111–121. <https://doi.org/10.1007/s11069-010-9554-1>
- Melsen, L.A., Teuling, A.J., Torfs, P.J.J.F., Uijlenhoet, R., Mizukami, N., Clark, M.P., 2015. HESS Opinions: The need for process-based evaluation of large-domain hyper-resolution models. *Hydrol. Earth Syst. Sci. Discuss.* 12, 13359–13381. <https://doi.org/10.5194/hessd-12-13359-2015>
- Merz, B., Thielen, A.H., 2005. Separating natural and epistemic uncertainty in flood frequency analysis. *J. Hydrol.* 309, 114–132. <https://doi.org/10.1016/j.jhydrol.2004.11.015>
- Meyles, E., Williams, A., Ternan, L., Dowd, J., 2003. Runoff generation in relation to soil moisture patterns in a small Dartmoor catchment, Southwest England. *Hydrol. Process.* 17, 251–264. <https://doi.org/10.1002/hyp.1122>
- Michel-Kerjan, E., Kunreuther, H., 2011. Redesigning Flood Insurance. *Science* (80-.). 333, 408–409. <https://doi.org/10.1126/science.1202616>
- Moench, A.F., Sauer, V.B., Jennings, M.E., 1974. Modification of routed streamflow by channel loss and base flow. *Water Resour. Res.* 10, 963–968. <https://doi.org/10.1029/WR010i005p00963>
- Montanari, M., Hostache, R., Matgen, P., Schumann, G., Pfister, L., Hoffmann, L., 2008. Calibration and sequential updating of a coupled hydrologic-hydraulic model using remote sensing-derived water stages. *Hydrol. Earth Syst. Sci. Discuss.* 5, 3213–3245. <https://doi.org/10.5194/hessd-5-3213-2008>
- Moore, C., Doherty, J., 2005. Role of the calibration process in reducing model predictive error. *Water Resour. Res.* 41. <https://doi.org/10.1029/2004WR003501>
- Moriasi, D.N., Arnold, J.G., Van Liew, M.W., Binger, R.L., Harmel, R.D., Veith, T.L., 2007. Model evaluation guidelines for systematic quantification of accuracy in watershed simulations. *Trans. ASABE* 50, 885–900. <https://doi.org/10.13031/2013.23153>
- Mukolwe, M.M., Baldassarre, G. Di, Werner, M., Solomatine, D.P., 2014. Flood modelling: parameterisation and inflow uncertainty. *Proc. Inst. Civ. Eng. Manag.* 167, 51–60. <https://doi.org/10.1680/wama.12.00087>
- Muleta, M.K., Nicklow, J.W., Bekele, E.G., 2007. Sensitivity of a Distributed Watershed Simulation Model to Spatial Scale. *J. Hydrol. Eng.* 12, 163–172. [https://doi.org/10.1061/\(ASCE\)1084-0699\(2007\)12:2\(163\)](https://doi.org/10.1061/(ASCE)1084-0699(2007)12:2(163))
- Nash, J.E., 1959. A note on the Muskingum flood-routing method. *J. Geophys. Res.* 64, 1053–1056. <https://doi.org/10.1029/JZ064i008p01053>

- Nash, J.E., Sutcliffe, J. V, 1970. River Flow Forecasting Through Conceptual Models Part I-A Discussion of Principles. *J. Hydrol.* 10, 282–290. [https://doi.org/10.1016/0022-1694\(70\)90255-6](https://doi.org/10.1016/0022-1694(70)90255-6)
- Noe, G.B., Hupp, C.R., 2005. Carbon, nitrogen, and phosphorus accumulation in floodplains of Atlantic Coastal Plain rivers, USA. *Ecol. Appl.* 15, 1178–1190. <https://doi.org/10.1890/04-1677>
- Ogden, F.L., Lai, W., Steinke, R.C., 2014. ADHydro: Quasi-3D high performance hydrological model. *Proc. SEDHYD 2015, 10th Interag. Sediment. Conf. 5th Fed. Interag. Hydrol. Model. Conf.* April 19–23, Reno, Nevada, USA.
- Ogden, F.L., Raj Pradhan, N., Downer, C.W., Zahner, J.A., 2011. Relative importance of impervious area, drainage density, width function, and subsurface storm drainage on flood runoff from an urbanized catchment. *Water Resour. Res.* 47, 1–12. <https://doi.org/10.1029/2011WR010550>
- Osei-Twumasi, A., Falconer, R.A., Ahmadian, R., 2016. Coupling Surface Water and Groundwater Flows in a Laboratory Model Using Foam as Artificial Groundwater Material. *Water Resour. Manag.* 30, 1449–1463. <https://doi.org/10.1007/s11269-016-1232-y>
- Pahar, G., Dhar, A., 2014. A dry zone-wet zone based modeling of surface water and groundwater interaction for generalized ground profile. *J. Hydrol.* 519, 2215–2223. <https://doi.org/10.1016/j.jhydrol.2014.09.088>
- Panday, S., Huyakorn, P.S., 2004. A fully coupled physically-based spatially-distributed model for evaluating surface/subsurface flow. *Adv. Water Resour.* 27, 361–382. <https://doi.org/10.1016/j.advwatres.2004.02.016>
- Paniconi, C., Putti, M., 2015. Physically based modeling in catchment hydrology at 50: Survey and outlook. *Water Resour. Res.* 51, 7090–7129. <https://doi.org/10.1002/2015WR017780>
- Pappenberger, F., Beven, K., Horritt, M., Blazkova, S., 2005. Uncertainty in the calibration of effective roughness parameters in HEC-RAS using inundation and downstream level observations. *J. Hydrol.* 302, 46–69. <https://doi.org/10.1016/j.jhydrol.2004.06.036>
- Pappenberger, F., Matgen, P., Beven, K.J., Henry, J.-B., Pfister, L., Fraipont, P., 2006. Influence of uncertain boundary conditions and model structure on flood inundation predictions. *Adv. Water Resour.* 29, 1430–1449. <https://doi.org/10.1016/j.advwatres.2005.11.012>
- Pathiraja, S., Westra, S., Sharma, A., 2012. Why continuous simulation? the role of antecedent moisture in design flood estimation. *Water Resour. Res.* 48, 1–15. <https://doi.org/10.1029/2011WR010997>
- Patil, S.D., Stieglitz, M., 2015. Comparing spatial and temporal transferability of hydrological model parameters. *J. Hydrol.* 525, 409–417. <https://doi.org/10.1016/j.jhydrol.2015.04.003>
- Peters-Lidard, C.D., Clark, M., Samaniego, L., Verhoest, N.E.C., van Emmerik, T., Uijlenhoet, R., Achieng, K., Franz, T.E., Woods, R., 2017. Scaling, Similarity, and the Fourth Paradigm for Hydrology. *Hydrol. Earth Syst. Sci. Discuss.* 21, 1–21. <https://doi.org/10.5194/hess-2016-695>
- Pfister, L., Drogue, G., El Idrissi, A., Humbert, J., Iffly, J.F., Matgen, P., Hoffmann, L., 2003. Predicting peak discharge through empirical relationships between rainfall, groundwater level and basin humidity in the Alzette river basin (grand-duchy of Luxembourg). *J. Hydrol. Hydromechanics* 51, 210–220.
- Pohlmann, F.K., 1987. An investigation of the Ground-Water Resources in the Wabash Valley Glacial Deposits near West Lafayette, Indiana. Purdue University.

- Ponce, V.M., 1979. Simplified Muskingum Routing Equation. *J. Hydraul. Div. ASCE* 105.
- Price, K., 2011. Effects of watershed topography, soils, land use, and climate on baseflow hydrology in humid regions: A review. *Prog. Phys. Geogr.* 35, 465–492.
<https://doi.org/10.1177/0309133311402714>
- Rajib, M.A., Merwade, V., Yu, Z., 2016. Multi-objective calibration of a hydrologic model using spatially distributed remotely sensed/in-situ soil moisture. *J. Hydrol.* 536, 192–207.
<https://doi.org/10.1016/j.jhydrol.2016.02.037>
- Rassam, D.W., Peeters, L., Pickett, T., Jolly, I., Holz, L., 2013. Accounting for surface-groundwater interactions and their uncertainty in river and groundwater models: A case study in the Namoi River, Australia. *Environ. Model. Softw.* 50, 108–119.
<https://doi.org/10.1016/j.envsoft.2013.09.004>
- Rawls, W.J., 2004. Pedotransfer functions for the United States. *Dev. Soil Sci.* 30, 437–447.
[https://doi.org/10.1016/S0166-2481\(04\)30023-1](https://doi.org/10.1016/S0166-2481(04)30023-1)
- Rawls, W.J., Brakensiek, D.L., 1982. Estimating Soil Water Retention from Soil Properties. *J. Irrig. Drain. Div.* 108, 166–171.
- Rawls, W.J., Brakensiek, D.L., Saxton, K.E., 1982. Estimation of Soil Water Properties. *Trans. ASAE* 25, 1316–1320. <https://doi.org/https://doi.org/10.13031/2013.33720>
- Richardson, C.J., Flanagan, N.E., Ho, M., Pahl, J.W., 2011. Integrated stream and wetland restoration: A watershed approach to improved water quality on the landscape. *Ecol. Eng.* 37, 25–39. <https://doi.org/10.1016/j.ecoleng.2010.09.005>
- Risser, M.D., Wehner, M.F., 2017. Attributable Human-Induced Changes in the Likelihood and Magnitude of the Observed Extreme Precipitation during Hurricane Harvey. *Geophys. Res. Lett.* 44, 12,457–12,464. <https://doi.org/10.1002/2017GL075888>
- Saksena, S., 2015. Investigating the role of DEM resolution and accuracy on flood inundation mapping, in: *World Environmental and Water Resources Congress 2015: Floods, Droughts, and Ecosystems - Proceedings of the 2015 World Environmental and Water Resources Congress.* pp. 2236–2243. <https://doi.org/10.1061/9780784479162.220>
- Saksena, S., Merwade, V., 2017a. Integrated Modeling of Surface-Subsurface Processes to Understand River- Floodplain Hydrodynamics in the Upper Wabash River Basin. *World Environ. Water Resour. Congr. 2017, ASCE May*, 60–68.
<https://doi.org/https://doi.org/10.1061/9780784480595.006>
- Saksena, S., Merwade, V., 2017b. Deterministic Approach to Identify Ordinary High Water Marks Using Hydrologic and Hydraulic Attributes. *J. Irrig. Drain. Eng.* 143, 1–15.
[https://doi.org/10.1061/\(ASCE\)IR.1943-4774.0001148](https://doi.org/10.1061/(ASCE)IR.1943-4774.0001148).
- Saksena, S., Merwade, V., 2015. Incorporating the effect of DEM resolution and accuracy for improved flood inundation mapping. *J. Hydrol.* 530, 180–194.
<https://doi.org/10.1016/j.jhydrol.2015.09.069>
- Saksena, S., Merwade, V., Singhofen, P.J., 2019. Flood inundation modeling and mapping by integrating surface and subsurface hydrology with river hydrodynamics. *J. Hydrol.* 575, 1155–1177. <https://doi.org/10.1016/j.jhydrol.2019.06.024>
- Saleh, F., Flipo, N., Habets, F., Ducharme, A., Oudin, L., Viennot, P., Ledoux, E., 2011. Modeling the impact of in-stream water level fluctuations on stream-aquifer interactions at the regional scale. *J. Hydrol.* 400, 490–500. <https://doi.org/10.1016/j.jhydrol.2011.02.001>
- Salvadore, E., Bronders, J., Batelaan, O., 2015. Hydrological modelling of urbanized catchments: A review and future directions. *J. Hydrol.* 529, 62–81.
<https://doi.org/10.1016/j.jhydrol.2015.06.028>

- Sarkar, S., Singh, R.P., Chauhan, A., 2018. Anomalous changes in meteorological parameters along the track of 2017 Hurricane Harvey. *Remote Sens. Lett.* 9, 487–496. <https://doi.org/10.1080/2150704X.2018.1441562>
- Schaper, D., 2017. 3 reasons Houston was a “sitting duck” for Harvey flooding. *Natl. Public Radio* 1–13.
- Schilling, K.E., Jha, M.K., Zhang, Y.-K., Gassman, P.W., Wolter, C.F., 2008. Impact of land use and land cover change on the water balance of a large agricultural watershed: Historical effects and future directions. *Water Resour. Res.* 44. <https://doi.org/10.1029/2007WR006644>
- Schmadel, N.M., Ward, A.S., Lowry, C.S., Malzone, J.M., 2016. Hyporheic exchange controlled by dynamic hydrologic boundary conditions. *Geophys. Res. Lett.* 43, 4408–4417. <https://doi.org/10.1002/2016GL068286>
- Schoups, G., Hopmans, J.W., Young, C.A., Vrugt, J.A., Wesley, W., Tanji, K.K., Panday, S., 2005. Sustainability of irrigated agriculture in the San Joaquin Valley, California. *Proc. Natl. Acad. Sci. U. S. A.* 102, 15352–15356.
- Schumann, G., Matgen, P., Hoffmann, L., Hostache, R., Pappenberger, F., Pfister, L., 2007. Deriving distributed roughness values from satellite radar data for flood inundation modelling. *J. Hydrol.* 344, 96–111. <https://doi.org/10.1016/j.jhydrol.2007.06.024>
- Schumann, G.J.-P., Andreadis, K.M., Bates, P.D., 2014. Downscaling coarse grid hydrodynamic model simulations over large domains. *J. Hydrol.* 508, 289–298. <https://doi.org/10.1016/j.jhydrol.2013.08.051>
- Schuol, J., Abbaspour, K.C., 2006. Calibration and uncertainty issues of a hydrological model (SWAT) applied to West Africa. *Adv. Geosci.* 9, 137–143. <https://doi.org/10.5194/adgeo-9-137-2006>
- Sebastian, T., Lendering, K., Kothuis, B., Brand, N., Jonkman, B., van Gelder, P., Godfroij, M., Kolen, B., Comes, T., Lhermitte, S., 2017. Hurricane Harvey Report: A fact-finding effort in the direct aftermath of Hurricane Harvey in the Greater Houston Region. *Delft Delft Univ. Publ.* 102.
- Seyfried, M.S., Wilcox, B.P., 1995. Scale and the nature of spatial variability : Field examples having implications for hydrologic modeling. *Water Resour. Res.* 31, 173–184. <https://doi.org/https://doi.org/10.1029/94WR02025>
- Shokri, A., Bardsley, W.E., 2016. Development, testing and application of DrainFlow: A fully distributed integrated surface-subsurface flow model for drainage study. *Adv. Water Resour.* 92, 299–315. <https://doi.org/10.1016/j.advwatres.2016.04.013>
- Singhofen, P.J., McClung, G.L., 2014. Integrated 2D Surface-Groundwater Modeling of the Green Swamp, Florida. *Proc. 2014 ESRI User Conf. San Diego, CA.*
- Sivapalan, M., Blöschl, G., Zhang, L., Vertessy, R., 2003. Downward approach to hydrological prediction. *Hydrol. Process.* 17, 2101–2111. <https://doi.org/10.1002/hyp.1425>
- Skøien, J.O., Blöschl, G., Western, A.W., 2003. Characteristic space scales and timescales in hydrology. *Water Resour. Res.* 39. <https://doi.org/10.1029/2002WR001736>
- Sorooshian, S., Duan, Q.Y., Gupta, V.K., 1993. Calibration of Rainfall-Runoff Models - Application of Global Optimization to the Sacramento Soil-Moisture Accounting Model. *Water Resour. Res.* 29, 1185–1194. <https://doi.org/10.1029/92WR02617>
- Stisen, S., Jensen, K.H., Sandholt, I., Grimes, D.I.F., 2008. A remote sensing driven distributed hydrological model of the Senegal River basin. *J. Hydrol.* 354, 131–148. <https://doi.org/10.1016/j.jhydrol.2008.03.006>

- Straatsma, M., Huthoff, F., 2011. Uncertainty in 2D hydrodynamic models from errors in roughness parameterization based on aerial images. *Phys. Chem. Earth* 36, 324–334. <https://doi.org/10.1016/j.pce.2011.02.009>
- Streamline Technologies, 2018. ICPR4 Technical Reference Manual. Streamline Technol. Inc., Winter Springs, Florida. www.streamnologies.com/misc/ICPR4_DOCS.zip
- Streamline Technologies, 2016. ICPR4 Validation Report. Streamline Technol. Inc., Winter Springs, Florida. www.streamnologies.com/misc/ICPR4_DOCS.zip
- Sulis, M., Meyerhoff, S.B., Paniconi, C., Maxwell, R.M., Putti, M., Kollet, S.J., 2010. A comparison of two physics-based numerical models for simulating surface water-groundwater interactions. *Adv. Water Resour.* 33, 456–467. <https://doi.org/10.1016/j.advwatres.2010.01.010>
- Teng, J., Jakeman, A.J., Vaze, J., Croke, B.F.W., Dutta, D., Kim, S., 2017. Flood inundation modelling: A review of methods, recent advances and uncertainty analysis. *Environ. Model. Softw.* 90, 201–216. <https://doi.org/10.1016/j.envsoft.2017.01.006>
- Tuttle, A.K., McMillan, S.K., Gardner, A., Jennings, G.D., 2014. Channel complexity and nitrate concentrations drive denitrification rates in urban restored and unrestored streams. *Ecol. Eng.* 73, 770–777. <https://doi.org/10.1016/j.ecoleng.2014.09.066>
- USGS, 2006. Estimated Percentage of Impervious Surface in Indiana in 2006, Derived from the 2006 National Land Cover Database (United States Geological Survey, 30-Meter TIFF Image). *Indiana Geol. Surv.*
- van Oldenborgh, G.J., van der Wiel, K., Sebastian, A., Singh, R., Arrighi, J., Otto, F., Haustein, K., Li, S., Vecchi, G., Cullen, H., 2018. Attribution of extreme rainfall from Hurricane Harvey, August 2017. *Environ. Res. Lett.* 13. <https://doi.org/https://doi.org/10.1088/1748-9326/aa9ef2>
- VanderKwaak, J.E., Loague, K., 2001. Hydrologic-response simulations for the R-5 catchment with a comprehensive physics-based model. *Water Resour. Res.* 37, 999–1013. <https://doi.org/10.1029/2000WR900272>
- Viero, D.P., Peruzzo, P., Carniello, L., Defina, A., 2014. Integrated mathematical modeling of hydrological and hydrodynamic response to rainfall events in rural lowland catchments. *Water Resour. Res.* 50, 5941–5957. <https://doi.org/10.1002/2013WR014293>
- Vivoni, E., Entekhabi, D., Bras, R.L., Ivanov, V., 2007. Controls on runoff generation and scale-dependence in a distributed hydrologic model. *Hydrol. Earth Syst. Sci.* 11, 1683–1701. <https://doi.org/10.5194/hessd-4-983-2007>
- Vivoni, E.R., Ivanov, V.Y., Bras, R.L., Entekhabi, D., 2005. On the effects of triangulated terrain resolution on distributed hydrologic model response. *Hydrol. Process.* 19, 2101–2122. <https://doi.org/10.1002/hyp.5671>
- Weaver, C., Feaster, T., Robbins, J., 2016. Preliminary Peak Stage and Streamflow Data at Selected Streamgaging Stations in North Carolina and South Carolina for Flooding Following Hurricane Matthew, October 2016. *United States Geol. Surv. Open-File Rep.* 2016-1205 38. <https://doi.org/https://doi.org/10.3133/ofr20161205>
- Werner, M.G.F., Hunter, N.M., Bates, P.D., 2005. Identifiability of distributed floodplain roughness values in flood extent estimation. *J. Hydrol.* 314, 139–157. <https://doi.org/10.1016/j.jhydrol.2005.03.012>
- Winter, T.C., Harvey, J.W., Franke, O.L., Alley, W.M., 1999. Ground water and surface water: a single resource, U.S. Geological Survey Circular 1139.

- Wood, E.F., Sivapalan, M., Beven, K., Band, L., 1988. Effects of spatial variability and scale with implications to hydrologic modeling. *J. Hydrol.* 102, 29–47. [https://doi.org/10.1016/0022-1694\(88\)90090-X](https://doi.org/10.1016/0022-1694(88)90090-X)
- Woods, R.A., Sivapalan, M., Robinson, J.S., 1997. Modeling the spatial variability of subsurface runoff using a topographic index. *Water Resour. Res.* 33, 1061–1073. <https://doi.org/https://doi.org/10.1029/97WR00232>
- Wu, Y.H., Woolhiser, D.A., Yevjevich, V., 1982. Effects of spatial variability of hydraulic resistance of runoff hydrographs. *J. Hydrol.* 59, 231–248. [https://doi.org/10.1016/0022-1694\(82\)90089-0](https://doi.org/10.1016/0022-1694(82)90089-0)
- Xie, Z., Su, F., Liang, X., Zeng, Q., Hao, Z., Yufu, G., 2003. Applications of a Surface Runoff Model with Horton and Dunne Runoff for VIC. *Adv. Atmos. Sci.* 20, 165–172.
- Yu, Z., Lu, Q., Zhu, J., Yang, C., Ju, Q., Yang, T., Chen, X., Sudicky, E.A., 2014. Spatial and Temporal Scale Effect in Simulating Hydrologic Processes in a Watershed. *J. Hydrol. Eng.* 19, 99–107. [https://doi.org/10.1061/\(ASCE\)HE.1943-5584.0000762](https://doi.org/10.1061/(ASCE)HE.1943-5584.0000762)
- Zehe, E., Blöschl, G., 2004. Predictability of hydrologic response at the plot and catchment scales: Role of initial conditions. *Water Resour. Res.* 40, 1–21. <https://doi.org/10.1029/2003WR002869>
- Zhang, H.L., Wang, Y.J., Wang, Y.Q., Li, D.X., Wang, X.K., 2013. The effect of watershed scale on HEC-HMS calibrated parameters: A case study in the Clear Creek watershed in Iowa, US. *Hydrol. Earth Syst. Sci.* 17, 2735–2745. <https://doi.org/10.5194/hess-17-2735-2013>

VITA

Siddharth Saksena graduated with a Bachelor of Technology in Civil Engineering from the Indian Institute of Technology (IIT) Roorkee, India in 2012. He joined the graduate program in the Lyles School of Civil Engineering at Purdue University in 2012 and received a Master of Science in Civil Engineering in 2014. He continued to pursue his Doctor of Philosophy degree at Purdue University. His research focuses on quantifying the heterogeneity in complex physical processes that governs the watershed response during flooding and integrating surface, subsurface, and river hydrodynamics in a single system for improved flood risk estimation across large watershed scales. Recently, he has been working on developing a hyper-resolution distributed flood modeling framework for urban environments and evaluating the impact of land use change on future flood risk. He received the Consortium of Universities for Advancement of Hydrologic Sciences' (CUAHSI) Pathfinder Fellowship in 2017, as well as Purdue University's CE Munson Teaching Award in 2018.